On the assessment of numerical interface capturing methods for two fluid flow applications

By

Abdulaleem Albadawi
B.Sc., M.Sc.

A dissertation submitted in fulfillment of the requirements
for the award of the degree of
Doctor of Philosophy (Ph.D.)

Supervisor: Dr. Yan Delauré

School of Mechanical and Manufacturing Engineering
Dublin City University

July 2014

DECLARATION

I hereby certify that this material, which I now submit for assessment on the programme of study leading to the award of Ph.D. is entirely my own work, that I have exercised reasonable care to ensure that the work is original, and does not to the best of my knowledge breach any law of copyright, and has not been taken from the work of others save and to the extent that such work has been cited and acknowledged within the text of my work.

Signed: ID No.:59122749

Abdulaleem Albadawi

Date:

Acknowledgement

I wish to express my gratitude to my supervisor, Dr. Yann Delauré, for his continued support, guidance and constructive criticism. I feel privileged to have been able to work with him. I am truly thankful for everything he has done to help me to build the firm stepping stone towards my future career in the CFD domain.

Herewith, I would like to take the opportunity to express my gratitude and thanks to Professor Darina Murray and Dr. Anthony Robinson, the research collaborative team at the Fluid and Heat Transfer Research Group in Trinity College Dublin (Ireland), for their vital support and invaluable insights into the physics of the two-fluid flow processes. Special thanks to the team member Mr. David Donoghue for working hard to provide me with the valuable benchmarking experimental data.

I am also thankful to the staff of School of Mechanical and Manufacturing Engineering and the technical staff responsible for the DCU Sci-Sym Ampato cluster.

Special thanks to my father, my stepmother, and all my brothers and sisters for their never ending support and love. Despite the humanitarian situation in Syria and its dire consequences on their life, their endless support during my PhD is really far beyond words. Special thanks go also to my brother Dr. Abdulghani Albadawi for his support and guidance during my academic life. Thanks also go to all my friends and colleagues, with whom I shared very enjoyable and happy moments during the PhD.

Finally, the financial support by the Science Foundation Ireland under its Research Frontiers Programme (grant number 09/RFP/ENM2151) is acknowledged.

Dublin, In January, 2014 Abdulaleem Albadawi

To

My Dad and the soul of my Mum

Who Generously Devoted Their Lives to My Success and Pictured Their Own Happiness in My Achievements

Contents

Abstract

Two-fluid flows play an important role in many industrial applications. One attractive property is their ability to induce significant increases in mass and/or heat transfer. Bouncing and sliding bubbles are one of the two-fluid flow mechanisms which are known to give rise to very high heat transfer coefficients in heat exchangers. The present study of the full process of bubble growth, rise, impact, and bounce presents particular challenges because of the interaction between the three phases (gas, liquid, and solid) and in particular at the triple contact line.

The present work attempts to answer the following question: "To what extent can the available numerical interface capturing methods and contact line boundary conditions capture the correct behavior of bubble dynamics under several two-fluid flow processes (bubble growth, detachment, rise, and bounce)?"

Three different numerical methods (Volume of Fluid (VOF), Level Set (LS), and coupled CLSVOF) are considered. The wetting dynamics of the bubble against solid surfaces are modeled using both static and dynamic contact angles. The numerical simulations are performed using both commercial and open source softwares (ANSYS-Fluent®-v13, OpenFOAM®, and TransAT©). A simple coupled VOF with LS method (S-CLSVOF) for improved surface tension implementation is also proposed and tested by comparison against the standard VOF solver in OpenFOAM. The numerical results are assessed by comparison against experimental data obtained by a research team at the Fluid and Heat Transfer Research Group in Trinity College Dublin (Ireland) as a part of a collaborative project funded by the Science Foundation of Ireland.

The assessment of the numerical results highlights the strong sensitivity of the bubble dynamics predicted numerically on the implemented surface tension model, the interface capturing method, and the Capillary number. The analysis of the bubble dynamics during the bouncing process demonstrates the importance of refining the mesh at solid surfaces in order to capture accurately the bubble behavior during the collision process.

Nomenclature

Latin Letters

Symbol	Description
a	Constant
$\mathbf{a}$	Random vector variable
$[A]$	Square matrix
AR	Bubble aspect ratio
AR_{emp}	Empirical aspect ratio
AR_{∞}	Terminal aspect ratio during bubble rise
b	Constant
$[b]$	Source term matrix
Bo	Bond number $g\Delta\rho D_{eq}^2/\sigma$
c	Constant
C	Volume fraction in diffuse interface method
c_{α}	Compression factor
C_M	Added mass coefficient
Ca	Capillary number $V_b\mu_l/\sigma$
Ca_{slip}	Slip Capillary number $u_{slip}\mu_l/\sigma$
CGy	Bubble center of gravity in the gravitational direction
Co	Courant number
Co_{max}	Maximum Courant number
$Co_{\alpha,max}$	Maximum interface Courant number
Co_{min}	Minimum Courant number
$\mathbf{d}$	Distance vector between owner cell and neighbor cell centers
D	Bubble diameter
D_{eq}	Bubble equivalent diameter
E	Error
f	Cell face

Symbol	**Description**
F_B	Buoyancy force
F_C	Capillary force
F_{CP}	Contact pressure force
F_D	Dynamic force
f_d	Linear interpolation weight in TVD scheme
F_f	Mass flux through the cell face f
$\mathbf{F}_\sigma$	Volumetric surface tension force
$\mathbf{g}$	Gravitational acceleration vector
$H(\phi)$	Heaviside function
K	Dimensional length in contact angle models
l_1	Average norm
l_∞	Maximum norm
L_{cap}	Capillary length
M	Mobility
m_1	Number of cells in the numerical domain
m_2	Number of cells in the numerical domain that have $\delta \neq 0$
Mo	Morton number $g\mu_l^4 \Delta\rho / \rho_l^2 \sigma^3$
$\hat{\mathbf{n}}$	Corrected unit interface normal satisfying the angle θ_i
$\hat{\mathbf{n}}_c$	Unit interface normal (calculated from the gradient of any indicator function)
$\hat{\mathbf{n}}_w$	Unit normal vector to the wall
N_x	Number of cells in x-direction
N_y	Number of cells in y-direction
Oh	Ohnesorge number $Oh = \mu_l / (\sigma \rho_l D)^{0.5}$
P	Static pressure
P_g	Gas pressure inside the bubble
P_{rgh}	Modified pressure
P_T	Liquid pressure at the bubble apex
$\dot{Q}$	Volumetric flow rate
$\dot{Q}_{crit}$	Critical volumetric flow rate
r	r-factor in TVD scheme
r_{macro}	Macroscopic length scale
r_{micro}	Microscopic length scale
R_0	Initial radius
R_c	Capillary radius

Symbol	**Description**
R_{eq}	Bubble equivalent radius
R_{det}	Detachment radius
R_{ini}	Initial bubble radius
R_{neck}	Neck radius
$\dot{R}_{neck}$	Time variation of the neck radius
R_o	Orifice radius
Re	Reynolds number $\rho_l V_\infty D_{eq}/\mu_l$
s	Cell surface
$\mathbf{S}_f$	Face area normal vector
t	Time
t_{det}	Detachment time
t_n	Non-dimensional time
t_p	Detachment time $t_p = t - t_{det}$
t_{phys}	Real physical time
$\hat{\mathbf{t}}_w$	Unit tangential vector to the wall
T_w	Total dissipation at the contact line region
u_1	Tangential velocity at the first cell close to the wall
u_{slip}	Contact line slip velocity
U	Velocity of solid wall
v	Cell volume
v_0	Inflow velocity
v_{max}	Maximum velocity at the inflow
v_P	Owner cell volume
$\mathbf{V}$	Velocity field vector
$\mathbf{V}_c$	Compression velocity
$\mathbf{V}_f$	Interpolated velocity field vector at the cell face
$\mathbf{V}_N$	Velocity field at the neighbor cell center
$\mathbf{V}_P$	Velocity field at the owner cell center
V_∞	Magnitude of the bubble terminal velocity
V_b	Magnitude of the bubble velocity
V_{det}	Bubble detachment volume
V_{eq}	Bubble equivalent volume
V_s	Bubble volume in the regions radially outward the orifice rim
V_T	Tate volume
W	Bubble width

Symbol	Description
We	Weber number $We = \rho_l D_{eq} V_\infty^2 / \sigma$
We_{local}	Local Weber number at the bubble neck $We_{local} = \rho_l \dot{R}_{neck}^2 R_{neck} / \sigma$
x	Cartesian coordinate
$\mathbf{x}$	Position vector
$\{x\}$	Variable field
x_{max}	Macroscopic length scale
x_{min}	Microscopic length scale
$\mathbf{x}_N$	Position vector of neighbor cell center
$\mathbf{x}_P$	Position vector of owner cell center
y	Cartesian coordinate
z	Cartesian coordinate

Greek Letters

Symbol	Description
α	Volume of Fluid fraction function
β	Complement value of the volume fraction $\beta = 1 - \alpha$
γ	Fluid indicator function
$\dot{\gamma}$	Shear rate at the interface
Γ	Initial LS value in the S-CLSVOF solver
δ_s	Dimensional coefficient $1/max(\frac{\mathbf{S}_f}{\lvert\mathbf{S}_f\rvert} \cdot \mathbf{d}, 0.05\lvert\mathbf{d}\rvert)$
Δ	Mesh space step size
ΔP_0	Pressure difference between bubble center and wall boundary
ΔP_{total}	Pressure difference in the averaged values inside and outside the bubble
$\Delta P_{partial}$	Pressure difference in the averaged values inside and outside the bubble ignoring the diffusion area
ΔP_{exact}	Exact pressure difference between inside and outside the bubble
Δt_{max}	Maximum time step determined by the user
Δx	Mesh step size on x-direction
$\Delta \tau$	Artificial time step size
ε	Interface thickness
ζ	Exponential power decay in the detachment volume

Symbol	**Description**
θ	Instantaneous contact angle
θ_{adv}	Advancing contact angle
θ_{app}	Apparent contact angle
θ_d	Dynamic contact angle
θ_e	Equilibrium contact angle
θ_i	Numerically implemented contact angle
θ_m	Microscopic contact angle
θ_{rec}	Receding contact angle
θ_s	Static contact angle
θ_α	Contact angle calculated from the gradient of VOF function
κ	Interface curvature
κ_{exact}	Exact value of the bubble curvature
λ	Interpolation factor in TVD scheme
μ	Mixture viscosity
μ_g	Gas viscosity
μ_l	Liquid viscosity
ν	Mixture kinematic viscosity
ξ	Interface compression limiter
ρ	Mixture density
ρ_g	Gas density
ρ_l	Liquid density
σ	Surface tension coefficient
τ	Artificial time step
τ_s	Viscous shear stress
φ	Chemical potential
ϕ	Level Set function
ϕ_{corr}	Number of artificial iterations
χ	Factor that determines the flow direction in TVD scheme
ψ	Random variable
Ψ	Bulk energy density
$\Psi(r)$	TVD limiter
ω	Exponential power parameter of the neck radius

Subscripts

Symbol	Description
0	Initial
∞	Terminal
app	Apparent
adv	Advancing
b	Bubble
c	Calculated
cap	Capillary
emp	Empirical
d	Dynamic
det	Detachment
e	Equilibrium
eq	Equivalent diameter
f	Face value
g	Gas
i	Implemented
ini	Initial
(i,j)	Cell indicator in Cartesian coordinates
l	Liquid
m	Microscopic
macro	Macroscopic
micro	Microscopic
n	Normal
N	Neighbor cell
o	Orifice
P	Owner cell
phys	Physical
rec	Receding
s	Static
S	Solid
slip	Slip
t	Tangential

Superscripts

Symbol	Description
$\tilde{}$	intermediate value
0	Initial time step value
1	First time step value
n	Old time value
$n+1$	New time value
R	Reconstructed
α	Volume fraction
β	Compressive volume fraction

Abbreviations

Symbol	Description
$2D$	Two-dimensional
$3D$	Three-dimensional
$Axi-Sym$	Axi-symmetrical
BC	Boundary condition
CD	Central differencing
CFD	Computational Fluid Dynamics
$CICSAM$	Compressive interface capturing scheme for arbitrary meshes
$CLSVOF$	Coupled LS with VOF method
$CLSVOF-Geo$	Geometrical coupled LS with VOF method
CPU	Central processing unit
CSF	Continuum surface force model
$D-A$	Donor-Acceptor method
DIC	Diagonal incomplete Cholesky
$DILU$	Diagonal incomplete LU pre-conditioner
emp	Empirical
ENO	Essentially non-oscillatory scheme
Exp	Experimental
FCT	Flux corrected transport scheme

Symbol	**Description**
GFM	Ghost fluid method
$GNBC$	Generalized Navier Boundary condition
HF	Height function method
$HLSVC$	Hybrid Level Set Volume Constraint method
$HRIC$	High resolution interface capturing scheme
KE	Kinetic energy
LS	Level Set method
NS	Navier Stokes
NVD	Normalized variable diagram
$PBiCG$	Preconditioned bi-conjugate gradient algorithm
PBM	Pressure boundary method
PE	Potential energy
$PISO$	Pressure implicit with splitting operators solver
$PLIC$	Piecewise linear interface calculation algorithm
PLS	Particle Level Set method
$PROST$	Parabolic reconstruction of surface tension technique
RGB	Red Green Blue
$RLSG$	Refined Level Set Grid method
$S - CLSVOF$	Simplified coupled CLSVOF method
$SIMPLE$	Semi implicit method for pressure linked equations
$SLIC$	Simple line interface calculation algorithm
SSF	Sharp surface tension force
$TPCL$	Three phase contact line
TVD	Total variation diminishing
$TVD - RK$	Total variation diminishing Rung-Kutta scheme
VOF	Volume of Fluid method
$VOF - Comp$	Compressive Volume of Fluid method
$VOF - Geo$	Geometrical Volume of Fluid method
vol	Volume
$WENO$	Weighted essentially non-oscillatory scheme
$Y - VOF$	Youngs VOF method

List of Figures

List of Tables

1 Introduction

1.1 Background

Two-fluid flows have received significant attention over recent decades due to their impact on several industrial applications such as bubble reactors, heat exchangers, nucleate pool boiling power plants, oil extraction, and flotation applications. The growth, detachment and dispersion of gas bubbles can induce significant and desirable convective mixing in the surrounding liquid phase. This may be used for local enhancement of mass or heat transfer from surfaces at the point of nucleation or gas injection but also to entrain heat or mass in the bubble wake with vortices playing an important role in the convective mixing (Delauré, Chan and Murray, 2003). Uniform distribution of small bubbles may be sought to achieve large mass transfer areas, for example for the aeration of biological processes (Martín, Montes and Galán, 2007; Painmanakula et al., 2004). Gas injection can also be used to create slug flows of rising Taylor bubbles and liquid plugs for example to increase permeate flux through filtration membranes in ultrafiltration applications (Taha and Cui, 2002; Cabassud, Laborie and Lainé, 1997). In heat exchangers where boiling occurs, vapor bubbles are known to enhance heat transfer as a result of both phase change and strong convective mixing (Cornwell, 1990). Although the benefits of two-fluid or two-phase flows are well documented, certain aspects of the bubble dynamics remain unclear.

The present study is concerned with the direct injection of an air bubble in water and considers bubble growth, detachment, rise and then impact on a solid horizontal surface. This work is intended to lead to further research on the impact of isolated bubble on heat transfer from immersed solid surface as it slides and bounces through thermal boundary layers.

The two aspects of bubble growth and bouncing are of primarily interest in the present work. Both are known to depend on several physical and geometrical properties which are still the focus of much research. The interaction between the different

phases as well as between the fluid/fluid interface and the solid surfaces present particular challenges affecting both numerical and experimental studies. Numerically, recent advances in two-fluid flow numerical methods have made more in depth investigations possible. However, it is still uncertain whether the most commonly used methods, in their current form, are capable of capturing accurately the bubble and the flow behavior under several critical conditions. The primary aim of the present research is to implement and validate several numerical methods for the study of bubble dynamics during both bubble growth and bouncing processes under adiabatic conditions. To the author's knowledge, there are no numerical analyses in the literature that cover the full process of bubble injection, detachment, rise and impact as a single process. Moreover, only a limited number of publications has covered the numerical simulations of a separated process using three-dimensional (3D) domains.

Fig. 1.1 shows a schematic diagram of the successive stages that the gas bubble undergoes during the process under investigation. The bubble growth and detachment is studied first. The bubble is formed by injecting the gas into a wall orifice using low flow rates in order to generate isolated bubbles. Following detachment, the bubble rises freely in the bulk liquid. The parameters of interest in this case include the bubble geometrical characteristics before impact. The distance the bubble travels, for instance, plays an important role in determining the bubble characteristics during the bouncing. The last stage of the process is concerned with the bouncing against the solid surface following impact. This is controlled mainly by two factors: the bubble geometrical characteristics and the surface material properties. The influence of the mesh resolution and the interface contact model are of particular importance in this case.

Over the past two decades, several numerical models have been developed for the study of two-fluid flow problems. One family of such methods relies on the solution of the full Navier Stokes (NS) equations coupled with an interface capturing technique to track the gas/liquid interface position. Several interface capturing methods, namely Volume of Fluid (VOF), Level Set (LS) and Coupled VOF with LS (CLSVOF) methods, have been developed and all are considered in the present research. They are known as 'one-fluid' methods because the two fluids in the numerical domain are defined as one single mixture with a special function being used to distinguish between the two fluids (phases) in the mixture. Each numerical method has its own pros and cons which makes it more appropriate for certain specific applications. The method's suitability can be characterized by its accuracy, simplicity of

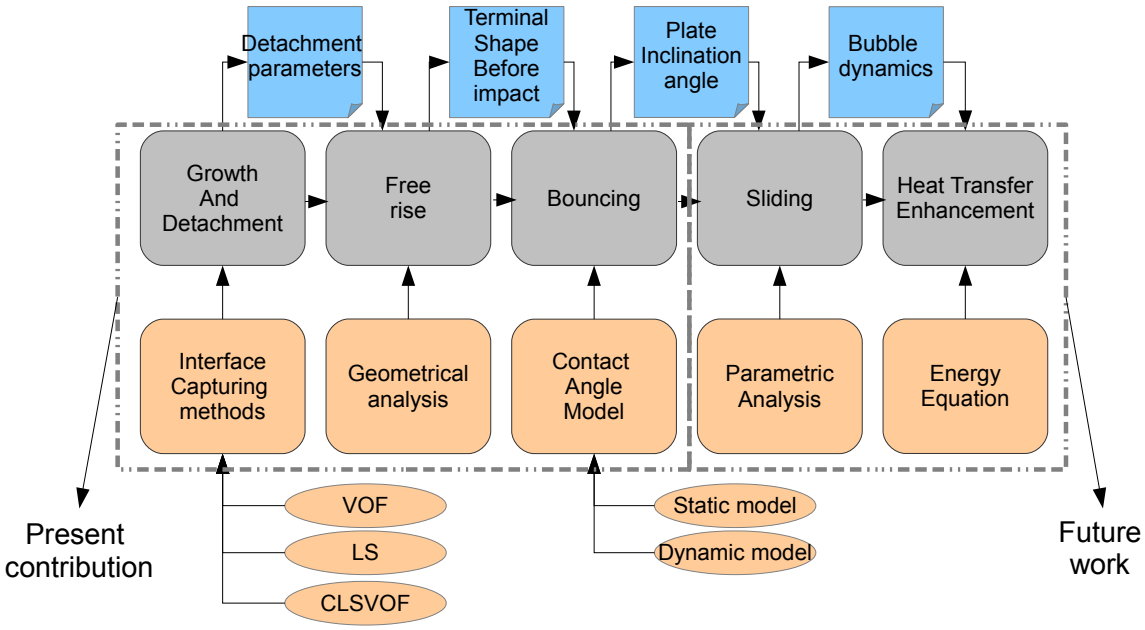

Figure 1.1: Schematic diagram of the different stages that the bubble goes through during the present work (Left dashed box) and other possible stages that might be studied in future works (right dashed box). The gray, orange, and blue boxes indicate the different possible stages, the different numerical models, and the physical parameters under investigation respectively.

implementation, generality, and computational efficiency. In this research, both the geometrical Volume of Fluid and Level Set methods implemented in the commercial softwares ANSYS-Fluent®-v13 and TransAT© respectively are considered for the study of bubble growth and detachment. Furthermore, the compressive Volume of Fluid method implemented in the open source library package OpenFOAM® is used for the study of both bubble growth and bouncing. The compressive VOF solver is also extended to a coupled LS with VOF method called in this thesis (S-CLSVOF). Whilst several commercial and open source softwares are employed in the present work, it is important to highlight that the main objective of this research is to investigate the suitability of some of the interface capturing methods implemented in these packages for the specific applications rather than carrying out a comprehensive assessment of the softwares.

1.2 Research objectives

The first aim of the present study is to assess the accuracy of different interface capturing methods for predicting bubble growth and detachment. The accurate modeling of the formation process is an essential step towards the study of the bubble rise and impact. This is due to the strong influence of the growth process on the bubble shape and trajectory after detachment. Although a few comparative studies between the interface capturing methods (VOF, LS, and CLSVOF) may be found in the literature, none have addressed the bubble growth and detachment. The numerical model of the full bubble formation and detachment, when the bubble is exposed to large topological changes, has generally not been compared adequately against experimental data.

The injection of the gas bubble is performed in this study using low volumetric flow rates so that small isolated bubbles are generated. The low flow rate ensures that the bubble forms under capillary dominant conditions so that surface tension plays an important role on the bubble behavior during the growth. The increased sensitivity to surface tension stresses allows for a better investigation of the suitability of the numerical methods and their surface tension model. The compressive VOF method implemented in OpenFOAM is extended into a simple coupled code (S-CLSVOF) that is shown to be better able to model capillary dominant fluid flow problems. The extension was found to be necessary to avoid spurious oscillations in the bubble positions before oscillations. This coupled code (S-CLSVOF) has been

verified and tested using both axi-symmetrical and 3D domains, and subsequently used to characterize the flow conditions as well as the dynamics of the bubble up to and including the detachment.

The third objective is to assess the suitability of the VOF based "compressive" interface capturing scheme for the analysis of bubble impact on and bounce from a flat horizontal surface using both axi-symmetrical and 3D domains. As noticed experimentally, the bubble impact entraps a small quantity of liquid in the thin film between the bubble upper surface and the wall. The film thickness is of the order of few micrometers and requires that a high resolution mesh is used to correctly capture the essential physics. The assessment of the model's sensitivity to the mesh resolution highlights the importance of an adequate mesh refinement. Part of the study is also dedicated to provide more in depth details on the energy dissipation during the collision process. At the last stages of the bouncing process, the film either stabilizes or drains fully leading to the formation of the three phase contact line (TPCL). This stage is controlled by the type of solid surface material and its surface energy. This interaction is a multi-scale process that is still not well understood both experimentally and theoretically. Even though there are several numerical studies on the wetting phenomena using drop spreading and impinging, there exist, to the author's knowledge, very few numerical studies on the bubble interaction with solid plates. Furthermore, the numerical study of the full bouncing process (impact, film formation, and contact line[1] interaction) is not available in the literature and, in addition, there exists no 3D numerical work for any stage during the bouncing.

Apart from the interface capturing techniques, both static and implemented dynamic contact angle models in the open source library (OpenFOAM) are investigated for the study of bubble growth and bouncing. In the former process, the influence of the static contact angle on the bubble detachment characteristics and the relationship between the static and the experimentally observed contact angle are also studied. At the last stage of the bouncing, the influence of both static and dynamic contact angle models on the contact line slipping is analyzed.

The free bubble rise has also been studied in the present research. In contrast to the growth and bouncing processes, significant research has been dedicated to the numerical analysis of rising bubbles. For the present work, the bubble rise stage has

[1]The contact line is the contour line formed due to the interaction between the free surface and the solid wall

been used to contribute to the model's validation and as a necessary step to achieve the pre-impact conditions.

To summarize, the study in this thesis is divided into three parts:

- Study of the bubble growth and detachment process using the three interface capturing methods: VOF, LS, and CLSVOF. The study compares the accuracy of both algebraic and geometric methods for predicting the bubble behavior under low Capillary and Bond numbers. The difference in the numerical results will be discussed and explained using the display of both velocity flow field and pressure distribution during the formation.
- Implement and validate a simple coupling code between VOF and LS methods (S-CLSVOF) for the study of bubble rise and growth, and compare the implemented solver against the original VOF method available in OpenFOAM. Study the influence of the contact angle boundary condition on the formation process.
- Study the influence of mesh resolution on capturing the essential physics during bubble impact (the film formation) and the corresponding influence on the bouncing mechanism. Implement a dynamic contact angle model coupled with the original VOF method in OpenFOAM, and compare the results with the dynamic model against those with the original static one for the last stage of the bouncing process.

1.3 Thesis outline

The remainder of the thesis is organized as follows:

- Chapter 2 reviews the literature on the numerical methods suitable for modeling the two-fluid flows and the wetting dynamics. The last section introduces the implementation of these methods for the study of bubble growth, rise, and bouncing.
- In Chapter 3, the governing equations employed in the present research and the techniques followed for discretizing and solving them are summarized.
- Chapter 4 presents the results on the analysis of bubble growth using different interface capturing methods.
- Chapter 5 presents the validation of the S-CLSVOF method.

- Chapter 6 includes the bubble bouncing analysis.
- Chapter 7 highlights the main conclusions of the present research and the corresponding thesis contribution. Some recommendations for further future works are also included.

The validation of the numerical results presented in this work has been assessed by comparison against experimental data performed by the Fluid and Heat Transfer Research Group at Trinity College Dublin (Dublin, Ireland). A short description of the experimental setup is presented in Appendix A. Some other experimental measurements collected from the literature have also been used. The source of the benchmarking data is highlighted in each results chapter.

2 Literature review

The following literature review considers first the development of the two-fluid flow methods with an emphasis on the interface capturing techniques. Then, the wetting dynamics is explained and the numerical strategies followed for modeling the interaction between the gas/liquid interface and the solid boundaries are described. Finally, a literature survey on the implementation of the two-fluid flow numerical methods for capturing the fundamental mechanism of several challenging applications, including bubble growth, free rise, and bouncing, is presented.

2.1 Two-fluid flow numerical methods

Over the last three decades, significant progress in numerical methods and computational resources have made it possible to study the gas/liquid interface deformation in viscous fluid flows. In Computational Fluid Dynamic (CFD) simulations, predicting the motion of the bubble interface involves solving the Navier-Stokes equations supplemented by an advection equation that allows tracking the interface position in the two-fluid flow processes. The governing equations are solved numerically using either moving mesh or fixed mesh. The former approach is a discontinuous method (Dandy and Leal, 1989) as the numerical domain is composed of two sub-domains defining the two fluids with a separating boundary representing the interface. This method is a complicated technique and not widely used as it requires grid re-meshing whenever the interface undergoes large distortions. On the other hand, few methods have been developed based on the fixed grid approach. They include the interface tracking and the interface capturing methods. There are also free mesh techniques for solving the two-fluid flow problems such as the smoothed particle hydrodynamics method (Monaghan, 1994).

In the interface tracking methods (Unverdi and Tryggvason, 1992), the interface is tracked explicitly. The flow field is discretized using a stationary fixed grid, while

the front (interface) position is tracked using a Lagrangian grid so that the moving front should have always the same velocity as the surrounding fluid. In general, this method can provide very accurate results, but it is numerically expensive as it requires mapping the interface data from one grid to another. Furthermore, some difficulties arise when the interface is exposed to large deformations or an interface coalescence/disappearance happens. Therefore, this method is a computationally expensive technique. The Interface capturing methods (also known as the Volume tracking methods), on the other hand, consider the two fluids as a single mixture solved on a fixed grid. A phase function is utilized to distinguish between the two immiscible fluids and to extract the distribution of each fluid (phase) at every time step. This procedure can provide reasonably accurate results with a simpler implementation than the interface tracking method. It is the most common method for solving multiphase flow problems in CFD. Two main approaches, namely Volume of Fluid (VOF) and Level Set (LS), have been developed and widely used as interface capturing methods. Recently, a new technique has also been developed by coupling the advantages of both VOF and LS into one single method called the coupled LS-VOF method (CLSVOF).

In the following sections, a literature review on the historical development of each interface capturing method (VOF, LS, and CLSVOF) will be presented focusing on the innovative steps proposed for improving the methods' accuracy and simplifying their implementations for different applications. Moreover, the pros and cons of each numerical method will also be highlighted.

2.1.1 Volume of Fluid

The building blocks of the Volume of Fluid method were proposed by Hirt and Nichols (1981). In this method, a separate phase function, called the volume fraction function α, is used to indicate which phase (fluid) is present in a specific cell on the fixed grid. The field function α takes the value 0 for the cells occupied by the first fluid, and a value 1 for the cells occupied by the second fluid. The mixed cells which have values in the range $(0 < \alpha < 1)$ contain the interface. The interface is tracked by advecting the volume fraction function, and therefore the method is generally known to conserve the mass of the traced objects under investigation (bubbles/drops). The fluid physical properties are determined in the computational domain using the function α. The discrete representation of the interface leads to a numerical error represented as unphysical flows around the interface (Spurious

currents). All the developments performed on this method aim at reconstructing the interface more accurately for any type of grids and reducing the spurious currents influence on the physical processes. In the following, a summary of the main developments is presented.

Although the volume fraction function detects the amount of fluid in each cell, the gradient of this function is required for determining the interface orientation. The interface capturing method based on the VOF technique is generally composed of two main steps: (i) The determination of the interface position and inclination using special discretization schemes, (ii) the time integration algorithm for advecting the volume fraction function. The first process enables obtaining the fluid fluxes and the flow field through the cell faces which are required for solving the advection equation. Two main approaches can be distinguished with respect to the interface orientation and advection; the interface can be determined accurately using a geometrical reconstruction scheme (Rider and Kothe, 1998; Youngs, 1982), or it can be advected using a spatial algebraic discretization scheme such as the method proposed by Muzaferija and Peric (1999) where the interface is smeared over few cells.

The former scheme for reconstructing the interface geometrically is the Simple Line Interface Calculation algorithm (*SLIC*) proposed by Noh and Woodward (1976). The interface line segment is reconstructed parallel to one co-ordinate direction using only the field details of the neighboring cells in the sweeping direction. *SLIC* is an operator-split method (For 1D problem, the fluxes are updated by sweeping the mesh only in one direction). The VOF method developed by Hirt and Nichols (1981) (Donor-Acceptor method '*D-A*') reconstructs the interface parallel to one co-ordinate direction, as well. However, the interface is reconstructed either horizontally or vertically according to the neighboring cells. This algorithm is implemented in the RIPPLE code (Kothe and Mjolsness, 1992). The interface direction depends on the magnitude of the interface normal components. The fluxes are calculated using either an upwind scheme (for fluxes parallel to the interface), or a combination of first order upwind and downwind schemes (for fluxes perpendicular to the interface). A more accurate interface reconstruction algorithm is proposed by Youngs (1982) (*Y-VOF*). The interface is approximated by a straight line (for 2D case) cutting the cell faces in such a way that the volume fraction function in that cell is satisfied. This method is a direction-split method as the fluxes through the cell faces and the volume fraction are updated first by sweeping the mesh in one direction, and then they are updated by sweeping the mesh in the other perpendicular

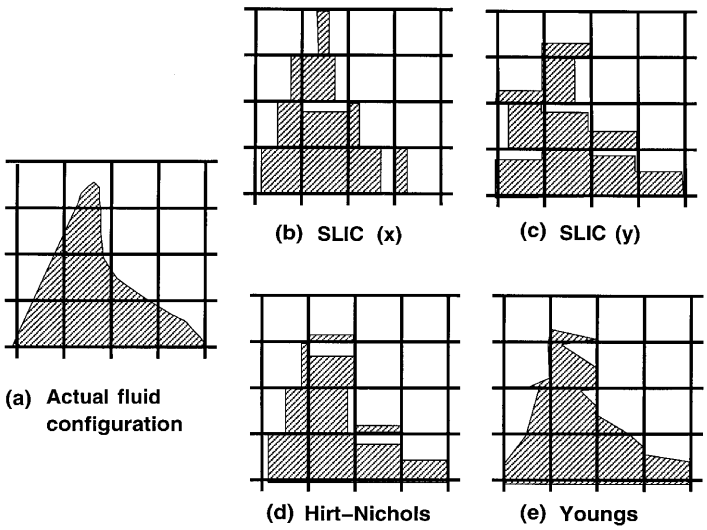

Figure 2.1: Comparison of different interface reconstruction schemes of an actual fluid configuration in (a), (b,c) SLIC with sweeping in both x and y directions, (d) The D-A scheme, (e) The Y-VOF scheme. Extract from (Rudman, 1997).

direction. A definition of the operator splitting technique and its disadvantages are explained in the review paper of Benson (2002). Both *D-A* and *SLIC* are defined as piecewise constant schemes as the interface is either horizontal or vertical. In contrast, the *Y-VOF* scheme is a piecewise linear scheme as the interface follows a specific orientation based on the normal calculation (See Fig. 2.1 for a comparison of the different reconstruction schemes).

Although the piecewise constant methods can be simply implemented, they fail to provide accurate results for cases with large topological changes, and they produce unphysical errors for cases with vorticity or shear near the interface since piecewise constant is a first order scheme. The *SLIC* method is no longer in use and it is substituted by other more accurate algorithms such as the Piecewise Linear Interface Calculation algorithm (*PLIC*) attributed to Youngs (1982) and developed by Rider and Kothe (1998). This method reconstructs the interface geometrically as a line segment with a specific slope determined using the gradient of the α function. The 2D *VOF-PLIC* algorithm presented by Rider and Kothe (1998) gives a second order accuracy in terms of the geometrical reconstruction of the VOF equation. It also provides second order temporal accuracy due to using un-split multidimensional time integration. During the last two decades, this method has been developed and implemented in many proprietary and in-house codes.

Aulisa presented another technique for reconstructing and advecting the interface using the VOF method in 2D spaces (Aulisa, Manservisi and Scardovelli, 2003) and 3D spaces (Aulisa, Manservisi and Scardovelli, 2004). In this method, surface markers are mixed with the volume fraction function to locate the interface within the computational cell. López et al. (2004) improved the multidimensional technique of Youngs' VOF (*Y-VOF*) by using Edge-matched Flux Polygons and Spline-based Interface Reconstruction techniques (*EMFPA-SIR*). In this method, the interface orientation is calculated first using the *Y-VOF* method, and then it is corrected using a cubic spline interpolation of the interface segments center points. Pilliod and Puckett (2004) provided another example of VOF reconstruction algorithm that can reproduce accurately lines in 2D spaces and planes in 3D spaces.

An alternative approach for reconstructing the interface geometrically using the Young technique is the Least Square method. The *ELVIRA* approach produced by Pilliod (1992) used a strategy where a 3×3 cells are considered for determining the interface orientation. The interface in the centered cell is approximated by a straight line with an inclination chosen as the one providing the least error among other six options given by the backward, central, and forward difference of the columns sums of the volume fractions along the axis x and y, respectively. The error in this method is defined as the difference between the actual volume function values and the approximated values obtained when extending the approximate interface over the 3×3 cells. Another reconstruction algorithm based on the least square fit technique is also proposed by Scardovelli and Zaleski (2003). The proposed method provides interface continuity at the boundaries of the neighboring cells.

In dispersed flows, where the numerical cell size is larger than the dimensions of a particular fluid part, the VOF method loses its accuracy, and reconstruction errors become more considerable. Correcting these errors requires using either an adaptive grid refinement of the interface as evidenced in Ginzburg and Wittum (2001), or using more accurate interface capturing algorithms. The improved algorithm *VOF-PLIC* of López et al. (2005) reconstructs the interface properly even for cases where the filaments have a thickness less than the mesh size. This is achieved by using markers in the reconstructed interface cells for better detection of the interface position and orientation.

The main advantage of the geometrical reconstruction algorithms is that they assure a linearity preservation with both first and second order accuracy. The early reconstruction schemes depend on direction splitting techniques to account for mul-

tidimensionality which gives typically first order accuracy (e.g. Rudman (1997)). Second order reconstruction and advection is achieved using more advanced schemes (Aulisa et al., 2007) as well as unsplit multidimensional advection schemes (Cervone et al., 2009; López et al., 2004; Rider and Kothe, 1998). Pilliod and Puckett (2004) have shown that it is necessary and sufficient for the reconstruction algorithm to be able to reconstruct a linear or planar interface exactly for it to be second order accurate on smooth interfaces. The interface linearity is satisfied in many existing interface reconstruction schemes including the Least Square Volume of Fluid Interface Reconstruction Algorithm (LVIRA) (Puckett, 1991), the Efficient Least Square Volume-of-Fluid Interface Reconstruction Algorithm (ELVIRA) (Pilliod, 1992) and the Least Square Fit (LSF) (Aulisa et al., 2007).

The geometrical reconstruction schemes, however, are computationally expensive because they require, at each time step, determining the shape of the truncated volume in each interface cell and also enforcing the local volume conservation by detecting the correct position of the planar interface, with the specified normal, in the cells. The advances in the geometrical methods during the last decade aim for obtaining new techniques that come closer to preserving linearity and are less computationally expensive for both 2D and 3D problems. This was achieved, for instance, by solving analytically the local enforcement of the truncated volume as presented by Scardovelli and Zaleski (2000) for orthogonal hexahedral grids. Recently, López and Hernández (2008) proposed another analytical method for the local enforcement that is suitable for general grids. Another main drawback of the geometrical methods is their complexity for 3D applications, in particular when coupled with an unstructured mesh. There are nonetheless many successful implementations which were employed for 3D two-fluid flows (López and Hernández, 2008; Aulisa et al., 2007; Annaland, Deen and Kuipers, 2005; Lörstad and Fuchs, 2004; Renardy and Renardy, 2002).

Another alternative approach to preserve the interface resolution without the need for any sophisticated, and computationally complex surface reconstruction schemes is solving the volume fraction advection equation using differencing schemes that guarantee boundedness and avoid smearing of the gas/liquid interface over several cells. An early algorithm of the VOF algebraic methods is based on the concept of Flux Correct Transport scheme (FCT) of Zalesak (1979). This scheme does not require any explicit interface reconstruction. The fluxes can be calculated using either operator-split or multidimensional technique (For 2D case, the fluxes are calculated in both directions at the same time). FCT combines the advantage of

both the upwind method (stability) and the downwind method (interface sharpness) by using a mixed technique. An intermediate value of the volume fraction function is calculated first using a diffusive scheme, the anti-diffusive fluxes are then calculated and corrected using a specific factor, the function α at the new time step is finally calculated using the corrected fluxes. Although FCT is faster than the geometrical reconstruction methods as it does not require geometrical reconstruction, Rudman (1997) found that it gives less accurate results than the *Y-VOF* method. However, its accuracy is still better than both *SLIC* and *D-A* methods.

Although the FCT scheme is not diffusive, small pieces of fluid might separate from the interface creating areas of unphysical flotsams and jetsams (Rudman, 1997). The Compressive Interface Capturing Scheme for Arbitrary Meshes (*CICSAM*) method by Ubbink and Issa (1999) is another algebraic method that relies on high resolution discretization techniques. This guarantees, to some degree, the interface sharpness while preserving the boundedness of the volume fraction field. The method is based on the Normalized Variable Diagram (*NVD*) (Leonard, 1991) for discretization, and it switches between different differencing schemes to attain the boundedness of the α function. The method is theoretically second order accurate in terms of the temporal discretization. However, lower accuracy might occur depending on the studied test cases (check Ubbink (1997) for more details). Another similar compressive model is the modified version of the High Resolution Interface Capturing scheme (*HRIC*) (Muzaferija et al., 1998) which is implemented in *ANSYS-13* (See section 19.3.1.9 in the theoretical user guide of Ansys (2011)). This scheme consists also of non linear blending of both upwind and downwind differencing schemes.

The interface sharpness is maintained in the algebraic VOF method available in the open source library (*OpenFOAM®*) (OpenFOAM, 2010) by introducing an extra term to the VOF advection equation. This term, called '*Counter gradient*' (Weller, 2008), assures the interface conservativeness and boundedness so that the shedding of extra pieces of volume from the interface (flotsams) is very limited. Furthermore, a compression factor is used to enhance the compression by using velocity values, called compression velocity, larger than the maximum velocity in the domain. When solving the compression term in the VOF advection equation, a limiter is used to achieve an interface boundedness with second order accuracy. For finer mesh cases, the compressive velocity decreases and the compression term vanishes leading to the original VOF advection equation. In comparison with the other algebraic methods, the *CICSAM* scheme has been shown to be particularly effective at limiting the interface smearing and avoiding interface oscillations (Andrillon, 2004). However, it

is also known to suffer from interface dispersion in zones of no flow where the velocity field is divergent. This has been linked, for example, to the interface diffusion at the stagnation point on the side of a stationary Taylor bubble (Ubbink, 1997). This breakdown has been explained by the diffusion of the interface triggered by the divergent flow and the loss of compression where the flow velocity is zero. On the other hand, the counter gradient formulation, has been shown to improve the interface sharpness in complex liquid-jet break-up (Villiers, Gosman and Weller, 2008).

In summary, since the early works on the VOF method (1970s), large advances in the techniques have been achieved due to the advantages of the VOF method and in particular its suitability for mass conservation. The improvements have been devoted to enhancing the method's accuracy and simplifying its implementation for different physical applications. The geometrical reconstruction technique can provide accurate interface representation, but it is computationally expensive. On the other hand, the compressive methods give an approximation of the interface with less CPU time compared to the geometrical technique. However, their accuracy tends to be lower than the geometrical methods. Other developments of the VOF method have been directed at alleviating the spurious currents generated due to the influence of the surface tension model (This will be discussed in section 2.1.4). Applications of the VOF method have been found in many industrial areas. Moreover, few benchmarking test cases have also been used to estimate or evaluate the accuracy and the mass conservativeness of the VOF methods. These include the Rudman's hollow square/circle (Rudman, 1997), Rider-Kothe single vortex and time reversed flows (Rider and Kothe, 1998), and Rayleigh-Taylor instabilities (Rudman, 1997; Brackbill, Kothe and Zemach, 1992). Recently, several hybrid methods which combine the advantages of VOF with other interface capturing techniques have also been proposed (Enright et al., 2002; Sussman and Puckett, 2000).

2.1.2 Level Set

The Level Set method (LS) was originally introduced by Osher and Sethian (1988) for propagating interfaces with curvature dependent speed. It was first applied for multiphase flow problems by Sussman, Smereka and Osher (1994). The Level set field ϕ is defined in this method as a signed distance function, giving the interface a specific thickness. The distance function is used to distinguish between the two fluids in the numerical domain. The iso-line contour $\phi = 0$ determines the position

of the interface. The physical properties are calculated in terms of the ϕ function. Therefore, a smooth variation of the properties across the interface can be achieved. The LS advection equation is solved to move the interface with time. Sussman, Smereka and Osher (1994) highlighted the significant features of the LS method including the robust normal and curvature calculation and the control of the surface topological changes. They also demonstrated the weakest point of this method; it is the significant dissipation that appears while discretizing the LS advection equation. Furthermore, the solution of the LS equation does not preserve the distance property of the ϕ function, and thus a correction procedure should be performed after each time step which leads to the well known mass conservation issues with the LS method. The correction process includes solving a non linear hyperbolic equation, called the "*reinitialization equation*", to steady state. Since this equation is solved with a characteristic velocity pointing outwards from the interface, Sussman et al. (1998) improved the reinitialization step by solving the equation with a fixed number of iterations in order to ensure that the LS function satisfies the distance property near the interface. Further developments of the LS technique were aimed at improving the accuracy of the method while retaining its simple implementation. This was achieved by using higher order discretization schemes, improving the reinitialization process to conserve the mass, and/or coupling the method with other techniques. In the following, a short summary of each aspect will be presented.

The simplest strategy to solve the reinitialization equation consists of using forward Euler time integration with a spatial upwind scheme. However, using the traditional discretization methods with the LS function leads to numerical dissipations evidenced as a loss of volume or a loss of the interface characteristic information (Losasso, Fedkiw and Osher, 2006). Using higher order accurate schemes is one of the remedies to solve the numerical dissipation issue with the LS method. Higher order scheme, the Total Variation Diminishing Runge-Kutta scheme (*TVD-RK*), was used by Shu and Osher (1988). Other high order schemes that have been suggested include the Essentially Non-Oscillatory (*ENO*) (Harten et al., 1987) and the Weighted Essentially Non-Oscillatory (*WENO*) (Liu, Osher and Chan, 1994) schemes. These have been constructed for problems with piecewise smooth solutions that contain discontinuity such as the LS method. *ENO* is a third order accurate scheme that is built based on the first order upwind scheme, while *WENO* is a fifth order scheme developed from *ENO* using a weighting factor. Thus, these two high order schemes are linear combination of lower order schemes to obtain higher accuracy. The main principle of the *ENO* algorithms is based on choosing the smoothest candidate sten-

cil[1] out of three possible ones near the discontinuity region for calculating the cell face values of the LS function. *WENO* scheme, on the other hand, uses a weighted average of the three possible stencil candidates. An example of using the third order *ENO* scheme for the LS method is illustrated by Sussman et al. (1998). For cases with large interface distortions, LS is coupled with adaptive projection methods to obtain higher resolution accuracy with low additional expenses (Sussman et al., 1999). For more details on other spatially adaptive methods such as the Octree based methods for solving the conservation issues, see the review work of Losasso, Fedkiw and Osher (2006).

The high order discretization schemes are unable to solve completely the mass conservation issues especially for compressible flows (Mulder, Osher and Sethian, 1992), and thus other procedures are required to improve the LS method. For this purpose, the research was dedicated to solving the conservation issue by improving the reinitialization equation so that a signed distance function is always attained near the interface. Olsson and Kreiss (2005) modified the LS method by using a regularized characteristic function (smeared out Heaviside function) instead of the LS function. This method is called "*conservative level set method*". In this case, the iso-contour line $\phi = 0.5$ represents the interface which is smoothed between the value 1 in the first fluid and 0 in the second fluid. This method conserves the volume surrounded by the iso-contour $\phi = 0.5$. Though, the interface thickness does not remain constant after the advection, and therefore an intermediate step is performed after each time step by solving a modified reinitialization equation that contains an artificial compression term. The method gives conservative results for free rising bubbles. But, it shows a slow convergence when refining the mesh. Olsson, Kreiss and Zahedi (2007) improved the convergence speed of their method by modifying the reinitialization equation, but this was achieved to the detriment of the method's simplicity. A different technique for solving the mass conservation is based on the Refined Level Set Grid method (*RLSG*) proposed by Herrmann (2005, 2008). RLSG relies on using a refined grid in the interface regions since the mass conservation errors in the LS method reduce proportionally with the grid refinement. Two different grids are considered in this method; the flow solver grid on which the fluid's physical properties are defined, and an additional Cartesian refined grid introduced in the regions occupied by the interface. The LS advection and reinitialization equations are solved on the refined grid which enables retaining the full order of accuracy of the *WENO* scheme when it is applied for the discretization.

[1]The stencil here means a set of three cells used for calculating the cell face value of the field.

Although the *RLSG* reduces the volume error in the LS technique, it does not eliminate that error.

An alternative approach of using the reinitialization procedure with the LS technique is to create the signed distance function following the principle of the fast marching method (Sethian, 1999). This technique relies on initializing the cell points neighboring the interface, and then finding the distance function by marching outwards. To explain this method, let's define the initialized cells as complete cells, and their neighboring ones as adjacent cells. All the other cells in the domain are called the far cells. Upon initialization, the adjacent cells take provisional values calculated from the complete ones. The adjacent cells with smallest provisional values are added to the complete ones, and their neighbors are added to the adjacent cells. New provisional values are calculated and the cells with smallest values are added again to the complete cells. This process is performed for a specific distance around the interface so that a distance function is achieved. The method can have a second order accuracy. However, its challenging step is how to determine accurately the initialized cells close to the interface.

In the quest to improve the mass conservation with Level Set, the method is hybridized with other mass conservative techniques. In this context, several numerical methods are introduced: The coupled Level Set with Volume of Fluid method (*CLSVOF*) which will be explained in the next section, the Particle Level Set method (*PLS*), and the Hybrid Level Set Volume Constraint method (*HLSVC*).

The Particle Level Set (Hieber and Koumoutsakos, 2005; Enright et al., 2002) combines the advantages of both the Eulerian LS method and the Lagrangian interface tracking technique. The particles from the Lagrangian method assure the connectivity of the interface points during the advection, while the Level Set method enhances the accuracy of the Lagrangian technique as it avoids the need to re-mesh in order to restore the interface elements in cases of large topological changes and interface distortion. In the under-resolved region[2], the Lagrangian particles are used for constructing the Level set function. The reconstructed interface satisfies the LS positive features including the accuracy of calculating the interface normal and curvature. Furthermore, the *PLS* method does not require using high order discretization schemes as the original LS method (Enright, Losasso and Fedkiw, 2005).

[2]Under-resolved region defines the area of the numerical domain where the mass conservation is lost due to large distortion in the interface.

Most recently, a novel Hybrid Level Set Volume Constraint method "*HLSVC*" (Wang, Simakhina and Sussman, 2012) has been developed to improve the mass conservation of the LS method. Contrary to the other conservative Level set techniques, *HLSVC* can preserve the interface linearity. Furthermore, the method can be coupled with dynamic adaptive mesh refinement, and it can also be extended from rectangular to curvilinear co-ordinate systems. The method evidenced similar accuracy and efficiency when it was compared against the coupled *CLSVOF* (Wang, Simakhina and Sussman, 2012).

The Sharp Interface methods have also been derived from the LS technique. It is based on the Ghost Fluid method (Fedkiw et al., 1999) that captures the physical discontinuities over the interface determined by the Level Set. The ghost fluid was first implemented for multiphase flow problems by Kang, Fedkiw and Liu (2000). Capturing the exact jump in the fluid properties across the interface leads to a more physical representation of the interface by comparison with the original LS (Sussman, Smereka and Osher, 1994). The alternative sharp interface method (Raessi and Pitsch, 2012) provides a stable solution even for fluids with large density ratios. A Finite Element formulation of this technique has been developed by Gross and Reusken (2007*a*). They coupled the surface tension formulation in Gross and Reusken (2007*b*) to the extended Finite Element code (*XFEM*) of Moes, Dolbow and Belytschko (1999). The numerical results of this coupled code reduces significantly the spurious currents. However, further work should be performed to address the stability issues which have been found to affect certain two-fluid flow problems.

Different simple test cases have been used to verify the accuracy and convergence of the Level Set methods. They include the Rayleigh Taylor instability test (Herrmann, 2008), single vortex flow (Hieber and Koumoutsakos, 2005), and Zalesak's disk test introduced by Zalesak (1979) (Herrmann, 2008; Sussman et al., 1998). The study of the free bubble rise and falling drops has also been used to test conservation of the volume surrounded by the interface (Olsson and Kreiss, 2005; Sussman, Smereka and Osher, 1994). Successful implementation of the Level Set method in commercial softwares has also been performed (See for example TransAT© software that is used in the present work (TransAT, 2011)).

In summary, the proposed Level set method for solving two-fluid flow problems represents a feasible solution for many applications due to its advantage in calculating accurately the interface normal and curvature. The main drawback of this method is the loss of mass (volume) when advecting the smoothed LS function.

Several strategies have been proposed to solve this problem including applying high order discretization schemes such as *WENO*, and improving the reinitialization equation by using a smoothed Heaviside function (The conservative Level Set method). The error in the volume conservation has also been reduced by refining the mesh in the under-resolved regions where large interface distortion takes place (The Refined Level Set method). LS has also been hybridized with other techniques such as the Ghost Fluid method to produce the exact jumps across the interface (the Sharp Interface method), and the particle Lagrangian method (Particle Level Set). In general, adding the reinitialization equation to solve the conservation issue with LS makes this method more expensive in terms of the CPU usage and more complicated in terms of the implementation.

2.1.3 Coupled LS with VOF

During the last decade, a significant amount of attention has been paid to combining the main particular advantages of both VOF and LS in one single method. The early coupled method (*CLSVOF*) was proposed by Sussman and Puckett (2000) and Sussman (2003). The main features of this coupling are (i) the mass conservation due to the advection of the VOF function and (ii) the interface sharpness due to the calculation of the interface normal and curvature using the LS function. Sussman and Puckett (2000) solved both VOF and LS advection equations. They used an operator splitting algorithm with Cartesian co-ordinates in order to get second order accuracy. For 2D Cartesian co-ordinates, this method can be summarized as follows:

1. At the initial time step, an initial value of the LS function is assumed (ϕ^0). This value satisfies the signed normal distance function from the correct position of the interface. The initial VOF function α^0 is then calculated from ϕ^0 using the Heaviside function.

2. An intermediate value $\tilde{\phi}$ of the LS function is calculated in terms of the fluxes of the LS function across the cell faces ($G(\phi^0)$). The new value of the LS function ϕ^1 is then updated using both $\tilde{\phi}$ and $G(\tilde{\phi})$. The LS fluxes are calculated using the LS values at the cell centers and the velocity field values at the cell faces.

3. The fluxes of the VOF function $G(\alpha^0)$ are calculated in terms of the reconstructed piecewise linear equation of the initial LS function ($\phi^R_{i,j} = a(x - x_i) + b(y - y_i) + c$), where x, y are the Cartesian co-ordinates, (i, j) indicates the cell ID, and a, b, c are constants. These fluxes represent the amount of fluid

being advected across the cell faces. The constant values a, b define the slope of the linear equation, while the value c adjusts the interface line position so that the intersection with the cell boundaries determines the same volume α of the cell.

4. An intermediate value $\tilde{\alpha}$ of the VOF function is calculated in terms of the VOF fluxes across the cell faces ($G(\alpha^0)$). The new value of the VOF function α^1 is then updated using both $\tilde{\alpha}$ and $G(\tilde{\alpha})$.

5. Once the new values ϕ^1, α^1 are obtained, a re-initialization process is performed to obtain the signed distance function. This process includes firstly truncating the volume fraction function outside the interface thickness region. The LS function is then updated using a geometrical procedure that determines the sign of the LS function at each cell, and then the shortest distance between each cell and the zero contour of the LS function (ϕ^1).

Son and Hur (2002) developed another technique for reconstructing the interface geometrically in the coupled *CLSVOF* method. This is achieved by following similar configuration to the PLIC method. The interface normal, in this case, is calculated using the smoothed LS function. The interface position is calculated using a new geometrical parameter representing the furthest distance between the cell corners occupied by the liquid and the interface. Once this distance and the interface normal are known, the interface is reconstructed so that the liquid volume fraction in that cell is satisfied. Son and Hur (2002) showed that this method preserves the bubble volume within an error equal or less than 0.01%. Furthermore, it is capable of studying the free bubble rise with results comparable to the literature. Since then, Son (2003) has also extended the previous technique for 3D incompressible two phase flows.

As shown above, the major difficulty in implementing *CLSVOF* is that the interface should be reconstructed geometrically in order to calculate the volume fluxes advected through the cell faces, and to reinitialize the LS function. To avoid this geometrical reconstruction, Ménard, Tanguy and Berlemont (2007) used an analytical procedure for calculating the constants in the reconstructed interface equation (ϕ^R) mentioned in the CLSVOF main steps above. The reinitialization of the LS function is calculated based on the iterative algorithm proposed by Sussman et al. (1998). This analytical coupled method provided good results in terms of the Rayleigh instability tests of the liquid jet, and it also gave promising results for 3D jet atomization simulations. Another development to the coupled *CLSVOF* method includes the

adaptive technique (*ACLSVOF*) presented by Yang et al. (2006) for interface flows on an unstructured triangular grid. This method is coupled to a Finite Element based Stokes solver, and the reconstructed line constant c proposed before for the function ϕ^R is calculated here on triangular grids. The *VOF-PLIC* method implemented in the commercial software *ANSYS-Fluent* has also been extended to a coupled CLSVOF by Nichita, Zun and Thome (2010).

All the above coupling techniques for the *CLSVOF* method solve the advection equation of both LS and VOF functions. This procedure makes the coupled method more computationally expensive compared to the standalone VOF or LS methods. To improve the computational efficiency of *CLSVOF*, Sun and Tao (2010) introduced a new coupled technique (*VOFSET*) that solves only the VOF advection equation. In this case, an initial value of the LS function is calculated using the VOF function after advection. The level set function is then reinitialized within a region of three mesh cells on each side of the interface. The signed distance function is each cell in this region is calculated as the shortest distance to the interface within a stencil of 7×7. Numerical tests on circular bubbles at equilibrium showed a large improvement in the mass conservation compared to the LS method. Kunkelmann and Stephan (2010) solved only the VOF advection equation in their extension of the VOF method implemented in the OpenFOAM library. The LS function, in this case, is initialized using the VOF function so that the $\phi = 0$ iso-contour corresponds to the $\alpha = 0.5$ iso-contour. The calculated LS field is reinitialized using the typical iterative reinitialization method proposed by Sussman, Smereka and Osher (1994), and then the interface is reconstructed geometrically following the method of López and Hernández (2008). The interface reconstruction process was performed in this study to determine the exact position of the interface at the solid boundaries and to model properly the contact line evaporation for boiling applications.

In the original LS method (Sussman, Smereka and Osher, 1994), the interface is spread over a finite thickness across which the calculation of the surface tension model in the Navier Stokes equations is considered. Numerical results published in Albadawi et al. (2013) and Chakraborty et al. (2009) for bubble growth simulations showed a sensitivity to the interface thickness (See section 5.3.1 for the analysis of the influence of the interface thickness). An alternative approach to limit this effect and to deal with the properties' discontinuities at the interface is based on the Ghost Fluid method "*GFM*" (Kang, Fedkiw and Liu, 2000; Fedkiw et al., 1999). This technique adds virtual cells, known as ghost cells, to the real cells around the interface so that both virtual and real domains are used when solving the multiphase flow

problems. The discontinuity in the field properties in the real cells are substituted with a continuous field in the ghost cells. This continuous field will then be used in the advection equations. For two-fluid flows, Sussman et al. (2007) introduced the Sharp Interface method by coupling *CLSVOF* with the *GFM* technique. In this method, the velocity field is extrapolated to avoid the discontinuity by creating a virtual field of the velocity whereby the velocity values in the cells occupied by the liquid remain the same while those in the gas domain are substituted by extrapolated velocity values. This virtual velocity field is then used for solving both LS and VOF advection equations. Based on the new position of the interface (the sign of the LS function), the data of the velocity in the virtual domain are mapped back to the real cells; the cells in the liquid domain will retain their values, and those in the gas side will be mapped back from the virtual cells. Ménard, Tanguy and Berlemont (2007) has also used the ghost cell method for treating the discontinuities in the interface.

In General, the coupled method is developed to combine the advantages of both VOF and LS methods. However, implementing the coupled method is more complicated than the standalone VOF and LS techniques. This is due to two main issues. First, it introduces a need for solving both VOF and LS advection equations in CLSVOF. Several techniques are proposed later to solve only the VOF advection equation while the LS function can be initialized using the VOF function. Second, a geometrical reconstruction procedure, similar to that of the *PLIC* technique, must also be implemented to determine the interface slope and position in each cell occupied by the interface. To avoid the complexity of the geometrical reconstruction, several attempts have been made at developing an analytical algorithm for determining the interface position in the CLSVOF method. Recently, the developments to the coupled method have tended to use the *GFM* in order to obtain continuous properties across the interface for solving the VOF and LS advection equations.

2.1.4 Surface tension modeling

In the CFD simulations with interface capturing methods, the surface tension model at the gas/liquid interface is one of the main key parameters for capturing accurately the physical phenomena. The most used surface tension model is the Continuum Surface Force (*CSF*) proposed by Brackbill, Kothe and Zemach (1992). In this model, a volumetric surface tension force is added as a source term to the momentum equation. At any point of the interface, this force is calculated in terms of the

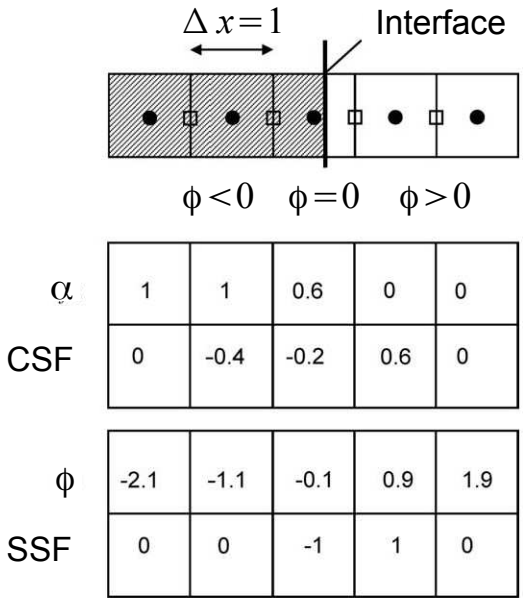

Figure 2.2: One dimensional example of surface tension force discrete values around the interface using both CSF and SSF models. The discrete values of the VOF function and the corresponding LS distance function are also displayed (Francois et al., 2006).

interface curvature at that point. The calculation of the curvature, itself, varies based on the interface capturing method; it is calculated using the gradient of the VOF function in the VOF methods, while it is calculated using the LS function for both LS and CLSVOF methods. An alternative surface tension model is the Sharp Surface tension Force (*SSF*) (Gueyffier et al., 1999). This model requires only the computation of the interface normal, and it provides a jump in the surface tension at the interface similarly to the Ghost Fluid method. A schematic comparison between the two previous models is illustrated by Francois et al. (2006) for one dimensional case (Fig. 2.2). In this figure, the first row shows the position of the interface while the second and the fourth rows display the values of the VOF function (α) and the LS function (ϕ), respectively. The calculated values of the surface tension model from both *CSF* and SSF are illustrated in the third and fifth rows, respectively. The values of the surface tension are assumed to be calculated at the first time step of the calculation with pressure initialized to zero. It is evident that the *CSF* model provides a smooth transition of the surface tension across the interface, while *SSF* gives more sudden transition with larger values compared to the previous model.

Both models have the tendency to produce unphysical flows (*spurious currents*) near the interface for cases with large surface tension influence. These currents are well demonstrated when studying numerically the flow around a stationary bubble under zero gravity. While no fluid motion should appear around the interface, the VOF simulations coupled with the surface tension model evidence an unphysical flow around the interface (Renardy and Renardy, 2002). For cases with strong surface tension and large density ratios, these unphysical velocities can grow and diverge. Francois et al. (2006) found that the intensity of the spurious currents in the interface capturing methods is influenced by the combination of the flow algorithm used for solving the governing equations, the surface tension model, and the curvature calculations algorithm.

The spurious currents originate from the imbalance between the pressure gradient and the surface tension stresses while implementing the governing equations for two-fluid flow problems. Francois et al. (2006) improved the flow algorithm in order to reduce the influence of the spurious currents by using a Pressure Balanced algorithm. This technique includes treating the total pressure gradient operator and the surface tension force as one single term during the solution of the predictor step of the momentum equation. In this algorithm the balance between the pressure and surface tension is calculated at the cell faces and then it is converted to the cell centers to calculate the intermediate velocity in the predictor step of the momentum equation. By contrast the surface tension is generally estimated separately from the pressure and directly at the cell center for calculating the intermediate velocity. Using this method, Francois et al. (2006) compared also the influence of both *CSF* and *SSF* models. It was found that the first method gives first order accuracy for the pressure, while the latter gives second order accuracy. Though, both models produce spurious currents with similar magnitude. They also concluded that better estimation of the interface curvature should be used for further reduction in the magnitude of the spurious currents.

Despite the successful employment of the CSF model in many two-fluid flow processes, the generation of the spurious currents in the vicinity of the interface limits this method for surface tension dominant flows. Several attempts have been introduced to alleviate these spurious currents. One of the remedies is to improve the curvature estimation at the gas/liquid interface. This is achieved in the coupled CLSVOF method by calculating the surface tension source term using the gradient of the LS smoothed distance function (Sussman and Puckett, 2000). Renardy and Renardy (2002) developed a new technique for representing the body force due to the

surface tension. The method was based on the Parabolic Reconstruction Of Surface Tension (*PROST*), and it was shown to achieve a significant reduction in the magnitude of the velocity induced by the spurious currents. However, the elimination of the spurious currents was to the detriment of the method's simplicity compared to the other surface tension models. Another alternative technique for improving the curvature calculations in the VOF method is the Height Function method (*HF*) (Afkhami and Bussmann, 2008). In this case, the interface normal and curvature are calculated using geometrical means (height function) rather than the gradient of the VOF function. This method provided converged results with mesh refinement for drops in equilibrium with contact line driven flows (Afkhami and Bussmann, 2008). Tong and Wang (2007) proposed the Pressure Boundary Method (*PBM*) for implementing the surface tension via a capillary pressure gradient term in the predictor step when solving the momentum equations.

2.1.5 Other two-fluid flow methods

The previous sections focused mainly on the development of the most widely used interface capturing methods (VOF, LS, and CLSVOF). However, there are other available techniques in the literature for the study the two-fluid flow problems. Some of these are classified in the group of interface capturing methods such as the Diffuse Interface method. Other techniques are solved on a moving Lagrangian mesh (Interface Tracking method). There are also methods that discretize only the gas/liquid interface (Boundary integral method). Apart from the techniques that use the mesh as a discretization tool, there exist other methods that rely on the motion of the fluid particles for solving the fluid flow problems (Lattice Boltzmann and Smoothed Particle Hydrodynamics method). As these techniques are also used for the study of the physical processes under investigation, it is important to shortly highlight the main key aspects of each method so that the reader can refer back to the prescribed method, if interested. In the following, a brief summary of each method is presented.

The *Boundary Integral Method* (Zhang et al., 2001; Best, 1993) simulates the bubble evolution by solving the boundary integral equation of the gas/liquid interface. This method discretizes only the interface between the bubble and the surrounding liquid and, thus, it is an efficient method in terms of the computational resources. The main drawback of this technique is the absence of the viscosity modeling as the boundary integral technique is based on the assumption that the solution is

governed by potential flow in each fluid. Furthermore, more complicated techniques should be applied when the interface is subjected to large shape deformations such as the interface merging and breakup.

In the *Interface Tracking method* (Unverdi and Tryggvason, 1992), the fluid flow is solved on a fixed grid, while the interface is represented using adaptive marker elements (Lagrangian approach). A smooth distribution function is employed to transfer the details of the interface position to the fixed grid, and to calculate the physical properties and the surface tension force. This function is calculated based on the interface position. The interface tracking method was extended by Hua and Lou (2007) in order to study wider ranges of density ratios. Navier-Stokes equations were discretized using finite difference scheme and solved using the *SIMPLE* method (Patankar and Spalding, 1972). The interface was tracked explicitly using the interface marker's velocity.

The interface tracking method provides more accurate results compared to the Eulerian methods (Fixed Grid methods) because the former technique uses connected particles to reconstruct the interface. However, mapping the data between the interface markers and the fixed grid makes the method more complicated than the Eulerian techniques. Moreover, this method is inefficient for 3D cases and interface deformations with highly distorted topologies. The particles in such cases change their position and a complicated re-meshing step is required to reconstruct the interface and redistribute the markers.

In the *Diffuse Interface method* (Ding and Spelt, 2007*a*,*b*; Jacqmin, 1999, 2000), the gas/liquid interface is smoothed over few cells with a specific thickness. The diffuse interface thickness is considered as a narrow miscible region separating the two fluids. In this method, a volume fraction C is used to distinguish between the two fluids in the domain, whereas $C = 1$ in the cells occupied by the first fluid and $C = 0$ in the cells occupied by the second fluid. This scalar field is advected using the convective Cahn-Hilliard equation (Cahn, 1961):

$$\frac{\partial C}{\partial t} + \mathbf{u} \cdot \nabla C = \nabla \cdot (M \nabla \varphi) \tag{2.1}$$

where M is the mobility, and φ is the chemical potential which is calculated in terms of the bulk energy density $\Psi(C) = \frac{1}{4}C^2(1-C)^2$. The main advantage of this method is its applicability to study the interaction of two-fluid flow problems with solid boundaries as it allows the interface slippage along the solid walls by convection

or diffusion due to the chemical potential gradient.

The Lattice Boltzmann method (Shan and Chen, 1993) is a mesoscopic scale[3] method that is based on the kinetic energy of the gas for describing the flow dynamics. A density distribution function is used in this method to represent the density of the particles in the domain while the fluid density is calculated based on the molecular mass of the particles. The interaction between two different fluids and the fluid - solid interaction are modeled using interaction potential parameters. One of the main advantages of the Lattice Boltzmann method is that the boundary conditions are implemented at the boundary particles rather than the domain itself (Yang et al., 2001). This enables modeling the interaction of gas/liquid interface with solid boundaries without the need of any additional procedures compared to other techniques as will be shown later for the interface capturing methods.

2.1.6 Summary

A literature review on the development of the main interface capturing techniques for two-fluid flow problems is introduced. Despite the widespread and successful employment of each method for many industrial applications, further research is required in order to improve their accuracy for cases with large interface topological changes and interface evolution under critical conditions such as surface tension dominant flows.

The main advantage of the Volume of Fluid method is its ability to conserve mass. However, this technique is not linearity preserving when advecting the VOF function. VOF methods that are capable of second order accurate curvature estimation have been developed but they are mostly limited to orthogonal grid. The VOF geometrical methods require an interface reconstruction in each cell in order to calculate the volume fluxes advected through the cell faces. This procedure is computationally expensive and further extension to 3D problems is not straightforward. Other VOF techniques use compression factors for advecting the VOF function whereas the interface position is smeared over 2-3 cells.

The Level Set method, on the other hand, is capable of handling large topological changes with robust geometrical information including the interface orientation and curvature. It is also equally straightforward to implement on either structured or un-

[3]The mesoscopic scale is an intermediate length scale between the size of the molecules (microscopic scale) and the size of the materials (macroscopic scale).

structured meshes. The advection of the LS function however does not preserve the distance property and therefore a reinitialization process is performed. The latter procedure leads to loss in the mass (volume) which is the main disadvantage of the LS method. Improving the mass conservation has been achieved using higher order discretization schemes for the LS advection equation and improving the reinitialization process. These procedures, however, have been at the cost of the method's simplicity.

The coupled CLSVOF method has recently been developed to overcome some of the disadvantages of the standalone VOF and LS methods. The mass conservation is obtained by relying on the advection of the VOF function, while the interface sharpness is preserved by using the smooth LS function. Implementing this method is more complicated and numerically prohibitive than the last two techniques due to the solution of both VOF and LS advection equations and the further reconstruction of the interface, in some of the CLSVOF implementations, similarly to the geometrical VOF methods. This can pose non negligible challenges when extending to three dimensional domains and in particular unstructured meshes.

In the present work, the three interface capturing methods will be employed for the study of different physical applications under critical flow conditions. The work aims to assess the accuracy of the different techniques for surface tension dominant flows. The three numerical methods are defined as: the algebraic Volume of Fluid (VOF) method developed in OpenFOAM library source code, the geometric VOF method implemented in ANSYS-Fluent®-v13, the Level Set (LS) method of the proprietary software TransAT©, and the geometric coupled VOF with LS (CLSVOF) recently implemented in ANSYS-Fluent®-v13. The algebraic VOF method in OpenFOAM® will also be extended to a simple coupled (S-CLSVOF) method in order to study the influence of the surface tension modeling on the accuracy of the interface capturing method.

2.2 Wetting dynamic

The interaction of a fluid-fluid interface with a flat solid surface can occur in a range of applications such as the withdrawal of a plate from a fluid, the spreading of a droplet on a solid wall, and the bouncing of a bubble on surfaces. The analytical solution of Navier-Stokes equations for this process leads to a stress singularity over

the contact region indicating that the contact line[4] is pinned on the solid surface. This, however, contradicts the physical observations as the contact line slips on the solid wall. During the contact line slippage, the experiments also show a time varying contact angle between the gas/liquid interface and solid wall. These variations depend on both fluids' physical parameters and surface properties. The precise description of the contact angle would require a study of molecular interactions over the contact region where the assumptions of Continuum Mechanics break down. In general, two main issues arise in the analysis of wetting dynamics; the contact angle model and the singularity conundrum at the contact line region. In this section, a review of the wetting process is introduced. This includes explaining the dynamics at the contact region, the singularity conundrum and the proposed models for solving it, the derivation of the contact angle models, and the numerical implementation of the wetting models for two-fluid flow problems.

2.2.1 Contact angle definition

In two-fluid flows, when a bubble/drop collides against a solid surface, two different regimes can be distinguished in terms of the generated contact angle (Fig. 2.3); partial wetting regime ($0 < \theta_e < 2\pi$), and fully wetting regime ($\theta_e = 0$), where θ_e is the equilibrium contact angle. It is defined as the angle between the free surface and the solid boundary located in the heavier phase. The first regime may also be classified according to the structure and the material properties of the solid surface as hydrophobic surface with equilibrium contact angle $\theta_e > 90°$ (e.g. bubble-Teflon surface interaction, See Fig. 2.3a) and hydrophilic surface with equilibrium contact angle $\theta_e < 90°$ (e.g. bubble-glass interaction, See Fig. 2.3b). For the bubble bouncing process, Zedníková et al. (2010) observed a minor influence of the surface material (hydrophobic and hydrophilic) on the bouncing amplitude due to the film formation between the bouncing bubble and the solid surface. The influence of the solid material is limited only to the last stage of the bouncing (the collision process) as it leads to either a liquid film stabilization (for super hydrophilic surfaces $\theta_e = 0°$) or to a three phase contact line formation (for hydrophobic surfaces) (Kosior et al., 2012). Over the contact line region, each interface (liquid-gas, solid-liquid, and solid-gas) has its own surface energy per unit area. They are defined as σ_{Sl}, σ_{Sg} and σ_{lg}, where the subscripts S, l, g represent the solid, liquid, and gas phases, respectively.

[4]The contact line is the contour line formed due to the interaction between the gas/liquid interface and the solid wall

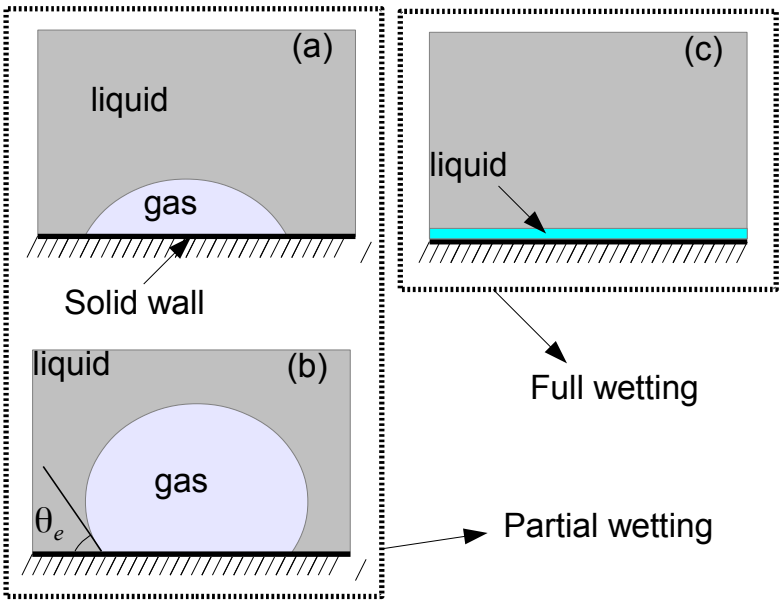

Figure 2.3: Different types of equilibrium contact angle generated on (a) hydrophobic surface (b) hydrophilic surface (c) and fully wetted surface.

The surface energy σ_{lg} is usually simplified to σ. The relationship between these energies is defined through the Young-Laplace equation as:

$$\sigma_{Sg} = \sigma_{Sl} + \sigma \cos(\theta_e) \tag{2.2}$$

Enlarging the view of the contact line region to a microscopic scale, where the three phases meet, shows that the relation between these phases is more complicated than initially suggested by its definition in the Young-Laplace equation. This is due to the influence of other forces such as the long range forces (Van der Waals forces) on the contact region (Gennes, 1985). In non-equilibrium cases, the above equation is not valid and the imbalance between the surface energies drives the bubble/drop to spread or contract on the solid surface. Two different cases are observed here (receding and advancing) based on the velocity of the contact line. The angle between the gas/liquid interface and the solid surface is shown experimentally to deviate from the equilibrium contact angle $\theta_{rec} < \theta < \theta_{adv}$, where θ_{rec} and θ_{adv} are the receding and advancing contact angles, respectively. These angles are dependent on surface conditions which themselves are influenced by the material properties and manufacturing processes.

2.2.2 Singularity and spreading dynamics

The early attempts to find a relationship that represents the spreading dynamics were based on several assumptions to simplify the analysis such as ignoring the gravitational effect and using viscous flows (Gennes, 1985). Hoffman (1975) tested internal flow through a capillary glass tube of diameter ~ 2 mm for a range of velocities. The apparent contact angle (θ_{app}) was found to be controlled by a universal relationship with the slip velocity defined in terms of the slip Capillary number ($Ca_{slip} = u_{slip}\mu/\sigma$) as:

$$Ca_{slip} = F(\theta_{app}) \tag{2.3}$$

where μ is the fluid viscosity, σ is the surface tension coefficient, and u_{slip} is the slip velocity of the contact line on the solid surface. The slip Capillary number varies here in the range $[10^{-4}, 1]$. For small Capillary numbers (bubble/droplets case), the last equation takes the form:

$$Ca_{slip} = const \times \theta_{app}^3 \tag{2.4}$$

When a drop spreads on a solid surface, Elizabeth, Dussan and Davis (1974) found that the motion of the liquid close to the contact line ($\sim 100\mu m$) can resemble a rolling motion similar to the caterpillar vehicle (Fig. 2.4). This motion produces a total viscous dissipation at the wedge, calculated using the lubrication approximation, as (Gennes, 1985):

$$T_w = \int_{x_{min}}^{x_{max}} \frac{3\mu u_{slip}^2}{y} d|x| = \frac{3\mu u_{slip}^2}{\theta_{app}} \ln|\frac{x_{\max}}{x_{\min}}| \tag{2.5}$$

The value $3\mu u_{slip}^2/y$ is the viscous dissipation over the wedge thickness. The total dissipation is calculated between the internal cutoff length x_{min} in the direction parallel to the wall in the contact line region, and the external cutoff macroscopic scale (x_{max}). The coordinates' origin is set at the contact line point where the three phases meet (See Fig. 2.4). Theoretically, applying a no slip boundary condition on the contact region, which is equivalent to setting $x_{\min} = 0$, drives to energy dissipation that is logarithmically diverging. To solve the singularity issue, $x_{\min}$ should be calculated considering the microscopic region to have a finite value of energy dissipation. The theoretical derivations by Hocking and Rivers (1982) showed

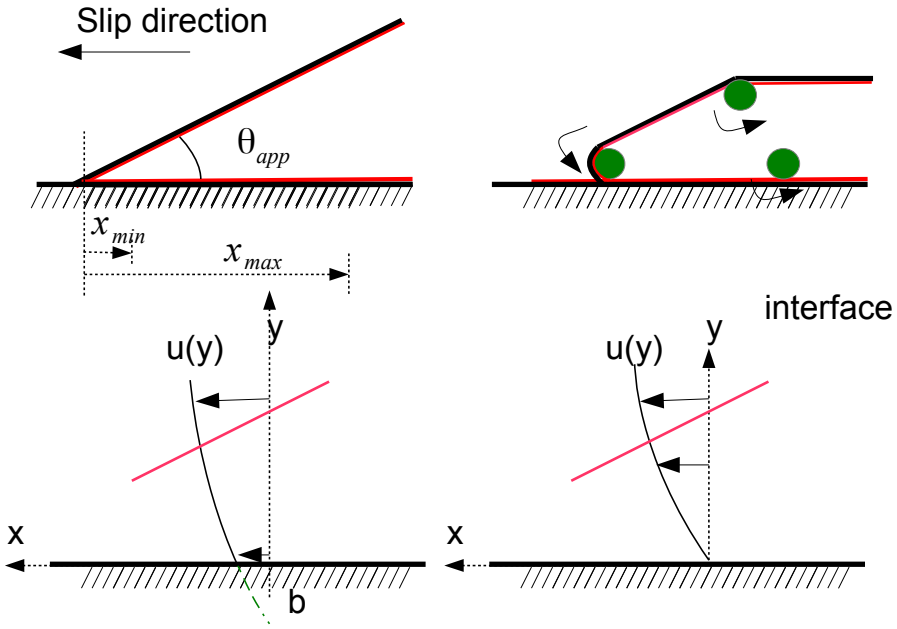

Figure 2.4: Slipping length representation at the contact line region

that slipping which occurs over the contact region is characterized by:

$$x_{\min} \cong b/\theta_{app} \tag{2.6}$$

where b is a slippage constant.

This definition removes the singularity by assuming that there exists a limited small region near the contact line where the fluid slips along the wall in this region. The assumption for the contact line slipping introduces the existence of two domains when studying the wetting dynamics; the microscopic region and the macroscopic region. The early calculations of the dynamic contact angle which used the relaxation principal at the contact line region did not recognize the need for using an intermediate region connecting the macroscopic and the microscopic scales (Dussan, 1979; Kafka and Dussan, 1979; Hocking, 1977), and their results were applicable only for small contact angles. Later on, Eggers (2004) derived a model for the dynamic contact angle using the lubrication theory. The contact line region was divided into three main domains (Bonn et al., 2009) (Fig. 2.5):

1. Outer region: its scale is of the order of the drop radius R (Cox, 1986). The

contact angle in this region is defined as the apparent contact angle which is measured at a finite distance from the contact line.

2. Intermediate region: The interface inclination and height are calculated here using the lubrication theorem by balancing the viscous and the surface tension forces. The region is defined by the scale $3CaR/\theta_{app}$ (Eggers, 2004). The dynamic contact angle in this region depends on the slip velocity.

3. The inner region: It forms the region around the contact point with a size of a few nanometers where the microscopic forces and fluctuations are taking place (Thompson and Robbins, 1989). The contact angle here is the microscopic contact angle.

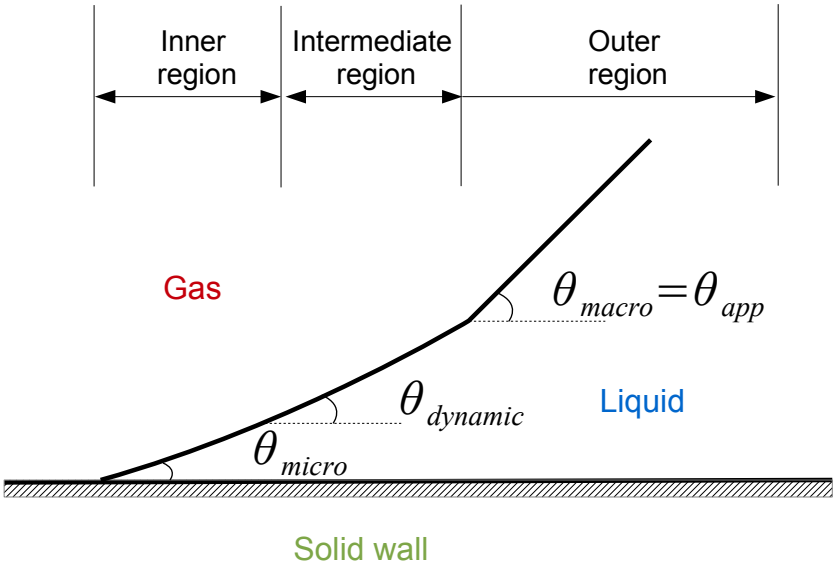

Figure 2.5: A schematic of the different angles at the contact line region.

In general, the analysis of the moving contact line has tended to be studied based on the scale of the domain. This includes the microscopic region (Molecular kinetic theory), mesoscopic (Lattice Boltzmann method), and macroscopic region (Hydrodynamics theory). The molecular kinetic theory is capable of studying the very small region close to the moving contact line, and it provides a suitable model that can explain the slipping on the solid surfaces (Qian, Wang and Sheng, 2006). Although this method provides a valuable contribution to the knowledge of the wetting in the immediate proximity of the contact line and it best represents the slipping dynamics, it is inefficient to extend the number of particles to study the flow behavior in the bulk fluid. However, the results obtained from Molecular dynamics can be used

as a boundary condition for the macroscopic Continuum models (Manservisi and Scardovelli, 2009).

Lattice Boltzmann method has also been used for the study of moving contact lines (Zhang, 2011; Latva-Kokko and Rothman, 2007; Briant, Wagner and Yeomans, 2004; Zhang and Kwok, 2004). The main advantage of this method is the possibility of applying a wide range of boundary conditions at the contact line. Furthermore, the boundary conditions are applied on the particles which represent the wall rather than on the velocity field at the wall. However, this method does not explain the slip of the contact line as the Molecular Dynamics method.

The hydrodynamics theory models balance between the viscous and surface tension forces at the intermediate region. The hydrodynamic study of the contact line region by Eggers (2004), for example, was based on the lubrication theorem. The singularity at the contact line is solved by allowing the slid of the fluid-fluid interface on the solid wall using the Navier slip law (Hocking, 1983). The asymptotic solution of the lubrication theory, called Cox-Voinov law (Voinov, 1976), shows the dependence of the hydrodynamic model on several microscopic parameters. The Continuum models, however, are not able to calculate these values and therefore the Continuum analysis should be combined with microscopic models for obtaining the unknown parameters (Bonn et al., 2009). A brief description of the available contact angle models derived from molecular, empirical, and hydrodynamic theory are available in Appendix B.

2.2.3 Slip law and slip velocity

Implementing a slip model in the numerical methods depends on the technique used for capturing the interface. The methods that track the interface implicitly require a suitable slip law at the boundaries (Fukai et al., 1993) to allow for contact line slipping. In contrast, other methods, like VOF, use the velocity at the cell faces for moving the interface. This implies that at the neighboring cells to the wall, there is an implicit slip velocity at a distance $\Delta/2$ from the solid wall, where Δ is the mesh size. Therefore, the slipping in this case is mesh dependent. Navier slip law is the most famous model for contact line slipping. It uses a slip length rather than the mesh size. With numerical simulations, if a slip model is required for allowing the contact line to move along the solid walls, the Navier slip boundary condition is applied on the wall boundary as:

$$u_{slip} = \lambda \dot{\gamma} \tag{2.7}$$

where λ is the slip length, and $\dot{\gamma}$ is the shear rate at the interface. In some cases, the Navier slip law is applied only over the contact line region, while the no-slip boundary condition is used far from the contact line.

The analysis of the Molecular Dynamics theory has determined that there exists another boundary condition, denoted as the Generalized Navier Boundary condition (*GNBC*), which can solve the singularity problem at the moving contact line (Qian, Wang and Sheng, 2003). Qian, Wang and Sheng (2006) derived the *GNBC* using the principal of minimum energy dissipation as:

$$\beta u_{slip} = -\mu(\partial_n u + \partial_\tau v) - \sigma \cos\theta_s \tag{2.8}$$

where u, v are the flow velocity components parallel and perpendicular to the wall. θ_s is the static contact angle imposed in the model. β is the slip coefficient which is a thermodynamic quantity related to the material type and has the unit of μ/λ. The above equation shows that the slip velocity is proportional to the viscous stress and the uncompensated Young stress. The GNBC has also been derived by Buscaglia and Ausas (2011) using the principal of the virtual work. However, the authors believed that this condition is equivalent to reformulating the standard Navier slip law along with the contact line equilibrium condition into one single formula.

Shikhmurzaev (1997) proposed a model for solving the singularity at the contact line region based on both hydrodynamic principals and non-equilibrium thermodynamics. This was achieved by assuming that a mass flux moves from the gas-liquid interface to the solid-liquid interface when the free surface slips on the solid wall. This transport leads to a molecular rearrangement at the solid-liquid interface due to the difference in the material properties between the two surfaces and results in a change in the solid-liquid surface tension. Thus, the balance in the surface tension between the different surfaces is changed. This motion provides a surface tension gradient at the contact line diffused over a specific distance along the solid-liquid interface. He proved that the slipping happens due to the interface diffusivity. By contrast, the hydrodynamic models relax the no-slip boundary condition at the contact line region to allow for the spreading of the interface.

Based on the analysis of the slip law models, the calculation of the slip velocity on solid boundaries is an essential step required for solving the singularity. Numerically,

this procedure varies based on the interface capturing method. Although the VOF method uses an implicit slip velocity, Afkhami, Zaleski and Bussmann (2009) have implemented the slip law to study the dependence of the mesh size on the results with/without slip length. The slip velocity along the solid boundaries was calculated as:

$$u_{slip} = \frac{U\Delta + 2\lambda u_1}{\Delta + 2\lambda} \tag{2.9}$$

where U, u_1 are the wall velocity and the tangential fluid velocity component at the first cell close to the wall, respectively. This formula allows for a wide range of slip conditions starting from no slip ($\lambda = 0$) to free slip boundaries ($\lambda \to \infty$). Yokoi et al. (2009) used the coupled CLSVOF method for the study of drop impact on dry surfaces. Although this method, similarly to VOF, introduces an implicit slip velocity allowing the free surface to move on the solid boundaries, they introduced a slip velocity formula as:

$$u_{slip} = \frac{u_1}{\lambda + \frac{\Delta}{2}}(\lambda - \Delta/2) \tag{2.10}$$

Sikalo et al. (2005) calculated the slip velocity by differentiating the diameter of the wetted spot on the solid boundary. The method, however, cannot be applied to 3D problems such as, in most practical cases, bubble bouncing after impact on a free surface. Roisman et al. (2008) calculated the slip velocity using the velocity of two material points adjacent to the wall. Their model assumes that the interface is a straight line close to the wall. The modeling of drop impact results obtained with this Roisman model are different from predictions achieved with the model applied by Sikalo et al. (2005) in particular at the beginning of the impact as the drop contact line is not a straight line. After the initial stages of impact, both Sikalo and Roisman models gave similar results.

2.2.4 Numerical implementation of contact angle models

The theoretical methods based on the hydrodynamics theory can be applied only for simple cases with no complicated topologies in the bulk fluid, while the outer flow is usually a complex domain which requires numerical strategies to solve. The main principle of the numerical methods with contact line modeling is similar to that followed by Somalinga and Bose (2000). At the contact region, they calculated the

apparent contact angle by using a dynamic contact angle model to get the velocity field at this region, while far from the contact line region, the no slip boundary condition is applied (see Fig. 2.6).

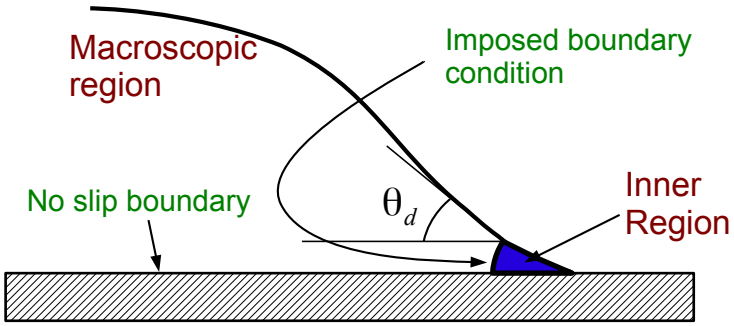

Figure 2.6: Schematic diagram of the inner region where imposed contact angle should be applied.

For a specific contact angle model, each numerical method treats the wall boundary condition in a different way; The VOF method reconstructs the volume fraction at the neighboring cells to the wall so that the reconstructed plane satisfies the contact angle condition (Bussmann, Mostaghimi and Chandra, 1999). With Lagrangian moving mesh methods, the nodes close to the wall are moved to satisfy the contact angle condition (Fukai et al., 1993). With the LS method, the contact angle calculated from the distance function at the interface position is corrected using the contact angle hysteresis and then the LS function is re-initialized to get a new corrected distance function that satisfies the contact angle (Liu et al., 2005; Spelt, 2005). With the LS method, the slip length is imposed explicitly compared to VOF. In this section, the literature survey on coupling the interface capturing methods with ad hoc boundary conditions for solving the wetting dynamics problems is presented.

Early attempts at coupling the VOF-PLIC method with a moving contact line model was made by Renardy, Renardy and Li (2001). They solved the Navier Stokes equations coupled with a fixed dynamic contact angle (No contact angle hysteresis was considered). This method was applied for the outer region of the bulk fluid up to the microscopic neighborhood of the contact line. It accounts for the slipping on the

solid wall in such a way that the slippage is proportional to the mesh size. Therefore, the method is computationally expensive as a finer mesh is required to consider smaller slip lengths. Sikalo et al. (2005) studied, numerically and experimentally, the impact of a single drop (water and glycerin) on a horizontal solid surface (wax and glass) under high Weber and Reynolds numbers (See the nomenclature for definitions of the non dimensional numbers). This numerical study using a VOF model aimed at finding a contact angle model that predicts properly the receding stage of the drop spreading. During the advancing stage of the drop, the results with both dynamic and static models were similar. However, during the recoiling stage and due to the dominance of the viscous drag, better results were obtained with the dynamic angle model. Saha and Mitra (2009) coupled different dynamic contact angle models with the VOF method in OpenFOAM-1.5 for the study of capillary filling in microfluidic channels with integrated pillars. Their results proved the applicability of both Kistler (Kistler, 1993) and Brake (Bracke, Voeght and Joos, 1989) models for the study of partially wetted surfaces. Recently, Annapragada, Murthy and Garimella (2012) studied numerically and experimentally the droplet sliding on an inclined PTFE surface using the VOF-CSF method in Fluent. The droplet terminal velocity while moving on an inclined surface were better predicted using the dynamic contact angle (Bracke and Jiang models, See details of the models in Appendix B) compared to the static model.

Afkhami, Zaleski and Bussmann (2009) studied the effect of using both no slip and slip boundary conditions coupled with the VOF Height Function method. In the case of withdrawing plate from a liquid with no slip boundary, the results did not converge with mesh refinement and the shear stress over the contact region was shown to diverge with the finer mesh. With a Navier-Slip boundary, on the other hand, the results were also dependent on the mesh resolution. However, further mesh refinement was found to give mesh independent results. Dupont and Legendre (2010) coupled the hydrodynamic contact line model described by Ngan and Dussan (1989) with the VOF method implemented in *JADIM* code (Bonometti and Magnaudet, 2007) for capturing the drop interface position while spreading on a flat surface. The dynamic contact angle model in this case is calculated at a distance 10 μm from the solid surface. Two values of the slip length were considered ($\lambda = 0$ and $\lambda = 0.01R_0$, with R_0 is the initial drop radius). The two previous values provided similar results with a good agreement with the experimental results. Dupont and Legendre (2010) also highlighted that the numerical simulations did not give good results for fluids that do not achieve certain restrictions on the non-dimensional numbers (Slip

Capillary and Reynolds numbers) for the contact angle model.

Spelt (2005) introduced a dynamic macroscopic model at the wall boundaries coupled with the Level Set method. This model is solved on a structured grid whereas different parameters are considered for representing the contact line region; they are the contact line speed, the dynamic contact angle, and the contact angle hysteresis. The Level Set simulations have been compared against the results of the lubrication theory for drop spreading. For small values of the slip Capillary number, the results with LS were very close to those obtained with the Lubrication theory. The difference between the two methods increased at higher values of Capillary number. More recently, the conservative Level Set method (Olsson and Kreiss, 2005) has also been used successfully for wetting problems with a specific treatment for the contact line at the solid boundaries (Sato and Niceno, 2012).

Yokoi et al. (2009) studied the droplet impact on a dry surface using the CLSVOF method. They also used a coupled dynamic contact angle model so that it switches between capillary dominant and inertia dominant (High Ca number) problems. It has been found that the dynamic contact angle model is the most suitable for predicting the drop diameter for both advancing and receding cases, while the equilibrium and static angles failed to give results similar to the experiments.

2.2.5 Summary

The non-physical diverging stress generated in the limit as the contact line is approached originates from the collapse of the Continuum Mechanics assumption. A strictly accurate representation of the fluid-fluid/solid interaction at the contact line would require Molecular Dynamics simulations to account for the physics of the contact line slippage. However, very small scales involved make such an approach impractical for most applications where macroscopic simulations are the most widely used. This requires that a slip model should be used to remove the stress singularity. Different models have been proposed and can been summarized as:

1. Precursor model: It assumes that a thin liquid film always exists at the wall even before the drop/bubble comes into contact with it so that no slip model is required at the solid surface (Spaid and Homsy, 1996; Gennes, 1985). These models do not allow for any kind of interaction between the bubble and the solid surface and therefore they are limited to specific applications.

2. Diffuse interface method (Ding and Spelt, 2007*b*; Jacqmin, 2000): This method

allows for interface slippage due to the diffusive flux in the interface region.

3. Slip model (Spelt, 2005; Cox, 1986; Huh and Scriven, 1971): This method is based on imposing a slip length at the solid surface so that it relaxes the stress singularity. The most famous slip models are the Navier slip law and the *GNBC* model.

4. Shikhmurzaev model (Shikhmurzaev, 1997): Slipping on the solid boundaries is due to the mass flux from the gas-liquid interface to the solid-liquid interface.

The contact angle models have been coupled to the VOF method with/without slip models at the contact region. It was found that using a slip law provides better mesh independent results compared to the cases with no imposed slip law boundary. Although there exists significant research on the influence of the contact angle models on drop spreading, much fewer studies have been dedicated to the effect of contact formulation in the case of bubble bouncing and sliding on solid surfaces. The initial position and size of the drop before impacting and spreading on the wall plays an important role in determining the slip Capillary number which is often used to characterize the slip model. For bubble bouncing, on the other hand, adjusting and studying a wide range of slip Capillary number is limited since the contact line region does not appear immediately when the bubble collides against the wall. Also, oscillations in the bubble rise trajectory and shape deformations create conditions before impact which are likely to affect the simulation's sensitivity to the contact model.

2.3 Isolated bubble flow modeling

Two-fluid flows are common in many industrial applications. They can be introduced to enhance mass or heat transfer in both mechanical and chemical processes. The bubbles may originate from nucleation sites as vapor bubbles or could be injected into the system as gas bubbles using different strategies. Although the whole process of bubble formation, rise, and bounce can be studied experimentally and has been modeled numerically, it presents particular challenges as it involves both fluid-fluid interaction (bubble rise) and fluid-solid interaction (bubble growth and bounce). In this section, a literature review of the interface capturing methods developed for the study of bubble growth, rise, and bounce is presented focusing on the main challenges relevant to the numerical simulations.

2.3.1 Bubble growth and detachment

This section considers the formation of single isolated bubble by injection of a lighter fluid (gas) into a heavier one (liquid). The gas can be injected either through a single orifice in a wall (Chen, Mertz and Kulenovic, 2009; Gnyloskurenko et al., 2003) or through a needle (Quan and Hua, 2008). The former case is employed when the effect of the wall wettability on bubble formation is under investigation. With needle injection, the contact line is always fixed at the needle rim. The bubble formation process is composed of two main stages; the bubble growth stage when the bubble takes a truncated spherical shape, and the bubble detachment stage when the bubble elongates vertically forming a neck close to the wall orifice. Under normal gravity conditions, the bubble passes through three different regimes according to the gas flow rate (McCann and Prince, 1971); static, turbulent, and dynamic regimes. In the present work, the first regime is considered where isolated bubbles with the same detachment frequency detach from the orifice. Oguz and Prosperetti (1993) determined a criterion based on the gas flow rate below which the bubble formation is quasi-static. Under this condition, they found that the buoyancy and surface tension forces are the most dominant forces acting on the bubble. The balance between these forces determines the bubble diameter during the growth. Detailed reviews of the experimental works on bubble formation are available in Yang, Du and Fan (2007) and Kulkarni and Joshi (2005).

The early theoretical studies of the formation process focused on the gas/liquid interface to predict the bubble behavior and its geometrical properties during the growth. The pioneering works of Davidson and Schuler (1960) and Walters and Davidson (1963) analyzed the bubble formation process assuming that the bubble has a spherical shape during the whole process. By using this assumption and balancing the buoyancy and the surface tension forces, Oguz and Prosperetti (1993) were able to predict the bubble radius. They derived the Young-Laplace Equation which can be solved numerically to track the position of the bubble interface during the growth. This equation is derived by balancing the pressure difference across the interface and the product of the interface curvature with the surface tension coefficient. Different techniques have been used for its solution including the fourth order Runge-Kutta (Gerlach et al., 2005) and the geometry method (Lee and Tien, 2009). The Young-Laplace equation can predict the bubble shape up to the critical point defined as the detachment point when the bubble takes its maximum volume. It is not possible to apply this equation for an accurate prediction of the pinch-off

of the bubble neck during the detachment stage. Numerical methods have also been used to study this initial phase of the bubble formation. Oguz and Prosperetti (1993) used the Boundary Integral Method to determine the interface position during the growth. This technique assumes that the fluid flow is irrotational so that a velocity potential exists. The bubble radius can be obtained in this method using the velocity potential itself. Recently, Gordillo et al. (2005) and Gekle et al. (2009) have used this method to study the axi-symmetrical bubble pinch-off, and analyzed the minimum bubble radius (neck radius) during pinch-off. The method's main drawback is its inability to account for viscous stresses effect or the influence of the solid boundaries in the vicinity of the bubble formation region.

Over the last three decades, significant progress in computational resources and numerical methods has made it possible to study complex gas/liquid interface deformation in viscous fluid flows over the full formation and detachment phase by solving Navier-Stokes equations coupled with a two-fluid flow method for capturing the interface. The bubble formation presents particular challenges due to the large and rapid changes in the magnitude and distribution of the surface tension stresses particularly in the vicinity of the injection point which characterize the growth and detachment. An early attempt to study the bubble growth using the Volume of Fluid method was by Li et al. (2001). The numerical simulations displayed the effect of the adjacent bubbles and the wake generated behind the bubble on the dynamics of the surrounding liquid and thus on the multi-bubbles formation process. The VOF geometrical reconstruction scheme based on the *PLIC* technique implemented in Fluent was used to study the bubble growth by Valencia, Cordova and Ortega (2002), but a comparison against theoretical predictions showed non negligible differences attributed to the effect of the wall adhesion model. The same *PLIC* scheme was used for an extensive two dimensional study of the influence of surface tension, liquid properties, and orifice diameters on the bubble characteristics during the bubble growth and detachment (Ma et al., 2012). The study, however, was conducted in 2D and did not account for any important 3D effects.

The LS method is widely used and developed for the study of bubble growth in nucleate boiling (Wu, Dhir and Qian, 2007; Son, Dhir and Ramanujapu, 1999). For adiabatic bubble formation, Chen and Fan (2004) used the LS method combined with the Lagrangian particle motion equations to study the effect of the solid particles concentration on the bubble formation process in a 3D domain. Although their code was validated experimentally for free bubble rise problems, only qualitative assessment of the bubble growth simulations was presented. Chen, Mertz and

Kulenovic (2009) employed the LS method to study bubble growth with different contact line models; a contact line velocity dependent model (Model-A, a commonly used model) and a stick-slip model (Model-B). They studied the effect of the wall wettability on the departure bubble volume where they found that the lower wall wettability leads to bubble interface spreading along the wall, and as a result, to bigger detachment values. Most recently, Di Bari, Lakehal and Robinson (2013) studied the influence of the gravitational acceleration on the bubble detachment volume using the LS method implemented in the *TransAT*© commercial software. The numerical results showed an inverse relationship between the gravity and the bubble volume at departure.

Most of the recent numerical studies on bubble growth relied on the coupled CLSVOF method (Sussman and Puckett, 2000) to study the formation process (Chakraborty, Biswas and Ghoshdastidar, 2011; Chakraborty et al., 2009; Badam, Buwa and Durst, 2007; Buwa et al., 2007). Gerlach et al. (2007) studied the influence of different physical properties on the bubble growth. They found that the bubble detachment volume increases with increasing liquid density, liquid viscosity, or surface tension. They also studied the periodicity of bubble formation when increasing the flow rate. The effect of increasing the static contact angle has also been investigated as it has been shown that increasing this angle above a certain value forces the interface to spread along the wall leading to larger bubbles at detachment. Buwa et al. (2007) used the CLSVOF method to study the bubbling regimes using high gas flow rates. The inertia effect in that study was more dominant than the capillary effect. Chakraborty et al. (2009) studied the effect of reduced gravity on the bubble shape and the detachment volume. They found that reducing the gravity gives larger detached bubbles and lower formation frequency. Later on, Chakraborty, Biswas and Ghoshdastidar (2011) looked into the co-flowing effect due to the ratio of liquid to gas velocity on the bubble formation. They also studied the minimum bubble radius (neck radius) in co-flowing flows which was found to follow a power law behavior. Ohta et al. (2011) used the sharp interface method (Sussman et al., 2007) to study bubble growth with large gas inflow velocity. They noticed that the bubbling process takes a specific amount of time before reaching a steady state as the agitated liquid around the first bubble affects the formation of the next formed bubbles.

In spite of the numerous studies published on bubble growth and detachment using VOF, LS, or CLSVOF, comparisons between the three methods are not available and the complete history of the formation including detachment has generally not been

compared adequately against experimental data. Gerlach et al. (2006) did compare different surface tension models (Kernal, PROST, and CLSVOF) using several test cases (equilibrium rod, capillary wave, and Rayleigh-Taylor instability). The least spurious currents were obtained with the PROST method. The results showed that CLSVOF can alleviate the spurious currents with less computational expense when compared to the PROST method. The comparison analysis, however, was not extended to bubble growth. Carlson, Kudinov and Narayanan (2008) studied the accuracy of both diffusive VOF-CICSAM scheme (Ubbink, 1997) and LS using two commercial softwares (Fluent and TransAT) for the study of slug flow. The VOF scheme was found in this case not to correctly predict the slug flow pattern. Although Gerlach et al. (2007, 2005) studied the bubble detachment parameters with respect to different geometrical and physical aspects, a comparison of CLSVOF with other interface capturing methods has not yet been done. The numerical studies available in the literature have not yet attempted to explain differences observed between experimental and numerical results by considering the velocity effect in the gas phase, and variations in the bubble shape which play a important role in the bubble behavior after detachment.

Most of the numerical studies of bubble growth to date have focused on the wake effect behind the first formed bubble on the formation of other bubbles, and on the bubble formation frequency (Chakraborty, Biswas and Ghoshdastidar, 2011; Buwa et al., 2007) using relatively large flow rates (> 100 cm^3/min), whilst there has been no focus on the analysis of the bubble growth under low volumetric flow rates. The numerical studies, however, are very sensitive to the flow rate in particular at smaller flow rates when surface tension becomes predominant allowing spurious currents to affect the solution. The analysis of the formation process under this critical condition allows for the investigation of the accuracy of the surface tension implementation as any error in the surface tension model is expected to lead to unphysical bubble behavior.

2.3.2 Free bubble rise

The bubble starts rising freely in the bulk liquid directly after the detachment from the wall orifice. The phenomenon is relatively simple compared to the bubble growth as there is no interaction between the bubble and the solid boundaries of the numerical domain. However, an accurate capture of the free rise phase is essential for a realistic study of bubble impact on a solid surface. For instance, the bubble

bouncing process is strongly influenced by the bubble shape, trajectory, and velocity reached during its free rise. The experimental study of free bubble rise in viscous liquids due to buoyancy has received considerable attention in the literature over the last decades (Raymond and Rosant, 2000; Clift, Grace and Weber, 1978; Grace, 1973). The work on bubble rise has aimed to study the bubble behavior and classify its geometrical characteristics under different physical properties in order to understand the influence of the bubble and the wake generated behind it on mass and heat transfer problems. It has been found that the bubble can deform to different shapes (spherical, ellipsoidal, and spherical cap) depending on three dimensionless numbers: the Morton number ($Mo = g\mu_l^4 \Delta\rho / \rho_l^2 \sigma^3$), the Bond number ($Bo = g\Delta\rho D_{eq}^2/\sigma$), and the Reynolds number ($Re = \rho_l V_\infty D_{eq}/\mu_l$) (Clift, Grace and Weber, 1978; Grace, 1973), where D_{eq} is the bubble equivalent diameter.

There exist several factors affecting the bubble rise in liquid. These parameters can be summarized as: gas-liquid physical properties (density, viscosity, and surface tension), type of the liquid flow (quiescent, co-flowing, and shear flow), and the operating conditions (pressure, temperature, and gravity). In the following, two parameters will be highlighted, namely the surfactants and liquid temperature, as they have a strong influence on the bubble terminal velocity[5] during its rise compared to the numerical simulations. In non-pure liquids, surfactants present in the liquid phase tend to gather around the bubble surface leading to a reduction in the bubble fluidity. Malysa, Krasowska and Krzan (2005) studied the effect of such interface contamination on the bubble terminal velocity during its rise. They found that the presence of surfactants decreases significantly the bubble terminal velocity as the bubble becomes increasingly immobile with increasing concentration of interface contamination. Leifer, Patro and Bowyer (2000) studied the effect of the water temperature on the bubble rise velocity using bubbles with equivalent radii in the range ($0.377 - 4.5$ mm). The experimental observations confirmed that the water temperature has a considerable influence on the bubble velocity. For bubble with equivalent radius 0.5 mm, the rise velocity drops approximately 40 mm/s when the temperature increases from 10° to 35°. This clearly highlights the importance of carefully checking the fluid properties when selecting experimental data for the purpose of validating numerical results.

The path of the bubble during its free rise is also an important feature that can affect the bouncing process. The instability in the bubble path is believed to be

[5]The terminal velocity is the bubble velocity when its shape takes a terminal constant form during the rise

due to bubble shape oscillation, surfactant contamination, and wake instabilities. Saffman (1956) conducted an experimental study to investigate the bubble path when it rises in filtered water. Three different trajectories were identified based on the bubble equivalent diameter: Rectilinear ($D_{eq} < 1.4$ mm), zig-zag motion in a fixed plane ($1.4 < D_{eq} < 2$ mm), and complex motion with either zig-zag or spiral like coiled spring motion ($2 < D_{eq} < 4.6$ mm). Tomiyama et al. (2002) also concluded that the way of the bubble is released at the beginning of the free rise plays an important role in determining the bubble motion, shape, and velocity during the free rise.

In the last decade, two-fluid flow numerical simulations have been recognized and employed as an efficient tool for studying the bubble rise behavior under a wide range of Morton and Bond numbers (Wang et al., 2010; Hua and Lou, 2007; Mukundakrishnan et al., 2007; Ohta et al., 2005). Most of the early bubble rise simulations were devoted to the study of the bubble dynamics with intermediate shape deformation (spherical and ellipsoidal). Several numerical studies have also managed to analyze the bubble rise dynamics and shape using a 3D domain (Amaya-Bower and Lee, 2010; Rabha and Buwa, 2010; Yu and Fan, 2008). The 3D numerical simulations performed by Yu and Fan (2008) , for example, provided information on the vortex generation behind the bubble using the streamlines vector plots. It was found that a closed vortex is formed behind the ellipsoidal bubble and two (close and far) vortices are formed behind the skirted bubbles. Recently, numerical analysis have been extended to cover larger bubbles. Ohta and Sussman (2012) studied the motion of single skirted bubbles using the Sharp Interface CLSVOF method coupled with a block structured adaptive grid refinement technique for capturing accurately the thin skirts of the bubble. The mesh refinement made it possible to analyze the density ratio effect on the trailing bubble skirts.

Finally, it is worth noting that the bubble motion induced by gravity alone, i.e. without other external effects such as confinement due to boundary walls, has also been considered as an appropriate test case for validating different two-fluid flow numerical methods. See Table 2.1 for a list of recent works which used the free bubble rise application to contribute to the validation of a range of numerical methods.

Table 2.1: List of some recent works in the literature that used the free bubble rise for validating of the numerical two-fluid flow methods.

Authors	Two-fluid flow method
Sussman et al. (1998)	LS
Son (2001)	LS
Annaland, Deen and Kuipers (2005)	VOF
Ohta et al. (2005)	CLSVOF
Hua and Lou (2007)	Interface Tracking method
Yu and Fan (2010)	Lattice Boltzmann
Sun and Tao (2010)	VOSET
Ohta and Sussman (2012)	Sharp Interface method
Albadawi et al. (2013)	CLSVOF
Chakraborty, Biswas and Ghoshdastidar (2013)	CLSVOF

2.3.3 Bubble bouncing

When a free rising bubble impacts on a horizontal solid surface, it either bounces or oscillates on that surface based on its kinetic energy. The mechanisms which influence the bubble dynamics during bouncing include bubble deformation, and film formation and drainage in the intervening region between the bubble and the wall. The last stage of the bouncing process includes a film rupture where the air in the bubble comes in direct contact with the solid surface. An experimental study of the bubble collision is particularly challenging because of the wide range of the length scales involved, going from macroscopic (bubble radius) to microscopic (film radius and thickness). Therefore, the mechanism of the bubble bouncing has tended to be categorized and grouped with different focuses which are: The geometrical analysis of the bubble shape during the full bouncing process, the study of the film formation and drainage, and finally the three phase contact line ($TPCL$) formation and surface de-wetting. Fig. 2.7 shows a schematic diagram of the bubble shape and the corresponding geometrical characteristics during the bouncing process.

In the first group, the bouncing process and the number of bouncing cycles have been analyzed based on the bubble initial kinetic energy before collision (Zawala et al., 2007; Tsao and Koch, 1997). The bubble behavior is described using geometrical characteristics such as the bubble center of gravity, aspect ratio, and coefficient of restitution (Zenit and Legendre, 2009; Legendre, Daniel and Guiraud, 2005). Other experimental studies focused on investigating the influence of the surfactant distribution in the bulk liquid (Malysa, Krasowska and Krzan, 2005) and the surface material properties (Kosior, Zawala and Malysa, 2012; Zedníková, Vobecká

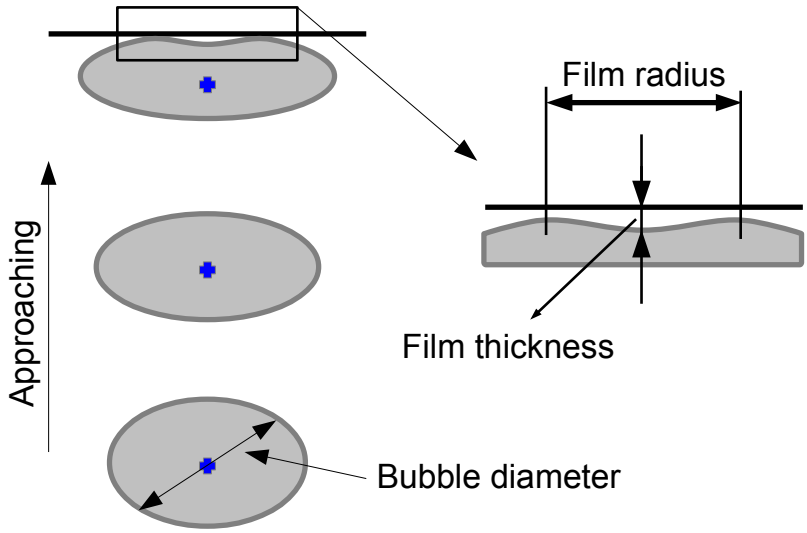

Figure 2.7: Schematic sketch of the bubble shape when it bounces on a solid surface. The main characteristic dimensions are shown.

and Vejrazka, 2010; Krasowska, Zawala and Malysa, 2009) on the bubble behavior during the bouncing. However, most of these studies have been limited to the first stage of the collision up to the moment when the bubble stops oscillating on the solid surface, while other more complicated experimental setups would have been required for the study of the liquid film and the TPCL formation.

In the second group, the flow field in the film region has tended to be studied using the lubrication theory to deal with the small characteristic thickness of the liquid film. Hendrix et al. (2012) and Klaseboer et al. (2001) used this theory to study the film thinning. They highlighted that the existence of the high pressure as the bubble gets closer to the wall is the reason of the bubble rebounding from the surface. Chan, Klaseboer and Manica (2011) presented a review of the different experimental approaches followed for the study of the spatio-temporal evolution of the film drainage between drop-flat surface, drop-particle, and drop-drop. The potential flow theory has been modified by Klaseboer, Manica and Chan (2012) to include the viscosity effect so that the method becomes capable of simulating bubble rise and bounce. The equations are is this case solved using the Boundary Element method. The amplitude of rebound predicted by the numerical simulation was found to be higher than that observed experimentally. This was attributed by the authors to ignoring the energy damping which occurs within the film.

The third group is concerned with the last stage of bouncing when the film thickness decreases to a value where the drainage is controlled by the intermolecular forces within the liquid. The properties of the surface material start to influence the bouncing process leading to either contact line formation (for hydrophobic surfaces) or to stabilizing of a permanent film between the bubble and the wall (for hydrophilic surfaces) (Kosior, Zawala and Malysa, 2012). The formation of the TPCL at the last stage of bubble bouncing highlights the dependence of the bubble dynamics on the wetting phenomena and the dynamic contact line. Fetzer and Ralston (2009) and Phan, Nguyen and Evans (2006) have studied experimentally the de-wetting process when a small air bubble rising in a deionized water hits a horizontal wall. This work focused only on the last stage of the bouncing starting from the moment when the three phase contact line forms. Phan, Nguyen and Evans (2006) used a combined model of both the Hydrodynamic and the Molecular Kinetic models to calculate the contact line velocity in terms of the apparent dynamic contact angle. This model is based on the assumption that the bubble is symmetric, and it avoids the need of using a macroscopic length scale as it otherwise would with the Hydrodynamics model. The coupled model, however, includes fitting parameters such as the slip length (microscopic length scale) and the molecules jumping distance and frequency. Fetzer and Ralston (2009), on the other hand, divided the de-wetting process into two different stages; the first stage was best described by the Hydrodynamics model indicating the dominance of the viscous shear in the dissipation mechanism. The second stage of the de-wetting process was defined by the low contact line velocity and was best described by the Molecular Kinetics model. In general, both models highlighted the difficulty in modeling the de-wetting process precisely as it depends strongly on many parameters that can only be obtained by fitting with experimental data.

Over the past decade, there has been an increasing focus on the numerical analysis of the bubble bouncing. Canot et al. (2003) managed to couple the Boundary Element method with a lubrication approximation. This coupling made it possible to model the full dynamics of the bubble bouncing. However, this study did not consider any 3D bouncing process and no quantitative comparison was performed to assess the numerical results. The analysis of the bubble-wall collision dynamics and the corresponding energy dissipation have been studied by Omori et al. (2010) using the interface tracking method (Muzaferija and Perić, 1997) for two-dimensional bubbles with equivalent diameters ($1,2$ mm). The Immersed Boundary approach was used in this case to deal with the rigid wall by imposing a no-slip boundary.

The authors managed to capture properly the thin liquid film (dimple) separating the bubble from the rigid wall. However, there was no detail about the contact angle modeling at the rigid wall, and the three phase contact line formation was not mentioned. Sanada, Watanabe and Fukano (2005) solved the full Navier-Stokes equations coupled with the Level Set method for the analysis of bubble bouncing against a free surface (air/water). Contrary to Tsao and Koch (1997), they found that when the bubble approaches the free surface, the pressure in the film does not increase acutely suggesting that the bouncing process is not completely controlled by the mechanisms happening in the entrapped film. Most recently, Qin, Ragab and Yue (2013) used an arbitrary-Lagrangian-Eulerian approach for the study of bubble-wall interaction at high Morton numbers. The flow field in the liquid domain was solved using a Finite Element formulation while the flow in the gas domain was neglected. The bubble interface was tracked using a moving mesh and the film drainage was simulated using an adaptive mesh so that at least three cells always exist in the region between the bubble surface and the wall. Even though the mesh was adaptive, simulating the film rupture was not possible and the simulation was stopped whenever the film thickness reached a value of 1/100th of the bubble radius.

In spite of the extensive numerical modeling work on disperse gas bubble flow and on the dynamics of drops impinging upon a solid surface [see for example Dupont and Legendre (2010); Sikalo et al. (2005)], there is still a distinct lack of understanding on the suitability of the commonly used VOF interface capturing method and some of the main contact line models to correctly capture the mechanisms of air bubble impacting on and bouncing from a surface. Its ability to model the correct spatio-temporal characteristics of the liquid film formation and drainage including pressure distribution and its effect on the bubble dynamics still needs to be studied. Furthermore, there is no track of any 3D numerical simulations performed on bubble bouncing in the literature.

2.4 Final Remarks

A review on the literature of interface capturing methods, wetting dynamics phenomena, and different challenging two-fluid flow problems has been presented. The innovative solutions proposed for improving the different interface capturing techniques were highlighted. Each numerical technique proved to be efficient at some points because of one of its properties. See Table 2.2 for the advantages and disad-

vantages of each interface capturing method employed in the present study.

Table 2.2: Advantages and disadvantages of interface capturing methods.

Numerical method	Advantages	Disadvantages
VOF-PLIC	Mass conservation	Computationally expensive
	Accurate interface reconstruction	Difficult to implement in 3D
		Interface discontinuities
VOF-Comp	Mass conservation	Diffused interface
	Simple implementation	
	Efficient execution time	
LS	Sharp interface characteristics	Loss of Mass (volume)
	Simple implementation	re-distancing is required
CLSVOF	Mass conservation	Difficult to implement
	Sharp interface	Computationally expensive

It can be concluded from the literature review that several distinctive features should be examined for validating the two-fluid flow numerical methods: CPU time efficiency, implementation for general grids, interface smoothness, spurious currents, and mass conservation. As noticed in the literature, a comparison between the numerical methods under critical conditions is seldom. The numerical simulation of bubble growth from a single orifice was chosen as a suitable application to compare the accuracy and efficiency of the three interface capturing methods. The literature review showed that there exists several numerical studies on the bubble growth using VOF, LS, or CLSVOF separately. Most of the research to date, however, has focused on the bubble formation frequency and the parametric study of the bubble growth. In contrast, the present work will aim to compare the three different methods using both bubble growth and detachment. Low flow rates will also be used in order to assess the surface tension modeling. The comparison will be performed by investigating the bubble geometrical characteristics during the full formation process until detachment.

A thorough review of the wetting dynamics has also been performed. Although it has been previously studied [see the reviews by (Bonn et al., 2009; Shikhmurzaev, 1997; De Gennes, 1985), the precise mechanism involved in the displacement of one fluid by another on a solid surface is still not well understood and there is still some uncertainty about the nature of the interaction between the gas/liquid interface and solid surface. In general, two different approaches have been followed, to date, to

describe the wetting phenomena based on the energy dissipation mechanism; the Hydrodynamic model (Cox, 1986), and the Molecular Kinetic model (Blake and Haynes, 1969). The numerical implementation of the proposed contact line and dynamic contact angle models has also been reviewed in the literature. It was found that most of the validation of the wetting dynamics models considered the study of the drop spreading and impact against solid surfaces. By contrast, there was little research on the implementation of the dynamic models for the de-wetting process when a bubble oscillates on the lower surface of a solid wall.

3 Mathematical formulation and numerical discretization

This chapter presents the mathematical formulation and discretization schemes of the interface capturing methods and contact angle models that will be used later for the study of bubble growth and bouncing. First, the Navier-Stokes equations are stated. The interface capturing methods are defined starting by introducing the Level Set method. The Volume of Fluid method is then presented considering both the algebraic and the geometric techniques for interface reconstruction. The geometrical coupled CLSVOF method is explained shortly. The principal equations of the coupled S-CLSVOF code implemented in this work are then introduced. The explanation of the numerical techniques is complemented with the surface tension model implemented in each method. The implementation of the contact angle models at the solid boundaries and the corresponding interface correction are described. The discretization techniques followed for converting the governing equations into algebraic equations are introduced. Finally, the solution procedure for the governing equations is presented.

The mathematical formulations and the numerical discretization schemes given in OpenFOAM® are described in detail as they will be used for all the applications under investigation. For the other interface capturing methods, including LS in TransAT and the geometrical methods in ANSYS-Fluent, a general description will be provided, and a comparison between the prescribed techniques will be discussed when it is required. Fore more details about the numerical methods and the corresponding discretization schemes in both ANSYS-Fluent®-v13 and TransAT©, the reader is referred to the corresponding theory guide for each software (Ansys, 2011; TransAT, 2011).

3.1 Governing equations

The governing equations for isothermal, incompressible, and immiscible fluids include the continuity (Eq. 3.1), momentum (Eq. 3.2), and interface capturing advection equation (Eq. 3.3):

$$\nabla \cdot \mathbf{V} = 0 \tag{3.1}$$

$$\frac{\partial(\rho \mathbf{V})}{\partial t} + \nabla \cdot (\rho \mathbf{V}\mathbf{V}) = - \boldsymbol{\nabla} P + \boldsymbol{\nabla} \cdot \boldsymbol{\tau_s} + \rho \mathbf{g} + \mathbf{F}_\sigma \tag{3.2}$$

$$\frac{\partial \gamma}{\partial t} + \nabla \cdot (\gamma \mathbf{V}) = 0 \tag{3.3}$$

where ρ is the fluid density, $\mathbf{V}$ the fluid velocity vector, $\boldsymbol{\tau_s}$ the viscous stress tensor for incompressible flow defined as $\boldsymbol{\tau_s} = 2\mu(0.5\left[(\nabla \mathbf{V}) + (\nabla \mathbf{V})^T\right])$, μ the fluid viscosity, P the scalar pressure, $\mathbf{F}_\sigma$ the volumetric surface tension force, $\mathbf{g}$ the gravitational acceleration, and γ the fluid (or phase) indicator function. The above equations do not account for any heat transfer or species transport in the flow field. This formulation implies that the fluid domain is considered as one single mixture with an indicator function γ to account for the difference in the physical properties between the two fluids (gas/liquid). The calculation of the volumetric surface tension force and the fluid physical properties, the density ρ and viscosity μ, varies according to the scalar field γ. The Continuum Surface Force proposed by Brackbill, Kothe and Zemach (1992) will be used for estimating the surface tension across the interface. However, different formulations will be employed depending on the interface capturing technique. The indicator function is defined as either a step function α (for VOF) or a smoothed function ϕ (for LS). The final form of the continuity and momentum equations may vary slightly based of the interface capturing method and the solver used.

3.2 Interface capturing methods

3.2.1 Level Set

In the Level Set method, the two immiscible fluids are characterized using a smoothed distance function ϕ , which can be defined in the following form:

$$\begin{cases} \phi(\mathbf{x},t) > 0 & \text{for } \mathbf{x} \text{ in the liquid phase} \\ \phi(\mathbf{x},t) < 0 & \text{for } \mathbf{x} \text{ in the gas phase} \\ \phi(\mathbf{x},t) = 0 & \text{for } \mathbf{x} \text{ at the interface} \end{cases} \tag{3.4}$$

where $\mathbf{x}$ is the position vector, and t is the time. The interface motion is achieved by advecting the LS function in the computational domain (Sussman, Smereka and Osher, 1994) using:

$$\frac{\partial \phi}{\partial t} + \mathbf{V} \cdot \nabla \phi = 0 \tag{3.5}$$

After a few time steps and due to numerical diffusion, the interface smears over few cells and the LS function ceases to act as a distance function $|\nabla \phi| \neq 1$. A re-initialization process is executed directly after the advection in order to re-distance the LS function. This is achieved by integrating a differential equation against an artificial time (τ):

$$\frac{\partial \phi}{\partial \tau} = S(\phi_0)(1 - |\nabla \phi|) \tag{3.6}$$

where $S(\phi_0)$ is the sign of the initial level set function, and the subscript $(_0)$ stands for the initial LS value before reinitialization. The mixture's physical properties (ρ, μ) are then calculated using a smoothed Heaviside function $H(\phi)$, so that the properties vary continuously across the interface.

$$\rho(\phi) = \rho_g + (\rho_l - \rho_g)H \tag{3.7}$$

$$\mu(\phi) = \mu_g + (\mu_l - \mu_g)H \tag{3.8}$$

$$H(\phi) = \begin{cases} 0 & \text{if } \phi < -\epsilon \\ \frac{1}{2}[1 + \frac{\phi}{\epsilon} + \frac{1}{\pi}\sin(\frac{\pi\phi}{\epsilon})] & \text{if } |\phi| \leq \epsilon \\ 1 & \text{if } \phi > \epsilon \end{cases} \tag{3.9}$$

where ε determines the interface thickness and is defined so that the interface does not smear beyond three cells. The main advantage of using the LS function is its ability to determine an accurate unit normal vector to the interface as:

$$\hat{\mathbf{n}}_c = (\nabla \phi)/(|\nabla \phi|) \tag{3.10}$$

The interface curvature can then be calculated precisely as:

$$\kappa = \nabla \cdot (\frac{\nabla \phi}{|\nabla \phi|}) \tag{3.11}$$

The volumetric surface tension force is estimated using the interface curvature κ, and it is limited to a narrow region around the interface by using the Dirac function δ defined in Eq. 3.13.

$$\mathbf{F}_\sigma = \sigma\kappa(\phi)\delta(\phi)\boldsymbol{\nabla}\phi \tag{3.12}$$

$$\delta(\phi) = \begin{cases} 0 & \text{if } |\phi| > \epsilon \\ \frac{1}{2\epsilon}(1+\cos(\frac{\pi\phi}{\epsilon})) & \text{if } |\phi| \leq \epsilon \end{cases} \tag{3.13}$$

The LS method employed in the TransAT software is used for the present study. This is a multi-physics, Finite Volume code based on solving the Navier Stokes equations on a structured orthogonal grid.

3.2.2 Volume of Fluid

In the VOF method, both the continuous and discrete fluids are defined by the volume fraction α. It lies in the range $[0, 1]$. The liquid (continuous fluid) is defined in cells where $\alpha = 1$, while the gas (dispersed fluid) is defined in cells where $\alpha = 0$. The cells with a volume fraction between 0 and 1 are intersected by the interface. The volume fraction satisfies the advection equation:

$$\frac{\partial\alpha}{\partial t} + \nabla\cdot(\alpha\mathbf{V}) = 0 \tag{3.14}$$

In this study, two methods have been considered for the solution of Eq.3.14. The interface is reconstructed using either the geometrical technique implemented in ANSYS-Fluent (It is referred to as *VOF-Geo* in this work), or it is defined using the algebraic *interFoam* solver of OpenFOAM (It is called here *VOF-Comp*). The physical properties of the two immiscible fluids are calculated using a volume fraction weighted average:

$$\rho = \rho_l\alpha + \rho_g(1-\alpha) \tag{3.15}$$

$$\mu = \mu_l\alpha + \mu_g(1-\alpha) \tag{3.16}$$

Compressive VOF method (VOF-Comp)

OpenFOAM uses an algebraic approach based on a counter-gradient transport scheme to advect the volume fraction α (Weller, 1993). This technique adds a compressive term to the α advection equation in order to retain the conservative-

ness, convergence, and boundedness (Weller, 2008). The advection equation is reformulated as:

$$\frac{\partial \alpha}{\partial t} + \nabla \cdot (\mathbf{V}\alpha) + \nabla \cdot (\mathbf{V}_c \alpha \beta) = 0 \tag{3.17}$$

where $\beta = 1 - \alpha$, and $\mathbf{V}_c = \mathbf{V}_l - \mathbf{V}_g$ is the compressive velocity (Berberović et al., 2009). The subscripts l and g stand for the liquid and the gas, respectively.

The compressive velocity is taken into consideration only in the region of the gas/liquid interface and it is defined in the normal direction to the interface to avoid any dispersion. This is achieved by multiplying the compression velocity by $(\nabla\alpha/|\nabla\alpha|)$. Moreover, a compression factor c_α is used to increase the compression as:

$$\mathbf{V}_c = min(c_\alpha |\mathbf{V}|, \max(|\mathbf{V}|)) \frac{\nabla \alpha}{|\nabla \alpha|} \tag{3.18}$$

where $(\max |\mathbf{V}|)$ is the maximum speed anywhere in the numerical domain.

Most of the computational results presented here are obtained with a compression factor $c_\alpha = 2$. Other values are also used as will be shown later. The volume fraction advection equation is solved using an additional limiter to cut-off the face fluxes at the critical values. This technique is similar to the Flux Corrected Transport scheme applied by Zalesak (1979). More details will be introduced in Section 3.4.4. The volumetric surface tension force is calculated using the Continuum Surface Force model (CSF) without the density averaging proposed by Brackbill, Kothe and Zemach (1992):

$$\boldsymbol{F}_\sigma = \sigma \kappa(\alpha) \boldsymbol{\nabla} \alpha \tag{3.19}$$

where $\kappa(\alpha)$ is the interface curvature calculated using the updated value of α after advection. The curvature represents the magnitude of the interface normal flux at a specific face of the cell, and it indicates the direction of this flux

$$\kappa = -\nabla \cdot \ \hat{\boldsymbol{n}}_{\boldsymbol{c}} \tag{3.20}$$

where $\hat{\mathbf{n}}_c$ is the unit interface normal. It is calculated using the volume fraction field and it refers to the direction of the largest phase field changes in the numerical domain.

$$\hat{\boldsymbol{n}}_{\boldsymbol{c}} = \frac{(\nabla \alpha)}{|(\nabla \alpha)|} \tag{3.21}$$

It is worth noting that the curvature sign is chosen in both VOF (Eq. 3.20) and LS (Eq. 3.11) methods so that the two calculated curvatures are with the same sign

and different absolute values.

Geometrical VOF method (VOF-Geo)

The geometrical VOF-Geo method is based on the PLIC scheme for reconstructing the interface in cells near the gas/liquid surface. This involves two main steps: The interface is first reconstructed using a piecewise interface segment whose normal direction and its position from the cell center are determined from the volume fraction α and the interface normal. This normal is calculated based on the gradient of the volume fraction at the cell center ($\mathbf{n}_c = \nabla\alpha$). The second step includes evaluating the fluxes of α required to determine $\nabla \cdot (\alpha \mathbf{V})$ in Eq.3.14. The amount of the advected fluid in each cell is determined from a geometrical reconstruction of the interface displacement through the cell faces and the distribution of the normal and tangential velocity field in the cell faces. Precise details of the schemes as implemented in Fluent are available from the software's theory guide (Ansys, 2011). The volumetric surface tension force is estimated using the Continuum Surface Force model (CSF) proposed by Brackbill, Kothe and Zemach (1992):

$$F_\sigma = \sigma \frac{\rho\kappa(\alpha)\nabla\alpha}{1/2(\rho_g + \rho_l)} \tag{3.22}$$

where σ is the surface tension coefficient, $\kappa(\alpha)$ is the interface curvature which is calculated in terms of the unit interface normal $\hat{\mathbf{n}}_c$, and ρ is the mixture density calculated using Eq. 3.15.

3.2.3 Coupled CLSVOF

In the present work, two different techniques for coupling Volume of Fluid with Level Set are employed. In the first case, the geometrical CLSVOF method (*CLSVOF-Geo*) recently implemented in the commercial software ANSYS-Fluent-13 is used. The second technique is based on a simple implementation of an algebraic coupling method (S-CLSVOF) using the open source library (OpenFOAM).

Geometrical CLSVOF method (CLSVOF-Geo)

The coupled CLSVOF method has recently been implemented in ANSYS-Fluent-13 with a view to obtain mass conservation by advecting the volume fraction α, and preserve the interface sharpness by calculating the interface normal using the smoothed function ϕ. In this method, both LS and VOF equations are solved which makes it more computationally expensive than the VOF-Geo method. The

re-initialization is accomplished by using the PLIC geometrical reconstruction.

The interface normal and curvature are calculated using the LS function (Eqs.3.10 and 3.11), while the exact position of the interface is adjusted by balancing the volume in each cell so that the volume fraction value calculated from VOF is satisfied. Once the interface is determined, its points of intersection with the cell faces are calculated geometrically. At this stage, the LS function is reinitialized by setting its values at the cell centers as the minimum normal distance from each cell center to the closest interface front. This technique enforces the mass conservation while re-distancing the LS function. The surface tension force and the physical properties are calculated in a similar manner to the LS method (Eqs.3.12, 3.7 and 3.8, respectively).

Implemented CLSVOF method (S-CLSVOF)

The extension of the VOF-Compressive scheme implemented in OpenFOAM into a new coupled method (S-CLSVOF) is explained here. The coupling takes the advantage of the mass conservativeness of the VOF method and the interface smoothness of the LS method. In the S-CLSVOF solver, a new Level Set field ϕ is introduced where the interface position is defined by the iso-line $\phi = 0$. Although two separate fields, namely VOF and LS, are defined to represent the fluid domain, only the VOF advection equation (Eq.3.17) is solved instead of the two Level Set and Volume fraction equations as required in the standard CLSVOF methods (Sussman and Puckett, 2000). The first step of the coupling is to assign an initial value to the Level Set function using the advected VOF fraction function and assuming that the interface position is located at the iso-line contour $\alpha = 0.5$:

$$\phi_0 = (2\alpha - 1) \cdot \Gamma \tag{3.23}$$

where $\Gamma = 0.75\Delta$ is a small non-dimensional number whose value depends on the mesh step size Δ [1]. The main criterion in choosing this value is to satisfy an initial value of ϕ which is close to the mesh step size. The initial function ϕ_0 is a signed function since it has a positive value in the liquid and a negative value in the gas. This value (ϕ_0) is then re-distanced by solving the re-initialization equation:

$$\begin{cases} \frac{\partial \phi}{\partial \tau} = S(\phi_0)(1 - |\nabla \phi|) \\ \phi(\mathbf{x}, 0) = \phi_0(\mathbf{x}) \end{cases} \tag{3.24}$$

[1] The calculated value of Γ is divided by a characteristics unit length so that the initial Level Set function in Eq. 3.23 is dimensionless. Similar procedure is applied when calculating $\Delta\tau$.

where τ is the artificial time, $\mathbf{x}$ is the position vector, and $S(\phi_0)$ is a sign function. The solution converges to a signed distance function achieving $|\nabla\phi| = 1$. The convergence starts from the interface and moves towards both fluids. The artificial time step is chosen as $\Delta\tau = 0.1\Delta x$, so that there are no sharp changes in the LS function during the reinitialization. Since the re-initialization equation gives a distance function around the interface before spreading towards each fluid, only a few iterations (ϕ_{corr}) are required. For specific values of Γ and $\Delta\tau$, the number of iterations (ϕ_{corr}) is found to meet the condition:

$$\phi_{corr} = \frac{\epsilon}{\Delta\tau} \tag{3.25}$$

where ε is the interface thickness which defines the number of cells used for the transition between both fluids, and is chosen as $2\varepsilon = 3\Delta$ where Δ is the mesh step size.

Since the Level Set function is a continuous function, it helps in determining accurately the interface normal as $\hat{\mathbf{n}}_c = \nabla\phi/|\nabla\phi|$. Hence, it provides a more precise and smoother interface curvature $\kappa = \nabla \cdot \hat{\mathbf{n}}_c$. It is important to mention here that special care should be taken when considering a contact angle boundary condition since the interface normal should be corrected to satisfy the imposed contact angle similarly to the VOF method as will be shown in the next section. The volumetric surface tension force can then be calculated as:

$$\mathbf{F}_\sigma = \sigma\kappa(\phi)\delta(\phi)\nabla\phi \tag{3.26}$$

where σ is the surface tension coefficient, and δ is the Dirac delta function (Eq.3.13) used to limit the influence of the surface tension to a narrow region around the interface. This function is centered at the interface and takes a zero value in both fluids. Eq. 3.26 means that the influence of surface tension is spread over a finite interface thickness. The extent of the interface smearing, which is determined in terms of the ε parameter, will be shown in Chapter 5 to have a non-negligible influence on the solution. However, the typical value proposed above provides good results for bubble growth problems. The physical properties of the fluid mixture can be defined either as in the VOF method (Eqs.3.15 and 3.16) or calculated using a Heaviside function (Eqs.3.7 and 3.8). Although calculating the fluid properties using the Heaviside function gives smoother transitions of the properties across the interface than using the VOF function, both methods have been found to give similar results for bubble growth problems. In the present work, Eqs.3.15 and 3.16 are used

for assessing the coupled code.

3.3 Contact angle modeling

The contact line region is decomposed into two main parts; the outer macroscopic region with non-negligible inertia and the inner region with very small inertia influence (Fig. 3.1). The details of the flow in the inner region can be simulated using a slip length of molecular scale. However, this very small area cannot be directly simulated. Therefore, it is substituted by a local force parallel to the wall. The force is calculated based on the inner dynamic contact angle and it is applied at the boundary cells of the numerical domain where a contact angle model is defined. Similar procedure is applied by Sikalo et al. (2005) for the contact angle model. This angle defines the interface slope in the matching area between the inner and the outer regions. In the present work, an implemented contact angle model (θ_i) is used to correct numerically the interface. This is done by using two different contact angle definitions; (i) the static contact angle ($\theta_i = \theta_s = \theta_e$), where θ_e is the equilibrium contact angle, and (ii) the dynamic contact angle ($\theta_i = \theta_d$) where an empirical model should be used to estimate the variations of the contact angle with time. It is important to highlight here that the contact angle θ_i differs from the apparent contact angle θ_{app}. The last one is the angle observed experimentally and it varies based on the resolution of the measurements tools.

Numerically, the local force in the inner region is represented in the contact angle boundary condition via the CSF model with a normal vector corrected at the interface as:

$$\hat{\boldsymbol{n}} = \hat{\boldsymbol{n}}_w \cos\theta + \hat{\boldsymbol{t}}_w \sin\theta \tag{3.27}$$

where $\hat{\mathbf{n}}_w$ is the unit normal to the wall and $\hat{\mathbf{t}}_w$ is the unit vector located at the wall and normal to the contact line formed between the gas/liquid interface and the wall (Brackbill, Kothe and Zemach, 1992).

In OpenFOAM, the interface normal calculated from the gradient of the VOF function (Eq. 3.21) satisfies a different contact angle ($\hat{\mathbf{n}}_c \cdot \hat{\mathbf{n}}_w = \cos\theta_\alpha$) than the imposed one ($\hat{\mathbf{n}} \cdot \hat{\mathbf{n}}_w = \cos\theta_i$). Therefore, the interface normal is corrected at the wall boundaries following a linear interpolation process (See Appendix C). Once the interface normal is re-oriented at the cells neighboring the wall boundary, the gradient of the volume fraction at these cells is corrected. However, this correction

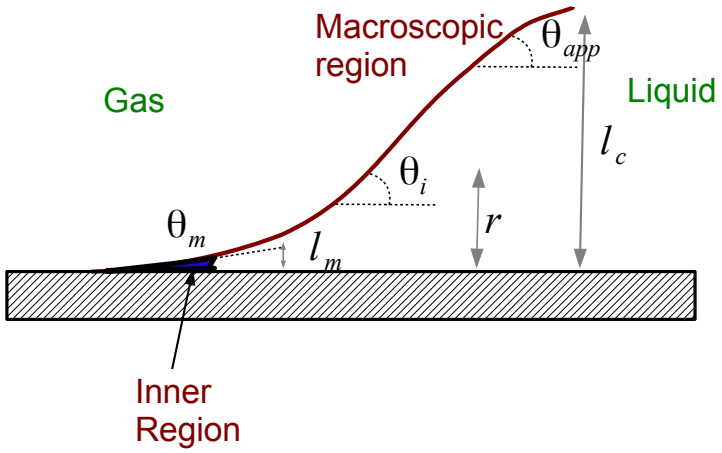

Figure 3.1: A schematic diagram of the contact line region including the microscopic, numerically implemented, and apparent contact angles.

might cause unbounded volume fractions at the wall boundaries. To resolve this problem, a limiter is used to bound the volume fraction. Four options are available for limiting the VOF function at the interface:

- Limit None: no limiter is applied to the gradient of α calculated during contact angle correction.
- Limit Gradient: The gradient of α is limited $(\delta_s \times \{max[min(\nabla\alpha + \frac{\nabla\alpha}{\delta_s}, 1), 0]\} - \nabla\alpha)$, so that the volume fraction is bounded on the wall , with δ_s is a dimensional coefficient for the distance between the cell centers of the neighboring cells. This limit is considered for the present work.
- Limit Alpha: The volume fraction on the wall is limited in the range $[0, 1]$.
- Limit Zero Gradient: zero gradient boundary condition is applied to the volume fraction at the wall.

In the present work, the dynamic contact angle model has also been implemented in OpenFOAM. This angle varies at each time step with the contact line slip velocity. It also affects the slipping of the three phase contact line (TPCL) on the solid surface at the last stages of the bouncing process after the film drainage (Fetzer and Ralston, 2009; Phan, Nguyen and Evans, 2006). In contrast to the static contact angle model, the dynamic angle accounts for the dependence of the contact angle on the fluid's physical properties (E.g. fluid-fluid surface tension and fluids viscosity)

and the surface material properties (friction coefficient, advancing/receding contact angle). Some models require extra parameters that can be only obtained by fitting with experimental measurements. The main models that are implemented for the dynamic contact angle are Jiang, Brake, Cox, Afkhami, and Kistler models (See Appendix B for the corresponding relations). In this thesis, the study of bubble bouncing compares the static contact model against the dynamic model calculated using the Kistler relation (Kistler, 1993) as follows:

$$\theta_i = \theta_d = f_H(Ca_{slip} + f_H^{-1}(\theta_e)) \tag{3.28}$$

$$f_H(x) = \arccos\left\{1 - 2\tanh\left[5.16\left(\frac{x}{1+1.31x^{0.99}}\right)^{0.706}\right]\right\} \tag{3.29}$$

where $f_H^{-1}(\theta_e)$ is the inverse of the "Hoffman's" empirical function. This model has been coupled with the VOF method (Roisman et al., 2008; Sikalo et al., 2005) or the interface tracking method (Muradoglu and Tasoglu, 2010) for the study of the drop impact on partially wetting surface. It was found that the numerical results with the dynamic model predicts more accurately the drop recoiling stage compared to the static contact angle model.

The slip model for solving the singularity issue at the solid boundaries depends on the method used for capturing the interface. In the present work, two different strategies are followed for calculating the slip velocity with the algebraic VOF method. In the first case, the slip velocity is calculated implicitly using the tangential velocity vector of the first cell close to the solid boundary:

$$u_{slip} = \frac{(\hat{\mathbf{n}}_c)_{t_w}}{|(\hat{\mathbf{n}}_c)_{t_w}|} \cdot (\mathbf{V})_{t_w} \tag{3.30}$$

where the subscript t_w indicates the tangential component to the wall. This implies that at the neighboring cells to the wall, there is an implicit slip velocity at a distance $\Delta/2$ from the solid wall, where Δ is the mesh step size. On the other case, the slip velocity is calculated explicitly using the Navier slip law which depends on using a slip length rather than the mesh size:

$$u_{slip} = \lambda\dot{\gamma} \tag{3.31}$$

where λ is the slip length, u_{slip} the slip velocity at the interfaces, $\dot{\gamma}$ is the shear rate at the interface. For cases with contact angle hysteresis, the equilibrium contact

angle in Eq. 3.28 is replaced by either the advancing or the receding contact angle. The following condition is applied for choosing the proper contact angle noting that the interface normal is always directed into the liquid:

$$\theta_e = \begin{cases} \theta_{adv} & \text{if bubble advances } (\hat{n}_c \times u_{slip} > 0) \\ \theta_{rec} & \text{if bubble recedes } (\hat{n}_c \times u_{slip} < 0) \end{cases} \tag{3.32}$$

3.4 Finite Volume discretization

In this section, a brief description of the discretization procedure followed in the open source library (OpenFOAM) is presented. The explanation includes descriptions of the solution domain, final form of the governing equations, main spatial and temporal discretization schemes, discretization of the VOF advection equation, pressure-velocity coupling, boundary conditions, and solution procedure. The discretization schemes in the other softwares, Fluent and TransAT, are chosen so that the spatial terms are discretized with second order accurate schemes and the temporal terms are discretized using the Euler implicit scheme (It will be explained below). The criterion in choosing the discretization schemes is to obtain similar order of accuracy for all the compared techniques in the results.

3.4.1 Discretization of the solution domain

In the CFD simulations, the governing equations should be discretized in order to obtain a numerical solution. The discretization process means converting the partial differential terms and the whole differential equations into discrete quantities and algebraic equations, respectively. The discretized equations can then be solved using iterative solvers for the unknown variables. The discretization is decomposed into two parts:

- Discretize the physical problem spatially and temporally: This can be achieved by choosing a numerical domain that conforms with the physical boundaries. The numerical domain is discretized into a finite number of cells using structured or unstructured grids. This discretization is prescribed by the mesh step size Δ. The numerical problem is then solved using finite time step size Δt. The last two parameters could take either fixed or adaptive values according to the analyzed problem.

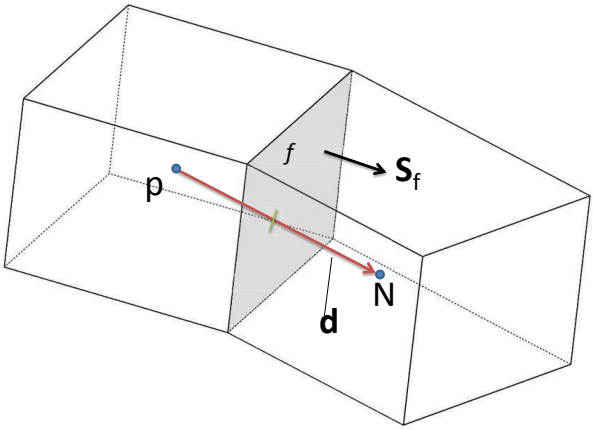

Figure 3.2: A schematic shape of the owner and neighbor cells in the discretized domain.

- Convert the differential terms of the governing equations into discrete quantities.

Fig. 3.2 shows a description of the mesh structure and the associated terminologies as defined in the OpenFOAM library. Two adjacent cells are shown in this figure; the *owner* cell and the *neighbor* cell. In the present work, two different types of numerical domains are considered for the study of the two-fluid flow problems; the axi-symmetrical domain with a wedge-like shape to define the physical boundaries. With both TransAT and Fluent, the axi-symmetrical simulations are defined using a rectangular space shape. For 3D problems, the numerical domain is discretized in this research using Hexahedral cells. These cells are all bounded by eight faces, given the label f. The area vector normal to the cell face is denoted as $\mathbf{S}_f$. The distance vector connecting the owner cell center point P to the neighbor cell center point N is labeled $\mathbf{d}$. The variables stored at the cell centers are called *volume fields*, while the variables stored in the cell faces are defined as *face fields*. As a non staggered grid arrangement is used, the Rhie-Chow momentum interpolation (Rhie and Chow, 1983) is applied to avoid checker-boarding.

The discretization converts the differential equations into a set of algebraic equations that have the general form:

$$[A]\{x\} = \{b\} \tag{3.33}$$

The matrix $[A]$ is a square matrix that includes all the coefficients obtained from the discretization. The vector $\{x\}$ represents the fields to be solved including velocity, pressure, and indicator function. $\{b\}$ in the right hand side of Eq.3.33 is the source vector. The coefficients of the finite volume matrix and the geometric fields are classified in $[A]$, $\{x\}$, and $\{b\}$ according to the field to be solved.

3.4.2 Momentum equation

In this section, the final form of the momentum equation (Eq. 3.2) employed for solving the algebraic *VOF* and simplified *S-CLSVOF* methods is derived. This includes substituting the relations that define the viscous stress tensor and the volumetric surface tension force. For two-fluid flows, the pressure used to set the boundary conditions is the modified pressure P_{rgh} instead of the static pressure P. The relation between these two variables is defined as:

$$P_{rgh} = P - \rho\, \boldsymbol{g} \cdot\ \boldsymbol{x} \tag{3.34}$$

where $\boldsymbol{x}$ is a position vector.

The modified pressure limits the pressure in particular across the interface between fluids with large density differences. Using the modified pressure, the right hand side of the momentum equation can be written as:

$$\ldots = -\ \boldsymbol{\nabla} P + \ \boldsymbol{\nabla} \cdot \boldsymbol{\tau_s} + \rho\, \boldsymbol{g} + \ \boldsymbol{F}_\sigma \tag{3.35a}$$

$$\ldots = -\ \boldsymbol{\nabla} P_{rgh} - \rho\, \boldsymbol{g} - \ \boldsymbol{g} \cdot \boldsymbol{x} \boldsymbol{\nabla} \rho + \ \boldsymbol{\nabla} \cdot \boldsymbol{\tau_s} + \rho\, \boldsymbol{g} + \ \boldsymbol{F}_\sigma \tag{3.35b}$$

$$\ldots = -\ \boldsymbol{\nabla} P_{rgh} - \ \boldsymbol{g} \cdot \boldsymbol{x} \boldsymbol{\nabla} \rho + \ \boldsymbol{\nabla} \cdot \boldsymbol{\tau_s} + \ \boldsymbol{F}_\sigma \tag{3.35c}$$

The divergence of the stress tensor for incompressible flows can be decomposed as:

$$\boldsymbol{\nabla} \cdot \boldsymbol{\tau_s} = \boldsymbol{\nabla} \cdot (\mu[\boldsymbol{\nabla} \boldsymbol{V} + (\boldsymbol{\nabla} \cdot V)^T]) = \boldsymbol{\nabla} \cdot (\mu \boldsymbol{\nabla} \boldsymbol{V}) + (\boldsymbol{\nabla} \boldsymbol{V}) \cdot \boldsymbol{\nabla} \mu \tag{3.36}$$

Considering all the last variables and using the surface tension form of the algebraic VOF method (Eq. 3.19), the momentum equation is expressed in the final general form:

$$\frac{\partial(\rho \mathbf{V})}{\partial t} + \boldsymbol{\nabla}\cdot(\rho \mathbf{V}\mathbf{V}) - \boldsymbol{\nabla}\cdot(\mu\, \boldsymbol{\nabla}\boldsymbol{V}) - (\boldsymbol{\nabla}\boldsymbol{V})\cdot \boldsymbol{\nabla}\mu = -\boldsymbol{\nabla}P_{rgh} - \boldsymbol{g}\cdot\boldsymbol{x}\,\boldsymbol{\nabla}\rho + \sigma\kappa\,\boldsymbol{\nabla}\alpha \tag{3.37}$$

3.4.3 Spatial and temporal discretization

In the finite volume formulation, the integral form of the governing equations is solved. The integration is performed over the mesh's cells but the discretization generally relies on surface integral to approximate diffusive and convective fluxes. The transformation is made possible by Gauss' theorem which substitutes the volume integration in the cell by a summation over the cell faces. The generalized form of the Gauss' theorem can be written for a random scalar variable ψ or a random vector variable $\mathbf{a}$ as:

$$\int_v \nabla \cdot \mathbf{a} dv = \int_s d\mathbf{S} \cdot \mathbf{a} = \sum_f \mathbf{S}_f \cdot \mathbf{a}_f \tag{3.38a}$$

$$\int_v \nabla \psi dv = \int_s d\mathbf{S}\psi = \sum_f \mathbf{S}_f \psi_f \tag{3.38b}$$

$$\int_v \nabla \mathbf{a} dv = \int_s d\mathbf{S}\mathbf{a} = \sum_f \mathbf{S}_f \mathbf{a}_f \tag{3.38c}$$

where v is the cell volume, ψ_f the interpolated value of the variable ψ at the cell face f. The discretization process is decomposed into spatial and temporal discretization. The flux approximation requires that estimates of the transported variable at face centers is interpolated using its value at cell centers. In the following, the interpolation process and the spatial and temporal discretization are presented shortly.

Face interpolation

Central differencing (CD) is the default scheme used for the interpolation process in this work (e.g. calculate the velocity face value when evaluating the gradient of the velocity vector field). This scheme is used in the present work for all the variables unless another scheme is determined precisely for a specific operation. The cell face value between the two neighboring cells in Fig. 3.2 is obtained as:

$$\psi_f = f_x \psi_P + (1 - f_x)\psi_N \text{ with } f_x = \frac{|\mathbf{x}_f - \mathbf{x}_N|}{|\mathbf{x}_f - \mathbf{x}_N| + |\mathbf{x}_f - \mathbf{x}_P|} \tag{3.39}$$

where $\mathbf{x}_P$ and $\mathbf{x}_N$ are the position vectors of the owner and neighbor cell centers, respectively. Although *CD* is a second order accurate scheme, it does not provide bounded solutions. For solving the volume fraction advection equation, the boundedness is a critical characteristic that should be retained during the discretization. For this purpose, other interpolation schemes, such as the Total Variation Diminishing scheme, are used to provide a volume fraction field with bounded values (See section 3.4.4).

Gradient

The gradient terms in the final form of the momentum equation (Eq. 3.37) are discretized using the Gauss integration as:

$$\int_v \nabla \psi dv = \int_s d\mathbf{S}\psi = \sum_f \mathbf{S}_f \psi_f \tag{3.40}$$

This process requires the value of the variable ψ at the cell face which can be obtained using the interpolation scheme described above. An example of the gradient term in the momentum equation is the gradient of the modified pressure P_{rgh}. Face normal gradient ($\nabla_f \psi$) is another important gradient term. It is defined as the component, normal to the cell face, of the gradient value at the cell face. This term is approximated in the present work using a second order accurate scheme as follows:

$$\nabla_f \psi = \frac{\psi_N - \psi_P}{|\mathbf{d}|} \tag{3.41}$$

This parameter appears usually in the diffusive term in the momentum equation (The 3rd term in Left hand side of Eq. 3.37), or it is applied for calculating the gradient of the volume fraction in Eq. 3.19.

Convection term

The volume integral of the convective term in the momentum equation, which is expressed in conservative form $\nabla \cdot (\rho \mathbf{V}\mathbf{V})$, is written as a discrete summation over the cell faces:

$$\int_v \boldsymbol{\nabla} \cdot (\rho \mathbf{V}\mathbf{V}) dv = \sum_f \mathbf{V}_f F_f \tag{3.42}$$

where f is the cell face index, $F_f = (\rho \mathbf{V})_f \cdot \mathbf{S}_f$ is the mass flux through the cell face f with $\mathbf{S}_f$ is the face area vector pointing out from the cell.

Diffusion term

The volume integral of the diffusion term in the momentum equation ($\boldsymbol{\nabla}\cdot(\mu\ \boldsymbol{\nabla V})$) is written as a discrete summation over the cell faces:

$$\int_v \boldsymbol{\nabla}\cdot(\mu\ \boldsymbol{\nabla V}) = \sum_f \mu_f (\mathbf{S}_f \cdot \nabla_f \mathbf{V}) \tag{3.43}$$

where $\nabla_f \mathbf{V}$ is calculated using the principal of the face normal gradient described above (Eq. 3.41).

Temporal derivatives

The temporal terms are discretized using the Euler implicit scheme for all the simulations. This scheme provides only first order accuracy but it is unconditionally stable. The Euler implicit scheme has been used for the numerical simulations presented by Rusche (2002) for the study of dispersed two phase flow problems. The volume integration of the first term in the momentum equation (Eq. 3.37) is discretized as:

$$\int_v \frac{\partial(\rho \mathbf{V})}{\partial t} dv \approx \frac{\rho_P^{n+1} \mathbf{V}_P^{n+1} - \rho_P^n \mathbf{V}_P^n}{\Delta t} v_P \tag{3.44}$$

where the subscripts $n+1$ and n indicate the new and the old time values, respectively. v_p is the volume of the owner cell P while $\mathbf{V}_P$ is the velocity field at the center of the owner cell P.

The Finite Volume discretization of the momentum equation (Eq. 3.37) is formulated by integrating all the terms using the schemes described above. The integration over time is obtained using the first order Euler scheme which guarantees, for orthogonal mesh, the boundedness of the solution (Rusche, 2002). After discretization, the momentum equation has the conventional form shown in Eq. 3.52. More details about solving this equation is available in Section 3.4.5.

3.4.4 Discretization of the VOF advection equation

Special discretization must be applied to the convective terms of Eq. 3.17 to minimize interface smearing and preserve boundedness.

$$\frac{\partial \alpha}{\partial t} + \nabla\cdot(\mathbf{V}\alpha) + \nabla\cdot(\mathbf{V}_c\alpha\beta) = 0 \tag{3.17R}$$

with $\beta = 1 - \alpha$

The discretization of the convective terms involve calculating the volume fraction flux $(\sum_f \mathbf{S}_f \cdot (\alpha\mathbf{V})_f)$ and the compression volume fraction flux $(\sum_f \mathbf{S}_f \cdot (-\alpha(1-\alpha)\mathbf{V}_c)_f)$. In cells containing the interface, the discretization of the mass flux (F_f) in Eq. 3.42 involves similar terms. Its interpolation takes account of the interface position through the volume fraction:

$$F_f = [\sum_f \mathbf{S}_f \cdot (\alpha\mathbf{V})_f + \sum_f \mathbf{S}_f \cdot (-\alpha(1-\alpha)\mathbf{V}_c)_f](\rho_l - \rho_g) + [\sum_f \mathbf{S}_f \cdot \mathbf{V}_f]\rho_g \tag{3.45}$$

This equation indicates using the volume fraction fluxes in calculating the mass flux through any cell face. The volume fraction convective term $\mathbf{S}_f \cdot (\alpha\mathbf{V})_f$ is calculated using the Van Leer second order Total Variation diminishing scheme (TVD) (Van Leer, 1979), while the compressive term is discretized using the interface compression scheme described by Weller (2008). The interpolated cell face value of velocity $\mathbf{V}_f$ is obtained in this study using the second order *TVD* scheme named *linearLimitedV* in OpenFOAM following the unstructured mesh method proposed by Darwish and Moukalled (2003). The method defines $\mathbf{V}_f$ according to:

$$\mathbf{V}_f = \lambda(\mathbf{V}_P - \mathbf{V}_N) + \mathbf{V}_N \tag{3.46}$$

where λ is the interpolation factor defined in terms of the TVD limiter $\psi(r)$ and the linear interpolation weight $f_d = (\overline{fN})/(\overline{PN})$ (for uniform grid $f_d = 1/2$):

$$\lambda = \psi(r)f_d + (1 - \psi(r))\chi(\mathbf{V}_f \cdot \mathbf{S}_f) \tag{3.47}$$

χ accounts for the flow direction and is defined by:

$$\chi(\mathbf{V}_f \cdot \mathbf{S}_f) = \begin{cases} 0 & for \mathbf{V}_f \cdot \mathbf{S}_f > 0 (\text{outflow}) \\ 1 & for \mathbf{V}_f \cdot \mathbf{S}_f \leq 0 (\text{inflow}) \end{cases} \tag{3.48}$$

r is the so-called r-factor used to define the TVD limiter in terms of consecutive gradients of the fluxed quantity, i.e. in the case of the convection term, the velocity vector $\mathbf{V}$. In the so-called exact r-factor formulation proposed by Darwish and Moukalled (2003), r is defined by:

$$r = \begin{cases} \frac{2\mathbf{d}_{PN} \cdot (\nabla |\mathbf{V}|)_P}{|\mathbf{V}|_N - |\mathbf{V}|_P} - 1 & for \mathbf{V}_f \cdot \mathbf{S}_f > 0 \\ \frac{2\mathbf{d}_{PN} \cdot (\nabla |\mathbf{V}|)_N}{|\mathbf{V}|_N - |\mathbf{V}|_P} - 1 & for \mathbf{V}_f \cdot \mathbf{S}_f \leq 0 \end{cases} \tag{3.49}$$

where $\mathbf{d}_{PN}$ is the distance vector between the cell center P and the center N of the neighboring cell which shares the face f. The gradient at the numerator is evaluated from the interpolated face values and the Gauss Theorem. The limiter in this LimitedLinearV scheme used in this study is defined by:

$$\psi(r) = max(min(2r, 1), 0) \tag{3.50}$$

which satisfies the second order TVD condition.

The interface compression scheme produced by Weller (2008) uses a limiter to guarantee the boundedness for the volume fraction compression flux (the third term in Eq. 3.17). The limiter is based on blending both central differencing and upwind schemes according to α value:

$$\xi = min(max(1 - max((1 - 4\alpha_P(1 - \alpha_P))^2, (1 - 4\alpha_N(1 - \alpha_N))^2), 0), 1) \tag{3.51}$$

Finally, it is worth noting the negative sign in the volume fraction compression flux in Eq. 3.45. This sign is equivalent to using both up-winding and down-winding at the same time. However, this results in a stability constraint on the time step. A sub-iteration process is used in OpenFOAM to reduce the VOF advection time step without affecting the Navier Stokes time stepping. For the S-CLSVOF method, the sub-iteration process is not adopted and a smaller time step is used to avoid solution divergence. This is performed to avoid the flux accumulation during the sub-iteration process as the flux is calculated directly after solving the VOF advection equation. The main disadvantage of the sub-stepping as highlighted by Weller (2008)

is its influence on the flux adjustment requiring that it is coupled with an Euler implicit time scheme only.

3.4.5 Pressure-Velocity coupling

The solution of the VOF advection equation provides details on the distribution of the volume fraction field at the new time step. The pressure and velocity fields are then updated by solving the velocity-pressure coupling using the Pressure Implicit with Splitting Operators solver (*PISO*) (Issa, 1986). To avoid checker-boarding, the Rhie-Chow interpolation procedure is adopted. The OpenFOAM implementation of the PISO pressure-velocity coupling is summarized below but further details on the formulation may be found in Brennan (2001). The discrete form of the momentum equation integrated over the volume V_P of the cell centered at P, and integrated over time using the Euler Implicit scheme is written in the conventional form:

$$a_P \mathbf{V}_P^{t+\Delta t} + \sum_N a_N \mathbf{V}_N^{t+\Delta t} = \mathbf{S}_{up} - (\boldsymbol{\nabla} P_{rgh} + \mathbf{g} \cdot \mathbf{x} \boldsymbol{\nabla} \rho) \tag{3.52}$$

where $\mathbf{V}_N$ is the velocity at the neighboring cells and a_P, a_N are the diagonal and off-diagonal velocity coefficients, which account for the central and neighboring cells' contributions. $\mathbf{S}_{up}$ accounts for uniform source terms, including the source part of the transient term from the Euler Implicit time integration. The equation can be re-arranged to give, having dropped the subscript $t + \Delta t$ for simplicity:

$$\mathbf{V}_P = \frac{1}{a_P}(-\sum_N a_N \mathbf{V}_N + \mathbf{S}_{up}) - \frac{1}{a_P}(\boldsymbol{\nabla} P_{rgh} + \mathbf{g} \cdot \mathbf{x} \boldsymbol{\nabla} \rho) \tag{3.53}$$

The first term on the right hand side (r.h.s) of Eq. 3.53 defines the operator $\mathbf{H}[\mathbf{V}]_p$ which contains all matrix coefficients from cell neighbors multiplied by the corresponding velocities plus all source terms other than the pressure gradient. Eq. 3.53 is solved by treating the pressure and density gradients and the source term explicitly using the Gauss Theorem to evaluate the gradients at cell centers from the pressure and density interpolated at the face centers, while all other terms are handled implicitly. This step is the momentum prediction step of the PISO loop.

The velocity approximation from this momentum prediction step does not satisfy continuity and a pressure correction is derived by coupling the momentum (Eq. 3.37) and continuity equations. The discretized continuity equation provides a constraint

on cell fluxes $\sum_f \mathbf{S}_f \cdot \rho \mathbf{V}_f = 0$ and $\mathbf{V}_f$ can be interpolated from Eq. 3.53:

$$\mathbf{V}_f = (\frac{1}{a_P})_f \mathbf{H}[\mathbf{V}]_f - (\frac{1}{a_P})_f (\boldsymbol{\nabla} P_{rgh} + \mathbf{g} \cdot \mathbf{x} \boldsymbol{\nabla} \rho)_f \tag{3.54}$$

Face values $(-)_f$, for all terms in Eq. 3.54 are evaluated by linear interpolation. The coupling provides an equation for pressure:

$$\sum_f \mathbf{S}_f \cdot [(\frac{1}{a_p})_f (\boldsymbol{\nabla} P_d)_f] = \sum_f (\frac{1}{a_p})_f \mathbf{S}_f \cdot [\mathbf{H}[\mathbf{V}]_f - (\mathbf{g} \cdot \mathbf{x} \boldsymbol{\nabla} \rho)_f] \tag{3.55}$$

Its solution requires that the operator $\mathbf{H}[\mathbf{V}]$ is estimated from the velocity approximation of the momentum prediction step. That is the operator is handled explicitly. The pressure solution from Eq. 3.55 is used to correct the velocity (Eq. 3.54) and face fluxes $F_f = \mathbf{S}_f \cdot \mathbf{V}_f$ which are therefore calculated as part of the *PISO* solution procedure. This step is known as the velocity correction. Since $[\mathbf{H}[\mathbf{V}]_f - (\mathbf{g} \cdot \mathbf{x} \boldsymbol{\nabla} \rho)_f]$ is treated explicitly in the derivation of Eq. 3.55, the correction relies entirely on an iterative correction of fluxes from P_{rgh}, that is the method relies on a single momentum correction step followed by a series of iterative pressure corrections.

Linear solvers and residuals

In the present study, the system is solved for velocity (Eq. 3.53) using the Preconditioned bi-conjugate gradient (*PBiCG*) algorithm with a Diagonal incomplete LU (*DILU*) pre-conditioner, while the pressure correction equation (Eq.3.55) is solved using a Conjugate Gradient iterative solver preconditioned with a Diagonal incomplete-Cholesky (*DIC*) method. The residuals are measured so that the pressure residual is calculated as a scaled value while the continuity residual is calculated using a weighted average of the rate of volume creation over the whole domain $((\sum_{cells} |\nabla \cdot (\mathbf{S}_f \cdot \mathbf{V}_f)| V_P)/(\sum_{cells} V_P))$. The pressure solution is converged to a normalized absolute residual of 10^{-7}, leading to continuity residual which is always lower than 10^{-6}. Convergence to lower orders for the pressure (down to 10^{-12}) did not pose problems and provided results which are very close to those presented in this work. It is important to mention here that the small values of the continuity residual are due to using the volume averaged in the calculation. The other solvers (TransAT and Fluent) use the mass flow rate for calculating the continuity residual which is typically larger than the volume averaged residual.

Time step constraints

Two different types of time step size are used for solving the algebraic equations; fixed time step (For bubble growth and rise problems) and adjusted time step (for bubble bouncing). The adjusted value is calculated based on the non-dimensional Courant number on the cell faces ($Co = [(\mathbf{V}_f \cdot \mathbf{S}_f)/(\mathbf{d} \cdot \mathbf{S}_f)]\Delta t$). Both types of the time step size mentioned above are always determined such that they satisfy the condition ($Co < 0.25$). More details about how to calculate the adjusted time step in OpenFOAM is presented in Appendix D.

Finally, it is important to mention here the schemes and solvers used in TransAT software. The *Quick* scheme (Leonard, 1979) is used for the advection term in the LS method, while the re-initialization process is solved using the *WENO* scheme (Liu, Osher and Chan, 1994) with 25 artificial iterations. The Semi Implicit method for Pressure-Linked Equations (*SIMPLE*) (Patankar and Spalding, 1972) is used to couple the velocity and pressure in the continuity and momentum equations. In ANSYS-Fluent, the *PISO* solver is also used for coupling the pressure-velocity. The *PISO* solver differs from *SIMPLE* in the number of times the pressure is corrected in the solver as *PISO* solves extra pressure correction steps to enhance the performance per iteration (See Chapter 6 in Versteeg (1995)).

3.4.6 Boundary conditions

The numerical domain is composed of internal cells and boundary cells. The boundary in OpenFOAM consists of a set of patches with a specific boundary condition for each patch. The last term is referred to a set of cell faces which share the same boundary condition. In this section, a general description of the boundary conditions is presented. More in-depth details will be given in the results chapters. Setting the boundary conditions determines the value of flow variables in boundary cells on the boundary faces. In general, two different boundaries are recognized:

- Dirichlet boundary (fixed value) which provides the value of the dependent variable at the face of the boundary cell, while the gradient at the cell face is calculated using both the boundary face value and the cell center value.
- von Neumann boundary (fixed gradient) which provides the value of the dependent variable gradient at the face of the boundary cell, while the face value is derived by interpolating the cell face gradient and the cell center value.

In general, the boundary condition values are assigned only for three variable fields in the present work; velocity, pressure, and the indicator function (VOF, LS). The

following boundary conditions are utilized in the present study for each variable:

- Inlet: The velocity field is defined here using two different types of fluid flow (constant and parabolic). The second type can be applied in OpenFOAM using the *funkySetBoundaryField* utility. The pressure field is defined in the inlet as zero gradient, and the volume fraction field is defined as fixed value boundary.
- Outlet: A fixed value equal to the atmospheric pressure is set for the pressure boundaries, while a zero gradient boundary is set for the velocity field. The indicator function in this case switches between fixed value and zero gradient depending on the flow direction (This is called *inletOutlet* in OpenFOAM)
- No slip wall: The velocity of the wall is set to zero (fixed value). The volume fraction function is set to either zero gradient or fixed gradient. The second case is applied when a contact angle model is required. The volume fraction boundary condition is corrected in this case using the limiter described in section 3.3. The pressure is set to fixed gradient calculated based on the buoyant flow, or calculated based on the mass flux at the boundary cell faces (for contact angle models).
- Symmetry: In this case, the component of the normal gradient of any variable field is set to zero. It is important to mention here that symmetry boundary used here corresponds to a 3D axi-symmetrical domain and not a 2D symmetrical plane.

3.4.7 Solution procedure

The solution sequence is summarized in this section. The solution procedure of the algebraic VOF method is described first and then the solution strategy for the coupled S-CLSVOF is presented. The algebraic VOF-Comp can be described in the following steps:

1. Create and initialize the variable fields (VOF function, pressure, velocity, density)
2. Adjust the time step parameters (Eq. D.3), if required.
3. Adjust the volume fraction boundary condition based on the contact angle (Eq. 3.27), if required.

4. Solve the volume fraction advection equation (Eq. 3.17).
5. Calculate the fluxes through the cell faces (Eq. 3.45).
6. Calculate the interface normal and curvature (Eqs. 3.21 and 3.20), then correct the interface at the contact angle boundaries (Eq. 3.27).
7. Update the mixture physical properties (density and viscosity Eqs. 3.15 and 3.16).
8. Perform the velocity-pressure correction loop (PISO loop)
   a. Construct the matrices in the velocity equation (Eq. 3.52).
   b. Predict the flux for solving the pressure equation (right hand side of Eq. 3.55)
   c. Solve the pressure correction equation (Eq. 3.55).
   d. Correct the fluxes and reconstruct the velocities (Eq. 3.54).
9. Move to the next time step starting from step 2

The S-CLSVOF solver can be described in eight main steps:

1. Define the required vector and scalar fields for the two-fluid flow problem including $\mathbf{V}$, P_{rgh}, ρ, μ, H, δ, α, and ϕ.
2. Initialize the numerical fields, reinitialize the Level Set function and calculate the initial values of the Heaviside and Dirac functions.
3. Start the time loop by correcting the interface and the volume fraction at the boundaries (Eq. 3.27), if required.
4. Solve the volume fraction advection equation (Eq.3.17), and correct the new values of α at the boundaries. The correction takes place only at the boundaries where a static contact angle is imposed so that the interface normal calculated from the gradient of the level set function and used by Eq.3.12 is corrected to satisfy the imposed static angle (Eq.3.27). Then, calculate the new LS function (Eq.3.23) using the results of the VOF advection equation.
5. Re-initialize the LS function using Eq.3.24 in order to obtain the signed distance function and correct the interface at the boundaries. Then, calculate the new values of interface normal and curvature (Eqs. 3.10 and 3.11).
6. Calculated the Heaviside function and the Dirac functions (Eq. 3.9 and 3.13).

7. Update the fluid physical properties and the fluxes using the volume fraction function α (Eqs.3.15 and 3.16).
8. Solve the Navier Stokes system of equations for velocity and pressure using the Pressure Implicit with Splitting of Operators (PISO) (Issa, 1986). Details of the solution loop is presented in the step 8 of the solution procedure of VOF-Comp solver.
9. Move to the next time step (starting from 3).

The accuracy of the numerical solution is validated and assessed against experimental benchmark data. The comparison is performed using instantaneous changes in the bubble geometrical characteristics. The characteristics selected include the bubble center of gravity, velocity, bubble maximum width, bubble maximum height, and aspect ratio. Other parameters will also be utilized as will be shown in the results chapters. The bubble center of gravity is calculated at the end of each time iteration following the general form:

$$\mathbf{Cg} = \frac{\sum_{cells}(1-\alpha_P)\mathbf{x}_P v_P}{\sum_{cells}(1-\alpha_P)v_P} \tag{3.56}$$

where $\mathbf{x}_P, \alpha_P, v_P$ are the position vector, volume fraction function, and the volume of the cell P.

The bubble velocity is calculated by differentiating the bubble center of gravity with respect to the time. The set of points that define the iso-line contours ($\alpha = 0.5$ and $\phi = 0$) are extrapolated in the numerical simulations using the *sampleField* utility in OpenFOAM. These points are imported into a simple code, written in Matlab (MATLAB, 2012), for calculating the other geometrical characteristics. Other visualization parameters including the pressure contour around the bubble and the vector plot of the mixture velocity field are obtained using the visualization software ParaView (ParaView, 2012).

3.5 Summary

This chapter described the interface capturing methodology employed in the present work. This includes the level set method, both geometric and algebraic VOF methods, and the geometrical CLSVOF method. The extension of the algebraic VOF into a simplified coupled method (S-CLSVOF) method has also been introduced. The

implementation of both static and dynamic contact angle models in OpenFOAM were then explained. Next, the discretization procedure followed in OpenFOAM was explained in detail with highlighting briefly the main schemes and solvers utilized in both Fluent and TransAT. Both time and space discretization schemes were described and the numerical schemes employed for the VOF advection equation were presented. Finally, the pressure-velocity coupling strategy based on the principal of the PISO solver and the solution procedure of the algebraic VOF and S-CLSVOF methods were described.

In the next chapters, the numerical analysis of the two-fluid flow methods for capturing the bubble behavior in different physical applications (Bubble growth, rise, and bounce) is presented.

4 Results and discussion: Comparison of interface capturing methods

In this chapter, the growth and detachment of a single bubble from an orifice is studied for low inflow flow rates kept under quasi-static surface tension dominant conditions[1]. Four different interface capturing methods are considered and results are compared against experimental measurements performed, as part of the project, by a collaborating institute (Fluid and Heat Transfer laboratory, Trinity College Dublin). With the VOF methods, the interface is captured using two different techniques; the Piecewise Linear Interface Construction (PLIC) scheme implemented in ANSYS-Fluent®-v13 (VOF-Geo) and the algebraic compressive scheme of OpenFOAM® (VOF-Comp). The LS method used is from the TransAT© commercial software. The CLSVOF method recently implemented in ANSYS Fluent®-v13 is also tested in this study (CLSVOF-Geo). The solvers considered here were selected on the basis of their broad availability to the general research community which meant that some of the latest developments mentioned in the literature review could not be included. Although an exhaustive analysis of all methods could not be conducted, a representative sample of some of the most commonly used commercial and Open Source codes was selected.

The main purpose of this comparative study is to identify the main issues affecting the above methods as implemented in the version accessed at the time of the research for modeling bubble growth and detachment at low Bond and Capillary numbers. This research involved six main tasks:

- Investigate, qualitatively and quantitatively, the accuracy of the interface capturing methods for predicting the bubble behavior during the growth.

[1] Quasi-static means here that the formed bubble preserves its shape and position at any time the flow rate is halted.

- Study the influence of the compression factor c_α in the VOF-Comp method for bubble growth simulations.
- Study the accuracy of the numerical methods using different inflow flow rates.
- Study the accuracy of the numerical methods in capturing accurately the detachment process.
- Examine the flow behavior inside the bubble.
- Explain the difference between the interface capturing techniques considered.

Although this chapter focuses mainly on a comparative study of bubble growth, the mechanisms of the formation process are also explained. The numerical set-up of the rig and the mesh resolution are presented first. Then, the process of bubble growth and detachment is studied with reference to the bubble center of gravity in the vertical direction, the bubble aspect ratio, and the instantaneous contact angle. Next, the influence of the compression factor and the inflow flow rate is studied. The detachment process is analyzed in Section 4.4. Finally, the velocity field inside the bubble is displayed using the four numerical methods and then used to explain the process of the neck pinching at detachment and the difference between the employed techniques. Most of the results and discussion points mentioned in this chapter are presented in the manuscript published in the Journal of Chemical Engineering Science (Albadawi, Donoghue, Robinson, Murray and Delauré, 2012) and the Journal of Physics (Albadawi, Delauré, Donoghue, Robinson and Murray, 2012).

4.1 Problem setup

The formation of air bubbles at an orifice in a quiescent liquid is considered. The gas phase is injected through the orifice using a small and constant volumetric flow rate $\dot{Q}$, so that the bubble growth can be studied using an axi-symmetrical domain as sketched in Fig. 4.1 where R_o and D_{eq} are the orifice radius and bubble equivalent diameter[2], respectively. This flow satisfies the condition proposed by Oguz and Prosperetti (1993) for the quasi-static regimes ($\dot{Q} < \dot{Q}_{crit} \approx \pi(16/3g^2)^{1/6}(\sigma_L R_o/\rho_L)^{5/6} = 1.82 \times 10^{-6}$ m^3/s). Under this condition, the bubble is subjected only to the static forces during its growth. Duhar and Colin (2006) classified these forces according to

[2]The equivalent diameter is the diameter of a spherical object that has same volume to the bubble.

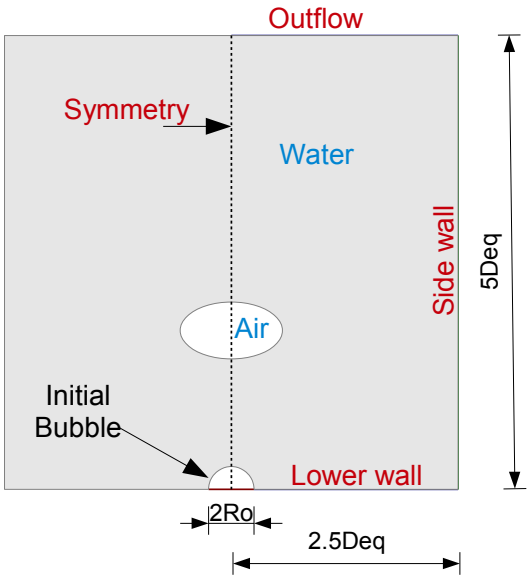

Figure 4.1: Schematic diagram of the rig and boundary conditions.

their influence on the bubble as detaching forces (Buoyancy and Contact pressure) and attaching forces (Drag and Capillary). The liquid and gas physical properties are defined in Table 4.1. The gas/liquid surface tension coefficient is assumed to be constant, and the bubble grows under normal gravitational acceleration.

The bubble growth is studied with orifice radius $R_o = 0.8$ mm and different volumetric flow rates as defined in Table 4.1. The Reynolds number $Re = \rho_L v_0 R_o/\mu_L$, where $v_0 = \dot{Q}/\pi R_o^2$ is the weighted inflow velocity, is in the range $5.51 \leq Re \leq 22.04$, while the Capillary number ($Ca = \mu_L v_0/\sigma$) falls in the range $9.45 \times 10^{-5} \leq Ca \leq 3.8 \times 10^{-4}$. The last values indicate that the influences of both the inertial and the capillary forces are larger than the viscous drag forces. On the other hand, the relation between the capillary and the buoyancy forces is determined using the Bond number ($Bo = \rho_L g R_o^2/\sigma$) which has an averaged value 0.086, indicating that the surface tension effect is dominant over buoyancy effect for the present work. The current value of Bo is relatively small in comparison with ($0.03 < Bo < 0.95$) by Chakraborty et al. (2009) and ($0.03 < Bo < 0.33$) by Gerlach et al. (2007).

The numerical dimensions used were chosen as (10×20 mm^2 $\sim 5R_{eq} \times 10R_{eq}$) to avoid any influence from the wall boundaries, where R_{eq} is the bubble equivalent radius at detachment. Larger wall dimensions than those proposed above would lead to bubble formation process with similar geometrical characteristics. The mesh step

Table 4.1: Fluids physical properties.

Parameters	Symbols	Values	Units
Liquid density	ρ_l	998.2	kg/m^3
Liquid viscosity	μ_l	0.001	kg/m$\cdot$ s
Gas density	ρ_g	1.225	kg/m^3
Gas viscosity	μ_g	$1.79 \cdot 10^{-5}$	kg/m$\cdot$ s
Surface tension	σ	0.073	N/m
Gravity	g	9.81	m/s^2
Orifice Radius	R_o	0.8	mm
Flow Rate	$\dot{Q}$	50,100,150,200	mlph

size taken for all the simulations is $\Delta x = 1 \times 10^{-4}$ m, so that the orifice diameter is modeled using 16 cells. This step size is relatively comparable to other bubble growth research (Chakraborty et al., 2009; Buwa et al., 2007; Gerlach et al., 2007) where the mesh size was chosen as $\Delta x = 2.5 \times 10^{-4}$ m. Two different time steps $\Delta t = 1 \times 10^{-5}$ s and $\Delta t = 1 \times 10^{-6}$ s were tested for the bubble growth process using the LS method and the flow rates $(100, 150, 200$ mlph) where the difference in the bubble detachment volume and time between the two time steps was found to be less than 0.2 mm^3 and 6 ms, respectively. In the present work, the time step was chosen as $\Delta t = 1 \times 10^{-5}$ s to satisfy the CFL constraints ($\Delta t \leq \Delta x/2max(|\mathbf{V}|)$ and $\Delta t < [(\rho_l + \rho_g)\Delta x^3/(4\pi\sigma)]^{1/2}$) (Gerlach et al., 2006).

The boundary conditions for axi-symmetrical bubble growth are shown in Fig. 4.1. At the inlet, the flow is assumed fully developed laminar and a parabolic inflow velocity is imposed with the axial velocity $v = v_{max}[1 - x^2/R_o^2]$, where $x = 0$ at the axis of symmetry, and v_{max} is the maximum velocity calculated from the volumetric flow rate applied by the injection device ($v_{max} = 2\dot{Q}/\pi R_o^2$). At the outlet, the outflow pressure is set to the atmospheric pressure, while at the wall, the no slip boundary condition is used. At the lower wall, a static contact angle is imposed as $\theta_s = 20°$. The equilibrium contact angle for air, water and stainless steel can vary depending on the water purity and the surface cleanliness. From a numerical modeling point of view however, it has been shown by Gerlach et al. (2007) that as long as the imposed static contact angle is kept below a critical value the bubble interface remains pinned to the orifice rim. Numerical results have also confirmed that reduction in the contact angle below this critical value does not influence the bubble detachment volume. The value of 20° was selected to ensure that the bubble would remain at the orifice rim as observed experimentally.

4.2 Validation of numerical methods

In this section, the mechanism of bubble growth process is explained highlighting the large topological changes in the interface curvature during the growth. The bubble interface predicted using the four numerical methods is compared against experimental data. The bubble detachment characteristics are then validated. Finally, the variation in the bubble geometrical properties are studied.

4.2.1 Mechanism of bubble growth

The numerical methods are assessed qualitatively in this section by comparing predictions against the interfaces reconstructed from the experimental visualization illustrated in Fig. 4.2. The six frames shown here correspond to $t/t_{det} \sim 0, 0.2, 0.4, 0.6, 0.8, 1$ where t_{det} is the detachment time predicted by the relevant method or measured experimentally and $t/t_{det} = 0$ is the initial time of the simulation where the bubble is assumed to have an axi-symmetrical and hemispherical shape. At the early stages of growth, the bubble has a truncated spherical shape ($t/t_{det} \sim 0.2$) determined by the dominant capillary force. As time increases, the gas volume inside the bubble grows, and the bubble elongates in the vertical direction as the buoyancy force undergoes a significant increase ($\propto R^3\Delta\rho$). At the last stages of growth ($t/t_{det} > 0.9$), surface tension cannot support the balance between the outer and the inner pressures leading to the neck formation before detachment.

The interfaces shown in Fig. 4.3 correspond to the iso-line contours $\phi = 0$ for the LS method and $\alpha = 0.5$ with the VOF and CLSVOF methods. The orifice diameter and the volumetric flow rate considered are 1.6 mm and 150 mlph, respectively. The comparison against the experimental interface shows that all methods produce a bubble shape with similar characteristics during the full process of bubble growth. A more in depth analysis shows that the CLSVOF-Geo model produces unstable bubble oscillations. Although VOF-Comp passes through the same topological changes during the growth as the experiments, it gives very early detachment (Fig. 4.3b). The bubble shapes which are in closest agreement with the experimental measurements are obtained with the LS method (Fig. 4.3a) and, to a lesser extent, the VOF-Geo method (Fig. 4.3d). Both methods however present some differences that are more obvious when examining the bubble height at detachment stage ($t/t_{det} \sim 1$). In the case of the CLSVOF and the VOF-comp methods, the difference in the bubble height is shown to grow with time. This is partly due to

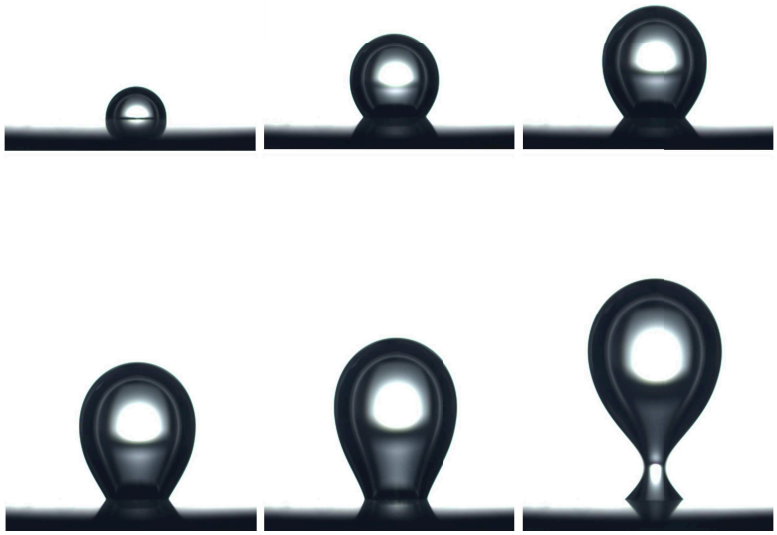

Figure 4.2: Experimental bubble shape at six different frames $t/t_{det} \sim 0, 0.2, 0.4, 0.6, 0.8, 1$ ordered from top left to bottom right with $R_o = 0.8$ mm, $\dot{Q} = 150$ mlph. The snapshots are obtained from the collaborative experimental team.

significant differences in detachment times between the two methods and experimental results. Since the rate of bubble volume growth, which is imposed by the injection flow rate as a boundary condition, is the same in all cases, a difference in t_{det} translates in a proportional difference in the bubble volume at the same relative time t/t_{det}. An order of magnitude analysis shows that this can account for up to 60% of the bubble height difference at detachment in the case of the VOF-comp methods. Another reason for the height difference can be linked to a growth in the aspect ratio as will be confirmed by Fig. 4.7 and discussed in Section 4.2.3. This suggests that the bubble is not allowed to stretch to its full height. Although it is difficult to pinpoint the exact reason for this, one can speculate that differences in the implementation of the surface tension model and its boundary condition are the most likely reasons for the observed discrepancies.

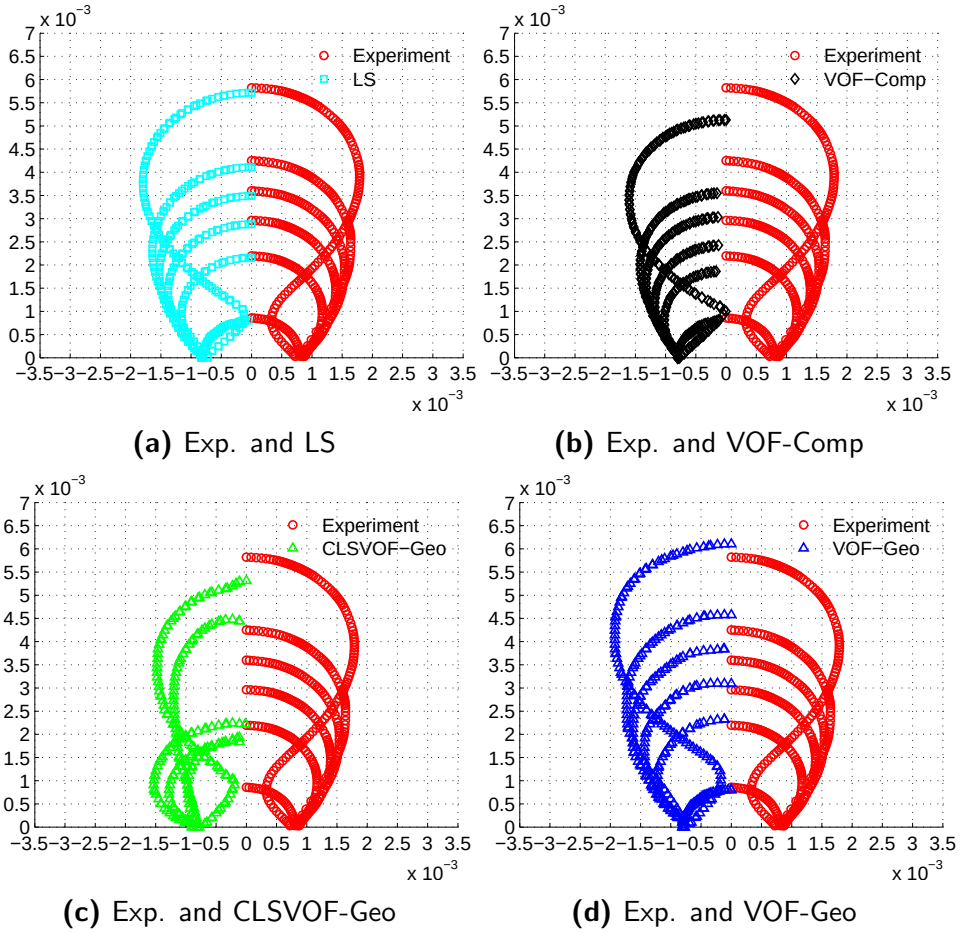

(a) Exp. and LS **(b)** Exp. and VOF-Comp

(c) Exp. and CLSVOF-Geo **(d)** Exp. and VOF-Geo

Figure 4.3: Bubble shape predictions at six time frames $t/t_{det} \sim 0, 0.2, 0.4, 0.6, 0.8, 1$ with $R_o = 0.8$ mm and $\dot{Q} = 150$ mlph.

The evolution of the bubble interface curvature during the growth illustrates the

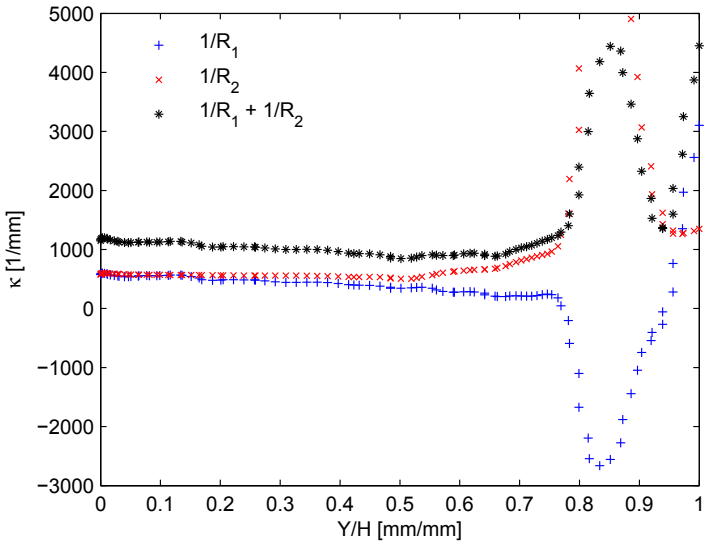

(a)

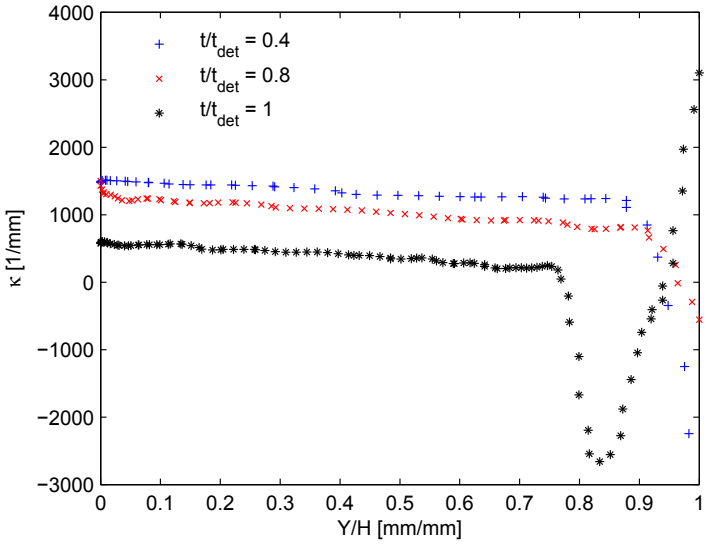

(b)

Figure 4.4: (a) Principal components of the bubble interface curvature at detachment ($t/t_{det} = 1$), (b) bubble interface curvature ($1/R_1$) at three different frames ($t/t_{det} = 0.4, 0.8, 1$), $R_o = 0.8$ mm, $\dot{Q} = 150$ mlph with the LS method.

topological changes experienced by the bubble during its growth (Di Bari and Robinson, 2013). It also highlight the smoothness of the curvature through the bubble interface. Plots of the inverse of the principal radii of curvature R_1 (local radius in the vertical direction) and R_2 (local radius in the azimuthal direction) at the detachment ($t/t_{det} \sim 1$) are given in Fig. 4.4a for the LS method. The horizontal axis represents the non-dimensional bubble height ($Y/H = 0$ at the bubble apex, and $Y/H = 1$ at the bubble base). The interface shape before detachment is shown to be divided into three distinct regions; the upper part ($Y/H \in [0 - 0.65]$) which has a spherical shape with two radii of curvature which are approximately constant and of equal value. The second part ($Y/H \in [0.65 - 0.75]$) represents the transition into the neck region characterized by a change in the sign of the radius R_1 and the corresponding switch from a convex to concave shape. The last part ($Y/H \in [0.75 - 1]$) represents the neck identified by a peak in the interface curvature. Fig. 4.4b shows the total curvature at three different frames ($t/t_{det} = 0.4, 0.8, 1$) and confirms that the curvature peak appears only at detachment. In the apex region, the decrease in the interface curvature between the different time frames is caused by the increase in the bubble volume during the growth.

A comparison with the VOF-Geo and LS predictions at $t/t_{det} = 0.8$ is illustrated in Fig. 4.5. The former method considers the VOF function for calculating the curvature ($\kappa = \kappa(\alpha)$) while the latter considers the LS function ($\kappa = \kappa(\phi)$). The figure confirms that both methods correctly capture the general trends in curvature. The still pictures shown in Fig. 4.2 show bubble shapes characterized by very smooth interface suggesting that the bubble curvature should vary smoothly from the neck to the apex. Experimental results do however show some oscillation that can be attributed to the sensitivity of the curvature calculation to the image pixellation and to other possible experimental perturbations in the rig. A smooth interface is indeed predicted by the LS method which gives a smooth and gradual decrease towards the bubble base with a curvature which agrees closely with the experimental data. The VOF-Geo however predicts an early flattening at this point. Fig. 4.5 displays a comparison of the bubble interface curvature between the experimental data and the two numerical methods (VOF-Geo and LS). It is evident that the interface curvature using the LS method is smoother than the VOF-Geo method. This can be explained by the difference in curvature calculation in each numerical method. The spurious currents generated with the VOF-Geo method might lead to oscillations in the interface curvature. Furthermore, the experimental and the numerical observations at the neck show a rapid decrease in the interface curvature.

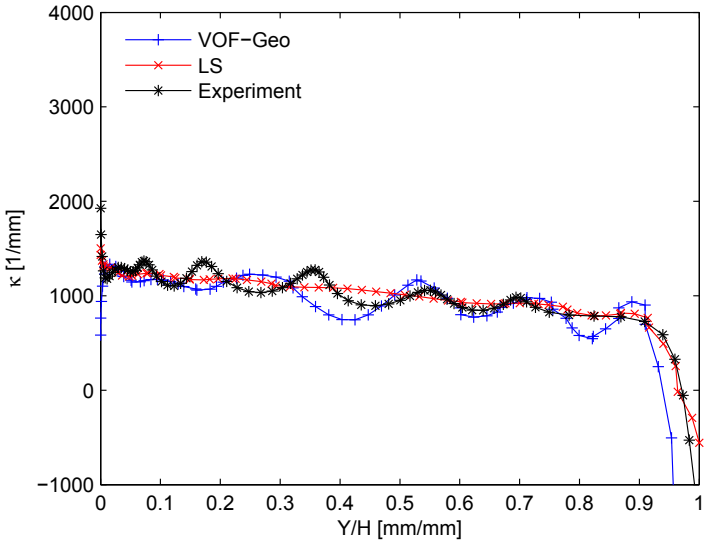

Figure 4.5: Comparison of bubble interface curvature between the experimental data and the numerical results (VOF-Geo and LS) at time frame $t/t_{det} = 0.8$, $R_o = 0.8$ mm, $\dot{Q} = 150$ mlph.

Curvature calculations based on theoretical models which assume a balance between the hydrostatic pressure and the capillary pressure all fail to predict this rapid change at the neck (Lesage, 2012). This difference suggests the existence of other forces acting on the bubble during the detachment as will explained in section 4.4.

4.2.2 Bubble detachment parameters

The bubble detachment parameters used to assess the numerical methods include the bubble detachment volume V_{det}, the detachment time t_{det}, and the position of the bubble detachment center of gravity in the gravitational direction CGy_{det}. The errors are defined as percentages so that the error in bubble volume, for instance, is calculated as $E_{vol} = 100 \times [(V_{num} - V_{exp})/V_{exp}]$. The bubble detachment volume corresponds to the air volume inside the bubble at the stage $t/t_{det} = 1$ while the rising detached bubble has a smaller volume since the bubble splits at the neck into two parts; the rising bubble and the embryo of the second formed bubble. Table 4.2 shows the detachment values for an orifice radius 0.8 mm and four different volumetric flow rates $50, 100, 150, 200$ mlph. With VOF-Geo, the bubble detachment volume and center of gravity are shown to vary either side of the experimental data with a bubble detaching at an earlier time with smaller volumes when using the

small flow rates 50 and 100 mlph. The other geometrical method, CLSVOF-Geo, always gives early detachment which leads to smaller volumes and centers of gravity. VOF-Comp also exhibits an early detachment, but the values of V and CGy at detachment are more stable than CLSVOF-Geo showing a lower sensitivity to the injection flow rate. The LS method gives results which are clearly the closest to the experimental data with errors in the detachment volume and time always within 2% and 1%, respectively. However, the bubble breaks up with smaller centers of gravity compared to the experimental observations.

Table 4.2: Bubble detachment characteristics for four different volumetric flow rates $50, 100, 150, 200$ mlph, $R_o = 0.8$ mm.

Flow rate	Method	t_{det} (s)	CGy_{det} (mm)	V_{det} (mm^3)	Et_{det} (%)	Ecg_{det}(%)	$Evol_{det}$(%)
50 mlph	Experiment	1.985	3.568	28.397	-	-	-
	VOF-Geo	1.597	3.101	23.249	-19.546	-13.068	-18.125
	CLSVOF-Geo	1.186	3.099	17.554	-40.226	-13.144	-38.180
	LS	1.971	3.559	28.255	-0.680	-0.246	-0.496
	VOF-Comp	1.144	3.204	20.363	-42.367	-10.198	-28.288
100 mlph	Experiment	1.013	3.631	29.134	-	-	-
	VOF-Geo	1	3.385	28.862	-1.283	-6.767	-0.932
	CLSVOF-Geo	0.563	2.916	16.729	-44.373	-19.672	-42.579
	LS	1.004	3.515	28.788	-0.888	-3.190	-1.187
	VOF-Comp	0.607	3.184	20.307	-40.079	-12.306	-30.295
150 mlph	Experiment	0.684	3.625	29.699	-	-	-
	VOF-Geo	0.834	3.917	35.804	21.929	8.054	20.553
	CLSVOF-Geo	0.425	3.205	18.782	-37.865	-11.592	-36.760
	LS	0.680	3.575	29.234	-0.511	-1.368	-1.568
	VOF-Comp	0.429	3.209	21.022	-37.207	-11.465	-29.216
200 mlph	Experiment	0.523	3.611	30.074	-	-	-
	VOF-Geo	0.639	3.915	36.577	22.275	8.426	21.621
	CLSVOF-Geo	0.370	2.979	21.692	-29.158	-17.499	-27.873
	LS	0.518	3.599	29.666	-0.956	-0.321	-1.356
	VOF-Comp	0.336	3.050	21.591	-35.755	-15.519	-28.209

The bubble detachment volumes have also been compared against the experimental correlation proposed by Di Bari and Robinson (2013) which defines the bubble detachment volume as a function of Tate volume ($V_T = 2\pi R_o \sigma/(\rho_l - \rho_g)g$) and the capillary length (and $L_{cap} = \sqrt{\sigma/(\rho_l - \rho_g)g}$): $V_{corr} = 0.6863(2R_o/L_{cap})^{-0.116}V_T$. The experimental detachment volume and the numerical volume predicted with LS compare well with this correlation with an average percentage differences are of 7% and 5.79%, respectively. With the LS method, it has also been found that the percentage differences increases from 3.13% for 50 mlph to 8.28% for 200 mlph.

This agrees with Di Bari and Robinson (2013) who have highlighted the increase in percentage error with the volumetric flow rate.

4.2.3 Bubble geometrical characteristics

Although the detachment parameters give an indication of the method's suitability to accurately predict the bubble shape, it is not sufficient to characterize and analyze their ability to model the full process of bubble growth. This is examined in this section using an orifice radius of 0.8 mm and flow rate 150 mlph. The initial times for both the experimental and numerical data are defined here to correspond to a hemispherical bubble with radius 0.8 mm. Fig. 4.6 plots the bubble center of gravity for both the numerical and experimental data. It is clear that the LS method provides the trajectory which agrees most closely with the experiments. At the start of the bubble formation, the numerical and the experimental curves follow the same trends. At time $t = 0.2$ s, the bubble from VOF-Comp tends to stretch more rapidly in the vertical direction than the other methods leading to an early detachment. The methods that reconstruct the interface geometrically (VOF-Geo and CLSVOF-Geo) exhibit bubble oscillations during the growth with an amplitude of oscillations which is larger with CLSVOF-Geo and increases closer to detachment. VOF-Geo is shown to give good results at the early stages of growth, but the accuracy is lost when the bubble approaches detachment at which the method fails to capture the correct time of neck formation ($t \sim 0.6$ s for the experiment). The differences in the detachment center of gravity presented in Table 4.2 are also clear from this figure.

The aspect ratio, defined as the maximum bubble height to the maximum width, is given in Fig. 4.7. It confirms the significance of shape oscillations modeled by the CLSVOF-Geo method and, to lesser extent, the VOF-Geo method. A visualization of the unsteady processes confirms the rapid growth of a stretch-shrink motion characterized by a periodic expansion and contraction of the bubble in the direction of the axis of symmetry. The significance of this oscillatory bubble stretching can be seen in Fig. 4.16a. These oscillations, however, are not observed in the experimental data. Both the VOF-Comp and LS methods reproduce the smooth and gradual increase in the aspect ratio, but an accurate profile is only achieved by the LS method.

Similar observations to the aspect ratio can be made from the contact angle at the orifice (Fig. 4.8). This is defined as the angle between the tangential wall axis

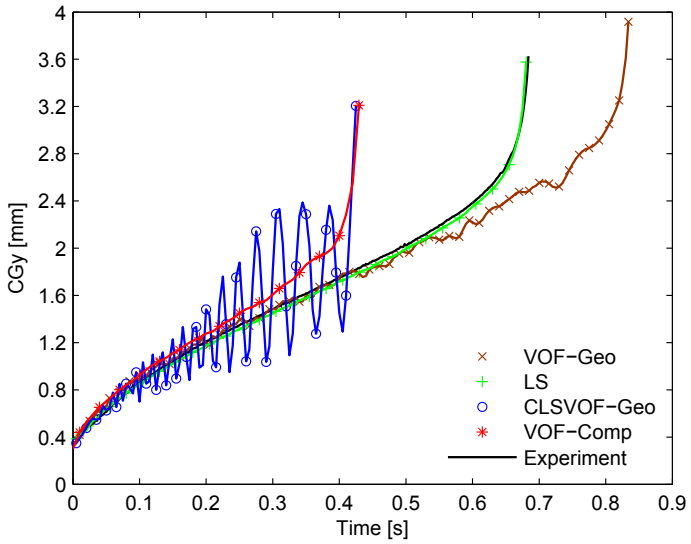

Figure 4.6: Bubble center of gravity versus time with $R_o = 0.8$ mm, $\dot{Q} = 150$ mlph.

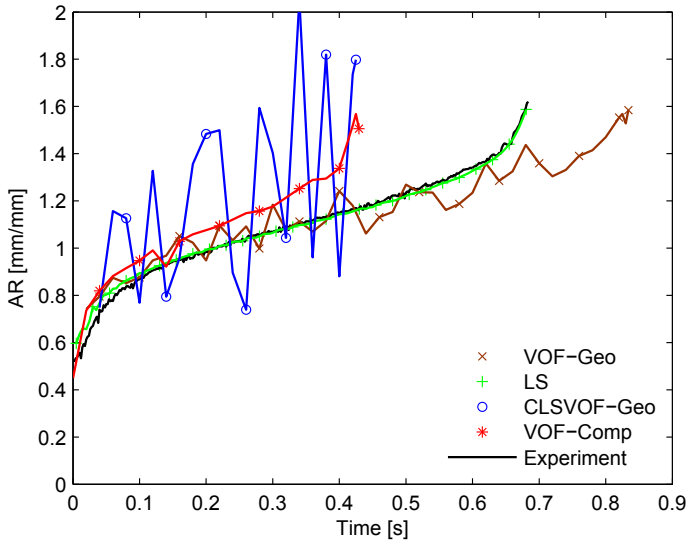

Figure 4.7: Bubble aspect ratio versus time with $R_o = 0.8$ mm, $\dot{Q} = 150$ mlph.

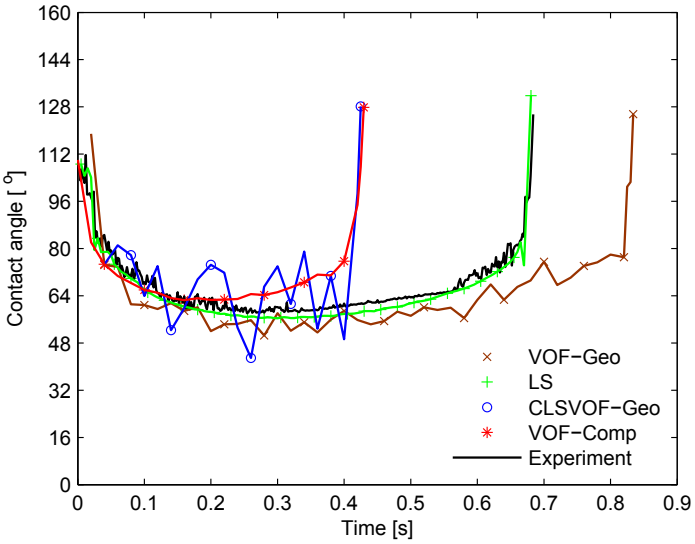

Figure 4.8: Bubble instantaneous contact angle versus time with $R_o = 0.8$ mm, $\dot{Q} = 150$ mlph.

and the gas/liquid contact line and is measured in the denser phase (water). At the onset of bubble growth, it decreases rapidly with time as the bubble evolves from a hemispherical to a truncated spherical shape. As the bubble elongates in the vertical direction, the contact angle increases slowly with time, but before detachment and as the neck forms, the angle increases rapidly until the bubble breaks off. This behavior has been reported by Di Bari and Robinson (2013) and Duhar and Colin (2006) in their experimental study of the bubble growth. Fig. 4.8 shows, once again, the same bubble oscillations predicted by both VOF-Geo and CLSVOF-Geo which are not observed experimentally. Although there are small oscillations in the experimental results, these can be attributed to the image's resolution and pixel ratios near the orifice wall where the angle is measured.

4.3 Numerical and physical parametric study

In this section, the compression factor in the VOF-Comp method is analyzed in order to examine its influence on the bubble growth dynamics. Then, the influence of the volumetric flow rate on the geometrical characteristics is investigated via the bubble center of gravity. This study is performed using both VOF-Geo and LS methods which have shown to provide the most accurate results.

4.3.1 Influence of compression factor in VOF-Comp

The numerical compression factor c_α is defined in the VOF-Comp advection equation (Eq. 3.17). Its influence is studied with reference to the formation process using several values of c_α. The numerical results presented in the previous sections with VOF-Comp are obtained using a compression factor $c_\alpha = 2$. As shown in these results, the bubble detaches at earlier times compared to the experimental data. This also corresponds to bubble detachment with smaller volumes than expected (See Table 4.2). The premature detachment occurs for all the volumetric flow rates considered. The compression factor (See Eq. 3.18) plays a significant role in determining the diffusivity through the gas/liquid interface. Fig. 4.9 provides color maps of the VOF function at the last stages of bubble growth using four different values of the compression factor ($c_\alpha = 0, 0.5, 1, 2$). For $c_\alpha = 0$, no interface compression is applied, and the VOF advection equation is simplified to the general form expressed in Eq. 3.3. In this case, the advection scheme clearly fails to preserve the interface. For $c_\alpha = 0.5$, the bubble looks more realistic. However, pockets of gas phase are shown to escape from the bubble along the axis of symmetry from the top of the bubble (flotsams separation). For compression factors $c_\alpha \geq 1$, the interface smearing is limited to over only three cells and the formation process shows a qualitatively similar behavior to that observed experimentally. At detachment, the neck forms at the foot of the bubble. This is accompanied by a transition in the interface curvature from concave to convex shape. In this region, the gas/liquid interface compression is found to be better preserved with the compression factor $c_\alpha = 2$ compared to the case with $c_\alpha = 1$. As noticed in the numerical simulations, the interface diffusivity increases during the detachment process. This happens mainly at the neck region where small pieces of gas might shed from the bottom of the detached bubble. Strong interface diffusivity is also noticed at the onset of the formation process when the capillary force is the most dominant.

Fig. 4.10 provides a plot of the bubble center of gravity displacement in the gravitational direction obtained with the VOF-Comp method with compression factors $c_\alpha = 1$ and 2. The figure confirms that the formation process is strongly influenced by the value of the compression factor. Although both values provide interface diffusivity over only few cells and guarantee the boundedness of the VOF function, the VOF-Comp method fails to provide the correct detachment time in both cases, and thus the correct detachment volume, compared to the experiments. To conclude, the numerical results of bubble growth show a strong sensitivity to the value

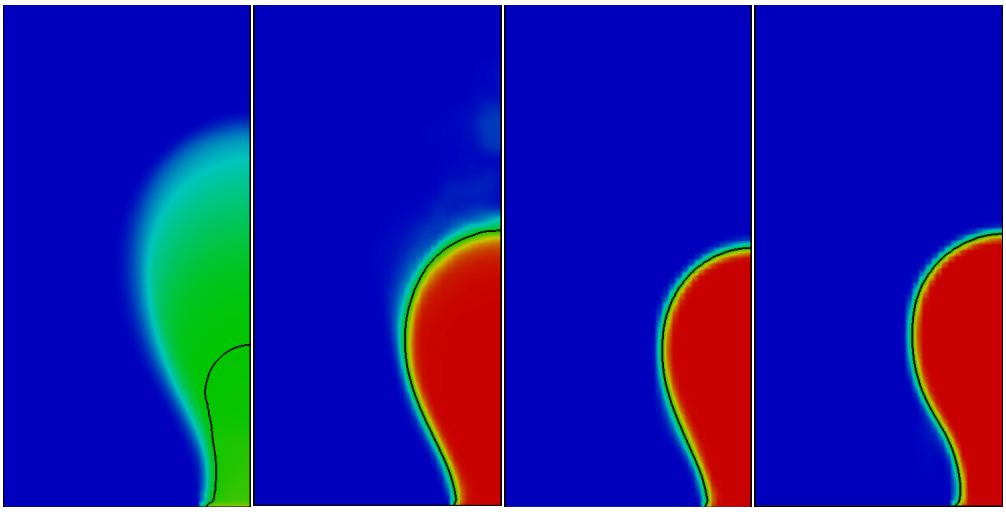

Figure 4.9: Color map of the volume fraction function with the VOF-Comp method using different compression factors arranged from left to right ($c_\alpha = 0, 0.5, 1, 2$). The black line represents the VOF contour $\alpha = 0.5$. The color map ranges from red ($\alpha = 0$) to blue ($\alpha = 1$).

of the compression factor. This value should be chosen carefully for each physical application in order to obtain realistic results compared to the experiments. In this chapter, the compression factor $c_\alpha = 2$ is considered for all the comparison data with the other interface capturing methods. The sub-stepping effect in solving the VOF advection equation is also examined using both one and three sub-stepping stages. The numerical results, however, did not change with the sub-stepping number of loops.

4.3.2 Influence of inflow flow rate

As long as the inflow flow rate satisfies the quasi static condition (Oguz and Prosperetti (1993)), the bubble growth and detachment characteristics should not be notably affected by the inflow rate. Increasing the gas flow velocity at the orifice can however be expected to influence the balance of forces at the triple contact point and can amplify or dampen the effect of the non physical oscillations originating from the surface tension models at wall boundaries. The effect of the four different volumetric flow rates, namely $50, 100, 150, 200$ mlph, on the evolution of the bubble growth for both the LS and VOF-Geo methods is examined in more detail in this section. A single orifice radius ($R_o = 0.8$ mm) is considered. The bubble center of gravity plots are shown in Figs. 4.11a and 4.11b against the non-dimensional time

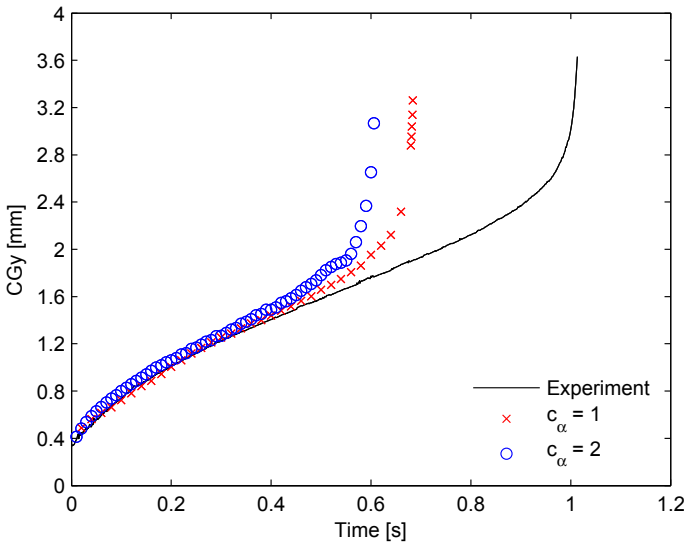

Figure 4.10: Bubble center of gravity versus time for two different compression factors with VOF-Comp method, $R_o = 0.8$ mm, $\dot{Q} = 100$ mlph.

$t_n = tv_0/R_o$ for the VOF-Geo and LS, respectively. Since constant flow rates under quasi-static conditions are used, the evolution of CGy should follow the same trend during the full formation process up to detachment. Fig. 4.11a shows that this is not the case with VOF-Geo with the smaller flow rates giving earlier bubble detachment and smaller center of gravity. The bubble growth with a 100 mlph flow rate in particular is also shown to oscillate as it approaches detachment. In contrast, the LS method (Fig. 4.11b) gives the same stable trend for the bubble center of gravity during the full process of bubble growth but not at detachment. The final stage of growth is found to be delayed slightly as the inflow flow rate increases. This is also observed experimentally. The difference in the bubble trajectory during the detachment process suggests that the formation process at the last stage is influenced by other forces than the surface tension and buoyancy as suggested by Oguz and Prosperetti (1993). More details about the bubble behavior during the detachment process are presented in the next section.

Predictions from the two methods are also compared with experimental measurements in Fig. 4.12 for the bubble center of gravity obtained with an orifice radius of 0.8 mm and a flow rate of 150 mlph. The LS method is clearly shown to achieve accurate predictions for the full unsteady growth while VOF-Geo can be seen to fail to detect the detachment stage at the correct time. The comparison with experimental data highlights the suitability of the LS method for all flow rates considered but also

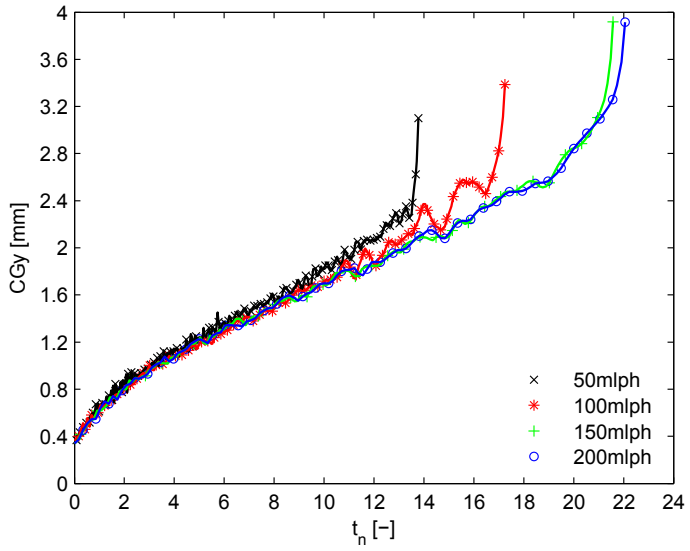

(a)

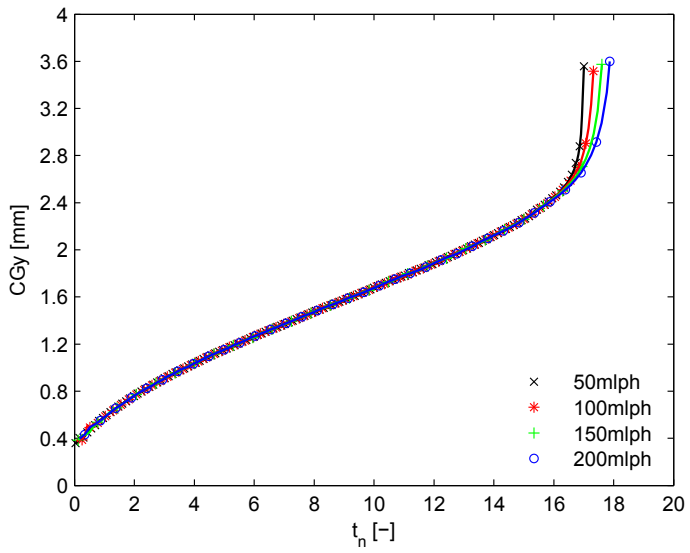

(b)

Figure 4.11: Influence of different orifice flow rates on the bubble center of gravity for both (a) VOF-Geo and (b) LS methods, $R_o = 0.8$ mm.

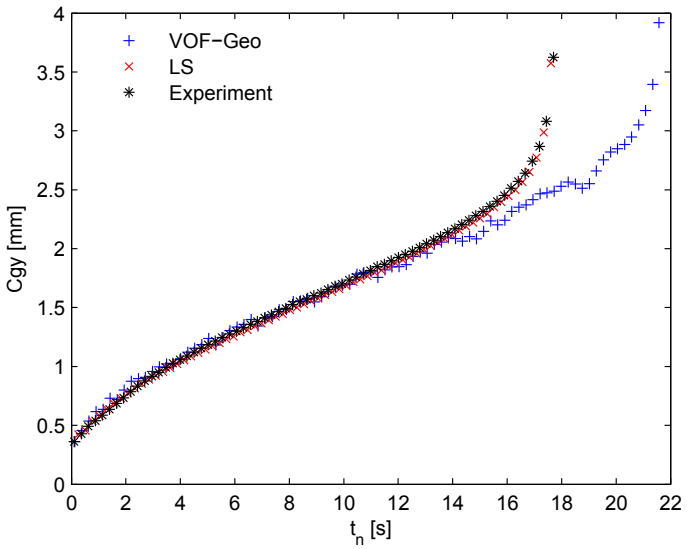

Figure 4.12: Comparison of bubble center of gravity using the non-dimensional time t_n for VOF-Geo, LS, and experiments, $R_o = 0.8$ mm, $\dot{Q} = 150$ mlph.

the sensitivity of the VOF-Geo method to the relative importance of surface tension forces. The latter method shows little error before the onset of neck pinch-off at a non dimensional time $t_n \sim 16$ but fails to predict the neck formation correctly with a clear delay in pinch-off. This delay, however, was found to vary with the inflow flow rate suggesting that it is influenced by the relative importance of the capillary forces to the inertial forces. Numerical tests have also shown that large reductions in the time steps during the detachment can help improve convergence of the simulation results to the correct experimental results but this approach can require unrealistically small time steps (as small as 10^{-7} s depending on the method used). Similar suggestions were made by Chen, Mertz and Kulenovic (2009) who recommended using smaller time steps for the last 100 iterations before and after detachment.

4.4 Detachment process

The onset of detachment is determined when the minimum bubble radius, defined here as the neck radius, falls below the orifice radius while detachment occurs when the neck pinches off. The interface deformation and flow conditions leading to pinch-off are characterized by rapid changes making the numerical models particularly

sensitive to the modeling assumptions and parameters, in particular the time step. When the density ratio is $\rho_l/\rho_g > 6.2$, the mechanism driving the pinch-off has been attributed to both the liquid and gas inertia as the surface tension forces become negligible when the neck radius tends to zero. The significance of gas inertia is linked to the high gas velocity through the neck and the resulting pressure drop due to the Bernoulli effect. The suction affects both the gas and surrounding liquid which is drawn in towards the neck axis. The result is an acceleration of the pinching of the bubble neck. These conclusions were reached by Gordillo et al. (2005) from a Boundary Integral solution of a potential model. Although their model did not consider viscosity, the applicability of results to an air/water system was justified by dimensional considerations and verified by experiments. The results confirmed that a power law $R_{neck} \propto t^{\omega}$ can be used to describe the rate of decrease in the neck radius R_{neck} immediately before detachment. Of particular interest to the present study is the effect of gas velocity through the neck on the value of the power ω. Gordillo et al. (2005) were able to confirm that $\omega = 1/2$ when the effect of gas inertia is negligible but as the neck radius reduces sufficiently with a corresponding increase in gas velocity a transition to a $1/3$ power law takes place.

Table 4.3: Exponential power parameter ω controlling the neck radius behavior during the detachment, $R_o = 0.8$ mm, $\dot{Q} = 150$ mlph.

VOF-Geo	CLSVOF-Geo	LS	VOF-Comp
0.356	0.329	0.338	0.348

The numerical predictions are assessed here by reference to the results of Gordillo et al. (2005). Because the detachment times between the four methods are different, the process is analyzed with reference to the detachment time $(t - t_{det})$ to evaluate ω defined according to $R_{neck} \propto [-(t - t_{det})]^{\omega}$. The bubble neck radius is shown in Fig. 4.13 for the last 15 ms with a time step of 0.5 ms. The figure shows that the bubble minimum radius during the growth is not exactly pinned to the orifice rim but rather slides slightly by up to 0.05 mm and clearly highlights the acceleration in the rate of decrease in the neck radius. This is also clear from the interface plots modeled by the LS and VOF-Geo methods and given in Fig. 4.14. In this case, the time step used between each successive interface is 0.5 ms. The values of the power ω obtained from the four methods over the time region $[-0.005, 0]$ s are given in Table 4.3. The four methods are shown to predict a similar behavior before detachment with expected power laws within 7% of $1/3$. The values that are

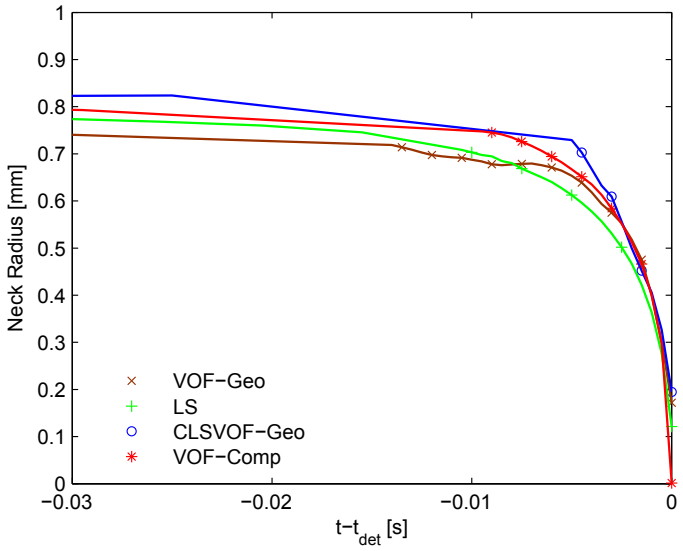

Figure 4.13: Bubble minimum radius, neck radius, during the detachment for the four numerical methods, $R_o = 0.8$ mm, $\dot{Q} = 150$ mlph.

in particular agreement with 1/3 are those of the CLSVOF-Geo and LS methods with relative differences of 1.3% and 1.4% respectively.

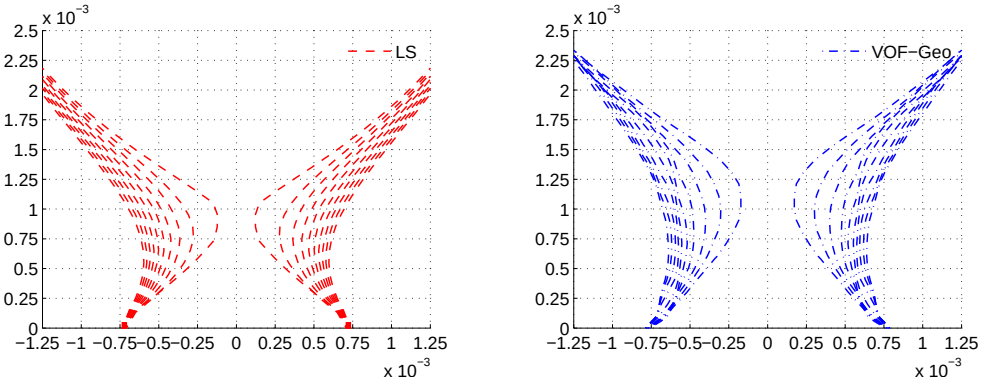

Figure 4.14: Local bubble shape at the neck region for both (a) LS and (b) VOF-Geo methods, $R_o = 0.8$ mm, $\dot{Q} = 150$ mlph.

4.5 Flow behavior inside the bubble

Although no experimental measurements of the flow velocity in the gas phase are available, certain flow features such as a flow convergence through the neck before

pinching or spurious currents can be expected to occur and can be used to assess the relevance of numerical predictions. The velocity vectors during the bubble formation for the four methods are given at three different time steps ($t/t_{det} \sim 0.4, 0.8, 1$) as displayed in Figs. 4.15 and 4.16. The velocity vectors are shown without any scaling. Instead, a color map is used to clarify variations in the velocity magnitude across the domain. The l_∞ and l_1 norms for the flow velocity in the gas phase are summarized in Table 4.4 and shown on the vector plots to provide details of the maximum and average velocities, respectively. The general behavior of the gas inside the bubble may be explained as follows: At the early stage of formation ($t/t_{det} \sim 0.4$) a circulation forms due to the gas injection and the confining effect of the interface. When the bubble elongates in the vertical direction ($t/t_{det} > 0.6$), two or more vortices are formed with one generally located towards the apex while a lower vortex remains close to the orifice. The flow induced by the lower vortex tends to channel the flow upward along the interface but induces currents which oppose the injection flow towards the axis of symmetry. With VOF-Comp, strong convective current flows through the core of the bubble from the apex towards the injection but the current is in the opposite direction with the CLSVOF-Geo and more complex interactions are observed with the other two models. This suggests that the internal flow is a very dynamic process which can be strongly influenced by bubble oscillations which are most significant with the CLSVOF-Geo model. At detachment ($t/t_{det} \sim 1$), the gas passes through the neck with a significant increase in the velocity. Both average and maximum velocity magnitudes can change by in excess of one order of magnitude depending on the model used. For instance, CLSVOF-Geo provides a very large velocity inside the bubble but this is concentrated in a narrow region near the orifice rim where the gas/liquid interface meets with the solid boundaries. With the other methods, the average velocity inside the bubble is approximately $2-3$ times larger than the inflow velocity and in all cases the lowest velocity is predicted by the LS method.

At detachment, the neck forces the gas to stream through the narrower region at the neck producing a flow pattern similar to viscous flow through a converging diverging nozzle. All methods model some level of separation along the interface on the diverging side of the neck but there are significant differences in the extent of the high velocity region. For the VOF-Comp, VOF-Geo and LS methods the velocity quickly drops off after the neck as expected while it persists all the way to the apex with the CLSVOF-Geo method. Again this could be attributed to the oscillatory nature of the bubble in the latter case. The occurrence of the high

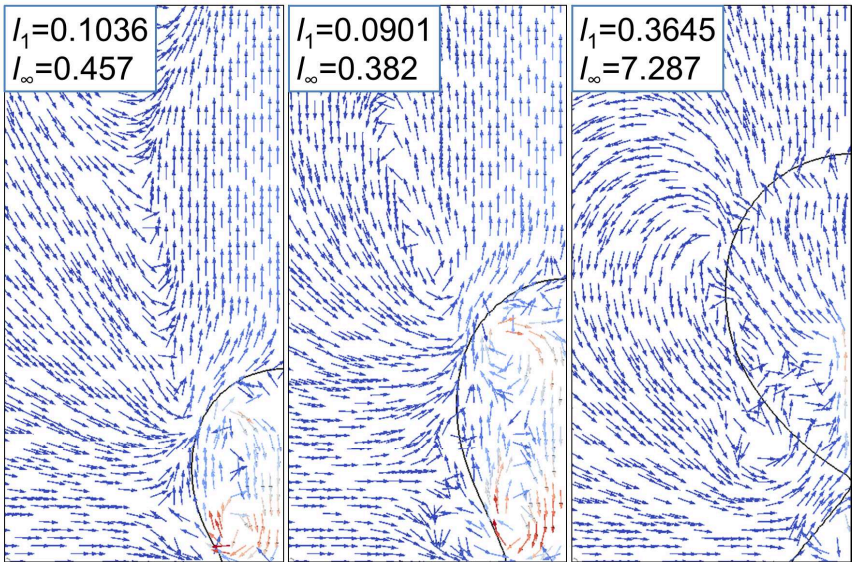

(a) VOF-Comp

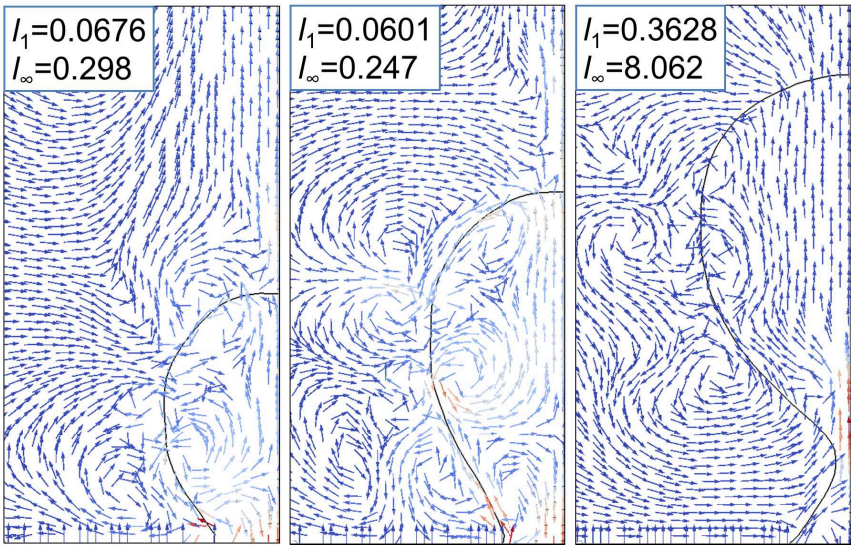

(b) VOF-Geo

Figure 4.15: Velocity vector plot for both VOF-Comp and VOF-Geo at three different stages of bubble growth $t/t_{det} \sim 0.4, 0.8, 1$. The scale of the velocity vector is set to off. The color range is from dark blue (minimum velocity) to deep red (maximum velocity). The norms are expressed in (m/s). $R_o = 0.8$ mm, $\dot{Q} = 150$ mlph.

velocity flow through the neck confirms the observation on the significance of gas inertia in accelerating the pinch-off.

Table 4.4: Magnitude of the maximum and the average velocity inside the bubble for the different numerical methods, $R_o = 0.8$ mm, $\dot{Q} = 150$ mlph.

method	$t/t_{det} = 0.4$		$t/t_{det} = 0.8$		$t/t_{det} = 1$	
	l_∞ (m/s)	l_1 (m/s)	l_∞ (m/s)	l_1 (m/s)	l_∞ (m/s)	l_1 (m/s)
VOF-Geo	0.29856	0.067647	0.24683	0.060148	8.0622	0.362843
CLSVOF-Geo	4.02355	0.950224	2.33933	0.870219	7.72665	1.857331
LS	0.20785	0.038458	0.14396	0.022695	4.3659	0.404789
VOF-Comp	0.457	0.103629	0.382	0.090399	7.278	0.364544

Predictions by all methods show that the onset of the neck formation is accompanied by a gradual increase in the gas velocity towards the neck as a result of the flow constriction. This effect coincides with a decrease in pressure towards the neck followed by a pressure increase consistent with flow through a converging-diverging nozzle. The gradual decrease in gas pressure at the neck with time during the initial stage of the process modeled by the LS method is shown in Fig. 4.17a, where the neck position is determined in terms of the minimum neck radius. Gordillo et al. (2005) argued that this low static pressure in the gas phase draws the external liquid phase towards the neck accelerating the pinching effect, so that the influence of gas inertia on the bubble detachment becomes significant during this stage of the pinching process. This is confirmed by both the liquid velocity plots of Figs. 4.15 and 4.16 and the static pressure plot of Fig. 4.17a. The LS prediction also provides some clarification on the distribution of pressure and velocity through the neck along the axis of symmetry of the bubble immediately before pinching (Fig. 4.17b). In that case the pressure is shown to increase sharply at the neck while the gas velocity reaches 0 indicating the existence of a stagnation point. The pinch off process at the final stage of bubble detachment effectively splits the gas stream into an upward stream into the bubble and a downward stream into the new generated bubble. This explains the reversal in the pressure trend at the neck in the last 2 ms of bubble detachment shown in Fig. 4.17a.

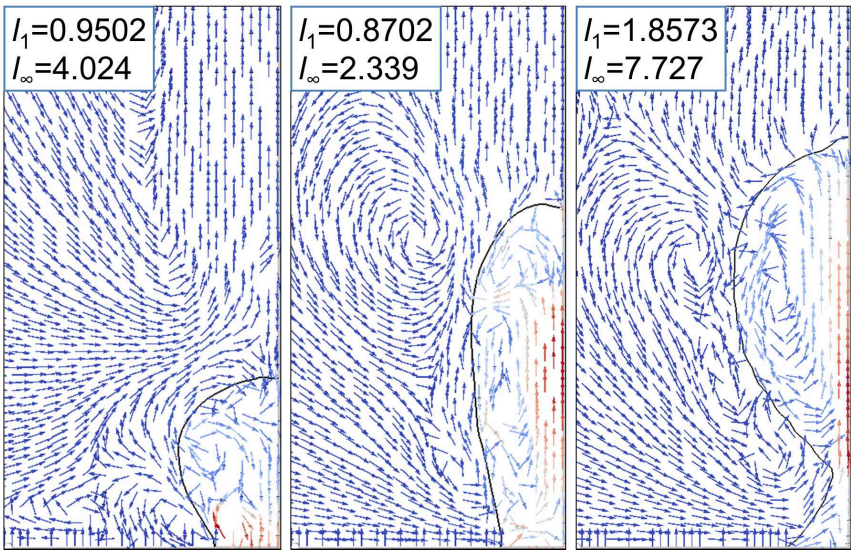

(a) CLSVOF-Geo

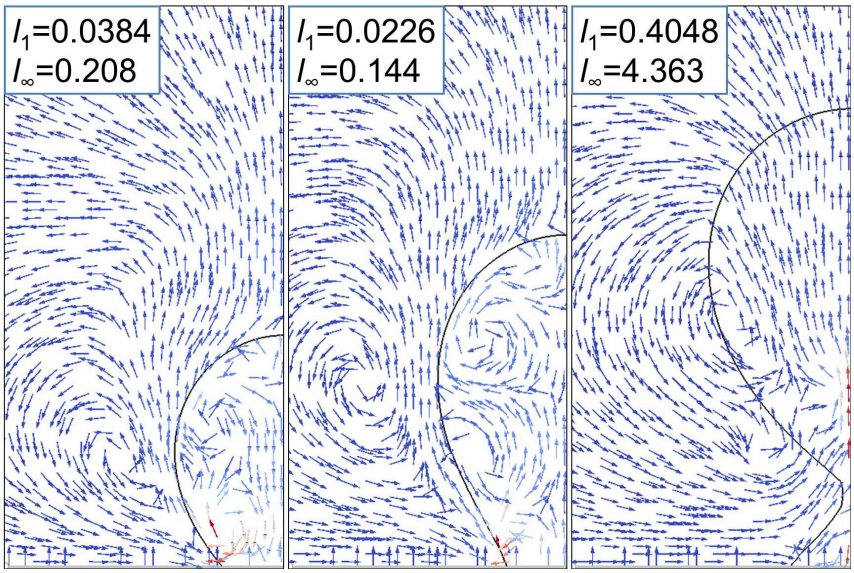

(b) LS

Figure 4.16: Velocity vector plot for both LS and CLSVOF-Geo at three different stages of bubble growth $t/t_{det} \sim 0.4, 0.8, 1$. The scale of the velocity vector is set to off. The color range is from dark blue (minimum velocity) to deep red (maximum velocity). The norms are expressed in (m/s). $R_o = 0.8$ mm, $\dot{Q} = 150$ mlph.

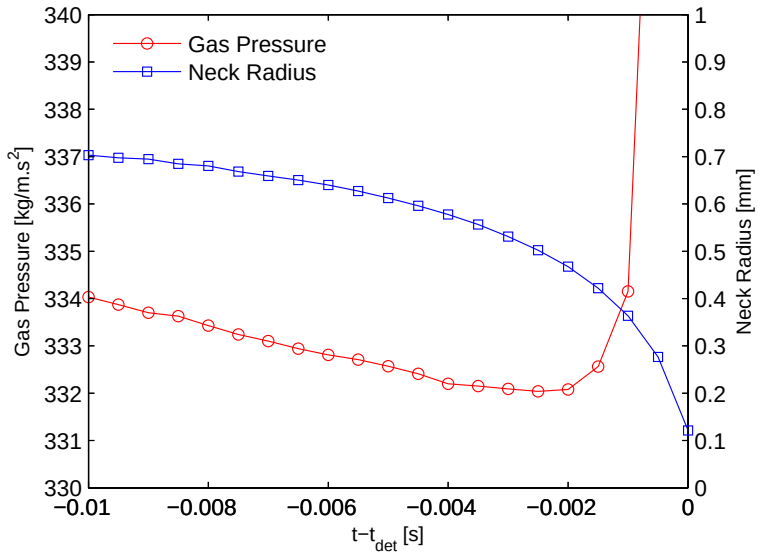

(a)

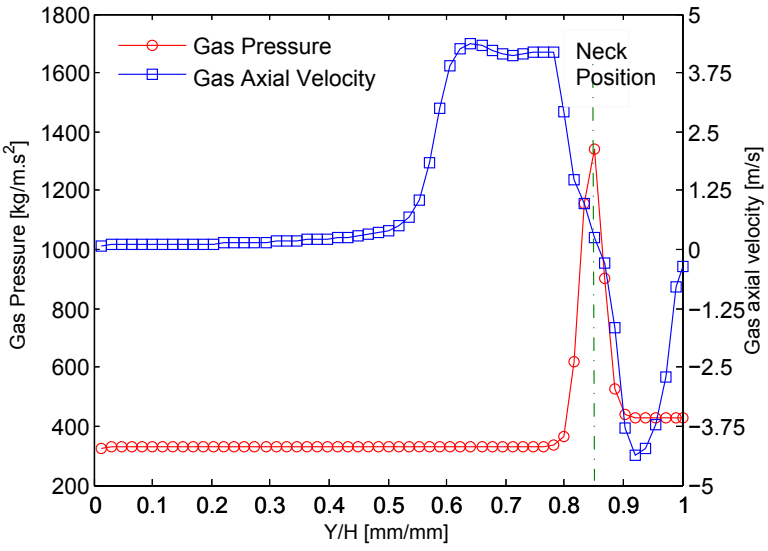

(b)

Figure 4.17: (a) Variations of gas static pressure and bubble minimum radius at the neck position during detachment. (b) Velocity and pressure field along the bubble symmetrical axis at time $t/t_{det} = 1$ using LS with $R_o = 0.8$ mm and $\dot{Q} = 150$ mlph.

4.6 Discussion on the bubble dynamics behavior

Surface tension has been found to induce strong currents at the injection orifice but differences in the numerical implementation are also likely to be responsible for the non negligible differences in the flow velocity patterns observed along the interface away from the injection point. With the VOF-Comp method, the surface tension force is implemented as a body force using the CSF model (see Eq.3.19). This model when coupled with a VOF method is known to generate non-physical spurious currents (Renardy and Renardy, 2002). The density averaging in cells containing the interface as applied in VOF-Geo to calculate the volumetric surface tension force skews this force towards the higher density region and can result in noticeably lower velocities in the gas phase. This averaging is not implemented in VOF-Comp which can explain the smaller average gas velocity obtained with VOF-Geo in particular when $t/t_{det} < 0.8$ (see Table 4.4). To further investigate the influence of the density averaging in the surface tension source term, the VOF-Comp method is solved using the surface tension calculated in Eq. 3.22. Fig. 4.18 plots the velocity vector field in the bubble region using the VOF-Comp method with/without density averaging in the surface tension source term. It is apparent that using density averaging decreases the intensity of the velocity field inside the bubble to less than half the value predicted using the original VOF-Comp method. This tends to support the benefit of the density averaging in reducing the spurious currents inside the bubble. However, the bubble with density averaged surface tension still detaches at earlier times compared to the experiments and no significant changes have been observed to the bubble detachment characteristics compared to the original VOF-Comp method.

A different surface tension model is implemented in the LS and CLSVOF-Geo methods. In this case, the source term which accounts for the capillary forces (Eq.3.12) is applied only over a narrow region around the interface by using the Dirac function (Eq.3.13). In addition, the physical properties are defined from a smoothed Heaviside function (Eq. 3.9). This is well known to reduce spurious currents since the mixture density is calculated using a smoothed function rather than a step function (volume fraction α). Although the CLSVOF-Geo does not appear to lead to very different fluid flow patterns along the interface when compared to the VOF-Geo, the LS velocity vector plot shows much more regular patterns with coherent structures over larger regions of the flow.

Although the CLSVOF-Geo and LS surface tension models are based on similar numerical implementations, CLSVOF-Geo provides an early bubble detachment and

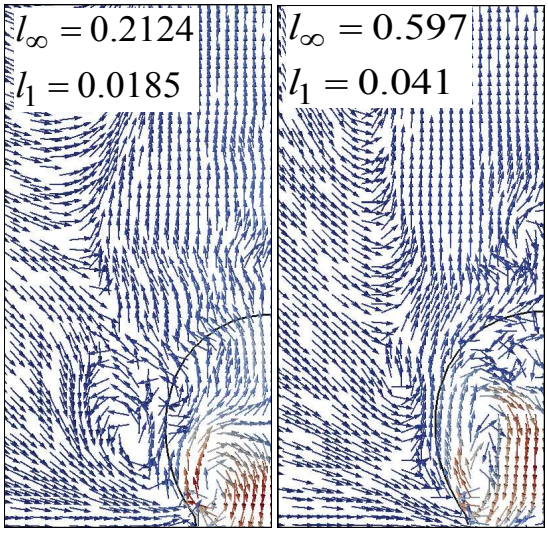

Figure 4.18: Velocity vector plot for VOF-Comp method with (Left)/without (Right) density averaging in the surface tension source term. The plot is at time $t = 0.24$ s from the onset of the formation process. The scale of the velocity vector is set to off. The color range is from dark blue (minimum velocity) to deep red (maximum velocity). The norms are expressed in (m/s). $R_o = 0.8$ mm, $\dot{Q} = 100$ mlph.

promotes bubble oscillations during the growth with large velocities in the vicinity of the orifice rim. Similar observations apply to VOF-Geo but to a lower extent. These oscillations were not observed experimentally and may be caused either by the interface advection methods coupled with the surface tension model or by the static contact angle formulation as a boundary condition. Free bubble rise tests however suggest that the interface motion and surface tension away from solid boundaries are correctly captured by both the CLSVOF and VOF-Geo methods. Results discussed here indicate that the shape instabilities are more likely to originate at the orifice rim due to the surface tension boundary condition. With the VOF and LS methods, the imposed static contact angle corrects the interface normal in the cells close to the wall so that the static contact angle is achieved under static conditions. In the case of the CLSVOF method both the VOF and LS fields must be corrected based on the new direction of the interface normal before solving the momentum equation. A number of alternative numerical implementations are possible but the ANSYS-Fluent theory guide (Ansys, 2011) does not provide sufficient details to allow definite conclusions to be drawn. Results presented in the present study, however, confirm that the CLSVOF-Geo method is particularly sensitive to the imposed static contact angle. This is evident from the velocity fields (Fig. 4.16a) which are characterized by

a maximum magnitude one order of magnitude larger than those observed with the other methods. The shape oscillations and the gas velocities inside the bubble were also found to be particularly sensitive to the time step and convergence criteria used for the solution of the continuity equation pointing to numerically induced instabilities. A significant dampening of the oscillations was achieved by a two order of magnitude reduction in the time step to 10^{-7} s but such a restriction can make computations and in particular three dimensional solutions impractical. The large localized velocities were also found to disappear when modeling the bubble growth process with both VOF geometrical reconstruction methods but without any contact angle corrections at the orifice rim. The change to the contact angle condition however leads to a spreading of the triple contact line away from the orifice rim. These observations strongly support the suggestion that the static contact angle implementation in the Geometrical reconstruction methods is the main cause of the un-physical bubble oscillations.

Based on the analysis of the velocity field inside the gas domain, it is found that for the prescribed physical properties and numerical methods, the LS method implemented in TransAT© can provide the most stable and accurate results for the bubble formation from a wall orifice. The main drawback of this method is the long execution time of the simulation compared to the VOF-Comp (It requires $4-5$ times larger than the algebraic VOF) due to the reinitialization process. Furthermore, the method might suffer from mass conservation issues if the bubble collides against solid boundaries. The VOF-Comp method of OpenFOAM® was found to induce significant spurious currents inside the gas phase and to predict an early bubble detachment. Although the CLSVOF method implemented in ANSYS-Fluent-v13® would be expected to improve the modeling accuracy by reducing the intensity of spurious currents, the bubble was exposed to oscillations during the growth which led to inaccurate geometrical detachment characteristics. This is thought to be due to the implementation of the static contact angle with CLSVOF rather than the features of the method itself, as the interface shape and surface tension are calculated using similar relations as the LS method. However, the Coupled technique used here requires more complicated strategies for the correction of the interface at the boundaries and it is more computationally expensive as it solves two interface capturing advection equations. In general, the geometrical methods, due to the interface reconstruction, are less efficient in terms of the simulation execution time for 3D bubble growth analysis since very small time steps ($O(10^{-7})$ s) are required for accurate results. In contrast, VOF-Comp is less time consuming as it advects

the VOF function algebraically and no interface reconstruction is required. Though it does not provide good results.

With the axi-symmetrical formation process, the geometrical coupled method (CLSVOF-Geo) requires a minimum of two times larger computational time compared to the geometrical VOF method (For $D_o = 1.6$ mm and $\dot{Q} = 100$ mlph, the axi-symmetrical formation process with the VOF-Geo method takes approximately $48 - 72$ h using a local virtual machine limited to only 8 processors). The computational time, however, varies with the operating conditions such as the volumetric flow rate and the orifice diameter. This is mainly due to the difference in the detachment time since using larger flow rates leads to smaller detachment time and thus smaller computational time. The increase in the computational time required by the CLSVOF-Geo method compared to the original VOF-Geo is attributed to the increase in the number of fields (unknown variables) and equations to be solved (CLSVOF-Geo solves both LS and VOF advection equations while VOF-Geo solves only the VOF advection equation).

With the VOF-Comp method, the computational time is smaller compared to the VOF-Geo method (For $D_o = 1.6$ mm and $\dot{Q} = 100$ mlph, the computational time with VOF-Comp is about $18 - 24$ h using 8 processors). It is worth noting that both techniques solve the same number of equations and include similar unknown variables. However, VOF-Geo is slower than VOF-Comp as it requires as extra procedure during the solution which is the geometrical reconstruction and determination of the interface position at every time step. The LS method requires also larger computational time compared to the VOF-Comp method due to solving the reinitialization equation in order to conserve the mass with LS (For similar operating conditions as mentioned above, the computational time with LS is approximately $50 - 60$ h). Even though all the numerical techniques with the axi-symmetrical formation process are solved using similar number of processors, a definite conclusion about the simulation execution time cannot be drawn in this work. This is because different virtual machines were employed for each numerical technique (Local virtual machines were used for both the geometrical and LS methods, while *Ampato* Cluster (High Performance Computing Cluster available in DCU) and *Stokes* super computer (www.ichec.ie) were used for solving the formation process with the algebraic techniques implemented in OpenFOAM).

Results presented in this section have motivated the work on the development of a simple coupling of LS and VOF methods (S-CLSVOF). This coupling focuses mainly

on calculating the surface tension source term using the Level set function rather than the VOF function. Its assessment is the focus of the next results chapter.

5 Results and discussion: Validation of S-CLSVOF method

In this chapter, the extended simple coupling code (S-CLSVOF), explained in section 3.2.3, is validated first by studying a circular bubble at equilibrium in order to examine the spurious currents at the bubble interface, and then both algebraic VOF and S-CLSVOF methods are used for the study of free bubble rise that is without any interaction between the bubble free surface and the wall boundary conditions. For simplicity, the results with the algebraic VOF (VOF-Comp as denoted in the last chapter) will be referred to as VOF in this chapter. The study of the adiabatic axi-symmetrical bubble growth to detachment is then considered. The growth process is characterized by complicated topological changes during the formation and the existence of a direct contact with the boundary condition where special care should be taken in this context. The effect of the imposed static contact angle on the instantaneous contact angle during the growth is investigated using S-CLSVOF. Finally, the bubble growth is studied using three-dimensional domain and compared against axi-symmetrical results.

Similarly to the the previous chapter, the process of bubble formation from a wall orifice is performed using small volumetric flow rates, so that the bubble grows in the static regime (McCann and Prince, 1971) where isolated bubbles with the same detachment frequency are detached from the orifice. Under these conditions, the bubble grows quasi-statically (Oguz and Prosperetti, 1993), where the buoyancy and the surface tension are the dominant forces.

The results of circular bubble and free bubble rise are validated against data obtained from the literature, while the experimental work performed by the collaborative team in Trinity College Dublin is used as a benchmark for validating the bubble growth numerical results. Most of the data and discussion points mentioned in this chapter are presented in the manuscript published in the International Journal of Multiphase Flow (Albadawi et al., 2013).

5.1 Circular bubble at equilibrium

The implementation of the CSF model in the momentum equation for interface capturing methods generates spurious currents in the vicinity of the interface (Renardy and Renardy, 2002). These currents are considered as numerical errors and evidenced as vortices in the interface region. A circular bubble at equilibrium in a zero gravity field is used to assess the strength of the currents and to characterize the fluid flow in the absence of any external forces. The physical properties of the gas phase are $\rho_g = 1$ kg/m^3, $\mu_g = 10^{-5}$ kg/m.s, and the liquid phase are $\rho_l = 1000$ kg/m^3, $\mu_l = 0.001$ kg/m.s. The surface tension is $\sigma = 0.01$ kg/s^2. The mesh domain is 0.05×0.05 m^2. The initial bubble of radius $R_0 = 0.005$ m is positioned at the center $(0.025, 0.025)$. The exact pressure difference between inside and outside the bubble is σ/R_0 while the exact curvature is $1/R_0$. Two different mesh resolutions are used: Coarse (Fine) mesh with 10 (20) cells per bubble diameter. The time step size is 10^{-5} s for the coarse mesh and 5×10^{-6} s for the fine mesh, and the results are considered at the physical time 0.1 s. The norm of the interface curvature is displayed in Table 5.1 and is calculated based on the calculated curvature κ in the VOF method and the S-CLSVOF method as follows:

$$l_{VOF} = \sqrt{\frac{\sum_{counter=1}^{m_1} (\kappa R - \kappa_{exact} R)^2}{m_1}} \tag{5.1}$$

$$l_{S-CLSVOF} = \sqrt{\frac{\sum_{counter=1}^{m_2} (\kappa R - \kappa_{exact} R)^2}{m_2}} \tag{5.2}$$

where m_1 is the total number of cells in the numerical domain and m_2 is the number of cells in the domain where the surface tension is calculated with the S-CLSVOF method (i.e. $\delta \neq 0$). The error in the magnitude of the spurious currents is calculated using the averaged velocity norm l_1 and the maximum velocity norm l_∞ (Renardy and Renardy, 2002)

$$l_\infty = \max_{i,j}(\|\mathbf{V}_{i,j}\|) \tag{5.3}$$

$$l_1 = \frac{1}{N_x N_y} \sum_{i,j} \|\mathbf{V}_{i,j}\| \tag{5.4}$$

Three different pressure definitions are considered in this analysis (Francois et al., 2006):

- $\Delta P_0 = P_0^{in} - P_\infty^{out}$ where P_0^{in} and P_∞^{out} are the value of the pressure at the bubble center and at the wall boundary, respectively.
- $\Delta P_{total} = P_{total}^{in} - P_{total}^{out}$ where P_{total}^{in} and P_{total}^{out} are the averaged value of the pressure inside ($0.5 \geq \alpha \geq 0$) and outside ($1 \geq \alpha \geq 0.5$) the bubble, respectively.
- $\Delta P_{partial} = P_{partial}^{in} - P_{partial}^{out}$ where $P_{partial}^{in}$ and $P_{partial}^{out}$ are the averaged value of the pressure inside ($0.05 \geq \alpha \geq 0$) and outside ($1 \geq \alpha \geq 0.95$) the bubble, respectively. This value ignores the pressure influence inside the diffusive interface region.

The relative pressure error $E_0 = |\Delta P_0 - \Delta P_{exact}|/\Delta P_{exact}$ is used to calculate the error in ΔP_0 where ΔP_{exact} is the exact pressure difference. The norms obtained with the two mesh resolutions are given in Table 5.1 for both the VOF and S-CLSVOF methods. These results confirm that the curvature error does not converge with grid refinement with either method. However, the error from the S-CLSVOF curvature estimate is one order of magnitude smaller than the VOF estimate. A similar conclusion can be reached by considering the errors for the pressure drop across the interface. A one order of magnitude reduction in E_0, in particular, is achieved with the S-CLSVOF method. In this case, however, the error from the region around the interface ($E_{int} = E_{total} - E_{partial}$) of arbitrary thickness defined by $0.05 < \alpha < 0.95$ is shown to contribute significantly to the total error E_{total}. This interface error is again shown to reduce under grid refinement with the S-CLSVOF method. The reduction in the pressure error between the VOF and S-CLSVOF method can be explained by the improved curvature estimate but it cannot justify the effect of grid convergence. This is most likely due to the reduction in the interface thickness and the resulting focusing of surface tension towards the central part of the interface where density increases. Refining the mesh also induces a decrease in $\varepsilon = 1.5\Delta x$, which in turn increases the maximum value of δ, as defined by Eq. 3.13, at the center of the interface region. This means that the surface tension source term is reduced in the gas phase where the higher velocity of spurious currents are observed and shifted instead towards the central part of the interface where the fluid mixture has a higher inertia. This can explain the reduction in spurious currents with grid refinement observed both in terms of the l_1 and l_∞ norm in the case of the S-CLSVOF method (see Table 5.1). This influence can also be seen in Fig. 5.1

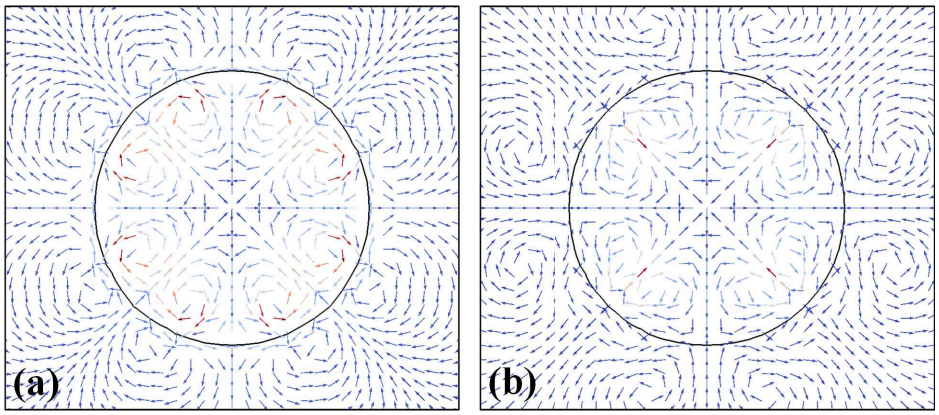

Figure 5.1: Velocity vectors plot at 10th time steps, $\Delta t = 1 \times 10^{-5}$ s and $\Delta x = 5 \times 10^{-4}$ m for (a) S-CLSVOF (max. velocity 0.0068 m/s) and (b) VOF (max. velocity 0.026 m/s). The color map varies from dark blue (min velocity) to dark red (max velocity).

where the velocity vector field for the two methods is plotted without using any vector scaling. Instead, the intensity of the velocity in the domain is measured in terms of a color map. The plots show a more gradual variation in the velocity field within the bubble with significantly lower velocity magnitudes predicted by S-CLSVOF while large velocities localized over specific areas of the bubble with the VOF method. These results agree with the findings of Tong and Wang (2007) for the comparison of VOF and S-CLSVOF methods with the CSF model.

Table 5.1: Norms of velocity and curvature, and errors in the pressure jump at 0.1 s with time step $\Delta t = 10^{-5}$ s (Coarse mesh) and $\Delta t = 5 \times 10^{-6}$ s (Fine mesh).

Method	Mesh size(m)	l_{VOF}	$l_{S-CLSVOF}$	l_∞ (m/s)	l_1 (m/s)	E_0 (%)	E_{total} (%)	$E_{partial}$ (%)	E_{int} (%)
S-CLSVOF	0.001	-	0.2478	0.0171	0.00029	0.416	13.302	2.526	10.778
S-CLSVOF	0.0005	-	0.1527	0.0068	0.00011	0.875	7.866	2.198	5.668
VOF	0.001	1.1752	-	0.0129	0.00019	14.523	24.968	15.672	9.296
VOF	0.0005	1.3289	-	0.0261	0.00017	11.729	19.611	14.144	5.467

If the reduction in spurious currents under grid refinement with S-CLSVOF is indeed due to a narrowing of the interface and focusing of surface tension force towards a region of higher density, grid convergence should fail in the case of uniform density across the interface and between the two phases. The two-dimensional stationary bubble test under zero gravity was repeated with density and viscosity

ratios $\rho_l/\rho_g = 1$ and $\mu_l/\mu_g = 1$ and a bubble diameter $D = 0.01$ m. This test was implemented by Popinet and Zaleski (1999) to confirm the linear proportionality between spurious currents and the surface tension to viscosity ratio σ/μ for a broad range of Ohnesorge numbers ($Oh = \mu_l/(\sigma\rho_l D)^{0.5}$). The results were achieved with a VOF method and surface tension model which was shown to converge to machine accuracy. The current test uses the same domain as considered above in this section with a mesh resolution ranging from 50×50 to 500×500 that is from 10 to 100 cells per bubble diameter and with $1/Oh^2 = 1000$. The time step in this case is defined by $\Delta t = 0.1\Delta x$. Results from both VOF and S-CLSVOF are reported in Table 5.2 in terms of the curvature norms and a capillary number Ca where the velocity in this non-dimensional number is the same as the l_∞ norm of the spurious current velocity measured at the physical time 0.1s that is 10 characteristic time scales ($t = t_{phys}\sigma/(D\mu)$).

Table 5.2: Convergence of non-dimensional maximum velocity with grid refinement for both VOF and S-CLSVOF, $\rho_l/\rho_g = 1$ and $\mu_l/\mu_g = 1$.

Grid size	NB cells/diameter	Ca_{VOF}	L_{VOF}	$Ca_{S-CLSVOF}$	$L_{S-CLSVOF}$
50	10	1.64×10^{-3}	1.184	1.38×10^{-3}	0.262
100	20	2.33×10^{-3}	1.284	1.34×10^{-3}	0.149
150	30	2.49×10^{-3}	1.379	1.29×10^{-3}	0.153
200	40	2.41×10^{-3}	1.455	1.23×10^{-3}	0.206
250	50	2.01×10^{-3}	1.550	1.01×10^{-3}	0.236
300	60	2.01×10^{-3}	1.630	1.00×10^{-3}	0.266
500	100	1.92×10^{-3}	1.921	1.13×10^{-3}	0.361

The two methods are shown to give amplitudes of spurious currents which are of similar orders of magnitude but approximately two times smaller with the S-CLSVOF, while the curvature norm is as observed in Table 5.2. Broadly similar results were observed when using adaptive time stepping with a Courant number $Co = 0.1$. Although grid refinement does induce some changes at the coarsest grid, the convergence of $Ca_{S-CLSVOF}$ tapers off quickly as the mesh is further refined and spurious currents are shown to increase again with the most refined mesh. This suggests that the benefit of the S-CLSVOF method presented here is limited to the improved curvature estimate in the case of low density ratio but further improvement can be expected in terms of the damping of spurious current at larger density ratio.

In particular when concerned with gas-liquid flow, previous results indicate that a non-negligible reduction in spurious currents can be expected as the zone of influence of surface tension is reduced.

5.2 Free bubble rise

In this section, the single bubble rise in a quiescent liquid is simulated using both VOF and S-CLSVOF methods. The main objective here is to validate the coupled S-CLSVOF code for bubble rise problems rather than studying the mechanism of the free rise itself. The analysis is performed for a wide range of physical properties as shown in Table 5.3 and for three different equivalent diameters (3, 5 and 7 mm). The simulation parameters and the corresponding dimensional numbers are listed in Table 5.4. Both the bubble terminal velocity (V_∞) and aspect ratio (AR) are analyzed in this study using two-dimensional (2D) and three-dimensional (3D) numerical simulations. The experimental observations by Raymond and Rosant (2000) are used to assess the bubble terminal velocity and aspect ratio in the 3D domain. The size of the numerical domain is (0.04 m, 0.075 m, 0.04 m) which corresponds to $(8D_{eq}, 15D_{eq}, 8D_{eq})$ for bubble diameter 5 mm. For the same physical and geometrical properties, Hua and Lou (2007) have shown that this size ensures no liquid influence from the boundary walls on the bubble motion. A regular mesh is used to discretize the fluid domain so that 25 cells are distributed along the bubble diameter. This mesh size has been shown to be sufficient for guaranteeing the convergence of the numerical results [Kumar and Delauré (2012) and Hua and Lou (2007) used 25 cells/diameter while 12 cells/diameter were with Annaland, Deen and Kuipers (2005)].

Table 5.3: Physical properties used for numerical bubble rise simulations

Series	μ_l (Pa.s)	ρ_l (kg/m^3)	σ (N/m)	Mo
S1	0.687	1250	0.063	7.5287
S3	0.242	1230	0.063	0.1057
S5	0.0733	1205	0.064	7.4492×10^{-4}

The terminal bubble shape for the different bubble diameters with the S5 fluid is displayed in Fig. 5.2 where the initial spherical bubble is shown to deform from

spherical to ellipsoidal shape as the initial diameter increases. The bubble shape compares well with the bubble diagram of Grace (1973) and similar behavior was also noticed by Raymond and Rosant (2000) due to the increase in both Re and Bo numbers.

Table 5.4: Simulation parameters for the rising of different sized bubbles in the series fluids

Bubble	S1		S3		S5	
Diameter (m)	Mo	Bo	Mo	Bo	Mo	Bo
0.003	7.529	1.75	0.106	1.7221	7.4492×10^{-4}	1.6607
0.005	7.529	4.862	0.106	4.7836	7.4492×10^{-4}	4.6131
0.007	7.529	9.529	0.106	9.3759	7.4492×10^{-4}	9.0416

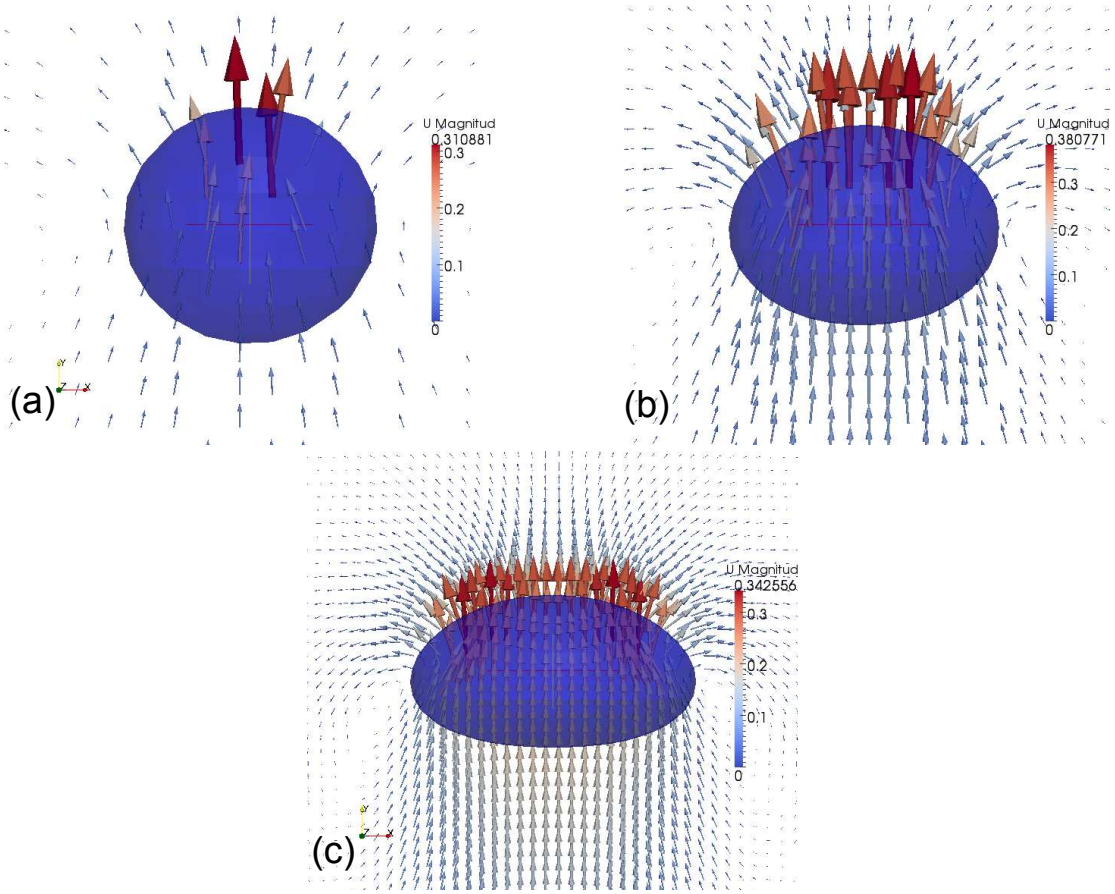

Figure 5.2: The bubble shape and the velocity vector plots for three diameters (a)$D_{eq} = 0.003$ m,(b)$D_{eq} = 0.005$ m,(c)$D_{eq} = 0.007$ m predicted by S-CLSVOF at time 0.14 s.

Fig. 5.3 presents a quantitative comparison between the numerical simulations

using the S-CLSVOF method and the experimental observations by Raymond and Rosant (2000). The numerical results are displayed for both the 2D and 3D simulations. Fig. 5.3a shows that the bubble terminal velocity increases as larger equivalent diameters are considered. An increase in bubble velocity can be obtained also by using fluids with smaller Mo numbers. For small bubble diameters, the 2D simulation gives bubble terminal velocity which compares reasonably well with experimental data. However, it fails to predict the correct V_∞ at high equivalent diameters, contrary to the 3D simulations. The discrepancy between the 2D and 3D cases is more apparent when considering the bubble aspect ratio (Fig. 5.3b) which highlights the importance to model the free bubble rise with large radii using 3D simulations. This difference is due to the nature of the wake behind the bubble which drives the bubble to follow a three-directional trajectory during its rise when it has an oblate ellipsoidal shape (Clift, Grace and Weber, 1978).

Finally, a comparison between both VOF and S-CLSVOF methods is presented. Table 5.5 shows the relative difference between the S-CLSVOF method and the VOF method for both the bubble terminal velocity ($E_{V_\infty} = (V_\infty^{S-CLSVOF} - V_\infty^{VOF})/V_\infty^{VOF}$) and aspect ratio ($E_{AR} = (AR^{S-CLSVOF} - AR^{VOF})/AR^{VOF}$). It is clear that the interface capturing method does not have a significant influence on the bubble terminal velocity and aspect ratio with maximum difference of 2.5% and 2%, respectively. This indicates that both methods, for the range of the physical and geometrical parameters considered, predict well the free bubble rise and the corresponding terminal shape. It is worth noting, however, that under the present conditions, the bubble does not deform into a complex shape and no bubble coalescence or merging has been considered.

Table 5.5: Relative difference between the bubble terminal velocity and aspect ratio from the S-CLSVOF method compared to the VOF predictions.

Bubble	S1		S3		S5	
Diameter (m)	$E_{V_\infty}(\%)$	$E_{AR}(\%)$	$E_{V_\infty}(\%)$	$E_{AR}(\%)$	$E_{V_\infty}(\%)$	$E_{AR}(\%)$
0.003	2.604578	0.406504	-0.05574	1.661475	-1.93252	1.982379
0.005	1.744186	1.422764	2.564103	2.33853	2.210015	1.949861

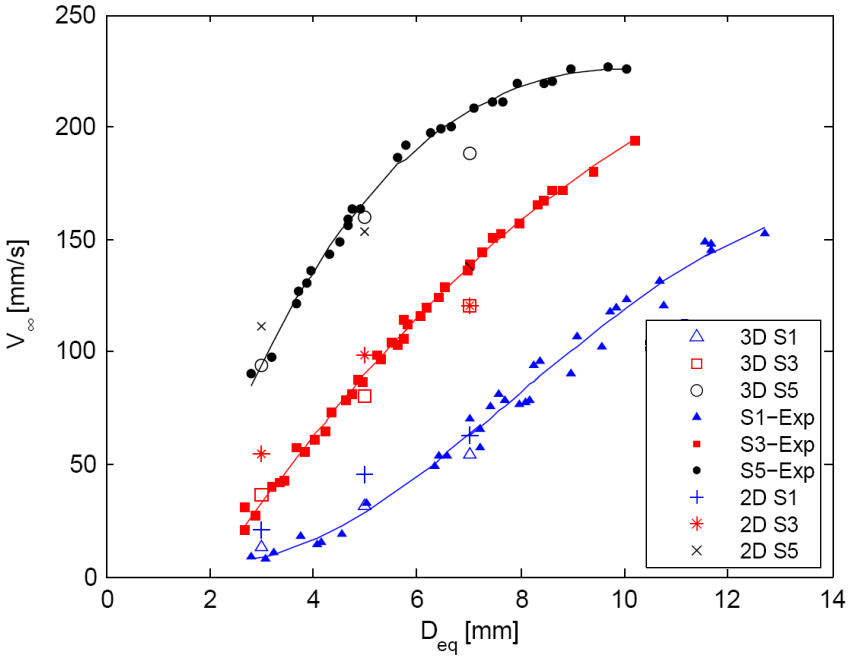

(a)

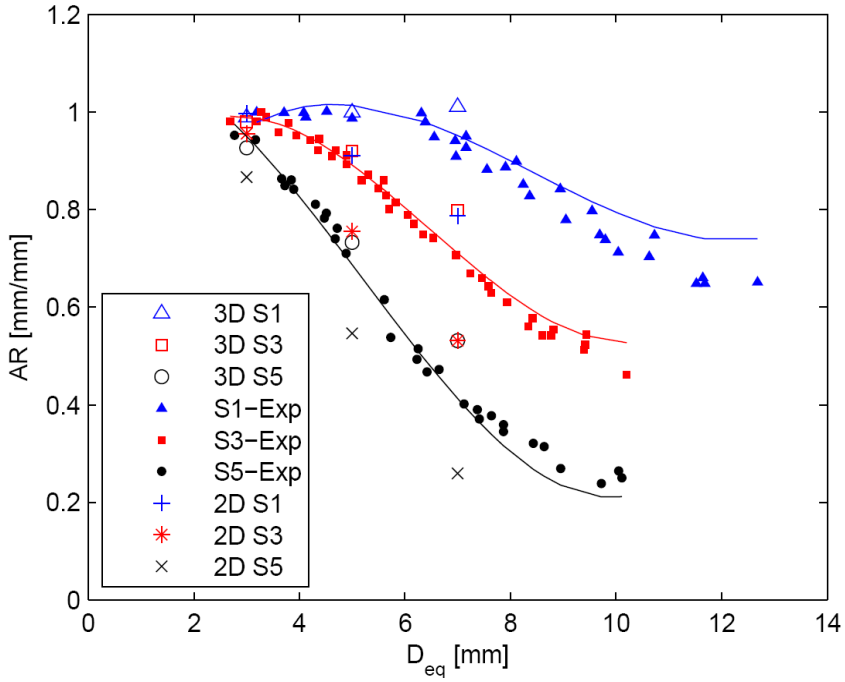

(b)

Figure 5.3: Comparison of (a) bubble terminal velocity and (b) aspect ratio predicted by simulations (2D and 3D S-CLSVOF) with experimental observations (Raymond and Rosant, 2000).

5.3 Validation of bubble growth dynamics

In the following section, the bubble formation process is studied numerically using both algebraic VOF and S-CLSVOF methods. The numerical domain and the computational parameters are discussed first, and then the numerical models are validated by comparison against experimental data following the same strategy and characteristic parameters studied in the previous chapter. Finally, the bubble growth in three-dimensional domain is studied.

5.3.1 Problem setup

The bubble formation process is studied numerically using axi-symmetrical simulations since it grows vertically without any lateral oscillations due to the absence of any shear flow in the bulk fluid (Duhar and Colin, 2006). The schematic diagram of the numerical domain is similar to the one used in the last chapter and it is shown in Fig. 4.1. The air bubble is injected through an orifice of radius $R_o = 0.5 \times 10^{-3}$ m or $R_o = 0.8 \times 10^{-3}$ m submerged in initially quiescent water. The gravitational acceleration is imposed in the axi-symmetrical direction, while the surface tension coefficient is assumed to be constant. The physical properties of both air and water are also constant and taken at room temperature (Table 5.6).

Table 5.6: Fluids' physical properties for bubble growth analysis.

Parameters	Symbol	Values	Units
Liquid density	ρ_l	998.2	kg/m^3
Liquid viscosity	μ_l	0.001	kg/m.s
Gas density	ρ_g	1.225	kg/m^3
Gas viscosity	μ_g	$1.79 \cdot 10^{-5}$	kg/m.s
Surface tension	σ	0.073	N/m
Gravity	g	9.81	m/s^2

The gas injection is assumed to be under constant flow rate and lower than the critical value determined by Oguz and Prosperetti (1993) for quasi-static flows ($\dot{Q}_{crit} \approx \pi(\frac{16}{3g^2})^{1/6}(\frac{\sigma_L R_o}{\rho_L})^{5/6} = 1.82 \times 10^{-6}$ m^3/s). The numerical domain has a width $2.5D_{eq}$ and height $5D_{eq}$, equivalent to 10×20 mm^2, where D_{eq} is the bubble equivalent diameter. The domain width is similar to that of Chakraborty et al. (2009)

and Gerlach et al. (2007) who have reported that the bubble growth is not affected by any liquid circulations close to the wall.

The bubble passes through two stages during its growth. They are defined as the expansion stage and the collapse (detachment) stage (Longuet-Higgins, Kerman and Lunde, 1991). The bubble detachment happens when the neck diameter is less than 10% of the orifice diameter (Oguz and Prosperetti, 1993). In the present chapter, several mesh sizes were tested for convergence analysis as shown in Table 5.7. The time step size used for each simulation is $\Delta t = 0.2\Delta x$. Results are reported in Table 5.7 in terms of the bubble detachment volume and time. The relative difference for each two successive mesh refinements is calculated with reference to the coarser mesh $(100 * (V_{finer} - V_{coarser})/V_{finer})$. The results show that the bubble detachment characteristics increases with mesh refinement as observed by Chakraborty et al. (2009) under similar mesh refinement. When the number of cells per orifice diameter is increased from 32 to 64 cells, the bubble detachment volume has increased by approximately 1.68% which corresponds to a relative difference in the bubble equivalent radius of about 1.19%.

Table 5.7: Convergence analysis of mesh discretization using S-CLSVOF with $R_o = 0.8$ mm and $\dot{Q} = 200$ mlph.

nb/diameter	Δx	Δt	V_{det} (mm^3)	t_{det} (s)	E_{vol} (%)	E_t(%)
8	2.0×10^{-4}	4.0×10^{-5}	26.595	0.455	-	-
16	1.0×10^{-4}	2.0×10^{-5}	28.082	0.484	5.30	6.01
20	8.0×10^{-5}	1.6×10^{-5}	30.283	0.525	7.27	7.79
32	5.0×10^{-5}	1.0×10^{-5}	31.448	0.547	3.70	4.02
64	2.5×10^{-5}	5.0×10^{-6}	31.985	0.560	1.68	2.32

Fixing the time step as a function of the mesh size does not guarantee a bounded Courant Number $Co = (V_{b,max}\Delta t)/\Delta x$ which can be affected by spurious currents and, to a larger extent, the flow acceleration which characterizes the detachment. Further tests were conducted to assess the influence of the time step on the bubble detachment time and volume (see Table 5.8). The time step $\Delta t = 5 \times 10^{-6}$ s gives similar results to $\Delta t = 10^{-6}$ s with a relative difference in the detachment volume of approximately 0.2%. Results obtained with $\Delta t = 5 \times 10^{-6}$ s are also compared against adaptive time step computations controlled with $Co = 0.2$. Other values of Co were considered and in all cases the relative difference in the bubble detachment

time and volume always remain below 0.5% . To conclude, $\Delta x = 5 \times 10^{-5}$ m and $\Delta t = 5 \times 10^{-6}$ s (32 cells per orifice diameter) were selected for all simulations in this study so that the detachment can be considered to occur when the neck radius is less than 50 μm. This resolution is comparable to or smaller than that used in previous bubble growth studies [$\Delta x = 0.2 \times 10^{-3}$ m in Buwa et al. (2007) and $\Delta x = 0.25 \times 10^{-3}$ m in Chakraborty et al. (2009); Gerlach et al. (2007)].

Table 5.8: Convergence analysis of time step discretization using S-CLSVOF with $R_o = 0.8$ mm and $\dot{Q} = 200$ mlph.

nb/diameter	Δx	Δt	V_{det} (mm^3)	t_{det} (s)	E_{vol}(%)	E_t(%)
32	5.0×10^{-5}	1.0×10^{-5}	31.448	0.547	-	-
32	5.0×10^{-5}	5.0×10^{-6}	30.919	0.537	-1.71	-1.86
32	5.0×10^{-5}	1.0×10^{-6}	30.981	0.539	0.20	0.37
32	5.0×10^{-5}	Courant (0.2)	31.004	0.5395	0.27	0.46

Four boundary conditions are set to represent the borders of the numerical domain. The inflow velocity is defined at the inlet where the gas is injected through the throat at a constant volumetric flow rate. Its velocity profile is parabolic and calculated as:

$$v(x) = v_{max}[1 - (\frac{x}{R_o})^2] \tag{5.5}$$

where x is set to zero at the axis of symmetry, and v_{max} is the maximum inflow velocity calculated as $v_{max} = 2v_0 = 2\dot{Q}/(\pi R_o^2) = 0.0276$ m/s for flow rate $\dot{Q} = 100$ mlph and orifice radius $R_o = 0.8$ mm. At the outlet, the outflow pressure is set to the atmospheric pressure while the gradient normal to the boundary of all the other quantities is zero. Any reverse flow at the outlet is assumed to be liquid. At the wall, a no slip boundary condition is imposed except for the lower wall where wall adhesion is considered. The wall static contact angle is $\theta = 20^\circ$ so that the bubble interface does not spread along the wall. At the initial time, a semi-circular bubble is patched at the inflow with a radius $R_{ini} = R_o = 0.8 \times 10^{-3}$ m. The existence of the initial bubble is essential to calculate the distance function for the LS method, while it minimizes interface diffusion at the initial stages of bubble growth for the VOF method.

With the smeared interface approach used in the present study, the interface

thickness ε constitutes an additional numerical parameter which determines the band thickness around the interface where the surface tension source term is applied. Sussman et al. (1998) defined ε as a function of the mesh size (Δx). The condition $\varepsilon \geq 1.5\Delta x$ guarantees that surface tension is spread over at least one cell on either side of the interface while the larger the value of ε, the more iterations are required for the solution of the re-distancing function as defined by Eq. 3.25. A value of $1.5\Delta x$ has typically been used by several researchers (Sun and Tao, 2010; Son and Hur, 2002; Sussman, Smereka and Osher, 1994) or in the case of bubble growth simulations using CLSVOF by Chakraborty et al. (2009). The sensitivity of the bubble growth simulations to this definition has been tested with ($\varepsilon = 1.5\Delta x, 3.0\Delta x, 4.5\Delta x$) in terms of its effect on the bubble detachment time and volume for an injection flow rate $\dot{Q} = 200$ mlph and an orifice radius $R_o = 0.8$ mm. Results given in Table 5.9 confirm that as the interface thickness is increased bubble detachment characteristics decrease to values which approach those modeled by the original VOF method (presented in Table 5.10).

Table 5.9: Bubble detachment characteristics at three different values of ε obtained with $\dot{Q} = 200$ mlph and $R_o = 0.8$ mm. $\Delta t = 5 \times 10^{-6}$ s and $\Delta x = 5 \times 10^{-5} m$.

Interface Thickness	t_{det} (s)	V_{det} (mm^3)
$\varepsilon = 4.5\Delta x$	0.446	25.87
$\varepsilon = 3.0\Delta x$	0.492	28.4
$\varepsilon = 1.5\Delta x$	0.537	30.92

The mixture's physical properties in the coupled S-CLSVOF can be calculated using either the volume of fluid function (Eqs. 3.15 and 3.16) or the Heaviside function (Eqs. 3.7 and 3.8). The influence of the different techniques on the bubble formation process is studied for flow rate 100 mlph and orifice radius $R_o = 0.8$ mm. The comparison of the bubble center of gravity during the full formation process up to detachment for both cases is displayed in Fig. 5.4. The figure highlights that during the bubble growth the coupled S-CLSVOF solver provides similar results regardless of the method followed for calculating the physical properties. During the detachment, the numerical results with physical properties calculated from the VOF function provide slightly later detachment compared to the results with physical properties calculated from the Heaviside function. Comparing the detachment characteristics for both methods gives relative differences in the bubble detachment time and volume which are 2.22 % and 2.27 %, respectively. This

confirms the small influence of averaging of the physical properties on the bubble growth results. The numerical results presented here are derived using the equations ($\rho = \rho(\alpha), \mu = \mu(\alpha)$). This facilitates the comparison with the VOF method as the main difference between the two different techniques is limited to the surface tension force model only.

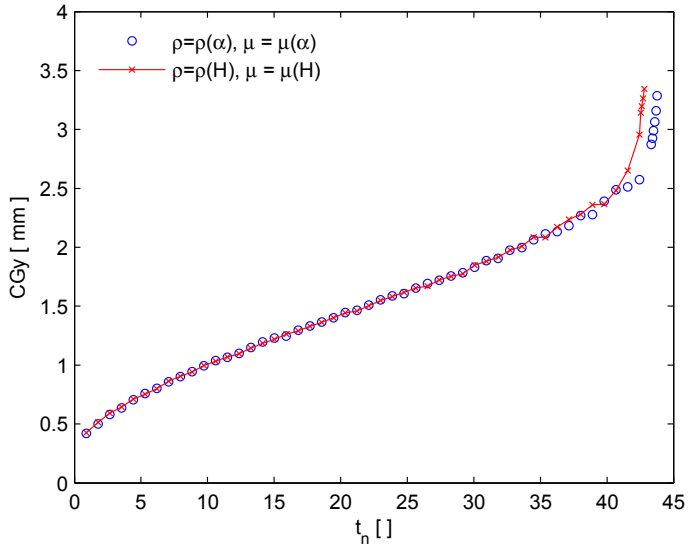

Figure 5.4: Bubble center of gravity versus the non-dimensional time $t_n = tv_0/R_o$ for S-CLSVOF numerical results with physical properties calculated using either VOF function ($\rho = \rho(\alpha), \mu = \mu(\alpha)$) or Heaviside function ($\rho = \rho(H), \mu = \mu(H)$), $\dot{Q} = 100$ mlph and $R_o = 0.8$ mm.

5.3.2 Qualitative comparison of bubble growth

The numerical results obtained by both VOF and S-CLSVOF are first assessed qualitatively by comparing the contour of the reconstructed interface against experimental observations. The initial bubble shape at time $t/t_{det} = 0$ is hemispherical. As shown in the last chapter (Fig. 4.2), the bubble passes through several topological changes during its growth. At the early stages ($t/t_{det} \sim 0.2$), the bubble has a truncated spherical shape whose volume increases linearly due to the constant injected flow rate. With time, the bubble elongates in the vertical direction while it retains its spherical shape at the upper part. During the detachment stage ($t/t_{det} > 0.8$), three different regions can be distinguished; the bubble dome which forms the upper part, the neck region which forms the lower part, and the transition region where the bubble interface curvature converts from concave to convex.

The analysis of the forces acting on the bubble and its evolution with time is analyzed. A schematic sketch of the bubble volume during the growth from a wall orifice with the corresponding forces that control the formation process is shown in Fig. 5.5. This analysis is performed on the numerical data with S-CLSVOF to highlight the significance of the capillary stress during the formation. Under quasi-static conditions, the forces acting on the bubble in the gravitational direction are divided into two main groups according to their influence on the formation (Di Bari and Robinson, 2013; Duhar and Colin, 2006). The first group, which acts in the positive direction of the Y-axis, promotes the bubble detachment and includes the buoyancy force ($F_B = (\rho_l - \rho_g)V_s$) and the contact pressure force ($F_{CP} = \pi R_o^2(P_g - P_T)$), where V_s is the bubble volume in the regions radially outward the orifice rim (the shaded region in Fig. 5.5), P_g and P_T are the gas pressure inside the bubble and the liquid pressure at the bubble apex (Di Bari and Robinson, 2013). The other group of forces, which acts in the negative direction of the Y-axis, resists bubble detachment and acts to keep the bubble attached to the orifice. It is a combination of both the capillary force ($F_C = 2\pi\sigma R_o sin\theta$) and the dynamic force ($F_D = F_C - (F_{CP} + F_B)$) which represents both the liquid inertia close to the bubble interface and the viscous forces, where θ is the instantaneous contact angle calculated at the same distance from the wall orifice for both the numerical and experimental data employed. Fig. 5.6 shows the temporal evolution of the forces acting on the bubble in the vertical gravitational direction. As noticed in this figure, the influence of the drag force is very small compared to the other forces. At the beginning of the growth, the bubble is controlled by a balance between the contact pressure force and the capillary force. During the growth, the influence of the buoyancy increases due to the increase in the bubble size while at the last stage of detachment, the influence of the capillary force decreases rapidly. Furthermore, the capillary force has a strong influence on the bubble during the whole process which highlights the importance of using an accurate surface tension model in the momentum equation in order to avoid any numerical errors leading to unphysical bubble formation.

A comparison between the experimental bubble and the numerical interfaces predicted by both VOF and S-CLSVOF is presented in Fig. 5.7. The orifice diameter is 1.6 mm and the volumetric flow rate is 200 mlph. With the VOF method, the bubble boundary is assumed to be at the iso-line contour $\alpha = 0.5$, while the iso-line contour $\phi = 0$ is considered for reconstructing the interface in the S-CLSVOF method. It is evident that the different topological changes during the bubble growth are well predicted by both methods. With the VOF method, the bubble is shown to grow

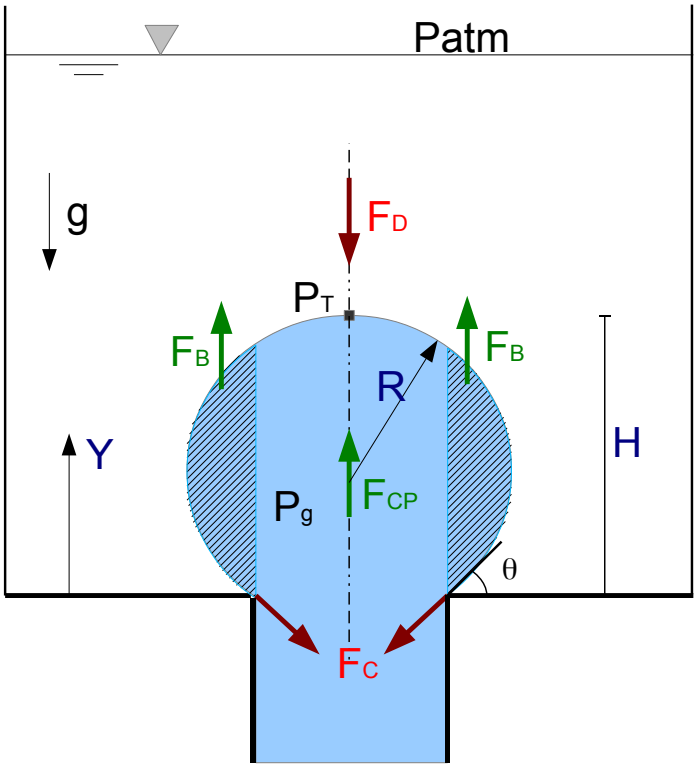

Figure 5.5: A schematic sketch of the bubble volume considered for calculating the forces acting on the bubble during the formation process.

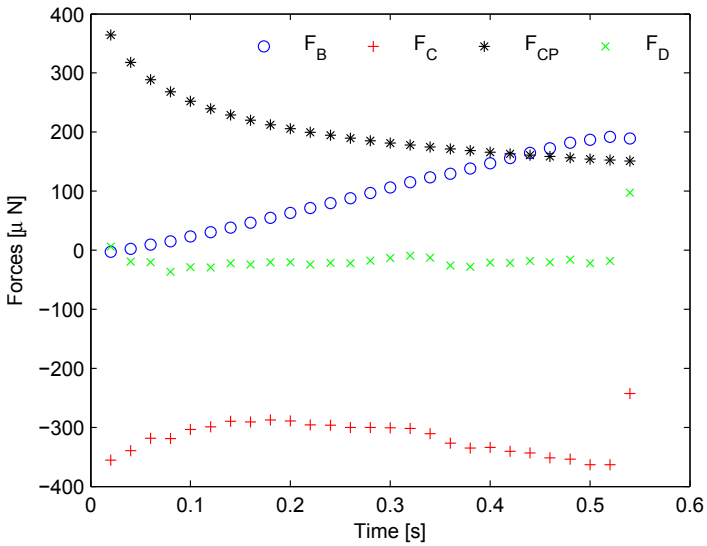

Figure 5.6: Forces acting on the bubble for $R_o = 0.8$ mm and $\dot{Q} = 200$ mlph.

faster compared to experimental observations, and it detaches with smaller volumes and a maximum bubble height which is smaller than that observed experimentally. In contrast, the bubble growth obtained with S-CLSVOF is in close agreement with experimental measurements. The early detachment modeled by the VOF method is most likely due to the implementation of surface tension (Eq. 3.19). With the VOF method, its influence is applied not only at the interface, but over the whole numerical domain. The analysis of the influence of the interface thickness parameter ε in Section 5.3.1 and the study of spurious currents in Section 5.1, highlight the importance of restricting surface tension to a narrow region across the interface. In particular it was shown that increasing the interface smearing with S-CLSVOF tends to provide detachment parameters which converge towards those predicted by the VOF method.

5.3.3 Quantitative comparison of bubble growth

The bubble detachment parameters, defined as the detachment time t_{det}, the detachment volume V_{det}, and the detachment center of gravity in the vertical direction CGy_{det}, are used to validate the correctness of the numerical methods by comparison against experimental data. With the VOF method, the bubble volume is measured based on the volume fraction function α as $\sum_{cells}(1-\alpha)dV$, while the bubble volume in the S-CLSVOF method is determined by the amount of air entrapped inside the iso-line contour $\phi = 0$. The detachment time is assumed at the moment before the bubble splits at the neck into two bubbles. The detachment parameters for orifice radius 0.8 mm with four different flow rates of $50, 100, 150, 200$ mlph are shown in Table 5.10. The relative error of the bubble volume is calculated as $E_{vol} = 100 * (V_{num} - V_{exp})/V_{exp}$. The experimental results show that the bubble detachment time decreases exponentially with increasing flow rate, following an exponential power law ($t_{det} = C\dot{Q}^{\zeta}$) where $\zeta = 0.96$. Similar decay is observed with S-CLSVOF with $\zeta = 0.95$. However, the value ζ is very close to 1 indicating the linear relationship between the detachment time and the flow rate for quasi-static conditions. With the VOF method, the detachment time decreases exponentially with increasing the flow rate, but the power exponent takes the value $\zeta = 0.77$. The small detachment time with the VOF method leads to small detachment volume compared to the experiments, while the detachment volume with S-CLSVOF is very close to the experimental results with maximum error of 3%. Both numerical methods results detach with smaller centers of gravity. However, the S-CLSVOF

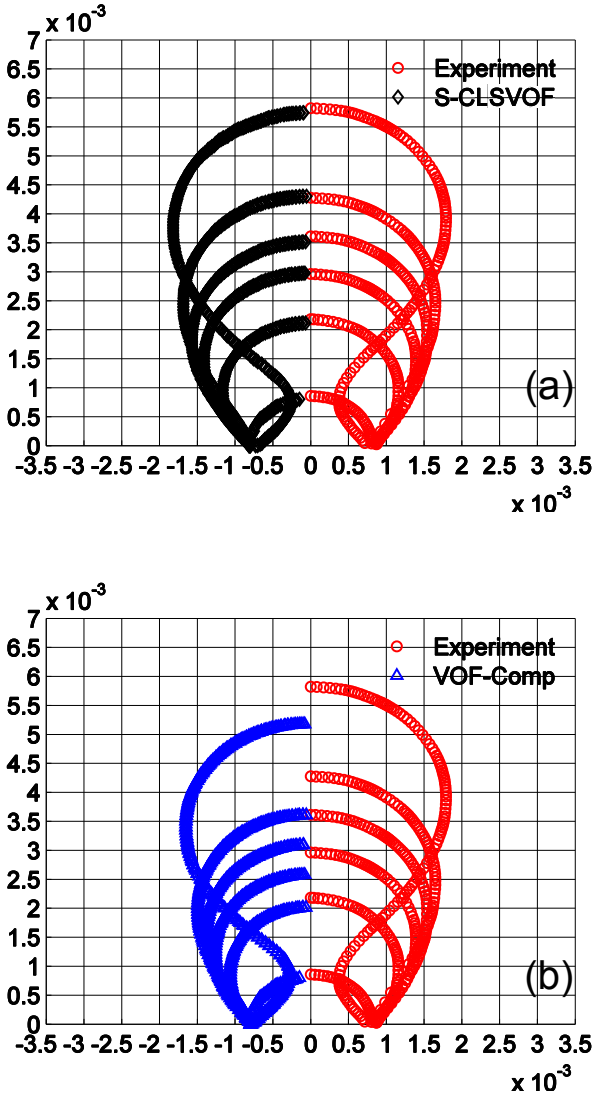

Figure 5.7: Bubble shape predictions at six time frames $t/t_{det} \sim 0, 0.2, 0.4, 0.6, 0.8, 1$ with $R_o = 0.8$ mm and $\dot{Q} = 200$ mlph for (a) Experimental and S-CLSVOF, and (b) Experimental and VOF.

predicts well the detachment CGy with an error less than 2% which corresponds to a difference smaller than 70 μm.

Table 5.10: Bubble detachment characteristics for four different volumetric flow rates $\dot{Q} = 50, 100, 150, 200$ mlph, $R_o = 0.8$ mm.

Flow rate	Method	t_{det}(s)	Cgy_{det}(mm)	V_{det}(mm^3)	E_t (%)	E_{cg} (%)	E_{VOL} (%)
50mlph	Experiment	1.985	3.568	28.396	0	0	0
	VOF	0.991	3.227	21.025	-50.050	-9.551	-25.959
	S-CLSVOF	2.033	3.497	29.276	2.443	-1.968	3.099
100mlph	Experiment	1.013	3.631	29.134	0	0	0
	VOF	0.597	3.245	22.057	-41.017	-10.614	-24.290
	S-CLSVOF	1.039	3.559	29.899	2.566	-1.973	2.626
150mlph	Experiment	0.684	3.625	29.7	0	0	0
	VOF	0.428	3.264	22.283	-37.427	-9.965	-24.971
	S-CLSVOF	0.704	3.551	30.368	2.923	-2.030	2.250
200mlph	Experiment	0.523	3.611	30.074	0	0	0
	VOF	0.339	3.269	22.751	-35.010	-9.453	-24.352
	S-CLSVOF	0.537	3.592	30.919	2.848	-0.531	2.809

The larger detachment volumes predicted by S-CLSVOF suggest that the numerical bubble may have larger CGy_{det} than observed experimentally, but this is not the case (see Table 5.10). In order to investigate this discrepancy and to examine the suitability of the numerical models for predicting the bubble behavior during the growth, the physical parameters characterizing the bubble dynamics during the formation are studied. Fig. 5.8 shows the time evolution of the bubble center of gravity for both the numerical methods and the experimental observations. The orifice diameter is 1.6 mm and the inflow flow rate is 200 mlph in this case. This figure confirms that using S-CLSVOF improves the prediction of the bubble center of gravity compared to the original VOF method. With VOF, the bubble is exposed to a series of contractions and expansions in the vertical direction which is interpreted as a small oscillation in the bubble center of gravity. With the S-CLSVOF method, the numerical predictions are similar to the observations from the experiments at the early stages of growth. At time $t \sim 0.35$ s, the neck starts to form when a sudden jump in the bubble center of gravity is observed. However, this motion is not observed experimentally and it may be due to the static contact angle implementation at the orifice rim.

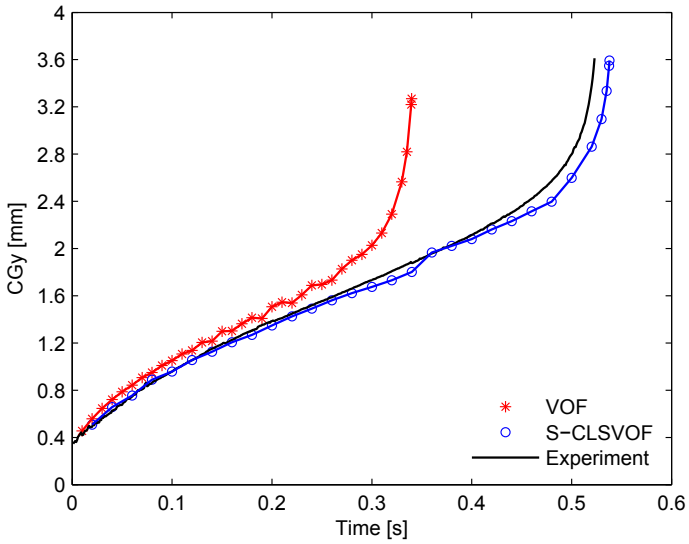

Figure 5.8: Bubble center of gravity versus time with $R_o = 0.8$ mm, $\dot{Q} = 200$ mlph.

The bubble evolution in the radial direction is examined by measuring the bubble maximum width as shown in Fig. 5.9. At the initial time, the bubble has a hemispherical shape with radius $R = R_o$ and its maximum width is 1.6. It is clear that the maximum width is well predicted by both VOF and S-CLSVOF. However, the bubble detaches at an earlier time with the VOF method. During the detachment, the bubble width with S-CLSVOF is slightly larger than that with the experiments which explains the smaller CGy at detachment obtained with the S-CLSVOF method.

The bubble instantaneous contact angle during growth is defined as the angle between the bubble interface and the wall and is measured in the liquid domain. Experimentally, this angle is related to the orifice radius (as will be shown later), while it is controlled by the numerically implemented contact angle in the numerical simulations. A comparison of its numerical predictions and experimental measurements is presented in Fig. 5.10. During the early stages of growth, the angle decreases with time as the bubble deforms from hemispherical to a truncated hemispherical shape, while the detachment stage is characterized by the increase in the contact angle due to the neck formation. Both numerical methods predict similar behavior of the contact angle during the formation. The bubble oscillations in the center of gravity CGy also affect the instantaneous contact angle with amplitudes of oscillations which grow gradually before the onset of detachment. The oscillations appear

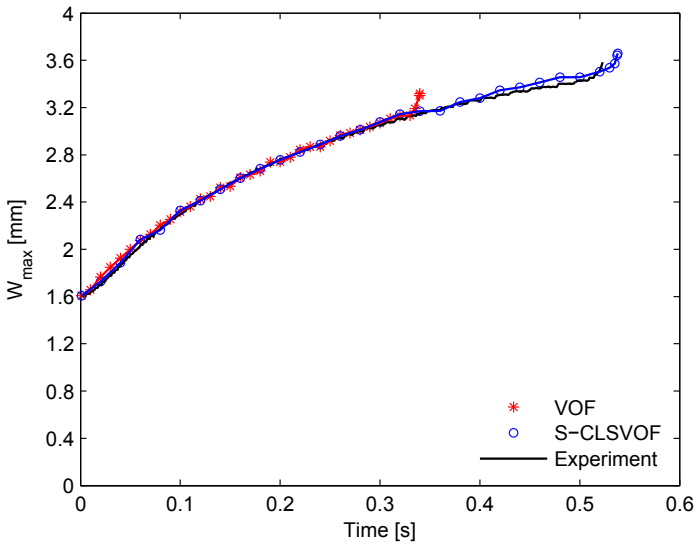

Figure 5.9: Bubble maximum width versus time with $R_o = 0.8$ mm, $\dot{Q} = 200$ mlph.

when the bubble starts elongating in the vertical direction and when the capillary force F_C reaches a maximum (see Fig. 5.6). The imposed static angle which is a constant is generally different from the instantaneous angle which is a flow variable. A large difference between the static and instantaneous angles ensures that the bubble remains pinned to the injection orifice rim as will be discussed in section 5.4 but also increases the magnitude of the numerically induced capillary force. The oscillation observed with the VOF method suggests that spurious currents induced by the surface tension model are thus intensified by the static angle formulation. This is shown to have a severe effect on the accuracy of the VOF model. The improved surface tension modeling of the S-CLSVOF method, however, is also shown to remove the model sensitivity to the static contact angle.

For quasi-static bubble growth (Oguz and Prosperetti, 1993), the bubble detachment volume and center of gravity remain constant regardless of the applied volumetric flow rate. The influence of the flow rate is limited only to the frequency of the bubble formation as increasing the inflow rate leads to bubble detachment at earlier times. However, the flow rate should also affect the very last stages of bubble detachment when gas inertia is known to influence the neck pinching. Fig. 5.11 plots the bubble center of gravity for both VOF and S-CLSVOF methods using the non-dimensional time $t_n = tv_0/R_o$ with the orifice radius of 0.8 mm. It is clear that when using the S-CLSVOF method the bubble center of gravity follows the same trend for all the flow rates contrary to the VOF method. This confirms that the bubble

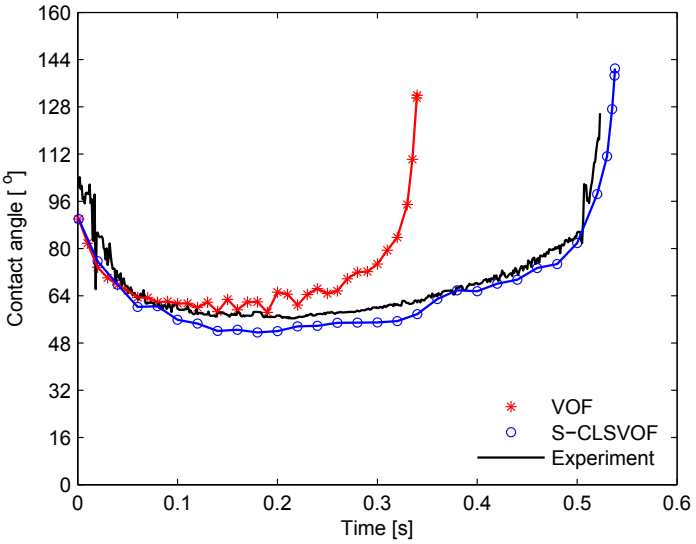

Figure 5.10: Bubble instantaneous contact angle versus time with $R_o = 0.8$ mm, $\dot{Q} = 200$ mlph.

dynamics are well predicted with S-CLSVOF since the bubble CGy history should follow the same trend, conforming to the conditions of quasi-static flow. With the VOF method, the bubble oscillates in the vertical direction before detachment, and the amplitude of these oscillations decreases with increasing flow rate. With the S-CLSVOF method and during detachment, the bubble neck pinch off is shown to be prolonged as the flow rate increases. This behavior is also observed with the experimental data. Compared to the experiments (Fig. 5.8), the S-CLSVOF method is clearly better for predicting the capillary dominant bubble growth than the VOF method at the low volumetric flow rates.

5.3.4 Bubble detachment process

The bubble detachment is characterized by very rapid changes in the bubble shape as the neck forms. The beginning of the neck formation is defined as the time when the bubble minimum radius (R_{neck}), also known as the neck radius, falls below the orifice radius (R_o). The local Weber number ($We_{local} = \rho_l \dot{R}^2_{neck} R_{neck}/\sigma$) at the neck is used to study the influence of the forces acting on the bubble during the detachment where ($\dot{R}_{neck} = dR_{neck}/dt_p$) is the neck radius velocity. Fig. 5.12 shows the logarithmic plot of the bubble neck radius versus the time to pinch-off

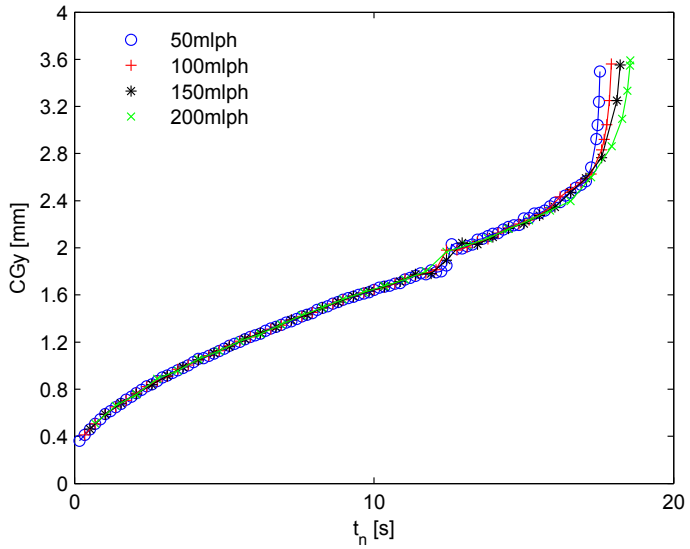

(a)

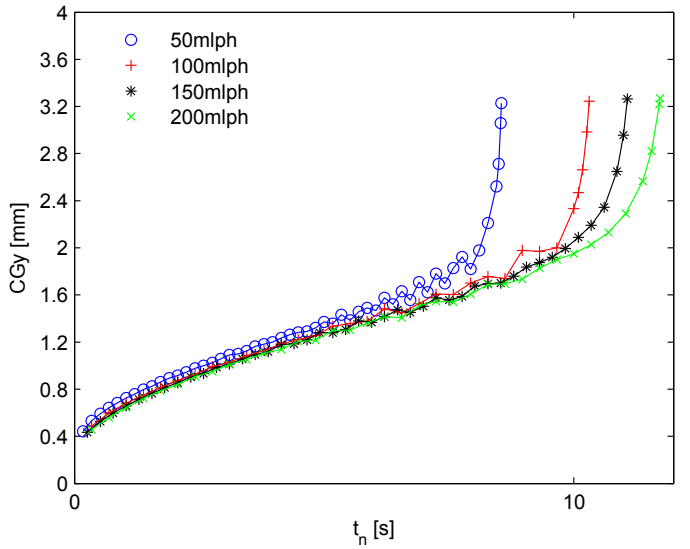

(b)

Figure 5.11: Influence of different orifice flow rates on the bubble center of gravity for (a) S-CLSVOF and (b) VOF methods, $R_o = 0.8$ mm.

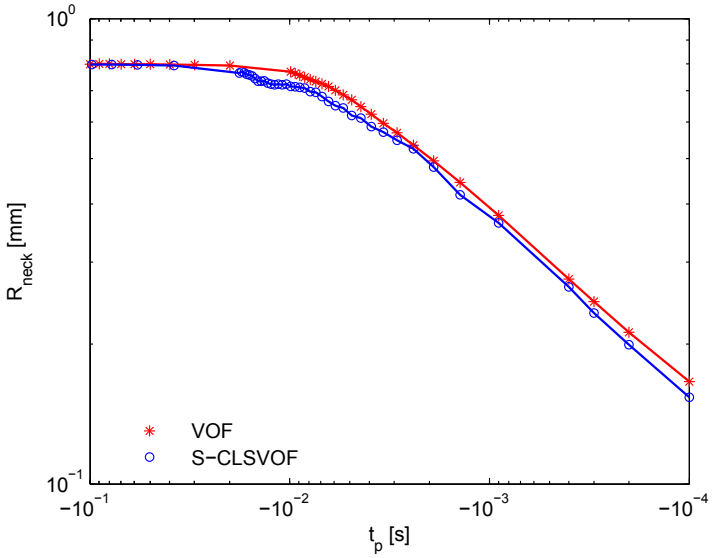

Figure 5.12: Bubble minimum radius, neck radius, during the detachment for the two numerical methods, $R_o = 0.8$ mm, $\dot{Q} = 200$ mlph.

($t_p = t - t_{det}$) for the two numerical methods with $R_o = 0.8$ mm and $\dot{Q} = 200$ mlph. The comparison does not include experimental data in this case as the image capture used could not achieve a frame rate suitable for this analysis. Numerical results however are assessed by reference to published power laws derived from previous experimental studies. It is shown that the time period for the detachment process is of the same order of magnitude for both methods. The two methods give similar trends during the collapse as the radius R_{neck} decreases exponentially at the final stages ($t_p < -10^{-2}$). The local Weber number during this process is of order 1 indicating that this stage is controlled by a balance between the inertial forces and the surface tension forces.

The exponential decrease in the bubble neck radius during the detachment can be described using a power law ($R_{neck} \propto (-t_p)^{\omega}$) where $\omega \sim 0.36$ for both VOF and S-CLSVOF methods. Thoroddsen, Etoh and Takehara (2007) reported from experimental observations that this value is close to 0.5 for bubble growth from nozzle with water/air systems. On the other hand and based on a potential flow model, Gordillo et al. (2005) found that this power varies from 0.5 to 1/3 where the latter case occurs when the gas inertia effect in the neck region is very large. The latter power law is in good agreement with the present results. Fig. 5.13 shows the velocity vector plots at three different stages of the formation process where the

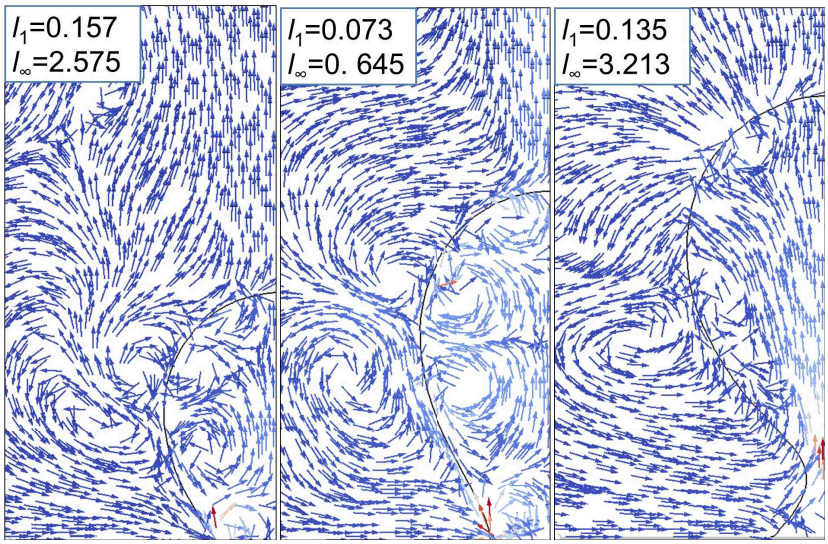

Figure 5.13: Velocity vector plot for S-CLSVOF at three different stages of bubble growth $t/t_{det} \sim 0.4, 0.8, 1$. The scale of the velocity vector is set to off. The color range is from dark blue (minimum velocity) to deep red (maximum velocity). Norms are expressed in (m/s). $R_o = 0.8$ mm, $\dot{Q} = 200$ mlph.

norms l_∞ and l_1 represent the maximum and the average velocity inside the bubble. The intensity of the velocity vector is depicted using a color map in this figure instead of a vector scaling. The existence of large gas velocities inside the neck at detachment ($t/t_{det} \sim 1$) compared to the other stages of bubble growth explains the large increase in the importance of the gas inertial effect during the detachment and, as a result, the value of $\omega \sim 0.36$ obtained. However, the power law may vary under the influence of other parameters such as using co-flowing flow instead of injection from a wall orifice (Chakraborty, Biswas and Ghoshdastidar, 2011). Furthermore, the onset of the detachment process varies based on the physical system such as injection through a needle or bubble in a straining flow (Gekle et al., 2009). To conclude, the analysis of the detachment process confirms that both numerical methods give similar results as the surface tension influence on the bubble dynamics is less significant than the case of the growth stage due to the large increase in the gas inertia effect inside the bubble.

5.4 Influence of contact angle model

In the present section, a static contact angle formulation is defined at the wall orifice and its influence on the bubble geometrical characteristics and detachment parameters is studied. The contact angle is calculated directly after solving the volume fraction advection equation and re-initializing the level set function. It is then corrected to satisfy the user defined static contact angle at the wall boundary. The relation between the experimentally observed contact angle with two different orifice radii (0.5 and 0.8 mm) and the imposed static contact angle on the detachment parameters is considered.

Fig. 5.14 shows the bubble detachment volume and time for two orifice radii (0.5 and 0.8 mm) with the S-CLSVOF method where it is shown that increasing the imposed contact angle above a certain threshold gives larger detachment volumes and later detachment time, confirming observations that were made by Gerlach et al. (2007). The critical value of the static contact angle is shown, however, to vary according to the orifice radius. For radius 0.8 mm, the static contact angle is $\sim 60°$, while it has the value $\sim 50°$ for the smaller orifice radius (0.5 mm).

The dependence of this threshold value on the orifice is explained by reference to the experimental observations of the bubble instantaneous contact angle during the growth (Fig. 5.10 for radius 0.8 mm and Fig. 5.15 for radius 0.5 mm). It has been found that during the formation process, the experimental bubble takes a minimum instantaneous contact angle of 58.33° for the orifice radius (0.8 mm), while this angle decreases to 48.45° for the orifice radius (0.5 mm). Fig. 5.16 combines the minimum contact angle observed experimentally [present work, (Di Bari and Robinson, 2013; Vafaei et al., 2010)], estimated numerically (Di Bari, 2011), and calculated by Capillary equation [(Lesage, 2012; Gerlach et al., 2005)] along with the threshold contact angles estimated numerically. It is apparent that the numerical threshold corresponds to the minimum contact angle observed experimentally. This confirms that the numerical predictions of the bubble detachment parameters can be within a 3% error (as shown in Table 5.10) as long as the static contact angle used as a boundary condition in the numerical formulation is less than that of the minimum instantaneous angle observed experimentally. Further increase in the static contact angle gives larger detachment characteristics. This increase is attributed to the changes in the bubble base radius during the growth. Fig. 5.15b shows the time evolution of the bubble minimum radius for orifice radius 0.5 mm and flow rate 200 mlph. It is clear that the numerical bubble follows the same trend as the

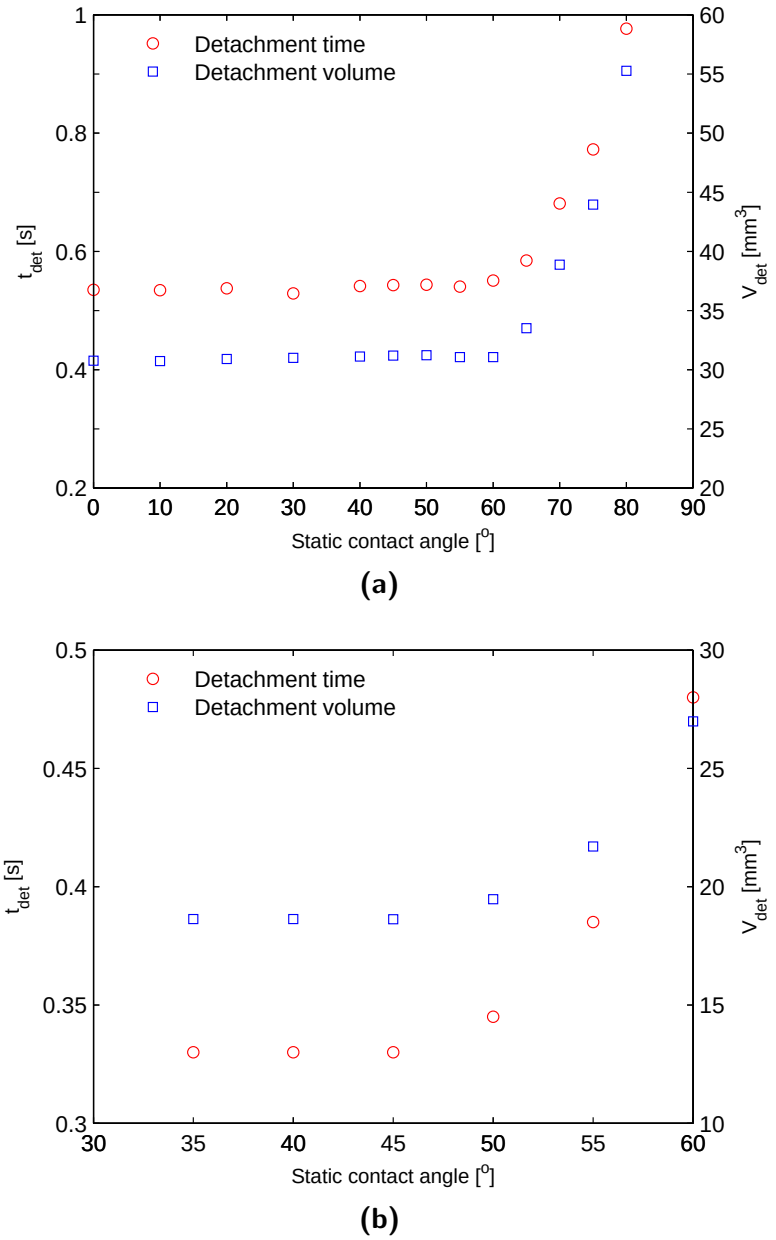

Figure 5.14: Influence of static contact angle on bubble detachment time and volume for S-CLSVOF method with orifice radii (a) 0.8 mm and (b) 0.5 mm, $\dot{Q} = 200$ mlph.

experimental measurements when using small static contact angles. For larger values of (θ_s), the bubble spreads quickly on the wall leading to later detachment with a relative difference of about 44% when using the static contact angle of 60°. The bubble interface spreading is due to the imposed static angle which encourages the bubble boundary to move away from the orifice rim. Fig. 5.15a shows that the instantaneous contact angle decreases linearly during the growth when using static angles above the threshold 48.45° for the orifice radius (0.5 mm).

The static contact angle corrects the gas/liquid interface in the cells adjacent to the wall. This leads to large velocities in the local gas region as the corrected bubble interface normal at the first cell is different than the calculated normal in the other neighboring cells (see Fig. 5.13). This large velocity is thought to be the reason for the jump in the bubble center of gravity at the beginning of the neck formation (Fig. 5.8). To avoid this issue, different strategies may be followed such as imposing a liquid film at the wall which prevents the bubble from spreading without any constraints to the bubble contact angle, or using a dynamic contact angle model as in Chen, Mertz and Kulenovic (2009) which may require mesh refinement at the wall. In other studies, the bubble growth process with an interface pinned at the rim has been achieved by using a co-flowing principal with zero liquid velocity (Chakraborty, Biswas and Ghoshdastidar, 2011) or by using a nozzle instead of a wall orifice (Quan and Hua, 2008). To conclude, a strong influence of the contact angle on the bubble formation process is found when using static angles larger than the minimum instantaneous contact angle observed experimentally. The minimum value itself varies according to the orifice radius as it decreases with decreasing the orifice radius.

5.5 Three-dimensional bubble growth

The numerical simulations of bubble growth using the coupled S-CLSVOF solver have also been validated for a three-dimensional domain. The main purpose of this section is to compare the 3D simulations against axi-symmetrical results. The detached bubble using the present 3D data will be used in the next chapter as a pre-initial condition for the 3D bouncing process. The bubble is injected from an orifice ($R_o = 0.5$ mm) centered at the lower wall. A schematic sketch of the 3D numerical domain with the corresponding boundary conditions is illustrated in Fig. E.3. The numerical mesh is made of multi-block orthogonal Hexahedral volume cells using

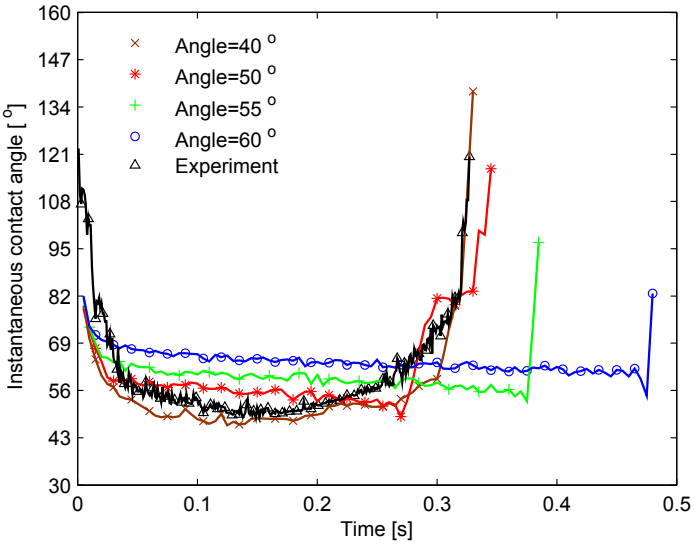

(a)

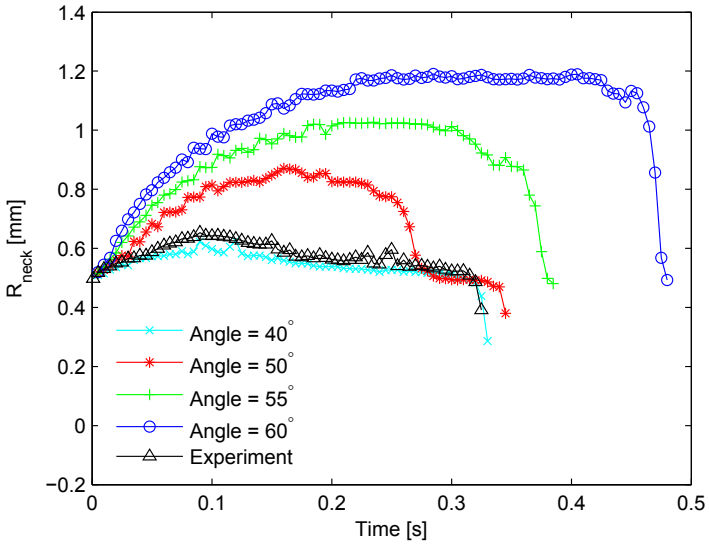

(b)

Figure 5.15: (a) Bubble instantaneous contact angle and (b) base radius using S-CLSVOF method with different static contact angles with $R_o = 0.5$ mm and $\dot{Q} = 200$ mlph.

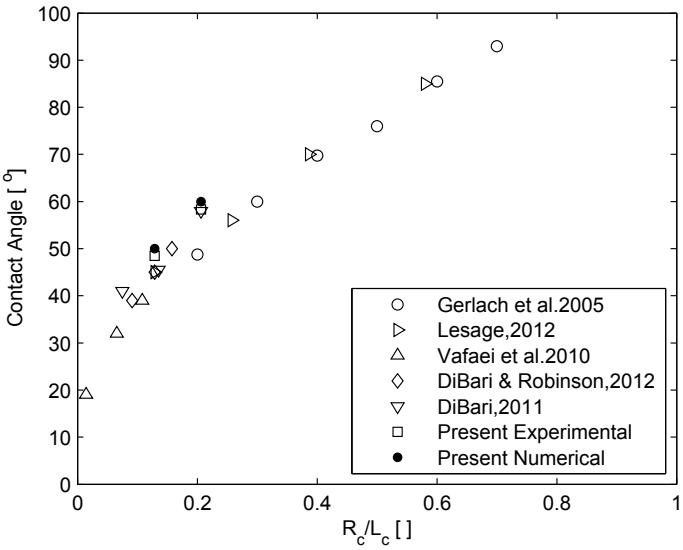

Figure 5.16: Variations of the Minimum instantaneous contact angle observed experimentally and the numerical contact angle threshold with the non-dimensional radius R_c/L_c, where $L_c = \sqrt{2\sigma/g(\rho_l - \rho_g)}$ and the capillary radius is $R_c = R_o$ in this plot.

ANSYS-ICEM meshing tool (Ansys, 2011). The height of the numerical domain is decomposed into several blocks (1, 2, or 3 blocks) of minimum height 10 mm for each block. This accelerates the simulation execution time as the lower block, where the bubble is generated, is discretized using a fine mesh to capture accurately the formation process while the upper blocks are discretized using coarser meshes. For the bubble growth data presented here, the height of the domain considered is 10 mm. More blocks can be used in future works to investigate the influence of the rig dimensions on the bouncing process. The gas is injected with an inflow velocity ($v_0 = 0.05$ m/s) at the bottom of a narrow throat of height 2 mm. This height is chosen so that the injected gas inside the bubble satisfies the fully developed laminar flow.

A sequence of snapshots of the bubble interface during the full formation process until detachment is presented in Figs. 5.17 and 5.18 for both S-CLSVOF and VOF methods, respectively. The bubble contours are represented in the (x-z) plane. The gravitational direction corresponds to the z-coordinate in these figures. The snapshots in the perpendicular plane (y-z) are presented in Figs. E.1 and E.2 in Appendix E. Both interface capturing methods are found to predict the same behavior by comparison to the experimental results (See Fig. 4.2). Similarly to the axisymmetrical case, the bubble detaches at a later time with the S-CLSVOF method

(t_{det} = 0.47 s) than the VOF method (t_{det} = 0.4 s). Contrary to S-CLSVOF, the VOF results exhibit large oscillations during the formation process. This is evidenced in the snapshots displayed in (y-z) plane (Fig. E.2). These oscillations happen in both vertical and lateral directions during the bubble growth. Their amplitude increases towards the later stage of detachment process. The lateral oscillations did not occur during the axi-symmetrical simulations due to the imposed symmetric boundary condition.

A quantitative comparison between the axi-symmetrical and 3D results is displayed in Fig. 5.19 for the bubble center of gravity in the vertical direction. There is no experimental data shown in this figure. However, a record of the bubble detachment volume is available. With the VOF method, the numerical data with axi-symmetrical domain provide earlier detachment time compared to the 3D results. The bubble oscillation with VOF (3D) results is clearly shown in this figure. In contrast, the numerical results with S-CLSVOF removes the oscillation regardless of the type of the numerical domain. The effect of the VOF boundary condition on the lower wall is also investigated by setting a fixed value ($\alpha = 1$) instead of a static contact angle ($\theta_s = 20$). These results are also displayed in Fig. 5.19 (they are denoted with the symbol F). The effect of the fixed boundary condition on the growth trend is shown to be minimal. However, the bubble detaches at a later time with the fixed value boundary condition.

Results for the bubble detachment volume and the corresponding detachment radius are illustrated in Table 5.11 for the orifice radius R_o = 0.5 mm with both axi-symmetrical and 3D domains. For both interface capturing methods, the bubble detaches with larger volume with the 3D domain compared to the axi-symmetrical domain, but this difference is much smaller with the S-CLSVOF method with an error in the detachment radius which is approximately 4 %. This is equivalent to a distance 0.07 mm which is less than the numerical mesh step size. Similar results are obtained with the S-CLSVOF method for different rig heights as displayed in Table E.1 in Appendix E.

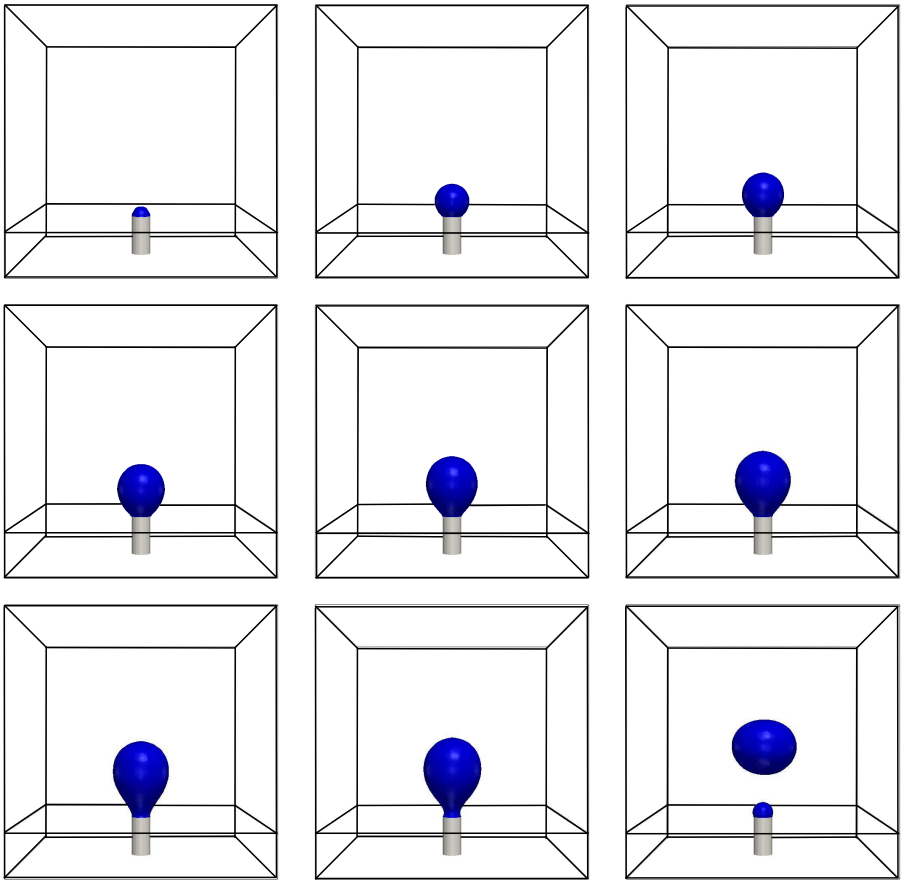

Figure 5.17: Sequence of screen shots in the (x-z) plane illustrating bubble growth from a wall orifice ($R_o = 0.5$ mm) using S-CLSVOF method with inflow velocity 0.05 m/s. The (z) coordinate indicates the direction of the gravitational acceleration. The frames are arranged from top left to bottom right with times $0, 0.08, 0.16, 0.24, 0.32, 0.4, 0.44, 0.46, 0.48$ s, respectively.

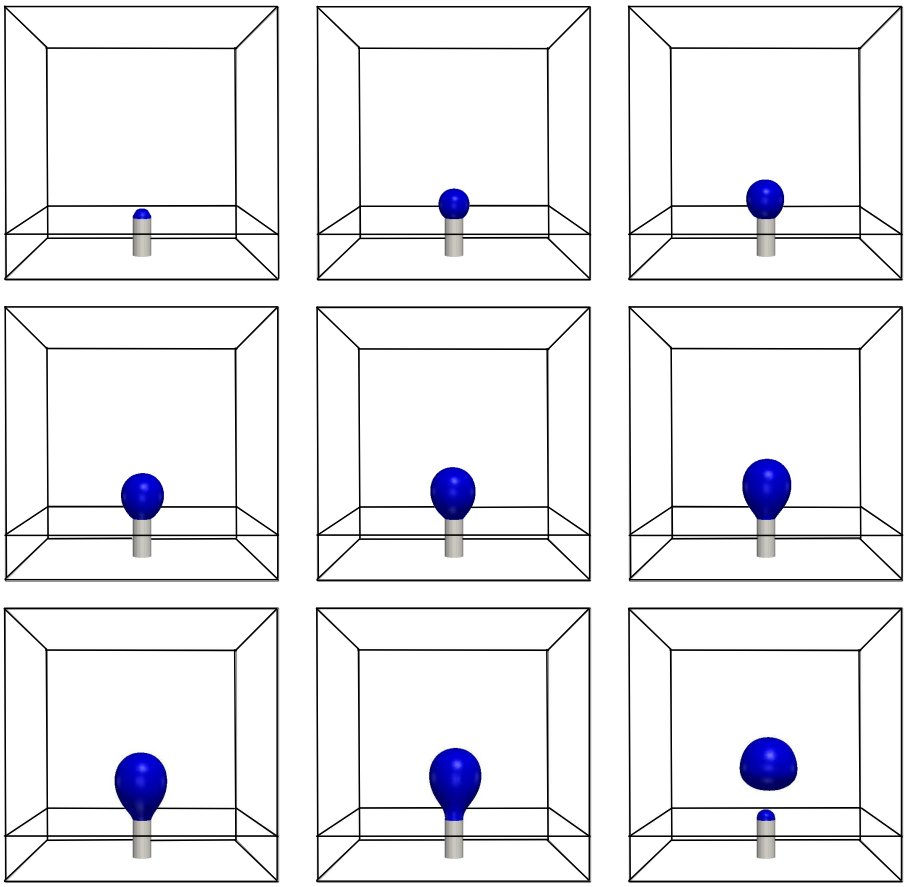

Figure 5.18: Sequence of screen shots in the (x-z) plane illustrating bubble growth from a wall orifice ($R_o = 0.5$ mm) using VOF method with inflow velocity 0.05 m/s. The (z) coordinate indicates the direction of the gravitational acceleration. The frames are arranged from top left to bottom right with times $0, 0.06, 0.12, 0.18, 0.24, 0.3, 0.36, 0.38, 0.4$ s, respectively.

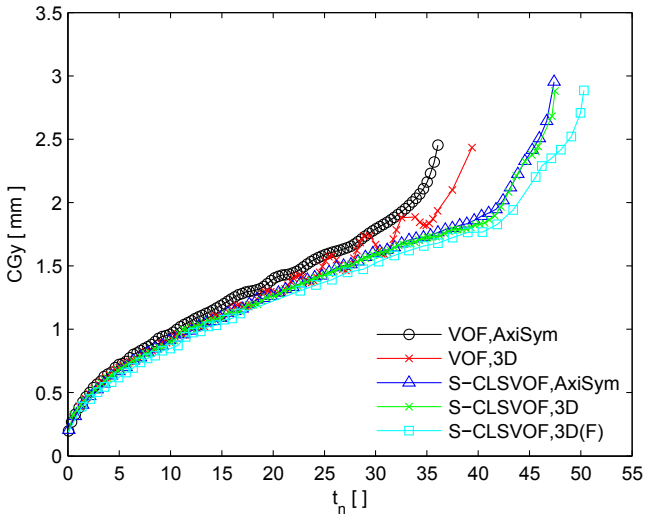

Figure 5.19: Comparison of the bubble center of gravity in the gravitational direction versus the non-dimensional time for both 3D and Axi-Symmetrical numerical domains. The numerical results are obtained using both VOF and S-CLSVOF methods with $R_o = 0.5$ mm. The symbol (F) here stands for Fixed BC for VOF function.

Table 5.11: Comparison of bubble detachment volume and radius using both 3D and axi-symmetrical domains. The numerical results are obtained with both VOF and S-CLSVOF, $R_o = 0.5$ mm.

	V_{det} [mm^3]	R_{det} [mm]	$E_{R_{det}}$ [%]
Exp	21.688	1.729	-
S-CLSVOF,3D	19.4023	1.667	3.643
VOF,3D	15.629	1.551	10.346
S-CLSVOF, AxiSym	18.948	1.654	4.402
VOF, AxiSym	15.052	1.532	11.463
S-CLSVOF,3D(F)	21.146	1.715	0.840

5.6 Discussion and final remarks

Several conclusions and remarks can be drawn on the accuracy and efficiency of the two interface capturing techniques studied here; For circular bubble at equilibrium, the spurious currents are reduced by one order of magnitude compared to the original VOF method. However, reducing the mesh did not decrease the intensity of these

spurious currents.

The main advantage of the coupled technique is highlighted when studying the bubble growth process as the coupled S-CLSVOF method provides a significant improvement compared to the VOF method. The numerical results in this case are in a good agreement with the experimental data. The enhanced accuracy arises from the fact the surface tension source force is represented more accurately using the Level Set function rather than the VOF function. During the detachment process, the influence of the gas inertia increases inside the neck region leading to a balance between the inertia and the capillary effects during this stage. The influence of the surface tension implementation becomes smaller and both interface capturing methods provide very close results. Similar observations can be drawn from the analysis of the free bubble rise. However, the bubble rise process examined here uses spherical and ellipsoidal bubbles where the topological changes remain modest compared to the skirted bubbles.

Despite the improvement of the numerical results with the S-CLSVOF method, the VOF simulations are $\sim 3/2$ times faster than the coupled S-CLSVOF method for axi-symmetrical bubble growth using the same number of processors and virtual machines for the solution (with S-CLSVOF, the computational time using 8 processors is approximately 36 h). For the 3D formation process, larger number of processors has been used for the solution (up to 32 processors). Nevertheless, the computational time has increased up to 7 days for bubble growth simulations. The difference in the computational time between S-CLSVOF and VOF is due to the re-initialization process performed during the time loop of the S-CLSVOF method. Furthermore, the coupled code requires more complicated techniques for implementing the contact angle boundary condition at the solid walls as both VOF and LS functions should be corrected after applying the imposed contact angle. However, this method is still faster than the geometrical CLSVOF method analyzed in the previous chapter, and the coupled code is mass conservative due to the advection of the VOF function. The reinitialization process adds extra numerical parameters (such as ε and ϕ_{corr}) to the algebraic VOF method. These parameters should be adjusted properly in order to obtain accurate numerical results. The estimation of the interface thickness ε across which the interface spreads introduces another complexity in the coupled code. This issue arises when using non-regular mesh as the interface thickness takes different values based on the mesh resolution. This issue was not addressed in the present work which considered regular meshes around the bubble during the growth.

To conclude on the results of the 3D bubble growth, the coupled S-CLSVOF method with a 3D domain provides results that compare quite well with the formation process using axi-symmetrical domain. With the VOF method, although the 3D bubble detaches at times which are very close to those predicted by the axi-symmetrical solver, the bubble evidences large oscillations in both vertical and lateral directions. As shown in the literature (Ohta et al., 2005; Tomiyama et al., 2002), these oscillations affect strongly the mechanism of bubble rise, especially the bubble trajectory. Increasing the inflow flow rate was found to decrease the amplitude of the bubble oscillations. This is due to the increased relative importance of gas inertia compared to surface tension stresses. However, the large values of the inflow flow rate would lead to bubble formation under the dynamic regime where the detached bubbles from the orifice are not isolated. This flow regime is not the scope of the present study.

In the next chapter, the bubble collision against solid surface will be examined using the algebraic VOF method. The aim of the study will be to investigate whether the algebraic VOF is capable of modeling accurately studying the bouncing process. This study will focus on the VOF solver alone to assess its sensitivity to the mesh resolution towards the solid boundary when the bubble interacts directly with the surface. A dynamic contact angle model will also be implemented and tested using the simple VOF method as a primary step to avoid the complexity arising with the numerical parameters of the coupled S-CLSVOF code.

6 Results and discussion: Bubble bouncing analysis

In the present chapter, the suitability of the algebraic VOF interface capturing method and the contact line models to correctly capture the mechanism of air bubble impacting on and bouncing from a solid surface is studied. The VOF method is coupled with a mesh refinement technique and contact line boundary condition in order to check the influence of the mesh resolution and the contact angle model on the bouncing process. It is clear from the literature that the VOF method is commonly used to study the interaction between gas/liquid interfaces and solid surfaces (Dupont and Legendre, 2010; Afkhami, Zaleski and Bussmann, 2009; Renardy, Renardy and Li, 2001). This can be partly explained by the fact that the coupling of the contact angle models with the VOF method is relatively simple compared to other interface capturing techniques. Besides, the VOF method allows for implicitly slipping interfaces along the solid surface. In contrast, the LS method requires special treatment for the interface correction at the solid boundaries in order to allow the contact line slipping on that surface. Furthermore, an interface correction is required after each pseudo-iteration in the re-initialization process (Spelt, 2005). This includes determining the interface position at each sub-stepping loop in order to calculate the slip velocity and the contact angle. The interface correction during the re-initialization in LS might lead to loss of mass (volume) inside the bubble/-drop. This, in general, makes the LS method more computationally expensive and less accurate compared to the VOF method for the study of bubble bouncing. Although the S-CLSVOF method presents more accurate results compared to the VOF method for capillary dominant problems, it includes several numerical parameters that are related to the mesh step size such as the interface thickness (ε). This makes the study of the influence of the mesh resolution on the bouncing mechanism less straightforward.

The main objective in this chapter is to assess whether the VOF method is suit-

able for the study of problems related to the wetting dynamics (bubble bouncing) similarly to the cases with free boundaries (bubble rise). This includes investigating the method's capability to model the spatio-temporal characteristics of the liquid film formation and drainage as well as studying the pressure distribution and its effect on the bubble dynamics. The 3D mechanisms of bubble bouncing (approach, collision, film formation, and contact line formation) on a horizontal surface are analyzed by solving the full Navier Stokes equations coupled with the compressive VOF method implemented in the open source solver library (OpenFOAM-2.1®). The analysis aims to answer the following points:

- clarify the importance of the mesh resolution in the neighboring cells to the solid plate on the bouncing mechanism by comparing modeled bubble and film characteristics with experimental results.
- quantitatively describe the film formation process and the variations in the film thickness.
- analyze the pressure distribution and flow velocity field in the film region in order to explain the damping reasons during the bouncing.
- study the influence of the contact line models on the bubble dynamics at the last stages of the bouncing process.

Axi-symmetrical results are assessed against experimental data available in the literature (Kosior, Zawala and Malysa, 2012; Zenit and Legendre, 2009). For validating the 3D simulations, the experimental data performed by the collaborating team in Trinity College Dublin are employed. The main structure of this chapter is described as follows: The numerical set-up of the domain and the mesh resolution are explained first. The free bubble rise is studied to provide the correct pre-initial conditions for the bouncing process. Then, the influence of the mesh resolution on the capture of the film formation and the correct bouncing mechanism is studied. The validated mesh is then used to assess the 3D numerical simulations. Next, the film formation and drainage are analyzed and compared against published correlations. Finally, the influence of both static and dynamic contact angle models on the last stages of bouncing is investigated.

6.1 Problem setup

6.1.1 Numerical domain and grid

The present chapter considers single gas bubbles rising freely in a quiescent liquid column before impacting and bouncing on a horizontal solid surface. The bubble is initially positioned at a distance $1.5D_{eq}$ from the bottom wall of the numerical domain where D_{eq} is the bubble equivalent diameter. The physical properties of the bulk liquid, gas phase, surface property through the equilibrium contact angle and the bubble characteristics are shown in Table 6.1. Different fluid and flow conditions are considered for comparison against experimental data from a range of published and new studies. The problem is studied using a wedge-like axi-symmetrical domain as sketched in Fig. 6.1 when appropriate and a 3D model in cases where the bubble trajectory is found to deviate from the vertical direction at any stage of the rise or bounce . The validation cases selected involve Reynolds ($Re = \rho_l D_{eq} V_\infty / \mu_l$), Weber ($\rho_l D_{eq} V_\infty^2 / \sigma$), and Capillary ($Ca = V_\infty \mu_l / \sigma$) numbers in the range $(202 - 830.5)$, $(2.13 - 3.69)$ and (0.004-0.0156), respectively. As confirmed by the bubble shape regime map produced by Bhaga and Weber (1981), the terminal bubble shape before impact is oblate ellipsoidal in all cases. The solid surfaces used are all hydrophilic satisfying equilibrium contact angles measured on the side of liquid phase always lower than 90°.

Table 6.1: Fluid physical properties and surface and bubble characteristics.

Parameter	Unit	Air	Water	Fluid A
Density	kg/m^3	1.225	998.2	1087
Viscosity	kg/m.s	1.79×10^{-5}	0.001	0.0038
Surface tension	N/m	-	0.072	0.0697
Gravity	m/s^2	9.81	9.81	9.81
Equivalent diameter	mm	-	1.48, 2.6,3.3	2.62
contact angle	°	-	0, 24	30
Morton number ($g\mu_l^4/\rho_l\sigma^3$)	-	-	2.63×10^{-11}	5.56×10^{-9}
Bond number ($\rho_l g D_{eq}^2/\sigma$)	-	-	0.298-1.48	1.05

The width of the numerical domain is defined in terms of the bubble equivalent diameter according to ($width = 8D_{eq}$) to avoid any confinement effects (Mukun-

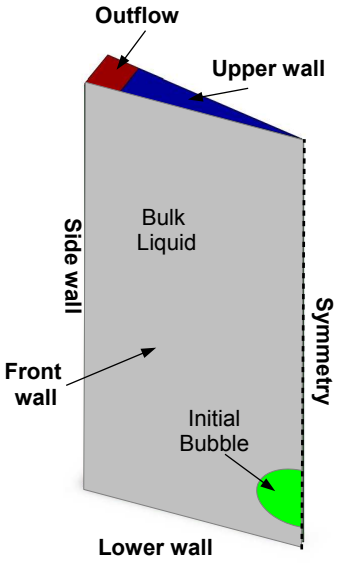

Figure 6.1: Schematic diagram of the numerical domain and the boundary conditions for axi-symmetrical simulations.

dakrishnan et al., 2007). This criterion is broadly in line with other free rise studies as summarized in Table 6.2. A height of 30 mm was used in most models. This ensures that the bubble reaches its terminal shape and velocity before collision but also corresponds to the height adopted in the experimental work of Kosior, Zawala and Malysa (2012) and Zenit and Legendre (2009) which are employed in the present study for benchmarking purposes. The height was reduced to 10 mm in the 3D simulations to keep the computational time within practical limit. The bubble does not reach its terminal velocity in this case and an experimental rig was adapted accordingly.

Table 6.2: Review of numerical domain width from recent free bubble rise studies.

Authors	Numerical Method	Rig width to bubble diameter ratio
Mukundakrishnan et al. (2007)	Front Tracking Method	8
Bonometti and Magnaudet (2007)	Volume of Fluid	5
Ansari and Nimvari (2011)	Level Set	3-4
Kumar and Delauré (2012)	Volume of Fluid	8
Ohta and Sussman (2012)	Sharp interface method	5
Chakraborty, Biswas and Ghoshdastidar (2013)	Coupled CLSVOF	8
Shu and Yang (2013)	Lattice Boltzmann	5

The domain is meshed using orthogonal and uniform cells of constant size Δx. In the axi-symmetrical domain, Δx is the radial width and height of the square cell section. In the 3D domain the cell depth is also uniform and equal to Δx as well. Results from a mesh convergence analysis of the bubble terminal velocity and shape (Aspect ratio) are reported in Table 6.3 for $D_{eq} = 1.48$ mm and the air/water mixture, and Table 6.4 for $D_{eq} = 2.62$ mm and the air/fluid A mixture. The relative difference between successively refined grids is calculated with reference to the finer mesh. For the aspect ratio, for instance, this relative difference between grids Δx and $\Delta x/2$ is defined by $E_{AR} = 100 \times (AR_{\Delta x} - AR_{\Delta x/2})/AR_{\Delta x}$. The mesh size to time step ratio was fixed to $\Delta x/\Delta t = 0.1$. This condition gave bubble terminal characteristics similar to those achieved with an adaptive time step based on a Courant number ($Co = 0.25$). In all cases, improvements in the relative difference is lower than 2%, when the mesh is refined to a bubble diameter to cell size ratio in the range $52 - 59$ from $25 - 30$. The discretization of between 25 to 30 cells per bubble diameter is used thereafter.

Table 6.3: Mesh convergence analysis of bubble in free rise with $D_{eq} = 1.48$ mm and air/water mixture.

Δx [mm]	NB of cells/diameter	V_∞ [mm/s]	AR [-]	E_{v_∞}[%]	E_{AR}[%]
0.2	7.4	156.4	1.242	-	-
0.1	14.8	299.06	1.344	47.702	7.589
0.05	29.6	322.03	1.4	7.132	4
0.025	59.2	315.822	1.39	-1.965	-0.719

Table 6.4: Mesh convergence analysis of bubble in free rise with $D_{eq} = 2.62$ mm and air/fluid A.

Δx [mm]	NB of cells/diameter	V_∞ [mm/s]	AR [-]	E_{v_∞}[%]	E_AR[%]
0.2	13.1	247.6	1.507	-	-
0.1	26.2	271.4	1.657	8.77	9.052
0.05	52.4	271.6	1.691	0.07	2.010

6.1.2 Boundary Conditions and Boundary Mesh Treatment

The boundary conditions for the axi-symmetrical domain are shown in Fig. 6.1. At the lower and side walls, no slip boundary condition is applied. Uniform and constant atmospheric pressure is set over the outlet surface. At the upper wall, the contact angle boundary condition is applied. It becomes effective as a portion of the bubbles interface enters the wall adjacent cell and can force the TPCL to form sooner than physically justified. Accurate modeling of the liquid film formation between the approaching bubble and the solid surface can have a thickness approaching 2.7μm (Krasowska, Krzan and Malysa, 2003) for $D_{eq} = 0.14$ mm in an air/water mixture. The implication for mesh requirements is obvious. Therefore, even though an orthogonal and uniform mesh is used everywhere else in the computational domain, the effect of mesh refinement at solid surfaces is also studied. Two different meshes will be considered (i) the Regular mesh without refinement and (ii) the Refined mesh where the wall adjacent cells are subdivided into 10 cells in the direction perpendicular to the wall with a min/max cell thickness ratio of 0.1 (See Fig. 6.2). This produces a wall adjacent cell with minimum thickness $\Delta x_{min} = 1.2\mu$m and an average growth ratio between successive refined cells of 1.29.

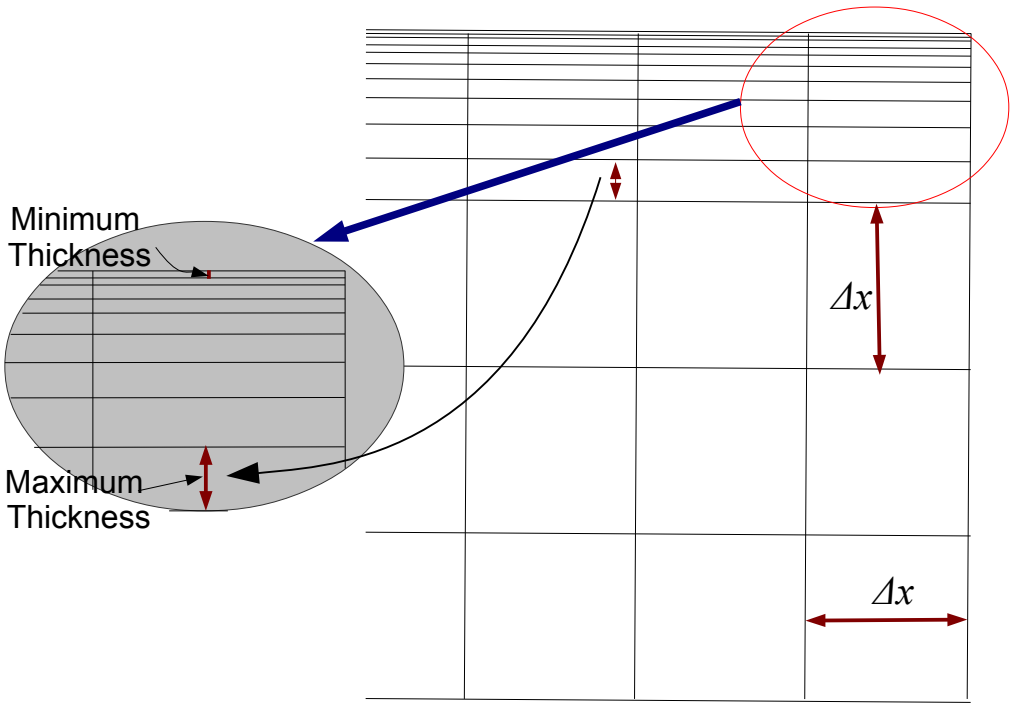

Figure 6.2: A schematic diagram of the mesh subdivision in the Refined case at the upper wall boundary.

6.2 Preliminary setup: Free bubble rise

The geometrical properties, terminal shapes, path trajectories, and wakes generated by gas bubbles in free rise in liquids covering a wide range of Morton numbers for both pure and contaminated systems have already been extensively studied experimentally (Fan and Tsuchiya, 1990; Bhaga and Weber, 1981; Clift, Grace and Weber, 1978; Saffman, 1956) and numerically with a range of two fluid flow methods [Front tracking (Hua and Lou, 2007); Lattice Boltzmann (Amaya-Bower and Lee, 2010); VOF (Annaland, Deen and Kuipers, 2005); Level Set (Sussman et al., 1998); sharp interface (Ohta and Sussman, 2012)]. It is not the main focus of the present chapter, but accurate free rise modeling is essential to achieve the correct pre-impact conditions and to allow comparison against benchmark data.

This initial free rise validation focuses on the bubble terminal velocity (V_∞) and aspect ratio (AR). Predictions for bubble rise in a clean water (no surfactant contamination) are compared in Fig. 6.3 against experimental data from a number of published studies. Furthermore, the bubble terminal aspect ratio is compared against the empirical correlation ($AR = 1/(1 - (9/64)We)$) proposed by Legendre, Zenit and Velez-Cordero (2012) for water systems with aspect ratios less than three. The present numerical results involve the two bulk liquids (water and fluid A) and the four bubble diameters ranging from 1 mm to 2.46 mm listed in Table 6.1. The experimental data of Zedníková, Vobecká and Vejrazka (2010) shows a scattering around the curve obtained from Moore correlation. This was attributed by the author to differences in the bulk liquid temperature between experiments. The numerical results compare well with the Moore correlation (Moore, 1965) and are within a reasonable uncertainty range of other experimental data (particularly given the relatively large variability between data at similar flow conditions).

Errors in the bubble terminal velocity and aspect ratio calculated with respect to selected experimental data are shown in Table 6.5. For a bubble diameter of 1.48 mm, the numerical simulations provide bubble terminal velocities with relative errors of 6.8% and 2.6% compared to results provided by Kosior, Zawala and Malysa (2012) and the Moore correlation. Similar error levels are found for bubble diameter 2.46 mm and the air/fluid A mixture. The numerical simulations appears to overpredict the terminal velocity for bubble diameter 1.58 mm by comparison to data from Tsao and Koch (1997). In this case, however, the influence of impurities in the liquid used in the experiments can explain the lower bubble terminal velocity. The accumulation of contaminants at the bubble surface can reduce the interface

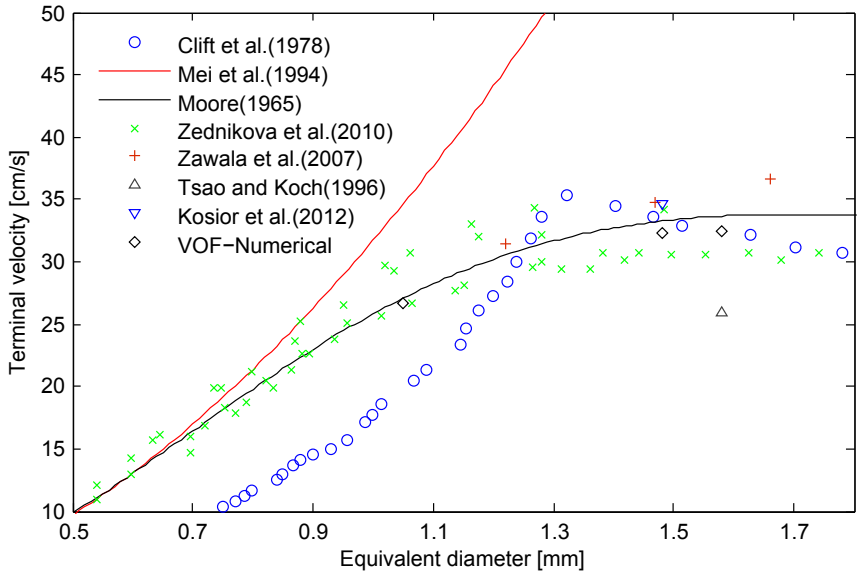

Figure 6.3: A comparison of the bubble terminal velocity from different experimental, empirical, and numerical data.

mobility and increase drag (Malysa, Krasowska and Krzan, 2005). The numerical predictions of the bubble aspect ratio are shown to produce larger relative errors ranging from 15% to 7.8% when compared with experimental data although this is reduced to 2% when compared with the empirical values AR_{emp} calculated from the correlation proposed by Legendre, Zenit and Velez-Cordero (2012).

Table 6.5: Comparison of the bubble terminal velocity and aspect ratio obtained numerically with other benchmarking experimental data.

Bubble diameter [mm]	Method	V_∞ [mm/s]	AR[-]	E_{V_∞} [%]	E_{AR} [%]	AR_{emp}	$E_{AR_{emp}}$[%]
1.48	Numerical	322.4	1.401	-	-	1.428	1.891
	Kosior et al. (2012)	346	1.65	6.821	15.091	1.527	-8.055
	Moore (1965)	331		2.598			
1.58	Numerical	323.6	1.475	-	-	1.476	0.068
	Tsao and Koch (1997)	260	1.6	-24.461	7.812	1.26	-21.25
	Moore (1965)	336		3.690			
2.46	Numerical	271.6	1.691	-	-	1.66	-1.867
	Zenit and Legendre (2009)	287.1	1.63	5.398	-3.742	1.8	9.444

For $D_{eq} = 1.48$ mm and air/water mixture, the bubble has also been tested in 3D primarily to test the validity of the axi-symmetrical assumption. Results produced relative differences in the bubble terminal velocity and aspect ratio equal to

0.1% and 2%, respectively. The model also confirmed the predominantly rectilinear characteristic of the rise trajectory (with a deviation from the centerline lower than 0.02 mm). For the air/fluid A mixture and $D_{eq} = 2.62$ mm, similar conclusions where confirmed by Zenit and Legendre (2009).

6.3 Mechanism of bubble bouncing

A brief description of the bubble impact and bounce is given here before assessing the solution accuracy. A sequence of the bubble interface defined as the iso-contour plot of $\alpha = 0.5$ is given in Fig. 6.4 to illustrate a typical interaction sequence between the bubble and the solid surface during the first bounce cycle. These results were obtained with a Refined mesh for the air/water mixture with $D_{eq} = 1.48$ mm. At the initial stage (Frames 1-3), the bubble approaches the wall with its terminal velocity and shape and is still unaffected by the upper boundary. At a distance $1.5D_{eq}$ (Frame 4), the bubble begins to decelerate before flattening rapidly under the combined effect of buoyancy and increasing forward pressure (Frame 5-6). As the bubble continues to approach the wall (Frame 7-8), a thin liquid film forms between the bubble and the wall. The bubble velocity continues to decrease rapidly down to zero at which point the bubble has reached its maximum deformation. The bubble kinetic energy has then been transfered to surface deformation energy. Under current conditions, no direct contact forms between the air inside the bubble and the solid surface so that the liquid film does not break and no triple contact line exists. The restitution process begins when the bubble starts to rebound creating a cusped tail shape (Frame 9). This tail forms as the liquid film expands and eventually disappears as the bubble moves away from the wall (Frame 10-13). The filling in of the liquid film increases rapidly generating pressure fluctuations which manifest themselves as large oscillations in the bubble interface. The bubble recovers its spherical shape as its velocity decreases back to zero once again (Frame 14-17). At this stage, the bubble resumes its upward motion starting the second bouncing cycle. The number of rebounds varies with the fluid and flow properties but also the solid surface properties which will dictate whether a TPCL forms or whether a liquid film stabilizes. Qualitatively similar behaviors have been observed experimentally with air/water mixtures (Tsao and Koch, 1997) and heavier liquids (Zenit and Legendre, 2009; Legendre, Daniel and Guiraud, 2005).

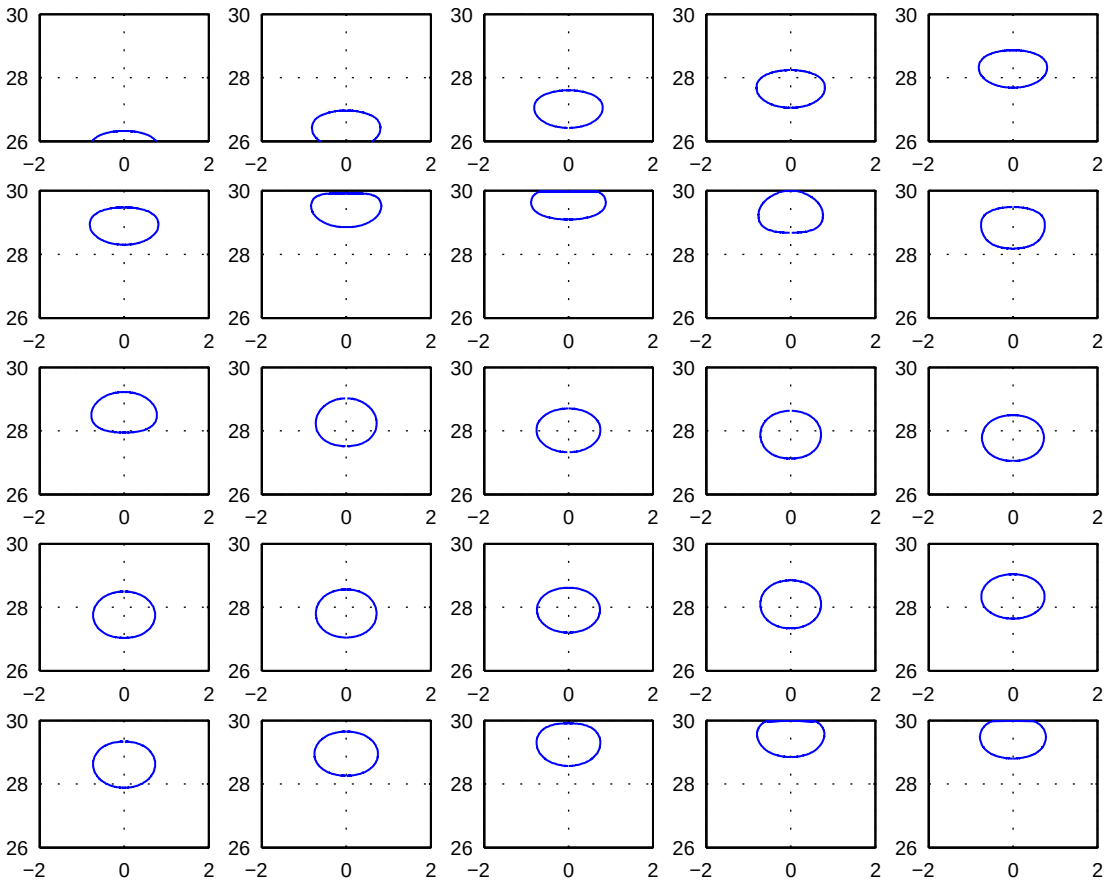

Figure 6.4: Bubble interface shown as iso-contour of $\alpha = 0.5$ during the first bouncing cycle. The sequence starts at top left (Frame 1) and progress to the bottom right (Frame 25) at intervals of 0.002 s. The computations were for the air/water mixture with $D_{eq} = 1.48$mm and the Refined mesh.

6.4 Numerical modeling Validation

The main purpose of this validation is to determine the importance of correctly resolving the liquid film and modeling its influence on the bubble dynamics. Two main test cases are considered to account for the effect of hydrophilic surfaces of varying strength. Flow conditions in these cases justify the use of an axi-symmetrical model and one additional test is included to consider full 3D conditions.

6.4.1 Influence of Mesh Refinement

The influence of the mesh resolution in the region immediately adjacent to the upper wall is assessed against experimental data from Kosior, Zawala and Malysa (2012) and Zenit and Legendre (2009). The two cases are characterized by:

- Case I; (Zenit and Legendre, 2009): Mixture of air and Fluid A with a bubble of diameter $D_{eq} = 2.62$ mm and an equilibirum contact angle $\theta_e = 30°$.
- Case II; (Kosior, Zawala and Malysa, 2012): Mixture of air and water with a bubble of diameter $D_{eq} = 1.48$ mm and an equilibirum contact angle $\theta_e = 0°$.

The fundamental difference between the two cases relates to the liquid film behavior. With a surface equilibrium contact angle $\theta_e = 0°$ the surface is highly hydrophilic and a liquid layer is in contact with the surface at all stages of the bounce cycle. With $\theta_e = 30°$ the TPCL is known to form under certain conditions. This initial analysis considers both the Refined and Regular meshes using the static contact angle boundary condition.

For Case I, results are presented in terms of the non-dimensional center of gravity ($2CGy/D_{eq}$), velocity (V_b/V_∞), and aspect ratio (AR/AR_∞) in Figs. 6.5,6.6 and 6.7 and only include the first bounce cycle for consistency with the benchmark data[1]. Both meshes provide numerical results which are similar to the experimental data up to the impact and slightly beyond. The amplitude of rebound however is larger with the Refined mesh and closer to the experimental values. With the Regular mesh the liquid film is found to drain entirely much sooner than with the Refined mesh. The formation of the TPCL can have a non negligible effect on the dynamics of the bubble. As the film breaks, the bubble can appear to stick to the surface. Although

[1]The constants (+2 and −1) are added to the non-dimensional center of gravity and aspect ratio respectively for consistency purposes with the plots obtained from the benchmarking experimental data.

this is physically consistent with a hydrophilic surface, the contact angle boundary condition can artificially increase the effect. The boundary condition is imposed as soon as the interface enters the wall adjacent cells even if its size is much larger than the active range of van der Walls forces. A coarse mesh can therefore be expected to induce an earlier TPCL formation and to effectively attract the bubble towards the surface. The comparison of bubble center of gravity with experimental data clearly supports this. The bubble velocity and aspect ratio show lower sensitivity to the mesh although some improvements in prediction with the Refined are still noticeable.

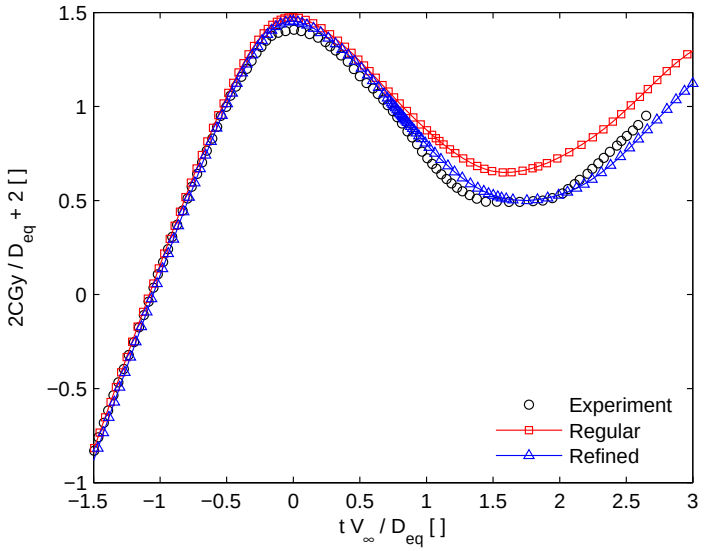

Figure 6.5: Non-dimensional bubble center of gravity for Case I: $D_{eq} = 2.46$ mm and the air/Fluid A mixture. Computational results with Refined and Regular mesh. Experimental results from Zenit and Legendre (2009)

With Case II, the liquid film should stabilize precluding any TPCL formation. The bubble velocity is shown in Fig. 6.8 over several bounce cycles in this case. Both mesh cases give results that are in broad agreement with the experimental data, but small although non negligible differences in the maximum velocity during the first bouncing cycle are also shown. The difference however is consistent with the difference in the bubble terminal velocity before impact against the wall. Both the bubble velocity plots and contour visualizations (not shown here) confirm that the bubble eventually stops bouncing. Results also confirm that a thin liquid film is always present with the Refined mesh but not with the Regular mesh. The TPCL formation is clearly shown to have an effect on the velocity but the small changes involved make it difficult to draw definite conclusions. Similar arguments

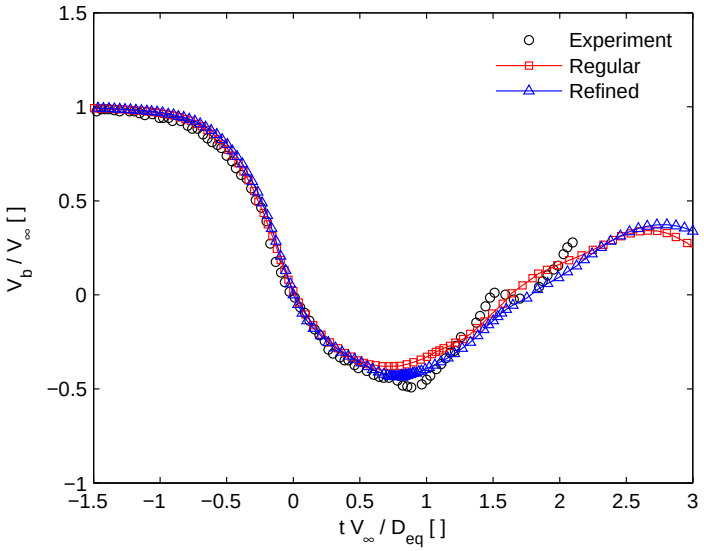

Figure 6.6: Non-dimensional vertical bubble velocity for Case I: $D_{eq} = 2.46$ mm and the air/Fluid A mixture. Computational results with Refined and Regular mesh. Experimental results from Zenit and Legendre (2009)

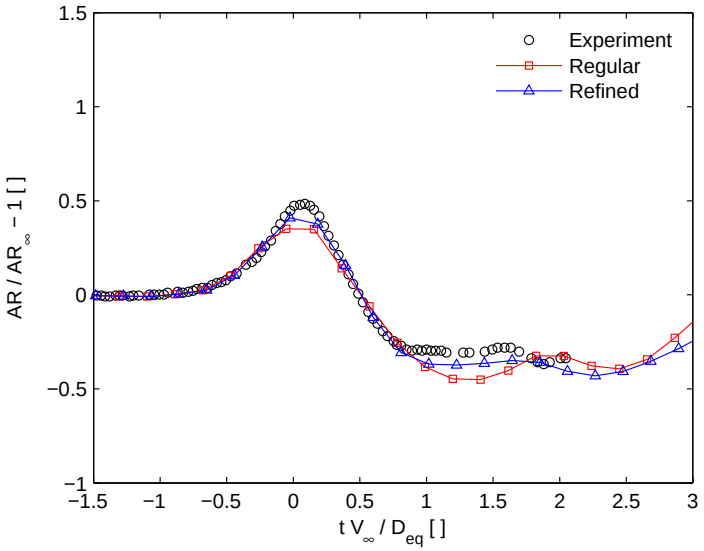

Figure 6.7: Non-dimensional bubble aspect ratio for for Case I: $D_{eq} = 2.46$ mm and the air/Fluid A mixture. Computational results with Refined and Regular mesh. Experimental results from Zenit and Legendre (2009)

can be made with respect to the bubble aspect ratio plots shown in Fig. 6.9. These show the same small and rapid oscillations as observed experimentally following the first rebound as the bubble returns to its initial spherical shape. The three main troughs and peaks corresponding to bubble flattening at impact and bubble stretching during rebound are predicted by both meshes with similar magnitude. In this case however, the peaks from the Refined mesh appear to be more notably in phase with experimental data.

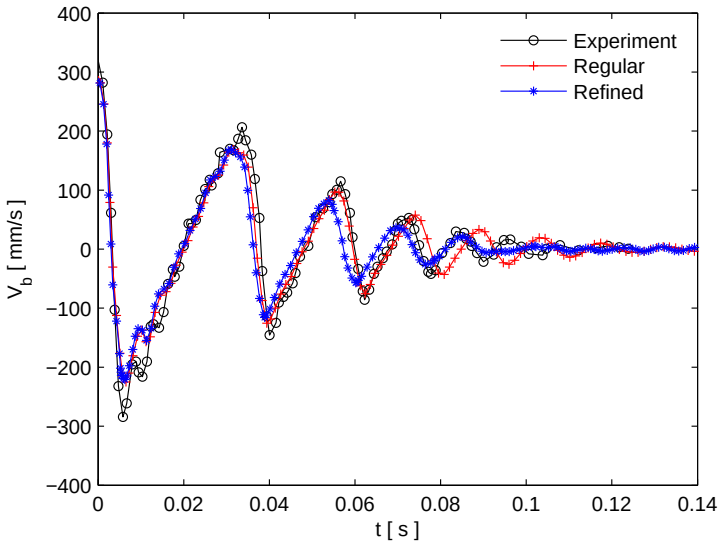

Figure 6.8: Bubble velocity for Case II: $D_{eq} = 1.48$ mm and the air/water mixture. Computational results with Refined and Regular mesh. Experimental results from Kosior, Zawala and Malysa (2012)

More definite conclusions on the model sensitivity to mesh refinement can be drawn by comparing the effect of the static contact angle on the bubble center of gravity during the successive rebounds. The two static contact angles ($\theta_e = 0°$ and $\theta_e = 30°$) are compared with the Case II fluid and bubble size. The Regular and Refined mesh results are given in Fig. 6.10a and Fig. 6.10b respectively. The Refined mesh computations indicate that the TPCL with $\theta_e = 30°$ only forms after the third rebound at approximately 0.1s, at which point little kinetic energy is left. The computations with the two contact angles show very little differences in this case. With the Regular mesh, the results show a very clear reduction in the rebound amplitude as well as a gradual phase shift in a pattern consistent with energy dissipation due to the TPCL formation. This affects primarily the case with the larger $\theta_e = 30°$ that is when the larger contact angle induces an earlier TPCL formation. Two main conclusion can be drawn from this. Firstly, the contact angle

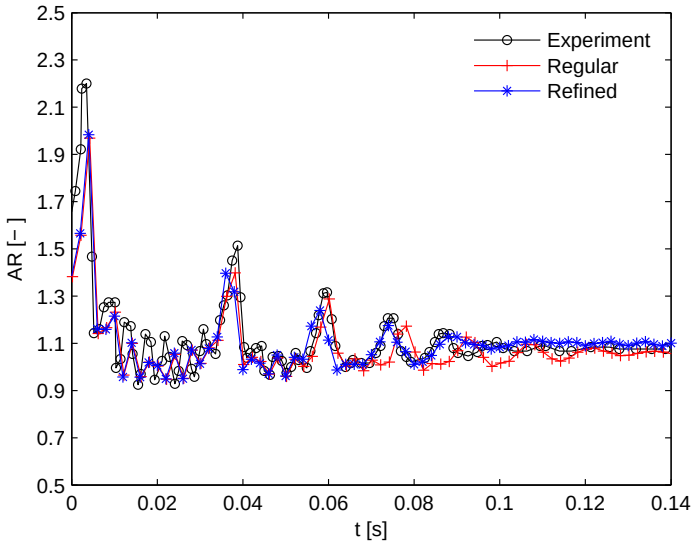

Figure 6.9: Bubble aspect ratio for Case II: $D_{eq} = 1.48$ mm and the air/water mixture. Computational results with Refined and Regular mesh. Experimental results from Kosior, Zawala and Malysa (2012)

formulation is likely to have a limited impact on the results once the liquid film is correctly resolved. Secondly, a coarse mesh is likely to induce significant errors with larger contact angles which tend to promote early TPCL formation. More generally, it is clear that correctly capturing the liquid film is essential for accurate prediction of the bubble bounce in particular when dealing with hydrophobic surfaces.

6.4.2 Validation in 3D flow

The 3D test case involves a single isolated air bubble in water generated from a wall orifice at the bottom surface of the domain and modeled with the Refined mesh. The bubble growth and detachment parameters studied in the previous chapters and published in Albadawi, Donoghue, Robinson, Murray and Delauré (2012); Albadawi et al. (2013) are considered here. Two bubble diameters $D_{eq} = 2.62, 3.3$ mm corresponding to wall orifices diameters $0.5, 1$ mm are included. Based on Fan and Tsuchiya (1990) and Clift, Grace and Weber (1978), both bubbles should assume a slightly zig-zagging trajectory shortly after detachment, but the domain height is kept relatively small at 10 mm to limit 3D effect. In this case, the bounce is assessed by comparison against experimental data obtained by the collaborative team in Trinity College Dublin following the procedure described by Donoghue et al. (2012) (See appendix A for a brief introduction to the experimental setup). The

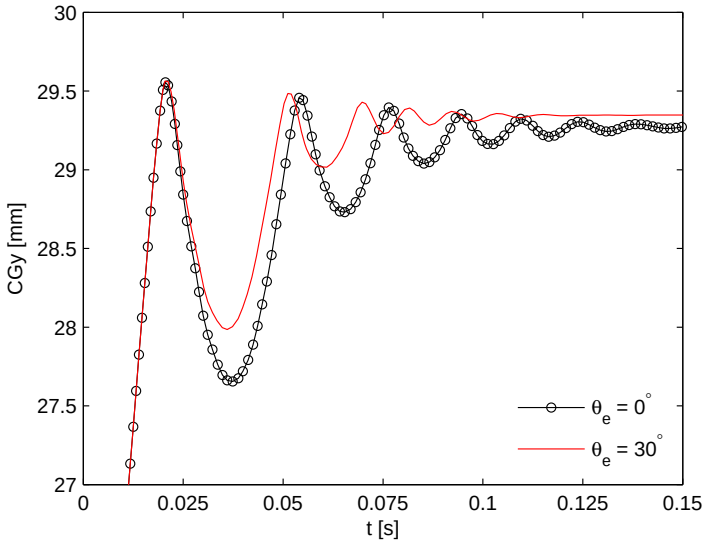

(a) Regular mesh

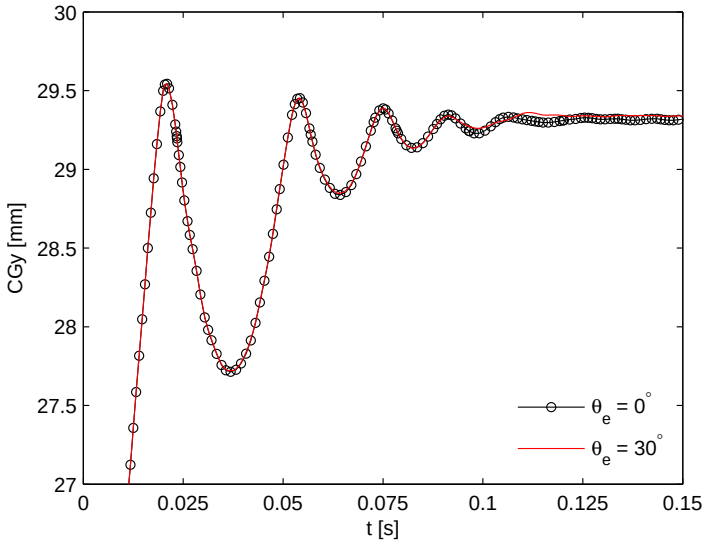

(b) Refined mesh

Figure 6.10: Bubble center of gravity for D=1.48mm with (a) Regular mesh and (b) Refined mesh, with equilibrium contact angles $0°$ and $30°$.

advancing contact angle on the upper surface was measured to be 24°.

The trajectory of the 3.3 mm bubble is plotted in Fig. 6.11. Although the bubble rise is predominantly rectilinear, it does move freely in all direction after impact and, after the first two bounces, oscillates consistently towards the right hand side boundary. This motion is believed to be influenced by the wake generated behind the bubble during its rise (Donoghue et al., 2012). A sequence of snapshots of the bubble interface viewed from a vertical plane is given in Fig. 6.12 for the first bounce cycle. Before reaching the upper surface, the bubble is shown to have an ellipsoidal shape with a plane symmetry (at $t = -0.006$ s). After that point, it deforms rapidly due to the collision with maximum deformation at the time ($t = 0$ s). When the bubble rebounds, it takes a seemingly random shape.

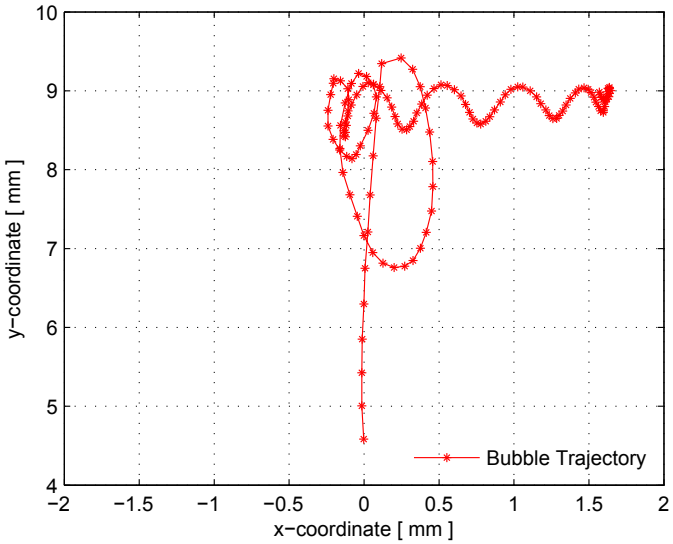

Figure 6.11: Air bubble trajectory in water with $D_{eq} = 3.3$ mm

The bubble center of gravity and velocity are compared against experimental data in Fig. 6.13 and Fig. 6.14, respectively. The numerical predictions are shown to be generally very close to measured data for the full process apart from the first rebound which shows a significant overshoot in the maximum rebound distance with an error of 25% compared to the experiments (See Table 6.6). This difference could be attributed to interface oscillations in the bubble which were not captured by the numerical model. It is indeed possible but difficult to verify that lower surface deformation energy translates in lower rebound amplitude. Interestingly it is seen that the experimental bubble velocity data (Fig. 6.14) shows rapid oscillations about a mean value which is close to the numerical predictions. This is consistent

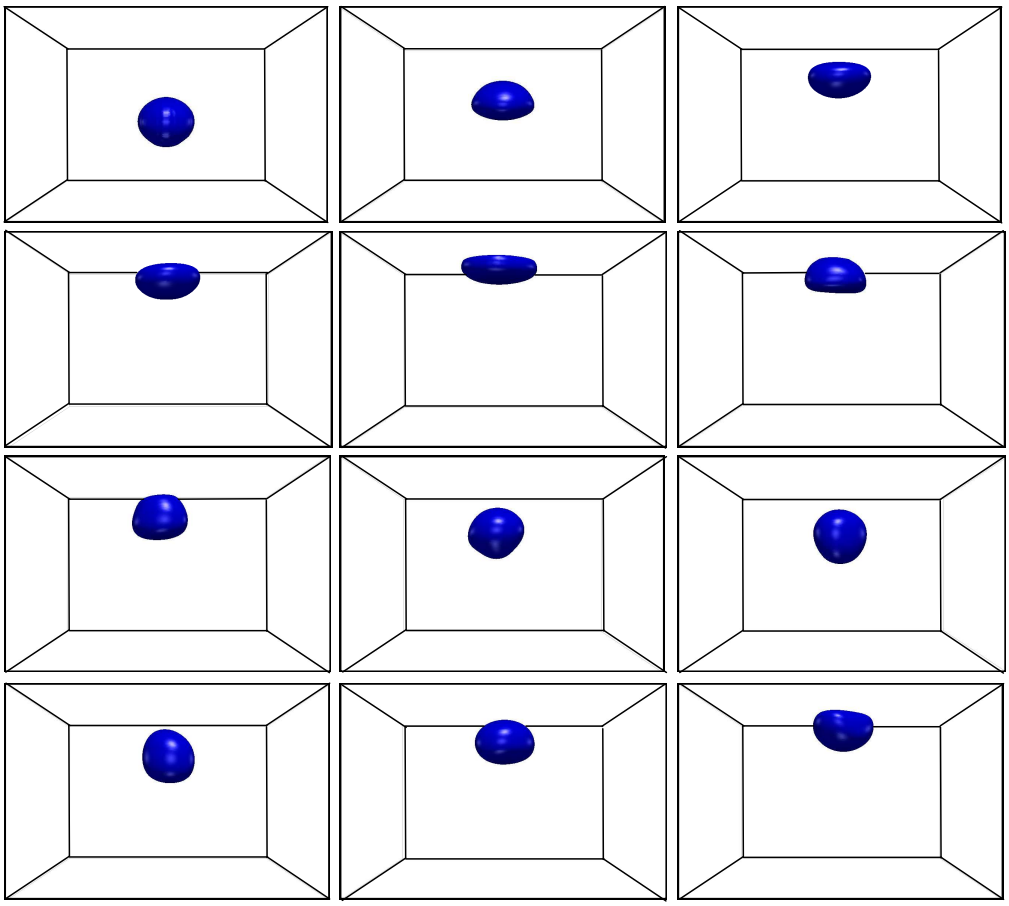

Figure 6.12: Sequence of screen shots of colliding air 3.3 mm bubble in water modeled using the Refined mesh. The contour plots are given from $t = -0.024$ s (top left) to $t = 0.042$ s (bottom right) at time intervals of 0.006 s between each two successive frames.

with rapid surface oscillations due to bubble shape oscillations. Depending on the deformation stage just before impact, one can conceive a larger or smaller rebound amplitude about its mean. Other observations which would tend to confirm these suggestions are the fact that in the case of the smaller $D_{eq} = 2.62$ mm bubble the rebound amplitude is under predicted rather than over predicted (see Fig. 6.13). The errors in the bubble maximum rebound distance compared to the experimental data for the first six bouncing cycles are summarized in Table 6.6. Two errors are given for the bubble center of gravity, one is calculated numerically using the projected area of the bubble (2d) and the other using the bubble total volume (3d). This table confirms that the numerical results provide a good quantitative comparison for the full bouncing process with errors lower than 8 % in all cases apart from the first rebound.

Table 6.6: Comparison of the bubble center of gravity at the point of maximum rebound measured from the upper wall for the first six bouncing cycles with air/water mixture and $D_{eq} = 3.3$ mm and Refined mesh.

	Exp	3D	E(3d) [%]	2D	E(2d) [%]
1st	2.583	3.240	-25.416	3.225	-24.816
2nd	1.874	1.861	0.682	1.884	-0.560
3rd	1.560	1.570	-0.640	1.561	-0.089
4th	1.408	1.493	-6.035	1.460	-3.685
5th	1.312	1.421	-8.306	1.422	-8.367
6th	1.252	1.352	-8.001	1.341	-7.155

6.5 Film formation and drainage

Accurate modeling of the liquid film formation and drainage is clearly important. Focus is turned here to this aspect of the process. A time sequence of the 3D contour of the 3.3 mm diameter air bubble after impact and viewed from the upper surface of the domain is shown in Fig. 6.15 to illustrate the extent of the film in the horizontal plane. Of particular interest is the clear formation of a dimple centered on the approximate axis of symmetry of the bubble. The liquid film trapped between the approaching bubble and the wall is initially uniformly distributed but as it drains under the action of buoyancy, the bubble spreads outward and the film thickness is shown to reduce more rapidly toward its outer rim creating the observed dimple

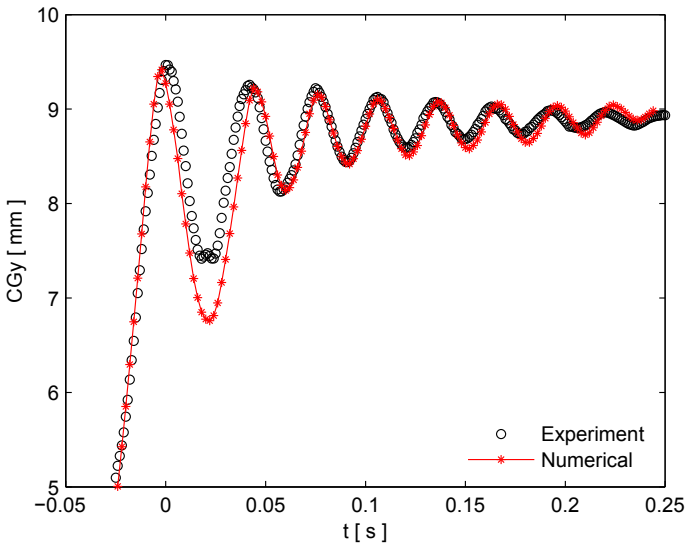

(a)

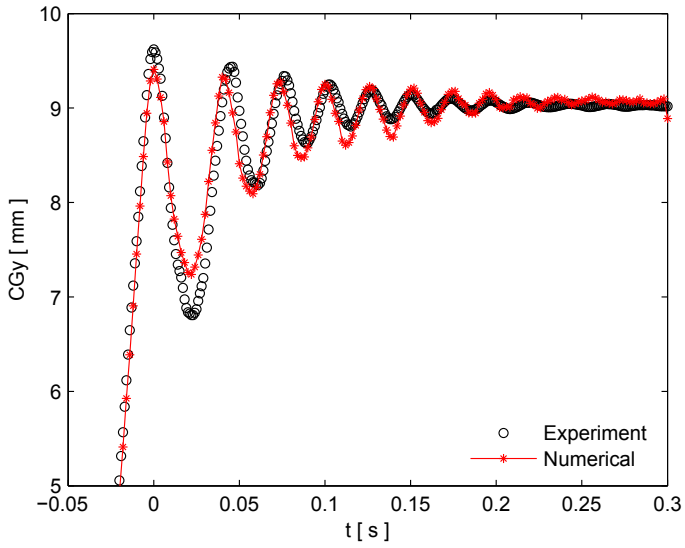

(b)

Figure 6.13: Comparison of bubble center of gravity with experimental data with the air/water mixture and (a) $D_{eq} = 3.3$ mm and (b) $D_{eq} = 2.62$ mm using a Refined mesh.

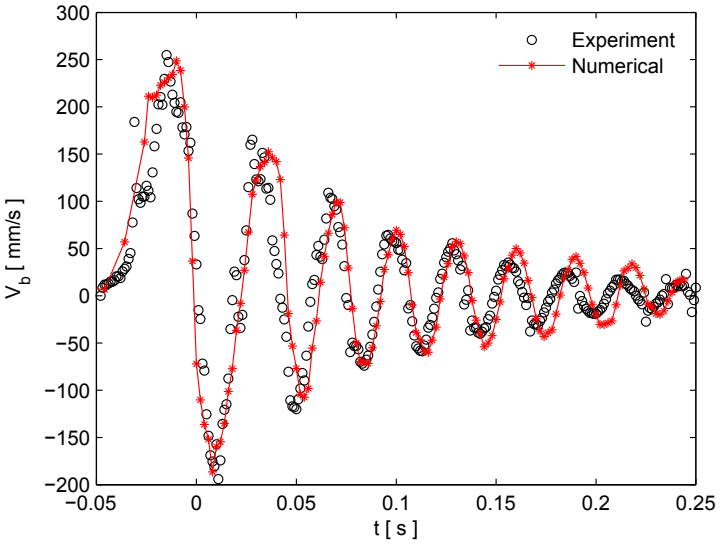

Figure 6.14: Comparison of bubble velocity in the gravitational direction with experimental data with air/water mixture and $D_{eq} = 3.3$ mm and Refined mesh.

in the bubble surface. This dimple is at its largest at the first bounce and reduces rapidly over successive bounces along with the spreading, in the horizontal plane, of the film and interface outer rim. As the kinetic energy of the bubble dissipates after successive rebounds, a stage is reached where the liquid film either drains to a minimum thickness and stabilizes or a TPCL forms. The steady state is determined by the surface properties, i.e. the contact angle boundary condition.

An axi-symmetrical model of a $D_{eq} = 1.48$ mm air bubble in water is considered next to provide a more detailed description of the film and dimple evolutions over time. Two static contact angles $\theta_{app} = 0°$ and $\theta_{app} = 30°$ are included and the Refined mesh is used to ensure that the liquid film is adequately captured at least over the first rebounds. The plots of the bubble interface at successive times over the advancing phase of the first bounce are given in Fig. 6.16 at 0.2 ms time intervals. As no TPCL forms at this stage, the static contact angle does not influence the process. The dimple formation starts when the bubble wall separation distance reaches approximately $\sim 50\mu$m which is twice the value proposed by Klaseboer et al. (2000) ($\sim 0.4R_{eq}\sqrt{2Ca} = 28$ μm). The minimum height of the dimple at the axis of symmetry is approximately 35 μm while the film thickness reduces to a much smaller $\sim$ 15 μm toward the rim of the bubble. The plot also confirms the radial spreading of this outer rim from the axis of symmetry.

The static contact angle has a significant influence on the last stage of the process

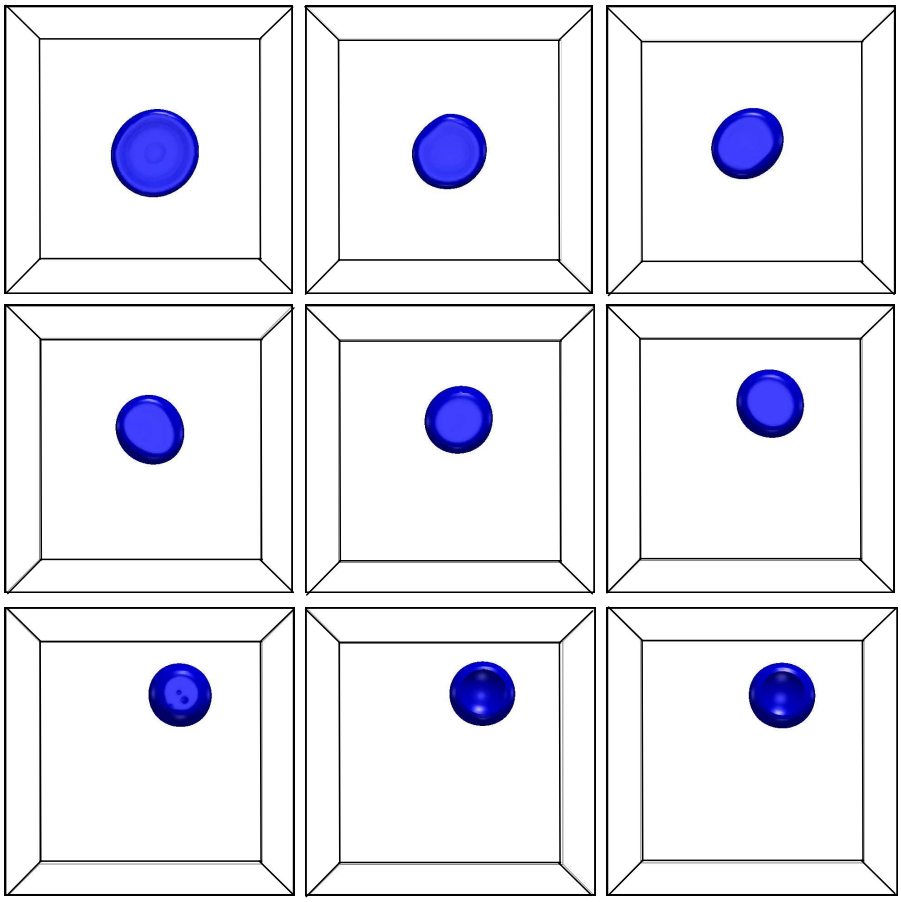

Figure 6.15: Sequence of screenshots illustrating the size of the maximum film formed at each bouncing cycle on the bubble top surface during collision, with air/water mixture and $D_{eq} = 3.3$ mm and Refined mesh. The data are from top left to bottom right with times $0, 0.044, 0.076, 0.106, 0.134, 0.166, 0.204, 0.23, 0.244$ s, respectively.

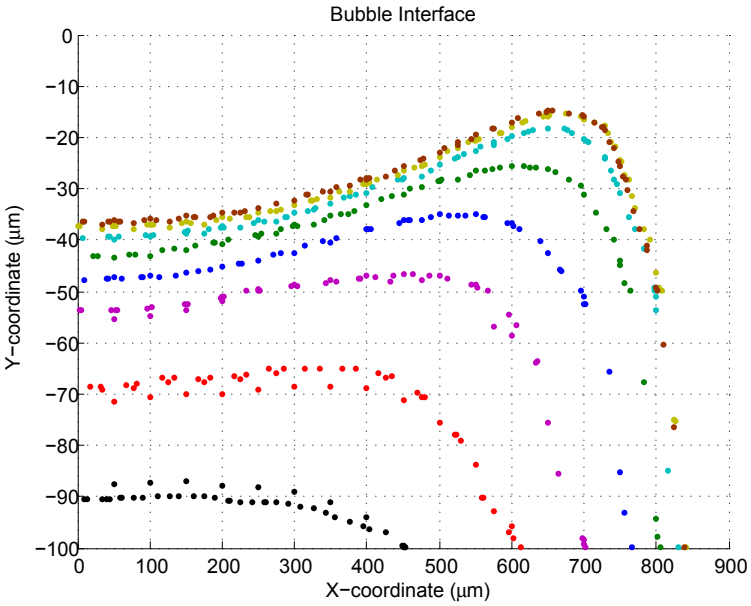

Figure 6.16: Temporal evolution of the film formation during the first bubble approach to the wall with contact angle 0° for air/water mixture and $D_{eq} = 1.48$ mm. The dotted lines represent the interface contour ($\alpha = 0.5$) at the top side of the bubble facing the solid wall.

as the bubble reaches steady state. When the contact angle is set to 0°, a continuous film stabilizes between the bubble and the solid wall (Fig. 6.17a). This occurs when in contact with a hydrophilic surface as observed by Kosior, Zawala and Malysa (2012). The film outer radius in the horizontal plan tends to 180 μm as it stabilizes; a value which is close to that suggested by Kosior, Zawala and Malysa (2012) for hydrophilic surfaces ($\sqrt{2R_{eq}^4 \Delta\rho g/3\sigma} \approx 168$ μm). When the equilibrium contact angle is greater than zero, a TPCL forms expanding outward until the imposed static contact angle is satisfied ($\theta_{app} = 30°$ in Fig. 6.17b).

The minimum film thickness at successive rebounds for both the $D_{eq} = 1.48$ mm air bubble in water mixture (case II) and the $D_{eq} = 2.62$ mm air bubble in Fluid A (case I) are given in Table 6.7. This is presented along with the bubble kinetic energy ($KE = 0.5 C_M \rho_l V_{eq} V_b^2$) and potential energy ($PE = \Delta A \sigma$), where ΔA and V_b are the changes in the bubble area, and the maximum rise velocity during the collision process at each rebound, respectively, V_{eq} is the bubble equivalent volume, and $C_M = 0.62AR - 0.12$ is the added mass coefficient (Klaseboer et al., 2001). Not surprisingly the minimum film thickness is shown to decrease after each bouncing cycle until the film ruptures and the TPCL forms. Similar observations were made by

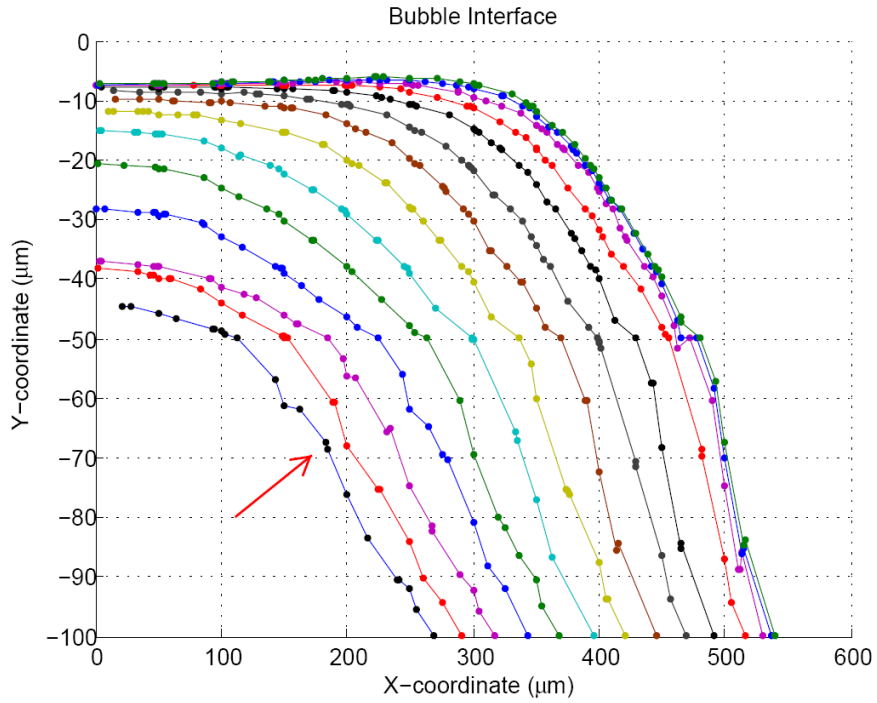

(a) Contact angle 0°

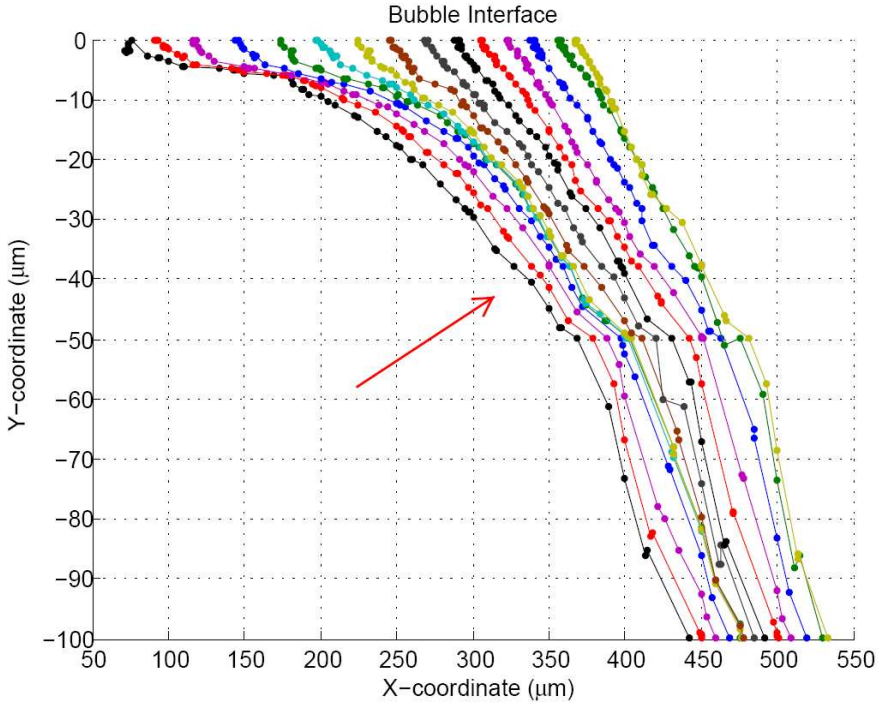

(b) Contact angle 30°

Figure 6.17: Film formation during the last bounce with air/water mixture, $D_{eq} = 1.48$ mm and contact angles (a) 0° and (b) 30°. The arrow is in the direction of time increase and successive plots are at time intervals of 0.4ms

Doubliez (1991) in the case of collision with a free surface. The minimum thickness found here for case II was 4.8 μm which is four times the mesh size across the film. This value is of the same order as those observed and predicted experimentally in Tsao and Koch (1997) ($O(10\mu m)$, Hendrix et al. (2012) (2.5 μm) for $D_{eq} \sim 0.7$ mm, and in (Krasowska, Krzan and Malysa, 2003) (2.7 μm).

Also for both cases presented in Table. 6.7, the bubble fails to rebound when its kinetic energy falls below $KE \sim 3 \times 10^{-9}$ J. A similar threshold value was found experimentally by Zawala et al. (2007) with a $D_{eq} = 1.47$ mm air bubble in water. The authors reported a similar behavior with several rebounds ending when the bubble kinetic energy fell below 10×10^{-9} J whereas bouncing was shown to occur when this value was above 1×10^{-7} J. Another interesting observation is the relationship between the film thickness and radius. The larger kinetic energy is found to generate larger projected contact areas between the bubble and the wall so that a larger film is generated requiring longer period to drain. This, in turn, leads to a longer bouncing cycle periods of time.

Tsao and Koch (1997) have argued from experimental observation that the formation of a surface dimple and the drainage of the liquid film were consistent with a peak in liquid pressure above the rising bubble prior to impact. This existence of a high pressure region however could not be reproduced by the numerical model of Sanada, Watanabe and Fukano (2005). The modified pressure (P_{rgh}) along a horizontal line parallel to the upper wall at a distance of 5 μm is plotted in Fig. 6.18. These results correspond to the $D_{eq} = 1.48$ mm air bubble in water case solved with the Refined mesh during the first bounce. The pressure profile is shown at several time steps starting from (t_a, *Approach*) when the bubble upper interface is at a distance 0.52 mm from the wall and ending at time (t_f, *Recede*) at a distance 0.02 mm following impact. The pressure is shown to increase by a factor of four times over a short period of time (5 ms).

Table 6.7: Film minimum thickness and bubble kinetic and potential energy for each bouncing cycle for both $D_{eq} = 1.48$ mm with air/water mixture (case II) and $D_{eq} = 2.62$ mm with air/Fluid A mixture (case I).

	Bouncing cycle	thickness [μm]	KE[J]	PE[J]
caseI	1st	14.8	6.34E-08	6.72E-09
	2nd	8.60	1.32E-08	3.83E-09
	3rd	6.00	3.00E-09	1.15E-09
	4th	4.80	5.93E-10	8.71E-10
caseII	1st	51.9	3.42E-07	2.07E-08
	2nd	24.6	4.35E-08	8.43E-09
	3rd	14.6	3.83E-09	1.07E-08

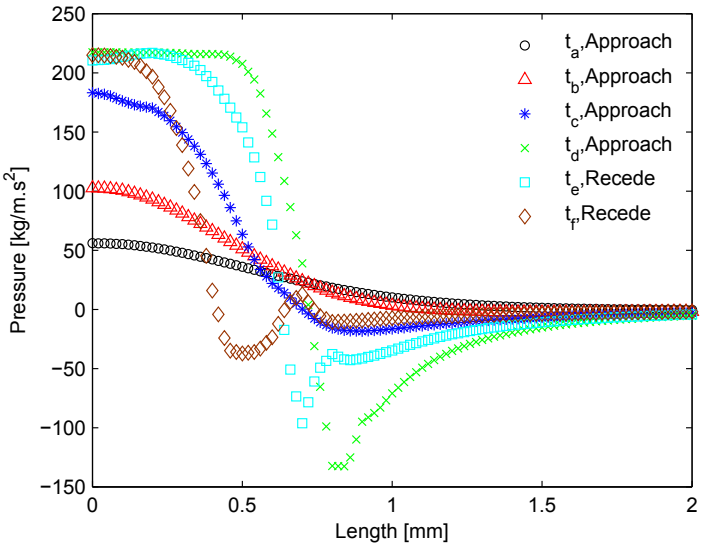

Figure 6.18: Horizontal pressure distribution at 5 μm from the wall during the first bouncing cycle with air/water mixture, $D_{eq} = 1.48$ mm.

A comparison of pressure contours and velocity plots provides some useful insight. Fig. 6.19 combines both data prior to and following impact and rebound when the bubble is approximately at 0.5 mm from the wall. The intensity of the velocity field in the liquid region is depicted using an off-scale vector plot with color variation from red (large value) to blue (small value). A similar color grading is used for plotting the pressure variation using 10 iso-contour lines dividing the full changes in the pressure. The black solid line in the figure represents the bubble interface with iso-line ($\alpha = 0.5$). As the bubble approaches the wall prior to impact, the liquid

flows radially outward in the film region and from high pressure to low pressure regions. After the rebound, the liquid flows in the opposite direction and against adverse pressure gradients leading to some localized flow reversal and separation near the axis of symmetry. This along with the the acoustic radiation of energy resulting from the large bubble oscillations during the rebound have been suggested as the main source of energy dissipation by Tsao and Koch (1997).

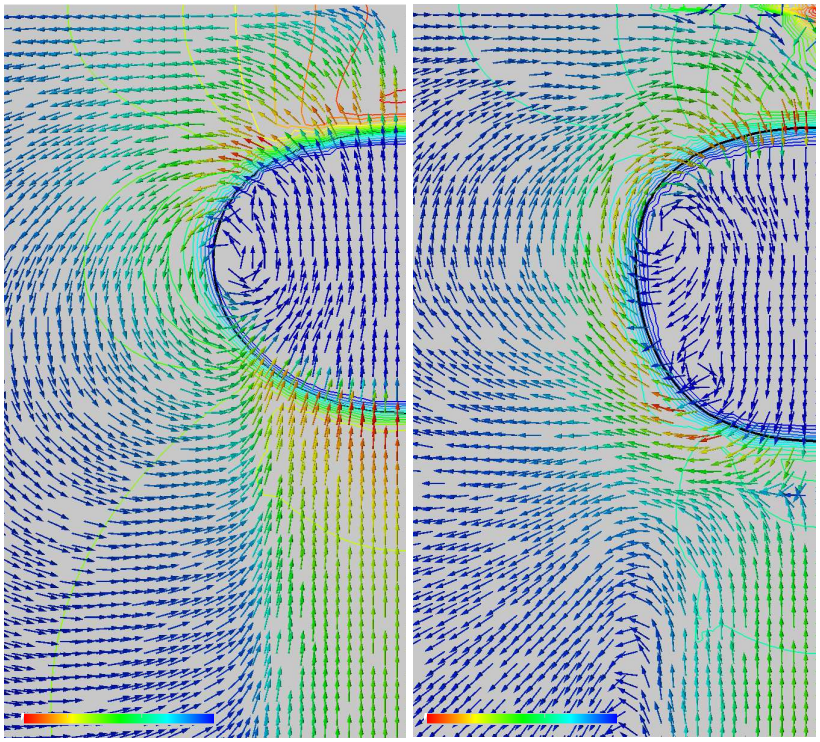

Figure 6.19: Velocity vector plot at two different stages of bouncing. The velocity vectors are not scaled. The color range is from red (large) to blue (small), (a-Left) approach stage with velocity magnitude range $[0, 0.259$ m/s] and pressure range $[-100, 63$ kg/m.s^2], (b-right) recede stage with velocity range $[0, 0.191$ m/s] and pressure range $[-100, 206$ kg/m.s^2], with angle 0° and air/water mixture, $D_{eq} = 1.48$ mm.

6.6 Dynamic contact angle model

Once the film ruptures and the TPCL forms, the influence of the surface properties in the form of surface tension becomes significant. This is interpreted numerically by the contact angle boundary condition. The sensitivity of computational results to boundary conditions is assessed here by reference to the bubble velocity considering

three contact angle formulations (static, dynamic with and without slip velocity model) and the two mesh types (Refined and Coarse). This section focuses on the case of a $D_{eq} = 1.48$ mm diameter bubble in water with a surface contact angle of 30°. The Coarse mesh model is used to assess the sensitivity of the contact formulation with an unsuitable mesh as the TPCL forms directly at the first bouncing cycle. With the dynamic no slip model, the bubble slip velocity at the wall boundary is calculated as the tangential velocity of the neighboring cell center so that results can be expected to be influenced by the mesh resolution near the wall. In the case of dynamic slip model, the slip velocity is calculated in terms of the velocity gradient in the vertical direction to the wall (Eq. 3.31) with $\lambda = 0.1\Delta x$. The value of λ is chosen so that it is of the order $O(10)$ μm and $O(0.1)$ μm with the Regular and Refined mesh, respectively. As shown in Fig. 6.20, the impact of the contact model is, as expected, most noticeable with the Coarse mesh due to the early formation of the TPCL. Fig. 6.20b clearly shows that the no slip model induces large and unphysical velocity fluctuations which are found to correlate with bubble shape oscillations. Both dampen slowly with time. The slip model compares well with the static contact angle model and matches the experimental results reasonably well. When the mesh is refined to capture the liquid film (Fig. 6.20a), the results show very little sensitivity to the contact angle formulation. The comparison between the two meshes show that capturing the TPCL with an adequate mesh resolution reduces the influence of the contact angle model and that the static contact angle model is sufficient. It is worth noting as well that some oscillations persist with all models, a behavior which is not observed experimentally and can be explained by spurious currents. Most interesting is the fact that very similar results are observed with the case of $D_{eq} = 2.62$ mm with air/fluid A mixture and equilibrium contact angle 30°. In this case the TPCL forms but this occurs late in the process when most of the kinetic energy has been dissipated due to increased influence of liquid viscosity. At that stage, changes induced by the contact model have little impact on the bubble velocity.

When the TPCL is formed at the solid surface, the air inside the bubble comes in direct contact with the wall and the three phases (Solid/ Liquid/ Gas) meet at the contact region. A new geometrical parameter, called the spreading radius, can be introduced at this stage. It is the equivalent radius of the non-wetted region at the interface between the bubble and the solid surface. Its time evolution is shown in Fig. 6.21 for both static and dynamic (with slip) contact angle models considering a $D_{eq} = 1.48$ mm air bubble in water mixture and an equilibrium contact angle

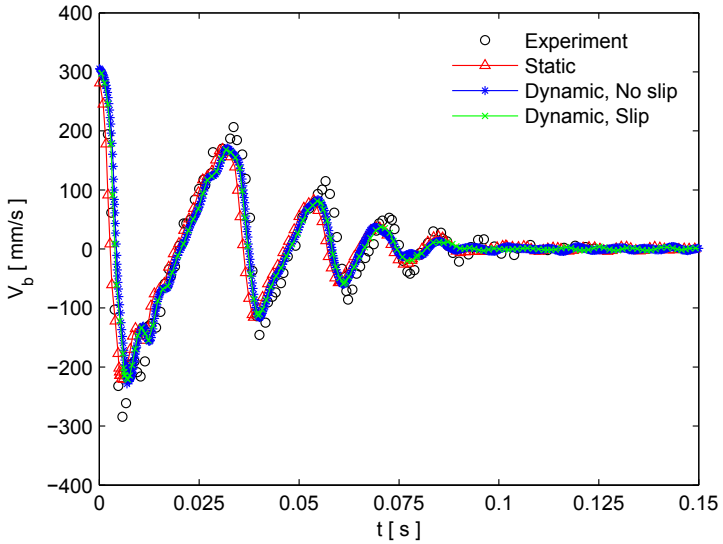

(a) Refined mesh

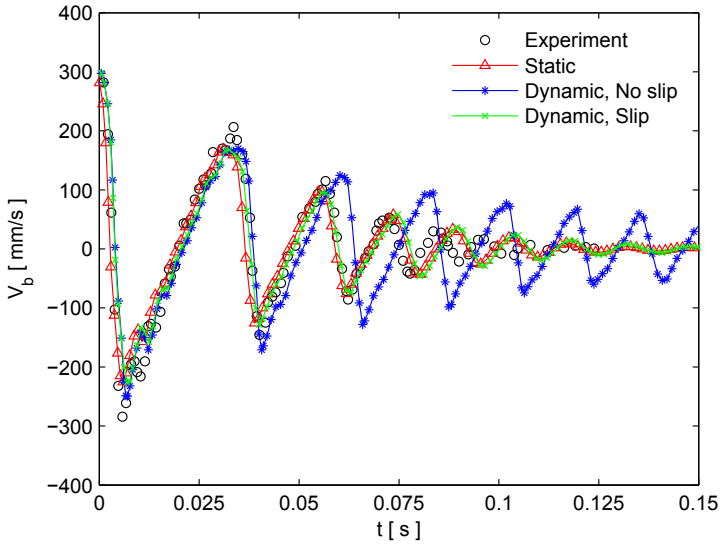

(b) Regular mesh

Figure 6.20: Comparison of slip model influence on the bubble velocity during the bouncing process with dynamic contact angle boundary, with $D_{eq} = 1.48$ mm and air/water mixture. The slip model implemented corresponds to Navier condition with ($\lambda = 0.1\Delta x$) slip length (Eq. 3.31). Experiments from Kosior, Zawala and Malysa (2012).

set at 30° to allow TPCL formation. The initial time is set here as the instant when the TPCL forms. Both models show a rapid increase in the bubble spreading radius immediately after the TPCL forms. This is followed by a slow variations of the radius around an average value (0.4 mm) and both contact model provide globally similar results. A difference appears and grows after 0.025 but remains reasonably small ($O(10)$ μm) and is difficult to explain. The bubble instantaneous apparent contact angle is also plotted in Fig. 6.22 and shows similar trends with an initial rapid increase from (5°) to approximately (25°) before leveling off with larger fluctuations about a globally steady mean. Here again consistent differences between the two models are difficult to identify and justify. In practice both models predict bubble oscillations with small amplitudes which are of the order (50 μm) for the bubble height.

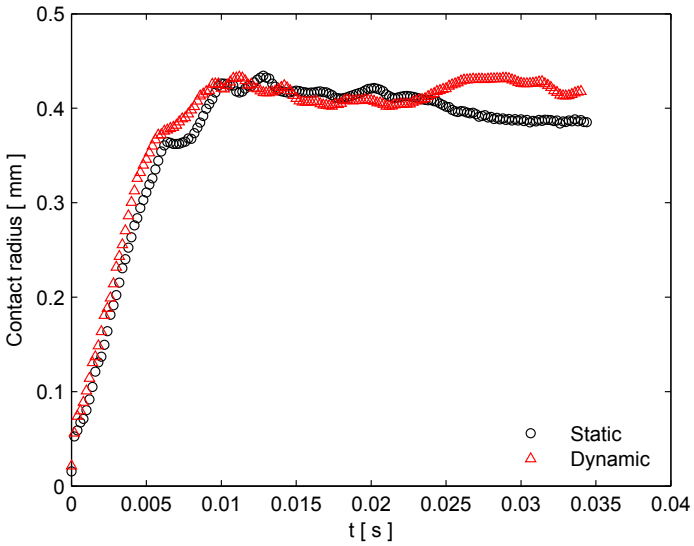

Figure 6.21: Evolution of the bubble spreading radius after the TPCL formation for $D_{eq} = 1.48$ mm and air/water mixture with Refined mesh and equilibrium contact angle 30°. The dynamic contact angle model is coupled with a slip boundary conditions.

6.7 Discussion and final remarks

Based on the analysis of the influence of the mesh resolution and the contact angle models on the mechanism of bubble bouncing, several general remarks can be drawn and discussed as follows:

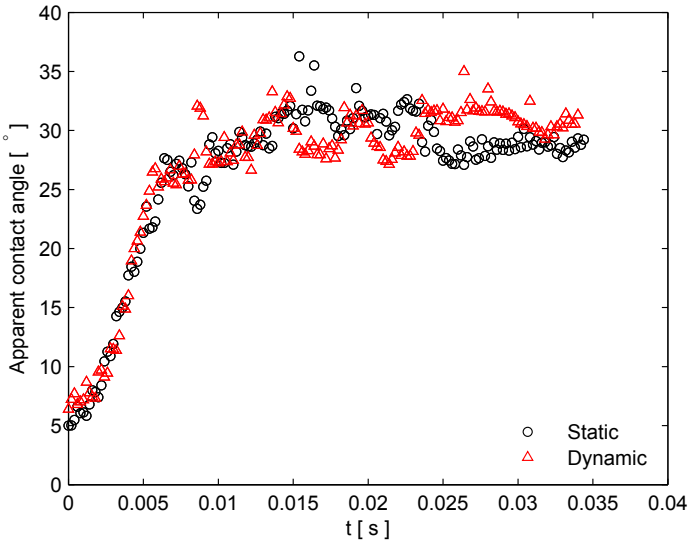

Figure 6.22: Evolution of the bubble apparent contact angle after the TPCL formation for $D_{eq} = 1.48$ mm and air/water mixture with Refined mesh and equilibrium contact angle $30°$. The dynamic contact angle model is coupled with a slip boundary conditions.

The VOF interface capturing method is sufficient for the analysis of bubble bouncing provided that an accurate mesh resolution is used in the neighboring cells of the solid surface. Thus, the algebraic VOF can provide good results for applications with/without solid surface interaction (bubble bounce and rise). However, for capillary dominant problems the VOF method should be extended to correctly estimate the influence of the surface tension as evidenced in both LS and CLSVOF methods. This is usually achieved at the cost of the simplicity of the method implementation and the mass conservativeness.

In order to numerically capture the mechanism of bubble collision against a solid surface, it is found that the fluid domain should be discretized to a very refined level (up to few micrometers). This refinement makes the computational simulation very expensive and practically impossible for 3D simulations. An alternative technique is to impose a film boundary condition so that there always exists a thin film of water located on the solid plate. However, this solution is valid only for super hydrophilic surfaces ($\theta_e = 0°$) while a TPCL, as shown in Fig. 6.17b, is noticed for larger contact angles. This suggests that hybrid boundary condition could be applied instead so that it switches between film and contact angle boundaries during the simulation. This switch should be performed at the moment when the TPCL forms on the solid plate. However, this is a complex procedure as the time of the TPCL formation

in each simulation varies based on the operating conditions. The present chapter showed that refining a small area below the solid surface to a few micrometers is sufficient to capture the film formation process and produce bubble bouncing results similar to those observed experimentally with the least computational costs compared to the option with fully refining the mesh.

The analysis of the contact angle model showed that similar results can be obtained using either the static or dynamic contact angle provided that the mesh is sufficiently refined to resolve the liquid film. This can be explained by the small influence of the contact line slipping velocity at the last stages of bouncing [$Ca_{slip} \approx 10 \times 10^{-4}, 4 \times 10^{-4}$] when compared to the case of drop spreading (Yokoi et al., 2009; Sikalo et al., 2005). This, in turns, limits the variations of the dynamic contact angle to a small range around the equilibrium contact angle value ($\theta_d = \theta_e + f(Ca_{slip}) \approx \theta_e$). It is important to mention that for non-regular surfaces where the advancing contact angle is significantly different from its receding and equilibrium values, the dynamic contact angle model should consider both advancing and receding angles instead of the equilibrium one. However, the influence of the contact angle hysteresis can be expected to be more important in cases where the bubble bounces or slides along inclined surfaces. The bubble dynamics, in this case, is influenced by the surface material properties and the plate inclination angle. A more in depth analysis is required to compare the different dynamic contact angle models implemented. The analysis should be devoted to the study of only the last stage of the bubble bouncing. This requires suitable experimental data to be used for benchmarking purposes. These data should focus on the spreading of the contact line rather than the bouncing process.

The analysis in this chapter accentuated the main reasons why the drop spreading has been used in the literature more than the bubble bouncing for validating the contact angle models. This can be summarized in the following points:

- The sensitivity of the numerical results to the dynamic contact angle model is more apparent with drop impingement and spreading than bubble bouncing. This is mainly due to the large slip Capillary number accompanied with the drop spreading ($Ca_{slip} = O(0.01)$ at the early stages of spreading) compared to the one observed with bubble bouncing ($Ca_{slip} \sim 0.001$ at the early stages of TPCL formation).
- The drop spreading allows also for validating the contact angle models at high slip Capillary numbers while this is not possible to attain with bubble

bouncing due to the film formation that prevents the three phase contact line formation.

- With drop spreading, wider range of physical and geometrical properties can be used for validating the dynamic contact angle models compared to the bubble bouncing. For large equivalent diameters, the bubble trajectory is not rectilinear before the collision. This leads to non-symmetrical bouncing analysis, while the contact angle models, based on the Lubrication theory, are derived based on the assumption that the drop/bubble is symmetrical.
- Furthermore, for benchmarking data, it is easier to investigate experimentally contact line dynamics with drops spreading compared to bubbles bouncing.

7 Conclusions and future work

7.1 Conclusions

The conclusions of the numerical implementation and assessment of interface capturing methods and contact angle models are summarized in this section. The conclusion is divided into three parts discussing the following points: the assessment of the different interface capturing methods for the study of bubble growth and detachment, the validation of the coupled S-CLSVOF method for bubble rise and growth, and finally the analysis of the bubble bouncing using VOF coupled with both static and implemented dynamic contact angle models.

The characteristics of bubble growth and detachment modeled by four interface capturing methods, VOF-Geo, VOF-Comp, CLSVOF-Geo, and LS, have been compared against experimental data. A single orifice radius $R_o = 0.8$ mm and four injection flow rates $(50, 100, 150, 200$ mlph) have been considered to study the formation under quasi-static conditions. The main conclusions on the comparison between the four interface techniques can be summarized as follows:

- The LS method has been shown to consistently predict the bubble detachment volume and time which were in closest agreement with experimental data with errors lower than 2% while the VOF-comp method gave results which were least accurate with earlier bubble detachment and smaller volumes.
- The full process of bubble growth was studied in more detail at a flow rate of 150 mlph by considering the bubble center of gravity, aspect ratio, and contact angle. With CLSVOF-Geo, the bubble was shown to oscillate during the formation leading to an early detachment. The other geometrical method, VOF-Geo, was found to be more stable than CLSVOF-Geo but also failed to achieve the bubble detachment correctly with a delayed pinch-off.
- In spite of the differences affecting the formation process, all methods behave similarly during the detachment correctly modeling the bubble neck radius

decrease as an exponential power law $R_{neck} \propto [-(t - t_{det})]^{\omega}$ with $\omega \sim 1/3$ and the formation of two semi-cones with two different semi-angles.

- The study of the velocity field inside the bubble highlighted the formation of a gas jet through the neck before pinch-off providing the driving force for the bubble rupture due to the Bernoulli effect which could be linked to the liquid suction around the neck before detachment. The largest gas flow velocity was obtained with CLSVOF-Geo method while the LS method gave more gradual velocity variations in both gas and liquid phases. The largest gas velocities during the growth were concentrated around the orifice rim and were attributed to the contact angle formulation for the wall boundary condition. The density averaging applied to the surface tension force modeled was linked to a decrease in gas velocities modeled by VOF-Geo compared to the VOF-Comp method.
- Using small injection flow rates highlighted the importance of an accurate implementation of the surface tension source term. Results confirmed the suitability of the LS method which was found to be the best at capturing the interface and representing the surface tension under the specific condition of low Capillary and Bond numbers and subject to the constraints of the softwares used. The larger flow rates however were found to reduce the relative influence of the surface tension by increasing gas inertia inside the bubble with a corresponding improvement in the VOF-Geo results. Using a smaller time step around detachment only was also found to improve predictions with all methods.

The original Volume of Fluid model implemented in the OpenFOAM® library is then extended into a simple coupled method (S-CLSVOF) which combines the advantages of both VOF and LS. The aim was to benefit from the smoothed curvature and the Dirac function available in the surface tension model in LS. Both VOF and S-CLSVOF methods were used first for the study of circular bubbles in equilibrium and a freely rising bubble for which exact analytical solutions and experimental data are available. The two methods have then been used for the study of axi-symmetrical bubble growth and detachment using small volumetric flow rates selected to satisfy the quasi-static condition and to ensure that the capillary forces are predominant. The main points discussed in this context can be summarized as:

- For the circular bubble at equilibrium, the combination of the LS and Dirac functions improves the curvature estimate and reduces the magnitude of the

spurious currents. Furthermore, the results' accuracy with S-CLSVOF can be improved slightly by refining the mesh.

- For the free rise bubble, both VOF and S-CLSVOF methods give similar bubble terminal velocity and aspect ratio with relative differences less than 2.5% and 2%, respectively. For 3D bubble rise, the numerical results with S-CLSVOF were in good agreement with the experimental observations by Raymond and Rosant (2000). The two dimensional simulations with large bubble diameters fail to provide the correct bubble aspect ratio as expected due to the bubble motion in three-directions.

- The analysis of the forces acting on the bubble during the growth showed the predominance of the capillary force during the bubble growth, which highlights the importance of using the accurate surface tension model. Both numerical methods are able to predict the complete process of bubble growth and detachment. However, the VOF method fails to provide the accurate bubble detachment time with a bubble growth rate substantially larger than the experimental observations. In contrast, the S-CLSVOF method was found to accurately predict the bubble detachment volume and time with errors less than 3%. Furthermore, the geometrical characteristics, center of gravity, maximum width and contact angle, were also well predicted by the S-CLSVOF method. With the VOF method and using smaller flow rates, the bubble was exposed to small oscillations in the vertical direction.

- Both numerical methods predict similar behaviors during the detachment stage with an exponential power law ~ 0.36 consistent with a flow where the influence of the surface tension and gas inertia inside the neck region are of similar magnitude.

- The static contact angle has a strong influence on the formation process. Increasing this angle above a certain value can significantly increase the bubble detachment volume and time by allowing the interface to spread away from the orifice rim. This threshold angle was found to be equal to the minimum contact angle observed experimentally which itself decreases with the orifice radius.

- The numerical simulations of bubble growth using S-CLSVOF with three-dimensional domain provided similar results to the axi-symmetrical simulations. In contrast, the compressive VOF method provided different results

compared to the axi-symmetrical case. Moreover, both lateral and longitudinal oscillations were observed during the formation process.

The Volume of Fluid model in OpenFOAM is finally employed for the study of free bubble rise and impact on and bounce from a horizontal solid surface. Although it has been found that S-CLSVOF improves the accuracy of the VOF method for capillary dominant problems, VOF provides good results for the free bubble rise. The VOF method is tested in this research for accurately predicting the bouncing process with different mesh resolutions for the solution domain. The main objective of the bouncing study is to investigate the mesh resolution influence on the bouncing process. Furthermore, the model is used also to validate the dynamic contact angle model which, itself, introduces extra numerical parameters to justify. Therefore, it is more complicated to study the dynamic angle model with the S-CLSVOF method compared to VOF. The models accuracy has been assessed against experiments and existing published benchmarking data. It has been found in this study that:

- The VOF model can predict bubble terminal velocities within 5 % of benchmark experimental data. The computed bubble aspect ratio tends to be larger than the experimental values but provides good comparison with the empirical correlation of Legendre, Zenit and Velez-Cordero (2012).
- The analysis of the bubble bounce with different mesh resolutions has highlighted the importance of relying on a Refined mesh in the vicinity of solid surfaces. A resolution of the liquid film with 4 cells was found to allow accurate representation of the unsteady process. For coarser mesh sizes, the contact angle boundary conditions force early formation of a TPCL with changes in the amplitude of rebound. The influence of the mesh resolution is dependent on the film thickness and increases with the equilibrium contact angle.
- 3D models capable of dealing with non linear rise and bounce trajectories have confirmed that similar levels of accuracy could be achieved in such cases. Some differences at the first rebound suggest that increased mesh resolution may be required to capture bubble shape oscillations that have been assumed to impact on the amplitude of rebound.
- The numerical model can provide physically consistent descriptions provided that adequate mesh resolution was used. The onset of the dimple formation and the size of the liquid film during the bubble approach were shown to compare well with published empirical correlations or observations. For zero

equilibrium contact angle, a continuous film is always observed beneath the bubble, while for larger contact angles the film ruptures as a TPCL forms. The film thickness decreases after each bouncing cycle along with bubble kinetic energy and the film was found to rupture when the bubble kinetic energy falls below a threshold of $KE = 3 \times 10^{-9}$ J.

- Computations confirmed the presence of a rapidly increasing pressure peak in liquid film prior to impact. The formation of the dimple has been attributed to this increase in pressure. The pressure distribution in the liquid film following impact and during the rebound forces liquid to flow against an adverse pressure gradients. The resulting flow separation previously discussed in Tsao and Koch (1997) was captured by the model.
- A dynamic contact angle model with an implicit slip velocity calculation produced large unphysical mesh dependent oscillations. In contrast both the Navier Slip dynamic and static contact angle models provided bubble velocity predictions shown to be in close agreement with experimental data. The slip Capillary number required for the dynamic contact angle calculation is sufficiently small to explain the limited influence of the dynamic formulation.

7.2 Present contribution

The following specific contributions have been made to the study of the numerical modeling of two-fluid flow problems:

- The bubble behavior during growth, rise, and bounce has been investigated adequately using the bubble geometrical characteristics. These parameters have been used for the assessment of the numerical methods by comparison with experimental data for the full process. In order to establish the sources of inaccuracy in the interface capturing methods for predicting the formation process, the flow field and pressure distribution inside the bubble have been visualized.
- Each interface capturing method has been found to have its own advantages and disadvantages. VOF, for instance, has been found to be sufficient for the analysis of bubble rise and bounce. For bubble growth, LS or CLSVOF should be used. The latter method is mass conservative compared to LS, but it is more complicated to implement.

- The present research has also compared the accuracy and efficiency of both algebraic and geometric methods for studying the bubble growth process. The simulation execution time with the geometrical reconstruction techniques is much larger than that with the algebraic methods. This makes the latter technique more practical for the study of 3D physical applications.
- In an attempt to increase the accuracy of the VOF method implemented in OpenFOAM for capillary dominant problems, the solver has been extended to a coupled method (S-CLSVOF) which preserves the fluid mass during the solution, and provides more accurate surface tension approximation by using both LS and the Dirac functions. The extended solver has provided accurate results for both bubble growth and rise. However, the simulation execution time has been found to be larger with S-CLSVOF than the original VOF method. This is due to the need to solve the re-initialization equation. Furthermore, the new solver adds extra numerical parameters related to the interface thickness. These parameters should be chosen carefully for applications with non-regular mesh resolution.
- A mesh refinement has been presented for capturing the film formation during the bouncing. It has been found that the VOF method can provide accurate results for bubble bouncing similarly to the bubble rise process provided that the thin liquid film formed between the bubble and the solid surface is correctly captured. Thus, choosing the accurate mesh resolution is an essential step for getting accurate results regardless the interface capturing technique.
- In order to investigate the influence of the contact angle boundary condition on the two-fluid flow problems, both static and dynamic models have been implemented and assessed. For the bubble growth process, the value of the imposed static contact angle at the orifice wall has been found to play an important role in determining the bubble geometrical characteristics during the detachment, especially the bubble volume. For bubble bouncing, both dynamic and static contact angle models have provided similar results at the last stages of bouncing. This is due to the small values of the slip Capillary number.
- The present work has included a three-dimensional analysis for the bubble growth and bouncing. For the former case, the inaccuracy in the numerical model implementation has lead to unrealistic errors represented by vertical and lateral oscillations. For bubble bouncing, the 3D simulations have provided a

deep insight into the dimple formation during the first bouncing cycles.

7.3 Future work

The following recommendations are proposed in terms of improving the numerical methods and further investigating the bubble dynamics under several processes:

- The S-CLSVOF solver should be validated for the study of physical applications with non-regular mesh resolution including the bubble bouncing process.
- Further analysis and assessment of the contact angle models (static and dynamic) can be performed concentrating on the last stages of bouncing after the TPCL formation. The study can also include surfaces with contact angle hysteresis so that both advancing and receding angles are included.
- Extend the bubble bouncing analysis to investigate the bubble dynamics during collision against inclined surfaces using both 2D and 3D domains. This process could also include an investigation of the influence of the dynamic contact angle on the film formation during the bubble sliding. Preliminary tests on this topic have been performed through a Master's project during this research. The results, however, are still incomplete and further analysis is required.
- Couple the energy equation with the VOF method in order to study the heat transfer enhancement due to bouncing and sliding. An early study on the analysis of air bubble sliding through a thermal boundary layer is presented in Delauré and Albadawi (2010). This study includes a comparative analysis of bubble dynamics predictions by OpenFOAM and Fluent's VOF schemes. To the author's knowledge, most of the research on heat transfer due to two-fluid flows has considered both the sliding and the evaporation at the same time. The study performed by Yoon et al. (2001) estimated that up to 80 % of the total heat transfer in nucleate boiling is due to the bubble dynamics during its motions.
- Perform a parametric study for both bubble bouncing and sliding under normal and reduced gravitational effect.

A Experimental Analysis

In this section, the experimental setup and work procedure performed by the collaborating group at Trinity College Dublin for the study of two-fluid flow problems are explained briefly.

A.1 Experimental apparatus

The experimental apparatus as shown in Fig. A.1 is made of a 3 mm thick glass and has the dimensions $110 \times 95 \times 195$ mm^3. The injection orifice is made of Aluminum with different radii ($D_o = 0.5, 0.8, 1, 2$ mm), and it is screwed into an adjustable height test surface so that the orifice is on the same level with the test surface (Fig. A.2). The upper foil where the bubble impacts is fixed at the top of the tank while the distance between the lower test surface and the upper foil is adjusted based on the selected height for the bubble to rise freely before impacting on the solid surface. The position of the injection orifice and the adjusted height are displayed in the schematic sketch of Fig. A.2. The experimental rig is designed so that it allows studying the bouncing process using both adiabatic and non-adiabatic conditions. Note that the numerical work presented in this thesis focuses exclusively on the adiabatic case. A preliminary numerical analysis of the heat transfer enhancement due to bubble impact on an inclined surface has nonetheless been presented in Delauré and Albadawi (2010).

The tank is supported using Aluminum structural elements which also integrates supports for the different high speed cameras around the rig. Three cameras are utilized in the experiments; two NAC Hi-Dcam II high speed digital video cameras to record the bubble motion. They are mounted in two perpendicular planes in order to create a 3D image of the bubble dynamics. A FLIR SC6000 high resolution, high frame rate infrared (IR) camera is fixed on the top of the upper surface to record the temperature variations on the upper plate during the test. The high speed

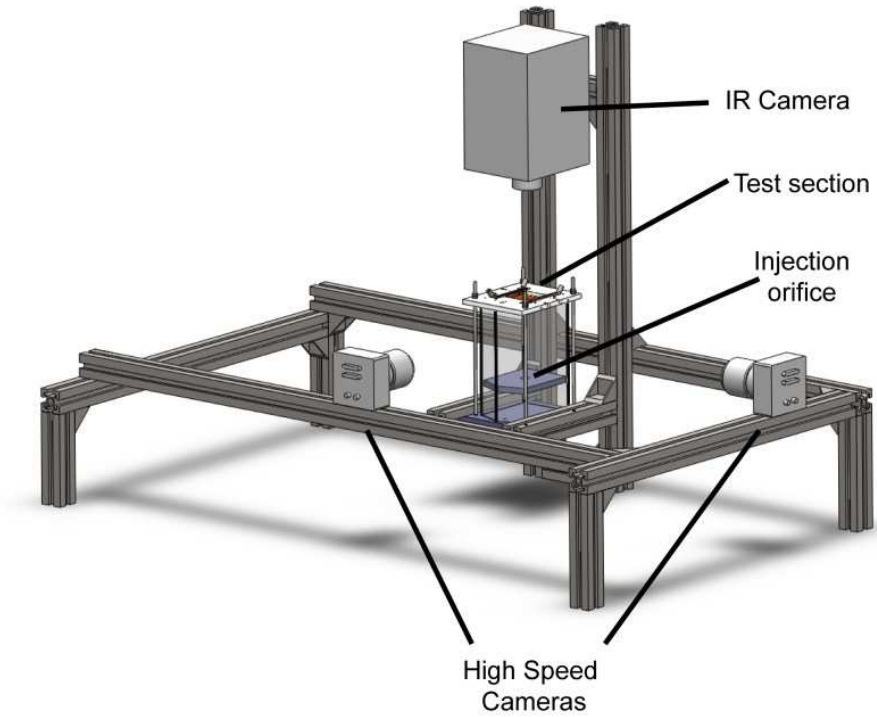

Figure A.1: Experimental apparatus (Donoghue et al., 2011).

cameras are synchronized by means of a signal cable to ensure the simultaneous recording of both cameras at the same time. The cameras have a spatial resolution of approximately 37 $\mu m/pixel$ and are set to record at a frequency of 1000 Hz. Three high intensity light emitting diode (LED) strips (15 bulbs per strip) are placed behind each camera in order to assure capturing the rapid motion of the bubble.

The air is injected through the orifice using a silicon tube, with inner diameter 0.8 mm and length 40 mm, connected to a gas tight syringe (Hamilton "GASTIGHT 1002 series" 2.5 ml was used). The volumetric flow rate is controlled using medical grade infusion pump manufactured by *ksScientific*. The pump is capable of providing flow rates up to 300 mlph. Both the injection device and the pump are located at the same height to avoid fluid issues with the height difference. The upper colliding plate is made of 10 μm thick Constantan foil (Cu55/Ni45) manufactured by *Goodfellow*. The foil is bonded between two copper bus bars. For heat transfer analysis, the rear face of the foil is sprayed with a matt black paint with high emissivity. A 3 mm air gap separates the upper face of the foil from the IR window (Calcium Flouride (CaF2) glass).

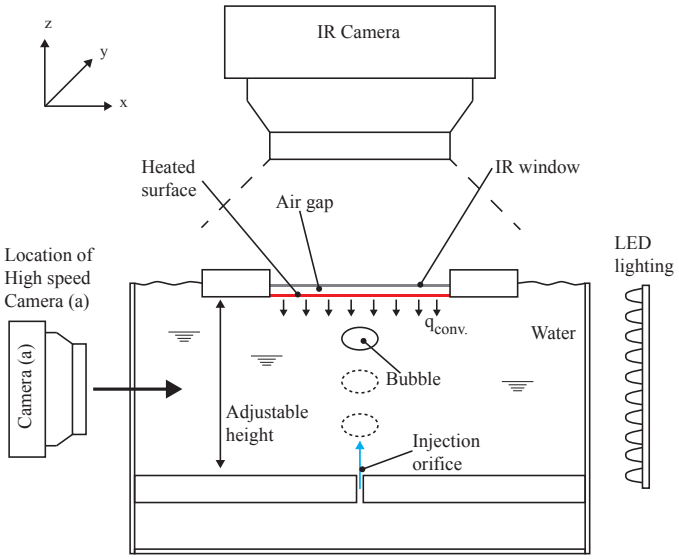

Figure A.2: Schematic sketch of the experimental apparatus showing the position of the bubble during its growth, detachment, free rise, and bouncing against the upper solid surface (Donoghue et al., 2012).

A.2 Experimental procedure

First, the position of the lower test surface, where the injection orifice is located, is set so that the distance between the injection orifice and the upper wall is fixed to the required height for the bubble to rise freely. The tank is filled with ultra pure water maintained at temperature 22 $°C$. Based on the studied mechanism, the cameras are positioned so that they record either the bubble growth and detachment, or the bubble free rise and bouncing. The injection pump is set to provide the required volumetric flow rate. The foil is electrically heated using a Lambda d.c. power supply (for non-adiabatic problems). Both the high speed and infrared cameras are set and synchronized. Once all the recording instruments are set, a single bubble is injected into the rig and the cameras are triggered. After recording and saving the images of the bubble motion, another bubble is injected into the rig. The test can be repeated 4-5 times before replacing the water in the rig with a new ultra pure water. To trigger all the cameras simultaneously, a Thurlby Thandar TG300 series function generator is used to produce a square wave signal that is sent from the IR camera to the PCI controller for the master camera (first camera), which, in turn, triggers the second camera (the slave camera). Sequence of images for the experimental results

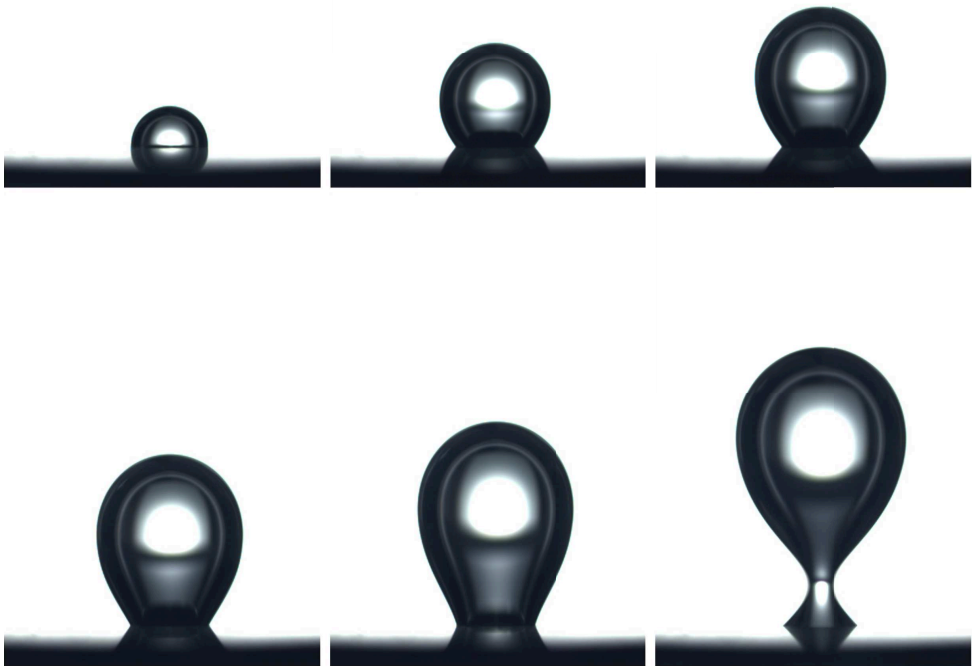

Figure A.3: Experimental bubble shape at six different frames $t/t_{det} \sim 0, 0.2, 0.4, 0.6, 0.8, 1$ ordered from top left to bottom right with $R_o = 0.8$ mm, $\dot{Q} = 200$ mlph.

of bubble growth and bouncing are shown in Fig. A.3 and Fig. A.4 respectively.

A.3 Image processing

The recorded images are analyzed in order to obtain the bubble geometrical characteristics during the bubble motion (See Fig. A.5 for a brief sequence description). The images saved from the high speed cameras have the form of RGB bitmaps. These images are processed using an in-house Matlab code. Three different images are required at the onset of the images processing; background image, calibration

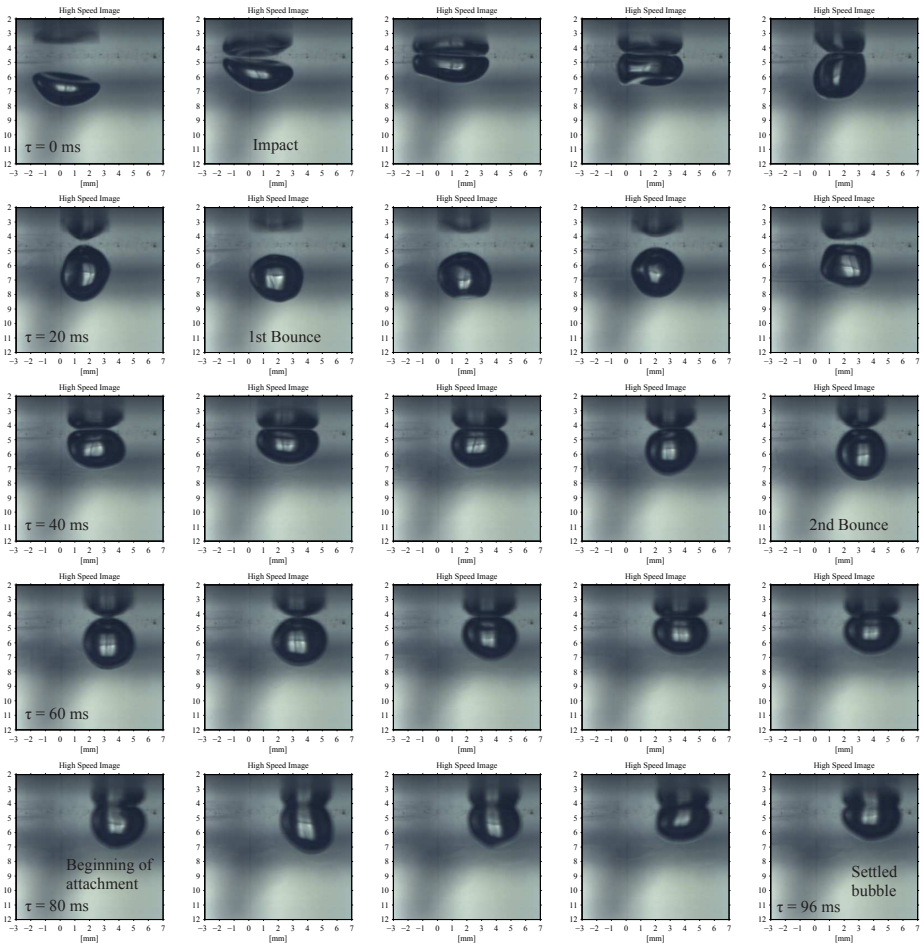

Figure A.4: Sequence of images of a bubble with $D_{eq} \approx 3.3$ mm released from a height of 30 mm away from the upper surface. Time spacing difference between two successive frames is 4 ms.

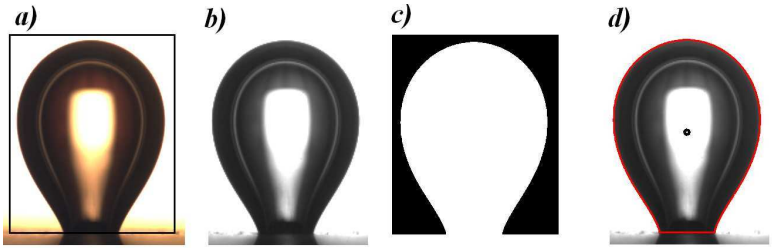

Figure A.5: Sequence of image processing: (a) selection of area of interest, (b) conversion to HSV image, (c) conversion to binary image, (d) determination of the bubble geometrical characteristics. Page 79 in Di Bari (2011).

image, and bubble image. The calibration image is used to set the scaling between the real bubble dimensions (mm) and the image dimensions (pixel). The bubble images are converted first from RGB to HSV color space (Hua, Saturation, and Value). The HSV provides a color space range [0-1]. Each HSV bubble image is subtracted from the background image providing a new space range where the value 0 represents the common elements between the bubble image and the background image (the places where no bubble is identified). The bubble outline is then determined using a thresholding algorithm that provides a binary image of the bubble. The bubble geometrical characteristics can then be calculated using the binary image.

B Available contact angle models in the literature

In the following, a short listing of the most common available models for calculating the dynamic contact angle are presented.

Cox and Voinov models

Cox (1986) and Voinov (1976) developed a hydrodynamic model for the dynamic contact angle in terms of the moving contact line velocity. Based on Cox (1986), the relationship between the microscopic and the macroscopic contact angles is:

$$g(\theta_d) = g(\theta_m) + Ca_{slip} \ln(\frac{r_{macro}}{r_{micro}}) + O(Ca_{slip}) \tag{B.1}$$

where

$$g(\theta) = \int_0^\theta \frac{d\theta}{f(\theta, q)} \tag{B.2}$$

$$f(\theta, q) = \frac{2\sin\theta\{q^2(\theta^2 - \sin^2\theta) + 2q[\theta(\pi-\theta) + \sin^2\theta] + [(\pi-\theta)^2 - \sin^2\theta]\}}{q(\theta^2 - \sin^2\theta)[(\pi-\theta) + \cos\theta\sin\theta] + [(\pi-\theta)^2 - \sin^2\theta](\theta - \cos\theta\sin\theta)} \tag{B.3}$$

The angle θ_m is the microscopic contact angle in the inner region, θ_d is the slope in the outer macroscopic region, and r_{macro}/r_{micro} is the ratio of the outer macroscopic radius to the inner microscopic radius. The slip Capillary number is calculated as $Ca_{slip} = u_{slip}\mu_l/\sigma$ where μ_l is the liquid viscosity. The ratio $q = \mu_l/\mu_g$ is the viscosity ratio with the liquid displaces the gas. The model evidences the dependence on the macroscopic length scale represented by the ratio $\epsilon = r_{micro}/r_{macro} \ll 1$. Eq. B.1 can be simplified to Hoffman-Voinov-Tanner law (Kistler, 1993) which is derived experimentally for small slip Capillary numbers:

$$\theta_d^3 = \theta_m^3 + 9Ca_{slip} \ln(\frac{r_{macro}}{r_{micro}}) \text{ for } \theta_m \leq \theta_d < 135^\circ \tag{B.4}$$

This equation was also approximated by Sheng and Zhou (1992) as:

$$\cos(\theta_d) - \cos(\theta_m) \approx 5.63Ca_{slip} \ln(K/r_{micro}) \tag{B.5}$$

provided that $\mu_l/\mu_g = 1$ and $|\cos\theta| < 0.6$, where K is a constant (with a dimension of length) that depends on the slip model and the outer region length scale r_{macro}. The most simplified form of the Cox model that has been numerically implemented can be written as (Saha and Mitra, 2009):

$$\theta_d^3 = \theta_e^3 + 144Ca_{slip} \tag{B.6}$$

Power law model

Esmail and Ghannam (1990) performed a dimensional analysis of the wetting process of a substrate during the coating process using the displacement depth and the dynamic contact angle as the unknown parameters. The experimental measurements showed that this contact angle follows a power law behavior $\theta = aCa_{slip}^b$, where a, b are constants and $b \sim 0.11$.

Kalliadasis model

Kalliadasis and Chang (1994) proposed a model derived from a complete matched asymptotic analysis for the case of advancing meniscus. They aimed for a constant value in the relation $\theta \sim const \times Ca^{1/3}$. Relieving the singularity at the fluid/fluid/-solid intersection has been achieved by using a finite force at the contact line capable of moving the interface on the solid wall. A universal relation for the dynamic contact angle for fully wetting fluids can be obtained by the asymptotic matching between the outer region (capillary length scale) and the inner region through a lubrication film as (Kalliadasis and Chang, 1994):

$$|\tan\theta_d| = 7.48Ca_{slip}^{1/3} - 3.28\lambda^{0.04}Ca_{slip}^{0.293} \tag{B.7}$$

where λ is a dimensionless number. It has the typical value $\lambda = 10^{-8}$ for wetting fluid flowing through a micro capillary channel with hydraulic radius of order (1mm) (Chakraborty, 2005).

Empirical models

Jiang model: The experimental work performed by Hoffman (1975) on the capillary tube concluded that the contact angle θ_d can be calculated as a function of the static contact angle θ_s and the slip Capillary number. The Hoffman curve was fitted Later by Jiang, Soo-Gun and Slattery (1979) into the form:

$$\frac{\cos\theta_s - \cos\theta_d}{1 + \cos\theta_s} = \tanh 4.96 Ca_{slip}^{0.702} \tag{B.8}$$

Bracke model: The empirical model developed for wetting phenomena and partially wetting surfaces by Bracke, Voeght and Joos (1989) is:

$$\cos\theta_d = \cos\theta_e - 2(1 + \cos\theta_e) Ca_{slip}^{0.5} \tag{B.9}$$

Kistler mode: The dynamic contact angle model proposed by Kistler (1993) is:

$$\theta_d = f_H(Ca + f_H^{-1}(\theta_e)) \tag{B.10}$$

$$f_H[x] = \arccos\left\{1 - 2\tanh\left[5.16\left(\frac{x}{1 + 1.31x^{0.99}}\right)^{0.706}\right]\right\} \tag{B.11}$$

The function $f(H)$ is the Hoffman function while the term $f_H^{-1}(\theta_e)$ is the inverse function of the "Hoffman's" empirical function.

Afkhami mesh dependent model

For droplet spreading, Afkhami mesh dependent model (Afkhami, Zaleski and Bussmann, 2009) is calculated based on Cox model (Cox, 1986) as:

$$\cos(\theta_{num}) = \cos(\theta_{app}) + 5.63 Ca_{slip} \ln(\frac{K}{\Delta/2}) \tag{B.12}$$

where K is constant with a length dimension. The correct value of K can always be obtained by fitting the numerical data to those obtained experimentally or theoretically. For drop spreading with equilibrium angle 60°, θ_{app} is considered equal to 60° and the angle θ_{num} will converge to this value as $Ca_{slip} \to 0$. The main advantage of the mesh dependent model is that it has been shown to be able to provide realistic results using coarse mesh. However, this model is restricted to the

condition $|\cos\theta| < 0.6$.

Newman model

The time dependent dynamic contact angle is given by Newman (1968) as:

$$\cos\theta_d = \cos\theta_e(1 - e^{-\sigma t/\mu M}) \tag{B.13}$$

The parameter M here is an empirical constant which can be obtained by fitting with experimental data. This parameter depends on the contact between the solid surface and the fluid.

Blake model

With the Molecular Kinetics theory, the motion of the contact line is influenced by the overall statistics of the gas-liquid molecules displacements in the contact region domain, so that the dynamics of the contact line is controlled by the adsorption and desorption near the contact point. The velocity of the contact line can be determined in terms of the frequency of the molecular displacement in the positive and negative directions. Blake and Haynes (1969) derived an equation for the microscopic contact angle dependence on the contact line speed as:

$$u_{slip} = -2Kl\sinh\{\frac{\sigma l^2}{2k_BT}(\cos\theta_e - \cos\theta_m)\} \tag{B.14}$$

where K is the frequency of the molecular displacement, k_B is the Boltzmann constant, and T is the absolute temperature, l is the average molecular jumping distance, and θ_e is the equilibrium contact angle. The equation shows that the inner microscopic angle is not constant, but it is related to the slip velocity. The values of these parameters were later determined by Blake (2006).

Shikhmurzaev model

The dynamic contact angle model is given as (Shikhmurzaev, 1997):

$$\cos\theta_s - \cos\theta_d = \frac{2V(\rho_{2e}^{s*} + \rho_{1e}^{s*}u_0)}{(1 - \rho_{1e}^{s*})[(\rho_{2e}^{s*} + V^2)^{1/2} + V]} \tag{B.15}$$

The three phenomenological constants (V, ρ_{2e}^{s*}, u_0) have the following values $(0.54, 12.5, 0.07)$, respectively (Popescu, Ralston and Sedev, 2008).

C Interface correction

At the wall boundaries where a contact angle model is imposed, the interface normal calculated from the gradient of the VOF function ($\hat{\mathbf{n}}_c$) is corrected to satisfy the implemented contact angle as shown in Fig. C.1. This correction is performed using a linear interpolation process described as:

$$\hat{\mathbf{n}} = a\hat{\mathbf{n}}_w + b\hat{\mathbf{n}}_c \tag{C.1}$$

where ($\hat{\mathbf{n}}$) is the corrected unit interface normal.

The calculated and corrected interfaces create the angles θ_α and θ_i respectively with the unit normal vector to the wall $\hat{\mathbf{n}}_w$:

$$\hat{\mathbf{n}}_c \cdot \hat{\mathbf{n}}_w = \cos\theta_\alpha \tag{C.2}$$

$$\hat{\mathbf{n}} \cdot \hat{\mathbf{n}}_w = \cos\theta_i \tag{C.3}$$

The constant values a and b in Eq. C.1 are obtained using the inner product of ($\hat{\mathbf{n}} \cdot \hat{\mathbf{n}}_w$) and ($\hat{\mathbf{n}} \cdot \hat{\mathbf{n}}_c$) as follows:

$$\hat{\mathbf{n}} \cdot \hat{\mathbf{n}}_w = (a\hat{\mathbf{n}}_w + b\hat{\mathbf{n}}_c) \cdot \hat{\mathbf{n}}_w \tag{C.4a}$$
$$\hat{\mathbf{n}} \cdot \hat{\mathbf{n}}_w = a\hat{\mathbf{n}}_w \cdot \hat{\mathbf{n}}_w + b\hat{\mathbf{n}}_c \cdot \hat{\mathbf{n}}_w \tag{C.4b}$$
$$\cos\theta_i = a + b\cos\theta_\alpha \tag{C.4c}$$

$$\hat{\mathbf{n}} \cdot \hat{\mathbf{n}}_c = (a\hat{\mathbf{n}}_w + b\hat{\mathbf{n}}_c) \cdot \hat{\mathbf{n}}_c \tag{C.5a}$$
$$\hat{\mathbf{n}} \cdot \hat{\mathbf{n}}_c = a\hat{\mathbf{n}}_w \cdot \hat{\mathbf{n}}_c + b\hat{\mathbf{n}}_c \cdot \hat{\mathbf{n}}_c \tag{C.5b}$$
$$\cos(\theta_\alpha - \theta_i) = a\cos\theta_\alpha + b \tag{C.5c}$$

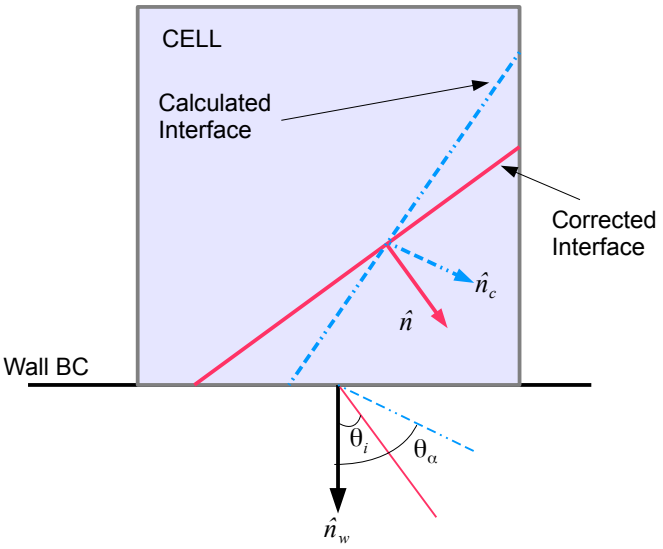

Figure C.1: Calculated and corrected interfaces at the neighboring cell to the wall boundary condition.

Solving Eqs. C.4 and C.5 together gives:

$$a = \frac{\cos\theta_i - \cos\theta_\alpha \cos\left(\theta_\alpha - \theta_i\right)}{\left(1 - \cos\theta_\alpha \cos\theta_\alpha\right)} \tag{C.6}$$

$$b = \frac{\cos\left(\theta_\alpha - \theta_i\right) - \cos\theta_i \cos\theta_\alpha}{\left(1 - \cos\theta_\alpha \cos\theta_\alpha\right)} \tag{C.7}$$

D Time step constraints

The adjusted time step is calculated in terms of the maximum Courant number (Co_{max}) and the maximum interface Courant number ($Co_{\alpha,max}$) which are calculated as:

$$Co_{max} = max(\frac{\mathbf{V}_f \cdot \mathbf{S}_f}{\mathbf{d} \cdot \mathbf{S}_f})\Delta t \tag{D.1}$$

$$Co_{\alpha,max} = max(\frac{[pos(\alpha_f - 0.01) * pos(0.99 - \alpha_f)] * (\mathbf{V}_f \cdot \mathbf{S}_f)}{\mathbf{d} \cdot \mathbf{S}_f})\Delta t \tag{D.2}$$

where *pos* function returns the positive value.

The adjusted time step at the beginning of the new time iteration is then calculated as:

$$\Delta t^{n+1} = min\{Co_{min} * \Delta t^n, (1 + 0.1Co_{min}) * \Delta t^n, 1.2\Delta t^n, \Delta t_{max}\} \tag{D.3}$$

with:

$$Co_{min} = min(Co_{max}, Co_{\alpha,max}) \tag{D.4}$$

where Δt_{max} is the maximum time step imposed by the user. The values 0.1 and 1.2 are damping factors used only when the time step is increasing. They reduce any possible oscillation in the solution.

E Numerical results

This section is a continuation of the numerical results presented for the two-fluid flow problems.

Table E.1: Comparison of bubble detachment volume and radius for different rig heights ($10, 20, 30$ mm) using the 3D numerical domain with S-CLSVOF and VOF methods, $R_o = 0.5, 0.25$ mm.

	R_o [mm]	Rig height [mm]	v_0 m/s	t_{det} [s]	Cg_{det} [mm]	V_{det} [mm^3]	R_{det} [mm]	$E_{R_{det}}$ [%]
Exp	0.25					9.203	1.3	
Exp	0.5					21.688	1.729	
S-CLSVOF	0.25	10	0.05	0.64	3.473	8.188	1.250	3.818
S-CLSVOF (F)	0.5	10	0.05	0.503	2.884	21.150	1.715	0.834
S-CLSVOF	0.5	10	0.05	0.472	2.681	19.4	1.667	3.648
VOF	0.5	10	0.05	0.394	2.433	15.630	1.551	10.344
S-CLSVOF	0.5	20	0.1	0.254	4.311	20.398	1.694	2.022
S-CLSVOF (F)	0.5	20	0.1	0.292	4.553	24.258	1.795	-3.803
S-CLSVOF	0.5	30	0.1	0.252	4.400	20.250	1.691	2.261

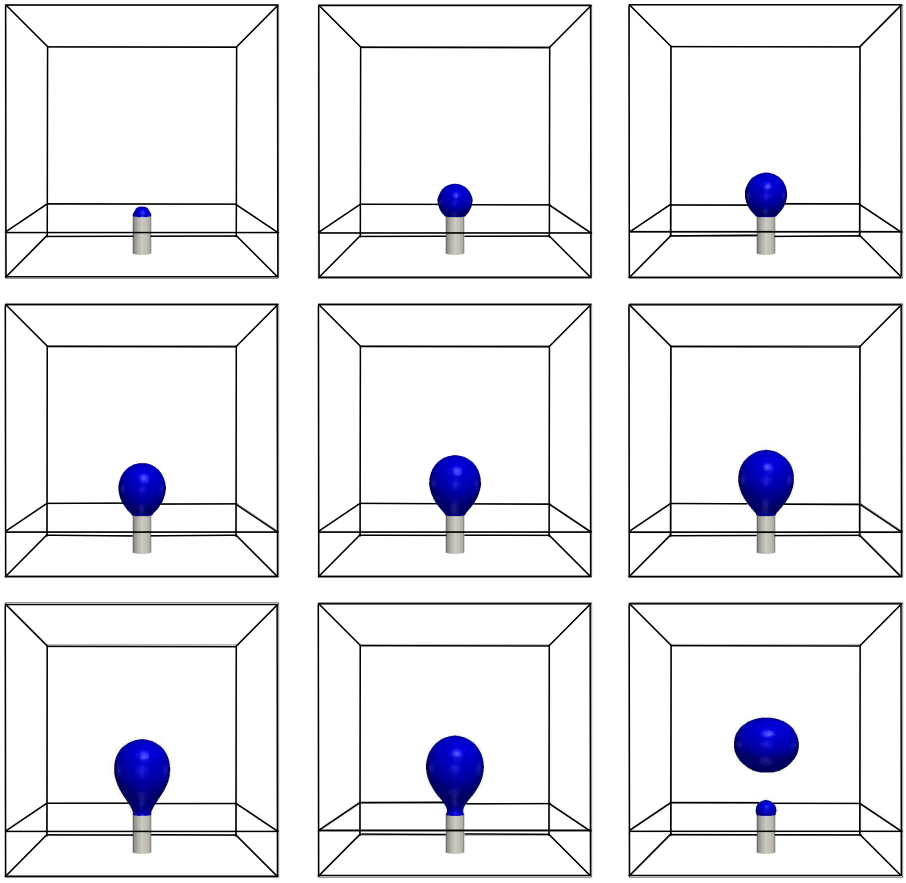

Figure E.1: Sequence of screenshots in the (y-z) plane illustrating bubble growth from a wall orifice ($R_o = 0.5$ mm) using the S-CLSVOF method with inflow velocity 0.05 m/s. The (z) coordinate indicates the direction of the gravitational acceleration. The frames are arranged from top left to bottom right with times $0, 0.08, 0.16, 0.24, 0.32, 0.4, 0.44, 0.46, 0.48$ s, respectively.

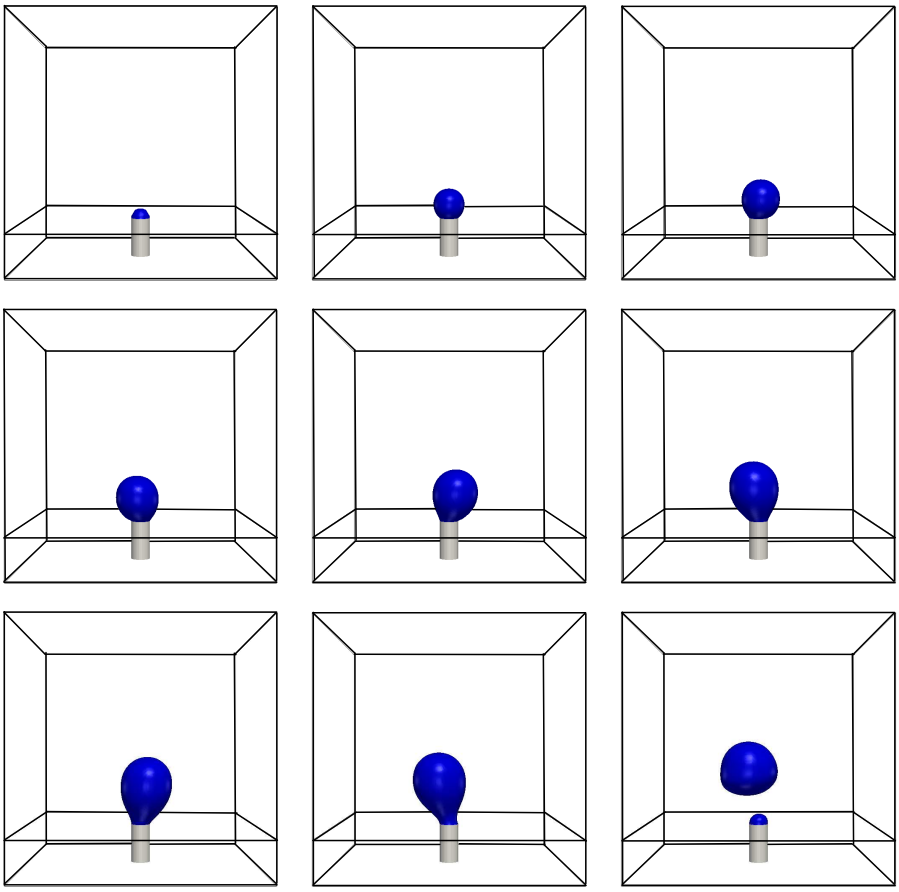

Figure E.2: Sequence of screenshots in the (y-z) plane illustrating bubble growth from a wall orifice ($R_o = 0.5$ mm) using the VOF method with inflow velocity 0.05 m/s. The (z) coordinate indicates the direction of the gravitational acceleration. The frames are arranged from top left to bottom right with times $0, 0.06, 0.12, 0.18, 0.24, 0.3, 0.36, 0.38, 0.4$ s, respectively.

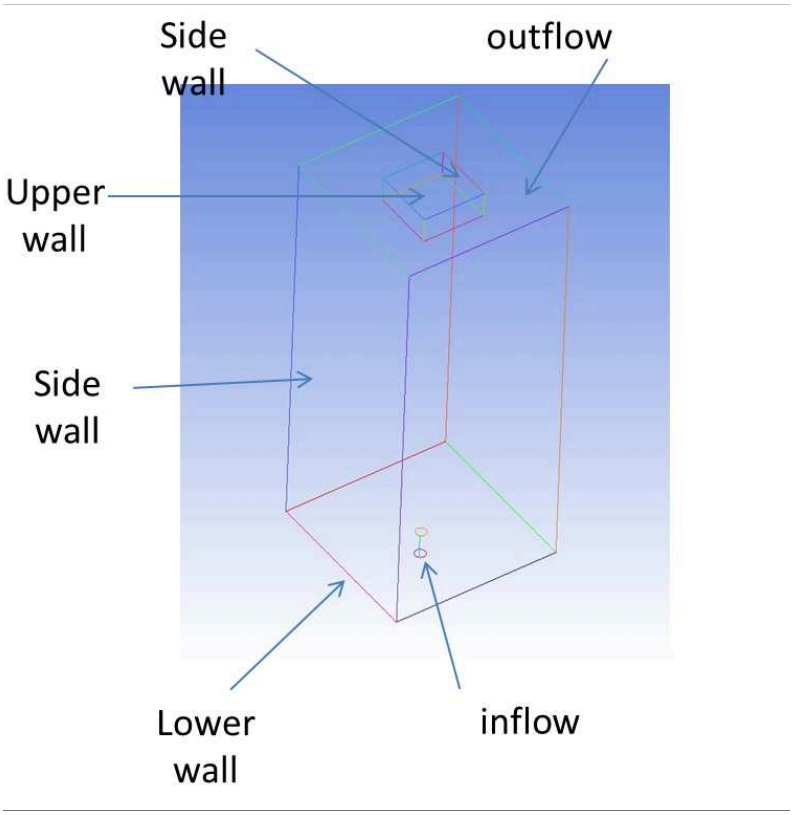

Figure E.3: Schematic diagram of the numerical rig in 3D domain.

Bibliography

Afkhami, S. and Bussmann, M. (2008), 'Height functions for applying contact angles to 2D VOF simulations', *International Journal for Numerical Methods in Fluids* **57**(4), 453–472.

Afkhami, S., Zaleski, S. and Bussmann, M. (2009), 'A mesh-dependent model for applying dynamic contact angles to VOF simulations', *Journal of computational physics* **228**(15), 5370–5389.

Albadawi, A., Delauré, Y., Donoghue, D. B., Robinson, A. and Murray, D. B. (2012), Numerical investigation of volume of fluid and level set interface capturing methods for bubble growth and detachment, *in* 'Journal of Physics: Conference Series', Vol. 395, IOP Publishing, p. 012166.

Albadawi, A., Donoghue, D. B., Robinson, A. J., Murray, D. B. and Delauré, Y. M. C. (2012), 'On the analysis of bubble growth and detachment at low Capillary and Bond numbers using Volume of Fluid and Level Set methods', *Chemical Engineering Science* **90**, 77–91.

Albadawi, A., Donoghue, D. B., Robinson, A. J., Murray, D. B. and Delauré, Y. M. C. (2013), 'Influence of surface tension implementation in Volume of Fluid and coupled Volume of Fluid with Level Set methods for bubble growth and detachment', *International Journal of Multiphase Flow* **53**, 11–28.

Amaya-Bower, L. and Lee, T. (2010), 'Single bubble rising dynamics for moderate Reynolds number using lattice Boltzmann method', *Computers & Fluids* **39**(7), 1191–1207.

Andrillon, Y. (2004), Simulation d'ecoulements a surface libre par une methode de capture d'interface en formulation totalement couplee, PhD thesis.

Annaland, M. V. S., Deen, N. and Kuipers, J. (2005), 'Numerical simulation of gas

bubbles behaviour using a three dimensional volume of fluid method', *Chemical engineering science* **60**(11), 2999–3011.

Annapragada, S. R., Murthy, J. Y. and Garimella, S. V. (2012), 'Prediction of droplet dynamics on an incline', *International Journal of Heat and Mass Transfer* **55**, 1466–1474.

Ansari, M. and Nimvari, M. (2011), 'Bubble viscosity effect on internal circulation within the bubble rising due to buoyancy using the level set method', *Annals of Nuclear Energy* **38**(12), 2770–2778.

Ansys (2011). ANSYS Fluent 13, ANSYS Inc, Canonsburg, PA 15317 U.S.A, http://www.ansys.com.

Aulisa, E., Manservisi, S. and Scardovelli, R. (2003), 'A mixed markers and volume-of-fluid method for the reconstruction and advection of interfaces in two-phase and free-boundary flows', *Journal of Computational Physics* **188**(2), 611–639.

Aulisa, E., Manservisi, S. and Scardovelli, R. (2004), 'A surface marker algorithm coupled to an area-preserving marker redistribution method for three-dimensional interface tracking', *Journal of Computational Physics* **197**(2), 555–584.

Aulisa, E., Manservisi, S., Scardovelli, R. and Zaleski, S. (2007), 'Interface reconstruction with least-squares fit and split advection in three dimensional Cartesian geometry', *Journal of Computational Physics* **225**(2), 2301–2319.

Badam, V., Buwa, V. and Durst, F. (2007), 'Experimental investigations of regimes of bubble formation on submerged orifices under constant flow condition', *The Canadian Journal of Chemical Engineering* **85**(3), 257–267.

Benson, D. J. (2002), 'Volume of fluid interface reconstruction methods for multi-material problems', *Applied Mechanics Reviews* **55**, 151.

Berberović, E., van Hinsberg, N. P., Jakirlić, S., Roisman, I. V. and Tropea, C. (2009), 'Drop impact onto a liquid layer of finite thickness: Dynamics of the cavity evolution', *Physical Review E* **79**(3), 36306.

Best, J. (1993), 'The formation of toroidal bubbles upon the collapse of transient cavities', *Journal of Fluid Mechanics* **251**, 79–79.

Bhaga, D. and Weber, M. (1981), 'Bubbles in viscous liquids: shapes, wakes and velocities', *Journal of Fluid Mechanics* **105**, 61–85.

Blake, T. D. (2006), 'The physics of moving wetting lines', *Journal of colloid and interface science* **299**(1), 1–13.

Blake, T. and Haynes, J. (1969), 'Kinetics of liquidliquid displacement', *Journal of colloid and interface science* **30**(3), 421–423.

Bonn, D., Eggers, J., Indekeu, J., Meunier, J. and Rolley, E. (2009), 'Wetting and spreading', *Reviews of modern physics* **81**(2), 739.

Bonometti, T. and Magnaudet, J. (2007), 'An interface capturing method for incompressible two-phase flows. Validation and application to bubble dynamics', *International Journal of Multiphase Flow* **33**(2), 109–133.

Brackbill, J., Kothe, D. and Zemach, C. (1992), 'A continuum method for modeling surface tension', *Journal of computational physics* **100**(2), 335–354.

Bracke, M., Voeght, F. D. and Joos, P. (1989), 'The kinetics of wetting: the dynamic contact angle', *Trends in Colloid and Interface Science III* **79**, 142–149.

Brennan, D. (2001), The numerical simulation of two-phase flows in Settling Tanks, PhD thesis, Imperial College of Science, Technology and Medicine, Department of Mechanical Engineering, London.

Briant, A., Wagner, A. and Yeomans, J. (2004), 'Lattice Boltzmann simulations of contact line motion. I. Liquid gas systems', *Physical Review E* **69**(3), 031602.

Buscaglia, G. C. and Ausas, R. F. (2011), 'Variational formulations for surface tension, capillarity and wetting', *Computer Methods in Applied Mechanics and Engineering* **200**(45), 3011–3025.

Bussmann, M., Mostaghimi, J. and Chandra, S. (1999), 'On a three-dimensional volume tracking model of droplet impact', *Physics of Fluids* **11**(6), 1406–1417.

Buwa, V. V., Gerlach, D., Durst, F. and Schlücker, E. (2007), 'Numerical simulations of bubble formation on submerged orifices: Period-1 and period-2 bubbling regimes', *Chemical Engineering Science* **62**(24), 7119–7132.

Cabassud, C., Laborie, S. and Lainé, J. (1997), 'How slug flow can improve ultrafiltration flux in organic hollow fibres', *Journal of Membrane Science* **128**(1), 3 – 101.

Cahn, J. W. (1961), 'On spinodal decomposition', *Acta metallurgica* **9**(9), 795–801.

Canot, E., Davoust, L., Hammoumi, M. E. and Lachkar, D. (2003), 'Numerical simulation of the buoyancy-driven bouncing of a 2-D bubble at a horizontal wall', *Theoretical and Computational Fluid Dynamics* **17**(1), 51–72.

Carlson, A., Kudinov, P. and Narayanan, C. (2008), Prediction of two-phase flow in small tubes: a systematic comparison of state-of-the-art CMFD codes, *in* '5th European Thermal-Sciences Conference, The Netherlands'.

Cervone, A., Manservisi, S., Scardovelli, R. and Zaleski, S. (2009), 'A geometrical predictor corrector advection scheme and its application to the volume fraction function', *Journal of Computational Physics* **228**(2), 406–419.

Chakraborty, I., Biswas, G. and Ghoshdastidar, P. (2011), 'Bubble generation in quiescent and co-flowing liquids', *International Journal of Heat and Mass Transfer* **54**, 4673–4688.

Chakraborty, I., Biswas, G. and Ghoshdastidar, P. (2013), 'A coupled level set and volume of fluid method for the buoyant rise of gas bubbles in liquids', *International Journal of Heat and Mass Transfer* **58**(1), 240–259.

Chakraborty, I., Ray, B., Biswas, G., Durst, F., Sharma, A. and Ghoshdastidar, P. (2009), 'Computational investigation on bubble detachment from submerged orifice in quiescent liquid under normal and reduced gravity', *Physics of Fluids* **21**, 062103.

Chakraborty, S. (2005), 'Dynamics of capillary flow of blood into a microfluidic channel', *Lab on a Chip* **5**(4), 421–430.

Chan, D. Y., Klaseboer, E. and Manica, R. (2011), 'Film drainage and coalescence between deformable drops and bubbles', *Soft Matter* **7**(6), 2235–2264.

Chen, C. and Fan, L. S. (2004), 'Discrete simulation of gas/liquid bubble columns and gas/liquid/ solid fluidized beds', *AIChE Journal* **50**(2), 288–301.

Chen, Y., Mertz, R. and Kulenovic, R. (2009), 'Numerical simulation of bubble formation on orifice plates with a moving contact line', *International Journal of Multiphase Flow* **35**(1), 66–77.

Clift, R., Grace, J. and Weber, M. E. (1978), *Weber, ME Bubbles, Drops and Particles*, New York: Academic Press.

Cornwell, K. (1990), 'The influence of bubbly flow on boiling from a tube in a bundle', *International Journal of Heat and Mass Transfer* **33**(12), 2579–2584.

Cox, R. (1986), 'The dynamics of the spreading of liquids on a solid surface. Part 1. Viscous flow', *Journal of Fluid Mechanics* **168**(1), 169–194.

Dandy, D. and Leal, L. (1989), 'Buoyancy-driven motion of a deformable drop through a quiescent liquid at intermediate Reynolds numbers', *Journal of Fluid Mechanics* **209**, 161.

Darwish, M. and Moukalled, F. (2003), 'TVD schemes for unstructured grids', *International Journal of Heat and Mass Transfer* **46**(4), 599–611.

Davidson, J. and Schuler, B. (1960), 'Bubble formation at an orifice in a viscous liquid', *Chemical Engineering Research and Design* **38**(a), 144–154. Transactions institute of Chemical Engineers.

De Gennes, P. G. (1985), 'Wetting, statics and dynamics', *Reviews of modern physics* **57**(3), 827.

Delauré, Y. and Albadawi, A. (2010), On air bubbles sliding through a thermal boundary layer, *in* '5th OpenFOAM workshop, Sweden'.

Delauré, Y., Chan, V. and Murray, D. (2003), 'A simultaneous piv and heat transfer study of bubble interaction with free convection flow', *Exp. Therm. Fluid Sci.* **27**(8), 911–26.

Di Bari, S. (2011), Bubble growth dynamics including gravitational and electric field effects, PhD thesis, Department of Mechanical and Manufacturing Engineering, Trinity College Dublin, Ireland.

Di Bari, S., Lakehal, D. and Robinson, A. (2013), 'A numerical study of quasi-static gas injected bubble growth: Some aspects of gravity', *International Journal of Heat and Mass Transfer* **64**, 468–482.

Di Bari, S. and Robinson, A. J. (2013), 'Experimental study of gas injected bubble growth from submerged orifices', *Experimental Thermal and Fluid Science* **44**, 124–137.

Ding, H. and Spelt, P. D. (2007*a*), 'Inertial effects in droplet spreading: a comparison between diffuse-interface and level-set simulations', *Journal of Fluid Mechanics* **576**, 287.

Ding, H. and Spelt, P. D. (2007*b*), 'Wetting condition in diffuse interface simulations of contact line motion', *Physical Review E* **75**(4), 046708.

Donoghue, D. B., Delauré, Y. M., Albadawi, A., Robinson, A. J. and Murray, D. B. (2012), Bouncing bubble dynamics and associated enhancement of heat transfer, *in* 'Journal of Physics: Conference Series', Vol. 395, IOP Publishing, p. 012167.

Donoghue, D. B., Delauré, Y. M., Robinson, A. J. and Murray, D. B. (2011), Heat transfer enhancement from bouncing bubble dynamics, *in* 'Proceedings of the 6th Baltic Heat Transfer Conference, Tampere, Finland'.

Doubliez, L. (1991), 'The drainage and rupture of a non-foaming liquid film formed upon bubble impact with a free surface', *International Journal of Multiphase Flow* **17**(6), 783–803.

Duhar, G. and Colin, C. (2006), 'Dynamics of bubble growth and detachment in a viscous shear flow', *Physics of Fluids* **18**, 077101.

Dupont, J. B. and Legendre, D. (2010), 'Numerical simulation of static and sliding drop with contact angle hysteresis', *Journal of Computational Physics* **229**(7), 2453–2478.

Dussan, E. (1979), 'On the spreading of liquids on solid surfaces: static and dynamic contact lines', *Annual Review of Fluid Mechanics* **11**(1), 371–400.

Eggers, J. (2004), 'Toward a description of contact line motion at higher capillary numbers', *Physics of Fluids* **16**(9), 3491.

Elizabeth, B., Dussan, V. and Davis, S. (1974), 'On the motion of a fluid-fluid interface along a solid surface', *J.Fluid Mech* **65**, 71–95.

Enright, D., Fedkiw, R., Ferziger, J. and Mitchell, I. (2002), 'A hybrid particle level set method for improved interface capturing', *Journal of Computational Physics* **183**(1), 83–116.

Enright, D., Losasso, F. and Fedkiw, R. (2005), 'A fast and accurate semi-lagrangian particle level set method', *Computers & Structures* **83**(6), 479–490.

Esmail, M. and Ghannam, M. (1990), 'Air entrainment and dynamic contact angles in hydrodynamics of liquid coating', *The Canadian Journal of Chemical Engineering* **68**(2), 197–203.

Fan, L. S. and Tsuchiya, K. (1990), *Bubble wake dynamics in liquids and liquid-solid suspensions*, Butterworth-Heinemann.

Fedkiw, R. P., Aslam, T., Merriman, B. and Osher, S. (1999), 'A non-oscillatory Eulerian approach to interfaces in multimaterial flows (the ghost fluid method)', *Journal of Computational Physics* **152**(2), 457–492.

Fetzer, R. and Ralston, J. (2009), 'Dynamic dewetting regimes explored', *The Journal of Physical Chemistry C* **113**(20), 8888–8894.

Francois, M. M., Cummins, S. J., Dendy, E. D., Kothe, D. B., Sicilian, J. M. and Williams, M. W. (2006), 'A balanced force algorithm for continuous and sharp interfacial surface tension models within a volume tracking framework', *Journal of Computational Physics* **213**(1), 141–173.

Fukai, J., Zhao, Z., Poulikakos, D., Megaridis, C. and Miyatake, O. (1993), 'Modeling of the deformation of a liquid droplet impinging upon a flat surface', *Physics of Fluids A: Fluid Dynamics* **5**, 2588.

Gekle, S., Snoeijer, J. H., Lohse, D. and van der Meer, D. (2009), 'Approach to universality in axisymmetric bubble pinch-off', *Physical Review E* **80**(3), 036305.

Gennes, P.-G. D. (1985), 'Wetting: statics and dynamics', *Reviews of modern physics* **57**(3), 827.

Gerlach, D., Alleborn, N., Buwa, V. and Durst, F. (2007), 'Numerical simulation of periodic bubble formation at a submerged orifice with constant gas flow rate', *Chemical engineering science* **62**(7), 2109–2125.

Gerlach, D., Biswas, G., Durst, F. and Kolobaric, V. (2005), 'Quasi-static bubble formation on submerged orifices', *International Journal of Heat and Mass Transfer* **48**(2), 425–438.

Gerlach, D., Tomar, G., Biswas, G. and Durst, F. (2006), 'Comparison of volume-of-fluid methods for surface tension-dominant two-phase flows', *International Journal of Heat and Mass Transfer* **49**(3), 740–754.

Ginzburg, I. and Wittum, G. (2001), 'Two-phase flows on interface refined grids modeled with VOF, staggered finite volumes, and spline interpolants', *Journal of Computational Physics* **166**(2), 302–335.

Gnyloskurenko, S., Byakova, A., Raychenko, O. and Nakamura, T. (2003), 'Influence of wetting conditions on bubble formation at orifice in an inviscid liquid. Transformation of bubble shape and size', *Colloids and Surfaces A: Physicochemical and Engineering Aspects* **218**(1-3), 73–87.

Gordillo, J., Sevilla, A., Rodríguez-Rodríguez, J. and Martínez-Bazán, C. (2005), 'Axisymmetric bubble pinch off at high Reynolds numbers', *Physical Review Letters* **95**(19), 194501.

Grace, J. (1973), 'Shapes and velocities of bubbles rising in infinite liquids', *Trans.Inst.Chem.Eng.* **51**(2), 116–120.

Gross, S. and Reusken, A. (2007*a*), 'An extended pressure finite element space for two-phase incompressible flows with surface tension', *Journal of Computational Physics* **224**(1), 40–58.

Gross, S. and Reusken, A. (2007*b*), 'Finite element discretization error analysis of a surface tension force in two-phase incompressible flows', *Siam Journal on Numerical Analysis* **45**(4), 1679–1700.

Gueyffier, D., Li, J., Nadim, A., Scardovelli, R. and Zaleski, S. (1999), 'Volume-of-fluid interface tracking with smoothed surface stress methods for three-dimensional flows', *Journal of Computational Physics* **152**(2), 423–456.

Harten, A., Engquist, B., Osher, S. and Chakravarthy, S. R. (1987), 'Uniformly high order accurate essentially non-oscillatory schemes, iii', *Journal of Computational Physics* **71**(2), 231–303.

Hendrix, M. H., Manica, R., Klaseboer, E., Chan, D. Y. and Ohl, C.-D. (2012), 'Spatiotemporal evolution of thin liquid films during impact of water bubbles on glass on a micrometer to nanometer scale', *Physical Review Letters* **108**(24), 247803.

Herrmann, M. (2005), 'Refined Level Set Grid method for tracking interfaces', *CTR Annual Research Briefs* pp. 3–18.

Herrmann, M. (2008), 'A balanced force refined level set grid method for two-phase flows on unstructured flow solver grids', *Journal of computational physics* **227**(4), 2674–2706.

Hieber, S. E. and Koumoutsakos, P. (2005), 'A lagrangian particle level set method', *Journal of Computational Physics* **210**(1), 342–367.

Hirt, C. W. and Nichols, B. D. (1981), 'Volume of fluid (VOF) method for the dynamics of free boundaries* 1', *Journal of computational physics* **39**(1), 201–225.

Hocking, L. (1977), 'A moving fluid interface. Part 2. The removal of the force singularity by a slip flow', *Journal of Fluid Mechanics* **79**(02), 209–229.

Hocking, L. (1983), 'The spreading of a thin drop by gravity and capillarity', *The Quarterly Journal of Mechanics and Applied Mathematics* **36**(1), 55–69.

Hocking, L. and Rivers, A. (1982), 'Spreading of a drop by capillary action', *Journal of Fluid Mechanics* **121**, 425–442.

Hoffman, R. L. (1975), 'A study of the advancing interface. I. Interface shape in liquid gas systems', *Journal of colloid and interface science* **50**(2), 228–241.

Hua, J. and Lou, J. (2007), 'Numerical simulation of bubble rising in viscous liquid', *Journal of Computational Physics* **222**(2), 769–795.

Huh, C. and Scriven, L. (1971), 'Hydrodynamic model of steady movement of a solid/liquid/fluid contact line', *Journal of colloid and interface science* **35**(1), 85–101.

Issa, R. (1986), 'Solution of the implicitly discretised fluid flow equations by operator-splitting', *Journal of Computational physics* **62**(1), 40–65.

Jacqmin, D. (1999), 'Calculation of two-phase navier stokes flows using phase field modeling', *Journal of Computational Physics* **155**(1), 96–127.

Jacqmin, D. (2000), 'Contact-line dynamics of a diffuse fluid interface', *Journal of Fluid Mechanics* **402**(1), 57–88.

Jiang, T.-S., Soo-Gun, O. H. and Slattery, J. C. (1979), 'Correlation for dynamic contact angle', *Journal of colloid and interface science* **69**(1), 74–77.

Kafka, F. Y. and Dussan, E. (1979), 'On the interpretation of dynamic contact angles in capillaries', *J.Fluid Mech* **95**(3), 535–565.

Kalliadasis, S. and Chang, H. C. (1994), 'Apparent dynamic contact angle of an advancing gas liquid meniscus', *Physics of Fluids* **6**, 12–23.

Kang, M., Fedkiw, R. P. and Liu, X. D. (2000), 'A boundary condition capturing method for multiphase incompressible flow', *Journal of Scientific Computing* **15**(3), 323–360.

Kistler, S. (1993), Hydrodynamics of wetting, *in* J. B. (Ed.), ed., 'Wettability', Marcel Dekker, New York, p. 311.

Klaseboer, E., Chevaillier, J. P., Gourdon, C. and Masbernat, O. (2000), 'Film drainage between colliding drops at constant approach velocity: experiments and modeling', *Journal of colloid and interface science* **229**(1), 274–285.

Klaseboer, E., Chevaillier, J.-P., Maté, A., Masbernat, O. and Gourdon, C. (2001), 'Model and experiments of a drop impinging on an immersed wall', *Physics of Fluids* **13**, 45.

Klaseboer, E., Manica, R. and Chan, D. (2012), rising and bouncing bubbles against a boundary with BEM; the effect of viscous stresses, *in* 'Ninth International Conference on CFD in the Minerals and Process Industries'.

Kosior, D., Zawala, J. and Malysa, K. (2012), 'Influence of n-octanol on the bubble impact velocity, bouncing and the three phase contact formation at hydrophobic solid surfaces', *Colloids and Surfaces A: Physicochemical and Engineering Aspects* .

Kothe, D. and Mjolsness, R. (1992), 'RIPPLE: A new model for incompressible flows with free surfaces', *AIAA Journal* **30**(11), 2694–2700.

Krasowska, M., Krzan, M. and Malysa, K. (2003), Bubble collisions with hydrophobic and hydrophilic surfaces in a-terpineol solutions, *in* 'Physicochemical Problems of Mineral Processing', Vol. 37, pp. 37–50.

Krasowska, M., Zawala, J. and Malysa, K. (2009), 'Air at hydrophobic surfaces and kinetics of three phase contact formation', *Advances in Colloid and Interface Science* **147**, 155–169.

Kulkarni, A. A. and Joshi, J. B. (2005), 'Bubble formation and bubble rise velocity in gas liquid systems: a review', *Industrial & Engineering Chemistry Research* **44**(16), 5873–5931.

Kumar, S. S. and Delauré, Y. M. C. (2012), 'An Assessment of Suitability of a SIMPLE VOF/PLIC - CSF Multiphase Flow Model for Rising Bubble Dynamics', *The Journal of Computational Multiphase Flows* **4**(1), 65–84.

Kunkelmann, C. and Stephan, P. (2010), 'Modification and extension of a standard volume-of-fluid solver for simulating boiling heat transfer', *V European Conference on Computational Fluid Dynamics* .

Latva-Kokko, M. and Rothman, D. H. (2007), 'Scaling of dynamic contact angles in a lattice-Boltzmann model', *Physical Review Letters* **98**(25), 254503.

Lee, S. L. and Tien, W. B. (2009), 'Growth and detachment of carbon dioxide bubbles on a horizontal porous surface with a uniform mass injection', *International Journal of Heat and Mass Transfer* **52**(13-14), 3000–3008.

Legendre, D., Daniel, C. and Guiraud, P. (2005), 'Experimental study of a drop bouncing on a wall in a liquid', *Physics of Fluids* **17**, 097105.

Legendre, D., Zenit, R. and Velez-Cordero, J. R. (2012), 'On the deformation of gas bubbles in liquids', *Physics of Fluids* **24**, 043303.

Leifer, I., Patro, R. K. and Bowyer, P. (2000), 'A study on the temperature variation of rise velocity for large clean bubbles', *Journal of Atmospheric and Oceanic Technology* **17**(10), 1392–1402.

Leonard, B. (1991), 'The ultimate conservative difference scheme applied to unsteady one-dimensional advection', *Computer Methods in Applied Mechanics and Engineering* **88**(1), 17–74.

Leonard, B. P. (1979), 'A stable and accurate convective modelling procedure based on quadratic upstream interpolation', *Computer Methods in Applied Mechanics and Engineering* **19**, 415–438.

Lesage, F. L. (2012), quasi static bubble shape analysis in the development of models for adiabatic and diabatic growth and departure, PhD thesis, McMaster University, Hamilton, Ontario.

Li, Y., Yang, G., Zhang, J. and Fan, L. S. (2001), 'Numerical studies of bubble formation dynamics in gas/liquid/solid fluidization at high pressures', *Powder Technology* **116**(2), 246–260.

Liu, H., Krishnan, S., Marella, S. and Udaykumar, H. (2005), 'Sharp interface Cartesian grid method II: A technique for simulating droplet interactions with surfaces of arbitrary shape', *Journal of Computational Physics* **210**(1), 32–54.

Liu, X. D., Osher, S. and Chan, T. (1994), 'Weighted essentially non-oscillatory schemes', *Journal of Computational Physics* **115**(1), 200–212.

Longuet-Higgins, M. S., Kerman, B. R. and Lunde, K. (1991), 'The release of air bubbles from an underwater nozzle', *J.Fluid Mech* **230**, 365–390.

López, J. and Hernández, J. (2008), 'Analytical and geometrical tools for 3D volume of fluid methods in general grids', *Journal of Computational Physics* **227**(12), 5939–5948.

López, J., Hernández, J., Gómez, P. and Faura, F. (2004), 'A volume of fluid method based on multidimensional advection and spline interface reconstruction', *Journal of Computational Physics* **195**(2), 718–742.

López, J., Hernández, J., Gómez, P. and Faura, F. (2005), 'An improved PLIC VOF method for tracking thin fluid structures in incompressible two-phase flows', *Journal of Computational Physics* **208**(1), 51–74.

Lörstad, D. and Fuchs, L. (2004), 'High order surface tension VOF model for 3D bubble flows with high density ratio', *Journal of Computational Physics* **200**(1), 153–176.

Losasso, F., Fedkiw, R. and Osher, S. (2006), 'Spatially adaptive techniques for level set methods and incompressible flow', *Computers & Fluids* **35**(10), 995–1010.

Ma, D., Liu, M., Zu, Y. and Tang, C. (2012), 'Two-dimensional volume of fluid simulation studies on single bubble formation and dynamics in bubble columns', *Chemical Engineering Science* **72**, 61–77.

Malysa, K., Krasowska, M. and Krzan, M. (2005), 'Influence of surface active substances on bubble motion and collision with various interfaces', *Advances in Colloid and Interface Science* **114**, 205–225.

Manservisi, S. and Scardovelli, R. (2009), 'A variational approach to the contact angle dynamics of spreading droplets', *Computers & Fluids* **38**(2), 406–424.

Martín, M., Montes, F. J. and Galán, M. A. (2007), 'Bubble coalescence at sieve plates: Ii. effect of coalescence on mass transfer. superficial area versus bubble oscillations', *Chemical Engineering Science* **62**(6), 1741 – 1752.

MATLAB (2012). MATLAB and Statistics Toolbox Release 2012b, The MathWorks, Inc., Natick, Massachusetts, United States.,http://www.mathworks.co.uk/.

McCann, D. and Prince, R. (1971), 'Regimes of bubbling at a submerged orifice', *Chemical Engineering Science* **26**(10), 1505–1512.

Ménard, T., Tanguy, S. and Berlemont, A. (2007), 'Coupling level set/VOF/ghost fluid methods: Validation and application to 3D simulation of the primary break-up of a liquid jet', *International Journal of Multiphase Flow* **33**(5), 510–524.

Moes, N., Dolbow, J. and Belytschko, T. (1999), 'A finite element method for crack growth without remeshing', *International Journal for Numerical Methods in Engineering* **46**(1), 131–150.

Monaghan, J. J. (1994), 'Simulating free surface flows with SPH', *Journal of computational physics* **110**(2), 399–406.

Moore, D. (1965), 'The velocity of rise of distorted gas bubbles in a liquid of small viscosity', *Journal of Fluid Mechanics* **23**(04), 749–766.

Mukundakrishnan, K., Quan, S., Eckmann, D. M. and Ayyaswamy, P. S. (2007), 'Numerical study of wall effects on buoyant gas-bubble rise in a liquid-filled finite cylinder', *Physical Review E* **76**(3), 036308.

Mulder, W., Osher, S. and Sethian, J. A. (1992), 'Computing interface motion in compressible gas dynamics', *Journal of Computational Physics* **100**(2), 209–228.

Muradoglu, M. and Tasoglu, S. (2010), 'A front-tracking method for computational modeling of impact and spreading of viscous droplets on solid walls', *Computers & Fluids* **39**(4), 615–625.

Muzaferija, S. and Perić, M. (1997), 'Computation of free-surface flows using the finite-volume method and moving grids', *Numerical Heat Transfer* **32**(4), 369–384.

Muzaferija, S. and Peric, M. (1999), 'Computation of free-surface flows using interface tracking and interface-capturing methods', *Advances in Fluid Mechanics* **24**, 59–100.

Muzaferija, S., Peric, M., Sames, P. and Schellin, T. (1998), A two-fluid Navier-Stokes solver to simulate water entry, *in* 'Proc 22nd Symposium on Naval Hydrodynamics', pp. 277–289.

Newman, S. (1968), 'Kinetics of wetting of surfaces by polymers; capillary flow', *Journal of colloid and interface science* **26**(2), 209–213.

Ngan, C. and Dussan, E. (1989), 'On the dynamics of liquid spreading on solid surfaces', *J.Fluid Mech* **209**, 191–226.

Nichita, B. A., Zun, I. and Thome, J. R. (2010), 'A Level Set Method Coupled With a Volume of Fluid Method for Modeling of Gas-Liquid Interface in Bubbly Flow', *Journal of fluids engineering* **132**(8).

Noh, W. and Woodward, P. (1976), SLIC (simple line interface calculation), *in* 'Proceedings of the Fifth International Conference on Numerical Methods in Fluid Dynamics June 28 July 2, 1976 Twente University, Enschede', Springer, pp. 330–340.

Oguz, H. N. and Prosperetti, A. (1993), 'Dynamics of bubble growth and detachment from a needle', *Journal of Fluid Mechanics* **257**, 111–145.

Ohta, M., Imura, T., Yoshida, Y. and Sussman, M. (2005), 'A computational study of the effect of initial bubble conditions on the motion of a gas bubble rising in viscous liquids', *International Journal of Multiphase Flow* **31**(2), 223–237.

Ohta, M., Kikuchi, D., Yoshida, Y. and Sussman, M. (2011), 'Robust numerical analysis of the dynamic bubble formation process in a viscous liquid', *International Journal of Multiphase Flow* **37**, 1059–1071.

Ohta, M. and Sussman, M. (2012), 'The buoyancy-driven motion of a single skirted bubble or drop rising through a viscous liquid', *Physics of Fluids* **24**(11), 112101–112101–18.

Olsson, E. and Kreiss, G. (2005), 'A conservative level set method for two phase flow', *Journal of Computational Physics* **210**(1), 225–246.

Olsson, E., Kreiss, G. and Zahedi, S. (2007), 'A conservative level set method for two phase flow ii', *Journal of Computational Physics* **225**(1), 785–807.

Omori, T., Kayama, H., Tukovic, Z. and Kajishima, T. (2010), Interface resolving simulation of bubble - wall collision dynamics, *in* '7th international conference on multiphase flow'.

OpenFOAM (2010). OpenFOAM 1.7, OpenFOAM Ltd, The open source CFD toolbox, //http://www.openfoam.com/.

Osher, S. and Sethian, J. A. (1988), 'Fronts propagating with curvature-dependent speed: algorithms based on Hamilton-Jacobi formulations', *Journal of computational physics* **79**(1), 12–49.

Painmanakula, P., Loubierea, K., Hebrarda, G. and Buffiereb, P. (2004), 'Study of different membrane spargers used in waste water treatment: characterisation and performance', *Chemical Engineering and Processing: Process Intensification* **43**(11), 1347 – 1359.

ParaView (2012). ParaView 3.98.1, Kitware, Inc., Clifton Park, New York 12065 USA, http://www.paraview.org/.

Patankar, S. V. and Spalding, D. B. (1972), 'A calculation procedure for heat, mass and momentum transfer in three-dimensional parabolic flows', *International Journal of Heat and Mass Transfer* **15**(10), 1787–1806.

Phan, C. M., Nguyen, A. V. and Evans, G. M. (2006), 'Combining hydrodynamics and molecular kinetics to predict dewetting between a small bubble and a solid surface', *Journal of colloid and interface science* **296**(2), 669–676.

Pilliod, J. E. (1992), 'An analysis of piecewise linear interface reconstruction algorithms for volume-of-fluid methods', *M.S. Thesis, University of California, Davis* .

Pilliod, J. E. and Puckett, E. G. (2004), 'Second order accurate volume of fluid algorithms for tracking material interfaces', *Journal of Computational Physics* **199**(2), 465–502.

Popescu, M. N., Ralston, J. and Sedev, R. (2008), 'Capillary rise with velocity-dependent dynamic contact angle', *Langmuir* **24**(21), 12710–12716.

Popinet, S. and Zaleski, S. (1999), 'A front tracking algorithm for accurate representation of surface tension', *International Journal for Numerical Methods in Fluids* **30**(6), 775–793.

Puckett, E. (1991), A volume of fluid interface tracking algorithm with applications to computing shock wave refraction, *in* 'Proceedings of the Fourth International Symposium on Computational Fluid Dynamics', pp. 933–938.

Qian, T., Wang, X.-P. and Sheng, P. (2003), 'Molecular scale contact line hydrodynamics of immiscible flows', *Physical Review E* **68**(1), 016306.

Qian, T., Wang, X.-P. and Sheng, P. (2006), 'A variational approach to moving contact line hydrodynamics', *Journal of Fluid Mechanics* **564**(333-360), 146.

Qin, T., Ragab, S. and Yue, P. (2013), 'Axisymmetric simulation of the interaction of a rising bubble with a rigid surface in viscous flow', *International Journal of Multiphase Flow* **52**, 60–70.

Quan, S. and Hua, J. (2008), 'Numerical studies of bubble necking in viscous liquids', *Physical Review E* **77**(6), 66303.

Rabha, S. S. and Buwa, V. V. (2010), 'Volume-of-fluid (VOF) simulations of rise of single/multiple bubbles in sheared liquids', *Chemical Engineering Science* **65**(1), 527–537.

Raessi, M. and Pitsch, H. (2012), 'Consistent mass and momentum transport for simulating incompressible interfacial flows with large density ratios using the level set method', *Computers & Fluids* **63**, 70–81.

Raymond, F. and Rosant, J. M. (2000), 'A numerical and experimental study of the terminal velocity and shape of bubbles in viscous liquids', *Chemical Engineering Science* **55**(5), 943–955.

Renardy, M., Renardy, Y. and Li, J. (2001), 'Numerical simulation of moving contact line problems using a volume-of-fluid method', *Journal of Computational Physics* **171**(1), 243–263.

Renardy, Y. and Renardy, M. (2002), 'PROST: a parabolic reconstruction of surface tension for the volume-of-fluid method', *Journal of Computational Physics* **183**(2), 400–421.

Rhie, C. and Chow, W. (1983), 'Numerical study of the turbulent flow past an airfoil with trailing edge separation', *AIAA Journal* **21**(11), 1525–1532.

Rider, W. J. and Kothe, D. B. (1998), 'Reconstructing volume tracking', *Journal of computational physics* **141**(2), 112–152.

Roisman, I., Opfer, L., Tropea, C., Raessi, M., Mostaghimi, J. and Chandra, S. (2008), 'Drop impact onto a dry surface: Role of the dynamic contact angle', *Colloids and Surfaces A: Physicochemical and Engineering Aspects* **322**(1), 183–191.

Rudman, M. (1997), 'volume tracking methods for interfacial flow calculations', *International Journal for Numerical Methods in Fluids* **24**(7), 671–691.

Rusche, H. (2002), 'Computational fluid dynamics of dispersed two-phase flows at high phase fraction, phd thesis, imperial college of science, technology and medicins, london'.

Saffman, P. (1956), 'On the rise of small air bubbles in water', *Journal of Fluid Mechanics* **1**(03), 249–275.

Saha, A. A. and Mitra, S. K. (2009), 'Effect of dynamic contact angle in a volume of fluid (VOF) model for a microfluidic capillary flow', *Journal of colloid and interface science* **339**(2), 461–480.

Sanada, T., Watanabe, M. and Fukano, T. (2005), 'Effects of viscosity on coalescence of a bubble upon impact with a free surface', *Chemical engineering science* **60**(19), 5372–5384.

Sato, Y. and Niceno, B. (2012), 'A new contact line treatment for a conservative level set method', *Journal of Computational Physics* **231**(10), 3887–3895.

Scardovelli, R. and Zaleski, S. (2000), 'Analytical relations connecting linear interfaces and volume fractions in rectangular grids', *Journal of Computational Physics* **164**(1), 228–237.

Scardovelli, R. and Zaleski, S. (2003), 'Interface reconstruction with least square fit and split Eulerian Lagrangian advection', *International Journal for Numerical Methods in Fluids* **41**(3), 251–274.

Sethian, J. A. (1999), *Level set methods and fast marching methods: evolving interfaces in computational geometry, fluid mechanics, computer vision, and materials science*, Vol. 3, Cambridge university press.

Shan, X. and Chen, H. (1993), 'Lattice Boltzmann model for simulating flows with multiple phases and components', *Physical Review E* **47**(3), 1815.

Sheng, P. and Zhou, M. (1992), 'Immiscible-fluid displacement: Contact-line dynamics and the velocity-dependent capillary pressure', *Physical Review A* **45**(8), 5694.

Shikhmurzaev, Y. D. (1997), 'Moving contact lines in liquid/liquid/solid systems', *Journal of Fluid Mechanics* **334**(1), 211–249.

Shu, C.-W. and Osher, S. (1988), 'Efficient implementation of essentially non-oscillatory shock-capturing schemes', *Journal of Computational Physics* **77**(2), 439–471.

Shu, S. and Yang, N. (2013), 'Direct numerical simulation of bubble dynamics using phase field model and lattice boltzmann method', *Industrial & Engineering Chemistry Research* .

Sikalo, S., Wilhelm, H.-D., Roisman, I., Jakirlić, S. and Tropea, C. (2005), 'Dynamic contact angle of spreading droplets: experiments and simulations', *Physics of Fluids* **17**, 062103.

Somalinga, S. and Bose, A. (2000), 'Numerical investigation of boundary conditions for moving contact line problems', *Physics of Fluids* **12**, 499.

Son, G. (2001), 'A numerical method for bubble motion with phase change', *Numerical Heat Transfer: Part B: Fundamentals* **39**(5), 509–523.

Son, G. (2003), 'Efficient implementation of a coupled level set and volume of fluid method for three-dimensional incompressible two-phase flows', *Numerical Heat Transfer, Part B: Fundamentals* **43**(6), 549–565.

Son, G., Dhir, V. K. and Ramanujapu, N. (1999), 'Dynamics and heat transfer associated with a single bubble during nucleate boiling on a horizontal surface', *Journal of Heat Transfer* **121**, 623–631.

Son, G. and Hur, N. (2002), 'A coupled level set and volume-of-fluid method for the buoyancy-driven motion of fluid particles', *Numerical Heat Transfer, Part B: Fundamentals* **42**(6), 523–542.

Spaid, M. and Homsy, G. (1996), 'Stability of newtonian and viscoelastic dynamic contact lines', *Physics of Fluids* **8**(2), 460–478.

Spelt, P. D. (2005), 'A level-set approach for simulations of flows with multiple moving contact lines with hysteresis', *Journal of Computational physics* **207**(2), 389–404.

Sun, D. and Tao, W. (2010), 'A coupled volume-of-fluid and level set (VOSET) method for computing incompressible two-phase flows', *International Journal of Heat and Mass Transfer* **53**(4), 645–655.

Sussman, M. (2003), 'A second order coupled level set and volume-of-fluid method for computing growth and collapse of vapor bubbles', *Journal of Computational Physics* **187**(1), 110–136.

Sussman, M., Almgren, A. S., Bell, J. B., Colella, P., Howell, L. H. and Welcome, M. L. (1999), 'An adaptive level set approach for incompressible two-phase flows', *Journal of Computational Physics* **148**(1), 81–124.

Sussman, M., Fatemi, E., Smereka, P. and Osher, S. (1998), 'An improved level set method for incompressible two-phase flows', *Computers & Fluids* **27**(5-6), 663–680.

Sussman, M. and Puckett, E. G. (2000), 'A coupled level set and volume of fluid method for computing 3D and axisymmetric incompressible two-phase flows', *Journal of Computational Physics* **162**(2), 301–337.

Sussman, M., Smereka, P. and Osher, S. (1994), 'A level set approach for computing solutions to incompressible two-phase flow', *Journal of computational Physics* **114**(1), 146–159.

Sussman, M., Smith, K., Hussaini, M., Ohta, M. and Zhi-Wei, R. (2007), 'A sharp interface method for incompressible two-phase flows', *Journal of Computational Physics* **221**(2), 469–505.

Taha, T. and Cui, Z. (2002), 'CFD modelling of gas-sparged ultrafiltration in tubular membranes', *Journal of Membrane Science* **210**(1), 13 – 27.

Thompson, P. A. and Robbins, M. O. (1989), 'Simulations of contact-line motion: slip and the dynamic contact angle', *Physical Review Letters* **63**(7), 766–769.

Thoroddsen, S., Etoh, T. and Takehara, K. (2007), 'Experiments on bubble pinch-off', *Physics of Fluids* **19**, 042101.

Tomiyama, A., Celata, G., Hosokawa, S. and Yoshida, S. (2002), 'Terminal velocity of single bubbles in surface tension force dominant regime', *International Journal of Multiphase Flow* **28**(9), 1497–1519.

Tong, A. Y. and Wang, Z. (2007), 'A numerical method for capillarity-dominant free surface flows', *Journal of Computational Physics* **221**(2), 506–523.

TransAT (2011). TransAT 2.0.3, ASCOMP GmbH, Zurich, Switzerland, http://http://www.ascomp.ch.

Tsao, H. K. and Koch, D. L. (1997), 'Observations of high reynolds number bubbles interacting with a rigid wall', *Physics of Fluids* **9**, 44.

Ubbink, O. (1997), 'Numerical prediction of two fluid systems with sharp interfaces'.

Ubbink, O. and Issa, R. (1999), 'A method for capturing sharp fluid interfaces on arbitrary meshes', *Journal of Computational Physics* **153**(1), 26–50.

Unverdi, S. O. and Tryggvason, G. (1992), 'A front-tracking method for viscous, incompressible, multi-fluid flows', *Journal of Computational Physics* **100**(1), 25–37.

Vafaei, S., Borca-Tasciuc, T. and Wen, D. (2010), 'Theoretical and experimental investigation of quasi-steady-state bubble growth on top of submerged stainless steel nozzles', *Colloids and Surfaces A: Physicochemical and Engineering Aspects* **369**(1-3), 11–19.

Valencia, A., Cordova, M. and Ortega, J. (2002), 'Numerical simulation of gas bubbles formation at a submerged orifice in a liquid', *International Communications in Heat and Mass Transfer* **29**(6), 821–830.

Van Leer, B. (1979), 'Towards the ultimate conservative difference scheme. V. A second-order sequel to Godunov's method', *Journal of Computational Physics* **32**(1), 101–136.

Versteeg, H. K. (1995), *An introduction to computational fluid dynamics the finite volume method, 2/E*, Pearson Education India.

Villiers, E. D., Gosman, A. and Weller, H. (2008), Large eddy simulation of primary diesel spray atomization, Technical report. Technical Report 2004-01-0100 SAE.

Voinov, O. (1976), 'Hydrodynamics of wetting', *Fluid Dynamics* **11**(5), 714–721.

Walters, J. and Davidson, J. (1963), 'The initial motion of a gas bubble formed in an inviscid liquid', *Journal of Fluid Mechanics* **17**(03), 321–336.

Wang, H., Zhang, Z.-Y., Yang, Y.-M. and Zhang, H.-S. (2010), 'Surface tension effects on the behaviour of a rising bubble driven by buoyancy force', *Chinese Physics B* **19**(2), 6801.

Wang, Y., Simakhina, S. and Sussman, M. (2012), 'A hybrid level set-volume constraint method for incompressible two-phase flow', *Journal of Computational Physics* **231**, 6438–6471.

Weller, H. (1993), The development of a new flame area combustion model using conditional averaging, Technical Report 9307, Citeseer. Forschungsbericht.

Weller, H. G. (2008), A new approach to VOF-based interface capturing methods for incompressible and compressible flows, Technical report. Forschungsbericht.

Wu, J., Dhir, V. K. and Qian, J. (2007), 'Numerical simulation of subcooled nucleate boiling by coupling level-set method with moving-mesh method', *Numerical Heat Transfer, Part B: Fundamentals* **51**(6), 535–563.

Yang, G., Du, B. and Fan, L. S. (2007), 'Bubble formation and dynamics in gas-liquid-solid fluidization-A review', *Chemical engineering science* **62**(1-2), 2–27. fluidized bed application.

Yang, X., James, A. J., Lowengrub, J., Zheng, X. and Cristini, V. (2006), 'An adaptive coupled level-set/volume-of-fluid interface capturing method for unstructured triangular grids', *Journal of Computational Physics* **217**(2), 364–394.

Yang, Z., Dinh, T.-N., Nourgaliev, R. and Sehgal, B. (2001), 'Numerical investigation of bubble growth and detachment by the lattice-Boltzmann method', *International Journal of Heat and Mass Transfer* **44**(1), 195–206.

Yokoi, K., Vadillo, D., Hinch, J. and Hutchings, I. (2009), 'Numerical studies of the influence of the dynamic contact angle on a droplet impacting on a dry surface', *Physics of Fluids* **21**, 072102.

Yoon, H. Y., Koshizuka, S. and Oka, Y. (2001), 'Direct calculation of bubble growth, departure, and rise in nucleate pool boiling', *International Journal of Multiphase Flow* **27**(2), 277–298.

Youngs, D. L. (1982), 'Time-dependent multi-material flow with large fluid distortion', *Numerical methods for fluid dynamics* **1**(1), 41–51.

Yu, Z. and Fan, L.-S. (2008), 'Direct simulation of the buoyant rise of bubbles in infinite liquid using level set method', *The Canadian Journal of Chemical Engineering* **86**(3), 267–275.

Yu, Z. and Fan, L.-S. (2010), 'Multirelaxation-time interaction-potential-based lattice boltzmann model for two-phase flow', *Physical Review E* **82**(4), 046708.

Zalesak, S. T. (1979), 'Fully multidimensional flux-corrected transport algorithms for fluids', *Journal of Computational Physics* **31**(3), 335–362.

Zawala, J., Krasowska, M., Dabros, T. and Malysa, K. (2007), 'Influence of bubble kinetic energy on its bouncing during collisions with various interfaces', *The Canadian Journal of Chemical Engineering* **85**(5), 669–678.

Zedníková, M. F., Vobecká, L. and Vejrazka, J. (2010), 'Effect of solid material and surfactant presence on interactions of bubbles with horizontal solid surface', *The Canadian Journal of Chemical Engineering* **88**(4), 473–481.

Zenit, R. and Legendre, D. (2009), 'The coefficient of restitution for air bubbles colliding against solid walls in viscous liquids', *Physics of Fluids* **21**, 083306.

Zhang, J. (2011), 'Lattice boltzmann method for microfluidics: models and applications', *Microfluidics and Nanofluidics* **10**(1), 1–28.

Zhang, J. and Kwok, D. Y. (2004), 'Lattice boltzmann study on the contact angle and contact line dynamics of liquid-vapor interfaces', *Langmuir* **20**(19), 8137–8141.

Zhang, Y., Yeo, K., Khoo, B. and Wang, C. (2001), '3D jet impact and toroidal bubbles', *Journal of Computational Physics* **166**(2), 336–360.

Publications

Journal and conference papers

- Delauré, Y.M.C. & Albadawi, A. (2010), On air bubble sliding through a thermal boundary layer, *in* '5th OpenFOAM workshop, Gothenburg, Sweden'.
- Albadawi, A., Delauré, Y.M.C., Donoghue, D.B., Robinson, A.J. & Murray, D.B. (2012), Numerical investigation of Volume of Fluid and Level Set interface capturing methods for bubble growth and detachment, *in* 'Journal of Physics: Conference Series', Vol.395, IOP Publishing, p.012166.
- Donoghue, D.B., Delauré, Y.M.C., Albadawi, A., D.B., Robinson, A.J. & Murray, D.B. (2012), Bouncing bubble dynamics and associated enhancement of heat transfer, *in* 'Journal of Physics: Conference Series', Vol.395, IOP Publishing, p.012167.
- Albadawi, A., Donoghue, D.B., Robinson, A.J., Murray, D.B. & Delauré, Y.M.C. (2013), 'On the analysis of bubble growth and detachment at low Capillary and Bond numbers using Volume of Fluid and Level Set methods', *Chemical Engineering Science* **90**, 77-91.
- Albadawi, A., Donoghue, D.B., Robinson, A.J., Murray, D.B. & Delauré, Y.M.C. (2013), 'Influence of surface tension implementation in Volume of Fluid and coupled Volume of Fluid with Level Set methods for bubble growth and detachment', *International Journal of Multiphase Flow* **53**, 11-28.
- Donoghue, D.B., Albadawi, A., Delauré, Y.M.C., Robinson, A.J., & Murray, D.B., (2013) Wake effects from a rising air bubble impacting a horizontal heated surface, *in* '8th World Conference on Experimental Heat transfer, Fluid Mechanics, and Thermodynamics, Lisbon, Portugal'.
- Donoghue, D.B., Albadawi, A., Delauré, Y.M.C., Robinson, A.J., & Murray, D.B., (2013), 'Bubble Impingement and the Mechanisms of Heat Transfer',

Accepted for publications in *International Journal of Mass and Heat Transfer*.

- Albadawi, A., Donoghue, D.B., Robinson, A.J., Murray, D.B. & Delauré, Y.M.C. (2014), 'Numerical analysis of bubble bouncing using the Volume of Fluid method', Submitted to *International Journal of Multiphase Flow*.

Posters and presentations

- Albadawi, A., & Delauré, Y.M.C. (2011), Dynamics of bubble bouncing, *in* 'Faculty Research day, Faculty of Engineering and Computing'. (2nd prize winner for poster and 1st prize winner as presenter).
- Albadawi, A., & Delauré, Y.M.C. (2012), Numerical analysis of bubble dynamics,*in* 'Faculty Research day, Faculty of Engineering and Computing'.
- Albadawi, A., & Delauré, Y.M.C. (2012), Numerical analysis of bubble growth and bouncing, *in* 'Center for Scientific Computing & Complex Systems Modeling, Annual meeting, Dublin City university'.
- Albadawi, A., & Delauré, Y.M.C. (2012 & 2013), Thesis in 3 Presentation, Numerical analysis of bubble dynamics, *in* 'Center for Scientific Computing & Complex Systems Modeling, Annual meeting, Dublin City university'. (1st prize winner for years 2012 and 2013).
- Albadawi, A., & Delauré, Y.M.C. (November 2013), symposium of Irish society for scientific and engineering computation, On the assessment of interface capturing methods for Multiphase Flow applications, *in* 'Univesity College Dublin, Irealnd'.

Co-supervising projects

- Mathilde Ciry (Summer, 2012), An assessment of CFD predictions of the dynamics of detaching air bubbles in water, Internship project, *in* 'School of Mechanical and Manufacturing Engineering, Dublin City University', *in co-operation with* Département Hydraulique et Mécanique des Fluides, ENSEEIHT, Toulouse, France.
- Thibaut Moy (Summer, 2013), An assessment of CFD predictions of the dynamics of air bubble in water and their interactions with solid surfaces, *in*

'School of Mechanical and Manufacturing Engineering, Dublin City University', *in co-operation with* Département Hydraulique et Mécanique des Fluides, ENSEEIHT, Toulouse, France.